Functionalisation and Characterisation of Bulk and Two-Dimensional Semiconductors

Maart Kate van Druenen, BSc. (Hons)

School of Chemistry

University College Cork

Ireland

University College Cork, Ireland
Coláiste na hOllscoile Corcaigh

Presented for the degree of Doctor of Philosophy to the National University of Ireland

Supervisor: **Prof. Justin D. Holmes**

Head of School: Dr. Humphrey Moynihan

August 2019

Table of Contents

Declaration

I, Maart Kate van Druenen, certify that this thesis is my own research and I have not obtained a degree in University College Cork or elsewhere on the basis of this PhD thesis.

Maart Kate van Druenen

Abstract

The continual scaling of semiconductor devices has created a high demand for new techniques and materials that satisfy Moore's Law: the number of transistors on a chip doubles every 12-18 months. The move from planar to three-dimensional (3D) transistor geometries requires compatible doping technologies that meet the demands of Moore's Law. Monolayer doping (MLD) has shown promise in achieving uniformly doped regions compared to currently implemented techniques. However, the continuous use of silicon (Si) as a device material to satisfy Moore's law is becoming challenging and new materials are currently being investigated to potentially replace Si. One of these materials is black phosphorus (BP) which displays a high carrier mobility making it a viable candidate for some electronic devices, although the ambient stability of BP is a key challenge, which makes its processing difficult, and functionalisation has been employed as a potential protection strategy to enhance its oxidation resistance. Additionally, antimonene (AM) has been proposed as a device material that displays a superior ambient stability compared to BP. This thesis aims to address some of the challenges faced when preparing three materials, Si, BP and AM, for device applications in order to satisfy Moore's Law. Functionalisation of SiO_2 surfaces was used for monolayer doping which resulted in tuning of the electrical properties of Si. The functionalisation of BP was used to enhance its ambient stability while the liquid exfoliation of AM was also investigated.

Chapter 1 discusses the recent developments in MLD and evaluates the role of surface chemistry in optimising dopant placement and concentration. The application of the MLD process to 3D architectures is also summarised. The characterisation of carbon contamination is discussed which is a significant concern of the MLD process, in

addition to evaluation of the strategies used to circumvent carbon incorporation. The production and use of new two-dimensional (2D) materials, such as BP and AM, have shown promise in becoming viable candidates to replace Si. The ambient stability of BP remains a key issue and recent progress in the elucidation of the degradation mechanism is assessed. Current protecting strategies are outlined including capping layers, covalent and non-covalent functionalisation as well as solvent- and polymer-based protection strategies. AM is also introduced, which shows promising electrical characteristics.

Chapter 2 discusses the functionalisation of SiO_2 surfaces with phosphonic acids for MLD applications. X-ray photoelectron spectroscopy (XPS) and attenuated total reflectance Fourier transform infrared (ATR-FTIR) spectroscopy were used to investigate the surface chemistry and its effect on the doping of Si. The oxide functionalisation strategy was compared to traditional functionalisation methods used for MLD, such as hydrosilylation. Electrochemical capacitance voltage (ECV) and secondary ion mass spectrometry (SIMS) analysis revealed similar active peak carrier concentrations can be achieved using hydrosilylation and oxide functionalisation, but more importantly the oxide layer successfully minimised carbon contamination, one of the limitations of MLD.

Chapter 3 introduces the liquid exfoliation of BP and describes its ambient degradation. XPS and ATR-FTIR spectroscopy were used to assess the degradation products and analysis indicated decomposition occurred through the conversion of non-bridging to bridging oxide species, resulting in the production of volatile oxidation products in a continuous oxidation cycle.

Chapter 4 focuses on the functionalisation of BP using iodonium salts and compares the strategy to functionalisation using diazonium salts. Iodonium functionalisation was found to inhibit bridged oxide formation, thereby greatly enhancing the ambient stability. In comparison, diazonium functionalisation resulted in oxidation, multilayer formation and an increase in solvent passivation. XPS and scanning transmission electron microscopy (STEM) analysis displayed an increase in the oxidation resistance of iodonium functionalised BP when compared to unfunctionalised BP or diazonium functionalised BP.

Chapter 5 investigates the simultaneous exfoliation and functionalisation of BP which provides a scalable method of synthesising air-stable BP flakes. The addition of a tetrabutylammonium salt that acts as an intercalating agent facilitates the formation of flakes with large lateral dimensions. The subsequent reaction with an aryl iodide results in aryl functionalisation, as characterised using XPS and ATR-FTIR. The immediate functionalisation directly after exfoliation significantly enhanced the ambient stability to a period of 1 week, as evaluated using XPS, STEM and atomic force microscopy (AFM).

Chapter 6 presents the liquid exfoliation of AM using various solvents. The exfoliation in common solvents results in the formation of flakes with small areas. The use of an intercalating agent significantly enhances the lateral dimensions of AM nanosheets, as analysed using AFM, making them more suitable for device applications.

Chapter 7 summarises the conclusions from each chapter and provides a future outlook.

Common Abbreviations and Acronyms

2D:	Two-Dimensional
3D:	Three-Dimensional
ABAPE:	Allyl boronic acid pinacol ester
ACN:	Acetonitrile
ADPO:	Allyldiphenylphosphine oxide
AFM:	Atomic Force Microscopy
AIBN:	Azodiisobutyronitrile
ALD:	Atomic Layer Deposition
AM:	Antimonene
AMQDs:	Antimonene Quantum Dots
APT:	Atom Probe Tomography
ATR-FTIR:	Attenuated Total Reflectance-Fourier Transform Infrared Spectroscopy
BA:	Boronic Acid
BE:	Binding Energy
BP:	Black Phosphorus
BN:	Boron Nitride
CHP:	N-cyclohexyl-2-pyrrolidone
CVD:	Chemical Vapour Deposition
DAP:	Diethyl Allylphosphonate
DCM:	Dichloromethane
DFT:	Density Functional Theory
DI:	Deionised water
DLTS:	Deep-level Transient Spectroscopy
DMF:	Dimethylformamide
DMSO:	Dimethyl Sulfoxide
DPA:	n-Dodecylphosphosphonic acid

DPP:	Diphenylphosphine
DVP:	Diethylvinyl phosphonate
ECV:	Electrochemical Capacitance Voltage
EELS:	Electron Energy Loss Spectroscopy
EG:	Ethylene Glycol
FBD:	3,5-Bis(trifluoromethyl)benzenediazonium Tetrafluoroborate
FET:	Field Effect Transistor
FFT:	Fast Fourier Transform
FinFET:	Fin Field Effect Transistor
FOPA:	1H,1H,2H,2H–Perfluorooctanephosphonic Acid
FPI:	Bis(4-fluorophenyl)iodonium Trifluoromethanesulfonate
FWHM:	Full Width at Half Maximum
Ge:	Germanium
HF:	Hydrofluoric Acid
IBF:	4-Iodobenzotrifluoride
IPA:	Isopropyl Alcohol
IL:	Ionic Liquid
ITO:	Indium Tin Oxide
KPFM:	Kelvin Probe Force Microscopy
LPE:	Liquid Phase Exfoliation
MBD:	Methoxybenzenediazonium Tetrafluoroborate
MLCD:	Monolayer Contact Doping
MLD:	Monolayer Doping
MPI:	Bis(4-methylphenyl)iodonium Hexfluorophosphate
NAOS:	Nitric Acid Oxidation of Silicon
NBD:	4-Nitrobenzenediazonium tetrafluoroborate
NMP:	N-methyl-2-pyrrolidone
NMR:	Nuclear Magnetic Resonance
NW:	Nanowire

OPA: Octadecylphosphonic Acid

PBA: Phenylboronic Acid

PDMS: Poly-dimethylsiloxane

PIL: Polymer Ionic Liquid

PL: Photoluminescence

PLGA: Poly(lactic-co-glycolic acid)

PMMA: Poly(methyl methacrylate)

PPA: Phenylphosphonic Acid

PPI: (Perfluoro-n-propyl)phenyliodonium Trifluoromethanesulfonate

PVP: Polyvinylpyrrolidone

QD: Quantum Dot

RCA: Radio Corporation of America

RTA: Rapid Thermal Anneal

SAED: Selected Area Electron Diffraction

SAM: Self-Assembled Monolayer

Si: Silicon

SIMS: Secondary Ion Mass Spectrometry

SOI: Silicon on Insulator

STEM: Scanning Transmission Electron Microscopy

TBA: Tetrabutylammonium

TBAFP: Tetrabutylammonium Hexafluorophosphate

TCNQ: Tetracyanoquinodimethane

TEM: Transmission Electron Microscopy

TGA: Thermogravimetric Analysis

THF: Tetrahydrofuran

TMD: Transition Metal Dichalcogenide

ToF-SIMS: Time of Flight Secondary Ion Mass Spectrometry

TTF: Tetrathiafulvalene

USJ: Ultra-shallow junction

UV-VIS: Ultraviolet-visible

VPA: Vinylphosphonic acid

WCA: Water Contact Angle

XPS: X-ray Photoelectron Spectroscopy

XRD: X-ray Diffraction

Acknowledgements

I would like to thank my supervisor, Prof. Justin Holmes, for his guidance during the course of my PhD. Thanks also to Brenda Long and Gillian Collins.

I would like to thank John and Giuseppe for helping me get set up in the lab and providing training in XPS analysis. I am also grateful to Dr. Ray Duffy for providing advice on the electrical side of my research. I would like to thank the other postdocs in the group, Subha and Eoin, for their guidance. This thesis would not have been possible without my collaborators: in particular Colm Glynn's endless help with electrochemical tests and optical measurements, Fionán Davitt's STEM/TEM expertise and Tim's AFM skills. I am also grateful to Prof. Zdeněk Sofer for providing the BP. I would like to thank the past members of MCAG/115/343, Andrés, Dave and Elaine, and present members, Adria, Alex Lonergan, Alex Game, Éadaoin, Debarati, Karzan, Louise, Noel, Mai, Ricky, Russell, Shane and Tandra for their assistance. To Darragh, Jess and Sally, thank you for brightening up 115 and making my time in UCC more enjoyable.

Thanks to Trevor and Ian for giving me experience in demonstrating and providing technical assistance. I would also like to thank the chemistry office for processing all my order requests. Thanks to Tina and Denis in the stores and Mick, Tony and Johnny for their help with anything that needed fixing.

I would like to thank all my friends and family for their encouragement. In particular, my mother, Ingrid, for her continuous support and advice for which I cannot thank her enough.

Dedication

Dedicated to my mother

Chapter 1

Introduction

This chapter is intended for publication as a review article and therefore sections may contain repeating concepts and paragraphs.

Van Druenen, M. Degradation of Black Phosphorus and Protection Strategies

1. Introduction

1.1 Abstract

The advancement of the nanoelectronics industry has relied on the downscaling of devices by doubling the number of transistors in a circuit every 12-18 months, which is known as Moore's Law. The use of Silicon (Si) has allowed this trend to proceed from the 1960s until the present day, however, the physical limits of transistor fabrication techniques are fast approaching and innovative solutions are required to maintain the predicted trend of Moore's Law.[1] A major challenge is the conformal and defect-free doping of these decreasing feature sizes, which current doping techniques, such as ion implantation, do not provide. Monolayer doping (MLD) has been proposed as a doping technique that overcomes the issues created by other doping techniques due to its high compatibility with current transistor architectures. However, the use of Si as a transistor material is likely to eventually reach its physical limit as a material and an alternative will be required. One of the most promising discoveries have been two-dimensional (2D) materials, such as transition metal dichalcogenides (TMDs) and 2D pnictogens, which display atomically flat thickness while providing significantly superior electronic properties to Si. A potential candidate is black phosphorus (BP) which displays a high carrier mobility and direct bandgap making it a potential candidate for transistor fabrication. Although it has extraordinary properties it has an extremely limiting ambient stability which creates a major hurdle to fully exploiting its properties. Antimonene (AM), another 2D pnictogen, displays similar properties to BP but does not suffer from the ambient instability that BP does.

This chapter outlines the advances in MLD as a doping technique and assesses the challenges of MLD, including carbon contamination. New 2D materials, specifically BP and AM, are introduced while the ambient degradation of BP is discussed in detail as well as the strategies used to prolong its lifetime.

1.2 Introduction

The consistent scaling down of nanostructures in accordance with Moore's Law has allowed an increase in performance at a low cost.[2] In order to comply with Moore's law, new techniques that allow doping of ever decreasing feature sizes are required. Current features sizes are predicted to approach 5 nm in 2021, which presents a major challenge, as current doping and patterning techniques are reaching their limits for the fabrication of transistors.[1] The small junction depth and feature sizes has led to a move from planar to 3D FinFET architectures to optimise performance at low dimensions, although current doping technologies are incompatible with these architectures. Doping of semiconductors, where impurities in the form of electrons or holes are introduced to modify the electrical properties of a material, is used to create junctions. Currently, ion implantation is used for the doping of devices which fires dopant atoms at a high speed at the substrate, but the technique suffers from crystal damage of the substrate caused by high energy ions and difficulty in controlling the dopant depth and distribution. Furthermore, ion implantation does not allow conformal doping of 3D nanostructures and shadowing effects are a major concern.

MLD involves the functionalisation of the semiconductor surface followed by an anneal step that drives the dopant into the substrate. MLD is a promising strategy for achieving conformal and shallow doping in nanostructures. Pioneered by Javey and

coworkers,[3] MLD offers a number of benefits over techniques such as ion implantation. Although ion implantation allows the dose to be tailored, achieving precise control over dopant atom placement remains challenging which will become essential with shrinking device sizes. Literature reports have progressively advanced in the conformal and deterministic doping of nanostructures using MLD.[3,4] While the impact of ion implantation often leaves defects in the doped substrate, MLD offers a gentle strategy of doping resulting in minimal defect formation due to the incorporation of a functionalisation step. Additionally, as MLD employs functionalisation of the surface to distribute dopant atoms uniformly across the surface of nanostructures, the strategy is highly applicable to 3D architectures, such as nanowires. The continual scaling and recent movement to finFET structures demands progression of doping technologies to achieve more precise atom placement, a requirement that MLD shows promise in fulfilling.

MLD has been established as a versatile doping technique, applicable to a variety of 3D device architectures and a range of different substrates; As well as Si, MLD has been used to successfully dope various semiconductors, including Ge,[5,6] InP,[7] InAs,[8] and InGaAs.[9] However, a major concern is the incorporation of carbon that is present in the dopant precursor during the MLD process, which is known as carbon contamination. The thorough characterisation of carbon contamination is vital, as it remains unclear if carbon introduced during the MLD process is electrically active or results in the creation of interstitial defects. The effect of carbon contamination on the electrical performance is also still uncertain. Alternatively, the complete elimination of carbon from the MLD process would be beneficial for the optimal performance of doped devices and efficient dopant activation.

In this chapter, the recent developments in the use of MLD to achieve controlled doping are discussed. The use of the surface chemistry of dopant precursors is highly advantageous in tailoring the dopant concentration while the rapid thermal anneal (RTA) conditions can also be used to tune dopant concentration and junction depth. The process has been successfully transferred to various 3D architectures including nanowire devices. Additionally, the characterisation and minimisation of carbon contamination is evaluated.

1.3 Monolayer Doping

1.3.1 Monolayer Doping of Silicon

MLD of Si nanostructures, reported by Javey and coworkers[3] in 2008, showed successful doping of Si nanowires and Silicon-on-Insulator (SOI) substrates with high doses and spatial distributions. **Figure 1.1** illustrates the MLD process which consists of 2 steps: (1) the functionalisation of the semiconductor surface with the dopant precursor, followed by (2) a rapid thermal anneal (RTA) which drives the dopant into the substrate. The use of functionalisation to attach dopant molecules allows application to p- and n-doping and gives increased control over dose and junction depth.

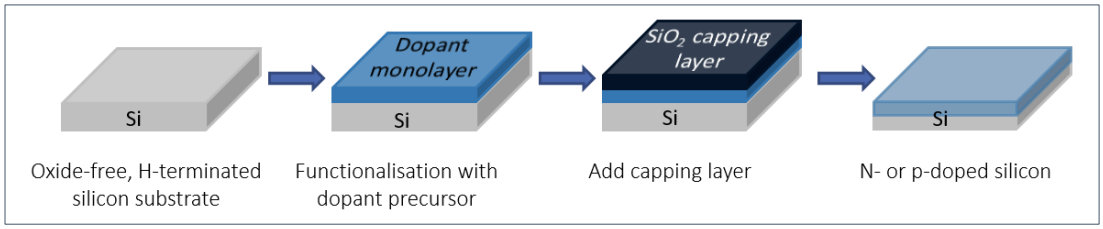

Figure 1.1: Illustration of the MLD process where a H-terminated Si substrate is functionalised with the dopant precursor. A capping layer is added, followed by RTA and removal of the capping layer results in n- or p-doping of the Si substrate.

Ho *et. al.*[3] used allylboronic acid pinacol ester (ABAPE), as shown in **Figure 1.2**(a), which resulted in a peak carrier concentration of ~5 × 10^{20} atoms/cm^{-3} decreasing to ~10^{17} atoms/cm^{-3} at depths of 18 nm and 43 nm for samples annealed at 950 °C and 1000 °C. This procedure was also applied to phosphorus doping using diethyl 1-propylphosphonate (DPP), resulting in the formation of an ultra-shallow junction (USJ) with a peak concentration of ~1 × 10^{22} atoms/cm^{-3} after a 5 s RTA at 950 °C. Peak carrier concentrations and junction depths can be varied by modification of the annealing time and temperature, as displayed in **Figure 1.2**(b).[3,10–12]

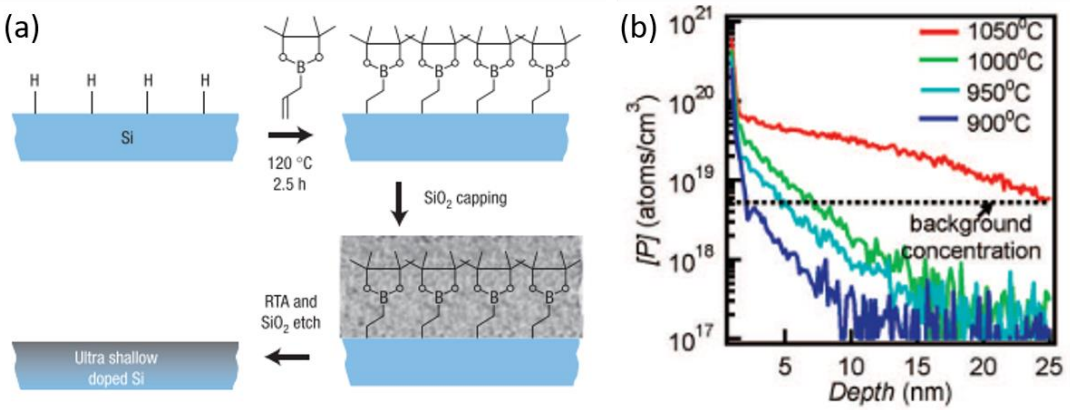

Figure 1.2: (a) The MLD process where the H-terminated Si surface is functionalised using the dopant precursor, ABAPE, followed by capping with an SiO_2 layer. An RTA allows the dopant to enter the substrate and removal of the capping layer exposes the underlying doped substrate. Reprinted from Ho, J. C. *et. al. Nat. Mater.* **2008**, *7* (1), 62–67. (3). (b) SIMS analysis displaying the phosphorus concentration as a function of depth. MLD using DPP for various annealing temperatures and times resulting in an increase in sheet carrier concentrations for higher temperatures but an increase in junction depth. Reprinted from Ho, J. *et. al. Nano Lett.* **2009**, *9* (2), 725–730. (10).

A longer annealing time of 20 s resulted in a decrease in sheet resistance from ~10^5 to ~10^3 Ω/□ until saturation occurred after 20 s, indicating a depletion of the limited dopant source.[3] The peak carrier concentration of 2.5 × 10^{20} atoms/cm^3 at 900 °C was increased to 3.5 × 10^{20} atoms/cm^3 at 950 °C, 4 × 10^{20} atoms/cm^3 at 1000 °C and 5.5 ×

10^{20} atoms/cm^3 at 1050 °C, indicating the peak carrier concentration is dependent on the dopant solubility at a given temperature. However, an increase in the annealing temperature also resulted in an increase in junction depth, which can be observed clearly in **Figure 1.2**(b). A junction depth of 2, 5, 7 or 25 nm is obtained for an anneal temperature of 900, 950, 1000 and 1050 °C which can be attributed to the enhanced dopant diffusivity at higher temperatures.[10] Although a high dose also resulted in a larger junction depth, the variation of the annealing temperature shows promise in fulfilling the required sub-5nm USJ.

In addition to the variation of temperature, MLD enables precise control over the dopant dose through variation of the molecular footprint of the dopant precursor or modifications to the functionalisation process through incorporation of non-dopant containing molecules. Ho *et. al.*[3] used a mixture of dodecene and allylboronic acid pinacol ester (ABAPE) in two different ratios to tailor the dopant doses, which was confirmed by a lower sheet resistance value for a higher concentration of dopant precursor. Further studies by Ye *et. al.*[13] achieved a lower doping dose by mixing the dopant-containing alkene with dopant-free alkenes as shown in **Figure 1.3**. The mixing ratio allowed precise tunability of the dopant dose in the (1.6×10^{19}) to (4.2×10^{18}) cm^{-3} range for boron doped substrates and (2.4×10^{19}) to (2.2×10^{18}) cm^{-3} for phosphorus doped substrates.[13] Alternatively, the dose can be enhanced by using a self-designed molecule that contains a higher amount of the dopant.[14] Carborane molecules contain an increased boron content at a dose of 2.2×10^{13} cm^{-2} compared to 0.3×10^{13} cm^{-2} for ABAPE, which was demonstrated using XPS analysis of boron functionalised surfaces. The higher dopant concentration for substrates doped using the carborane molecule compared to ABAPE was confirmed using SIMS analysis and

sheet resistance measurements. A dose of 2.2×10^{13} cm^{-2} was obtained for the carborane molecule compared to 0.3×10^{13} cm^{-2} for the ABAPE.[14]

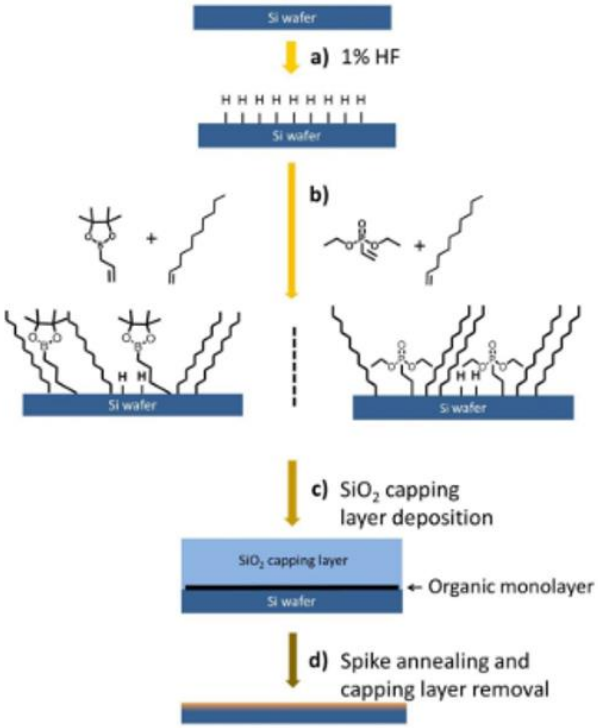

Figure 1.3: (a) a 1% HF dip is used to give H-termination. (b) Mixing of the dopant containing alkene molecule with 1-undecene followed by a hydrosilylation reaction with the Si surface. The substrate is (c) capped and (d) annealed. Reprinted from Ye, L. *et. al. ACS Appl. Mater. Interfaces* **2015**, *7* (5), 3231–3236. (13).

The dopant concentration can also be tuned by alteration of the molecular footprint of the dopant molecules.[3,11,15] The use of trioctylphosphine oxide resulted in approximately a six fold increase in the doping concentration compared to diethyl 1-propylphosphonate as determined by sheet resistance measurements which is in agreement with the six fold increase in its molecular footprint. The use of three different phosphonic acid precursors (vinylphosphonic acid, phenylphosphonic acid, n-dodecylphosphosphonic acid) resulted in a doping concentration in the (4×10^{19}) – (7×10^{18}) atoms/cm^3 range. [11] Similarly, the size of the phosphorus precursor can be varied using a phosphorus containing polyhedral oligomeric silsesquioxane, diethyl-

benzyl phosphonate and p-tosylate tributyl-ethyl-phosphonium to change the P dose from 1-0.6 P atoms/nm^2.[15] The use of a number of polymer deposition cycles with polystyrene (PS) or poly(methylmethacrylate) (PMMA) can also be employed to tune the dopant concentration.[16] The polymer chains are removed following grafting using O_2 plasma hashing. Repetition of deposition and hashing cycles allows fine control over the final dopant dose, as displayed in **Figure 1.4**.[16] The dopant dose can effectively be varied by tuning the molecular footprint of the dopant precursor or through the use of mixed monolayers or dopant-rich precursors.

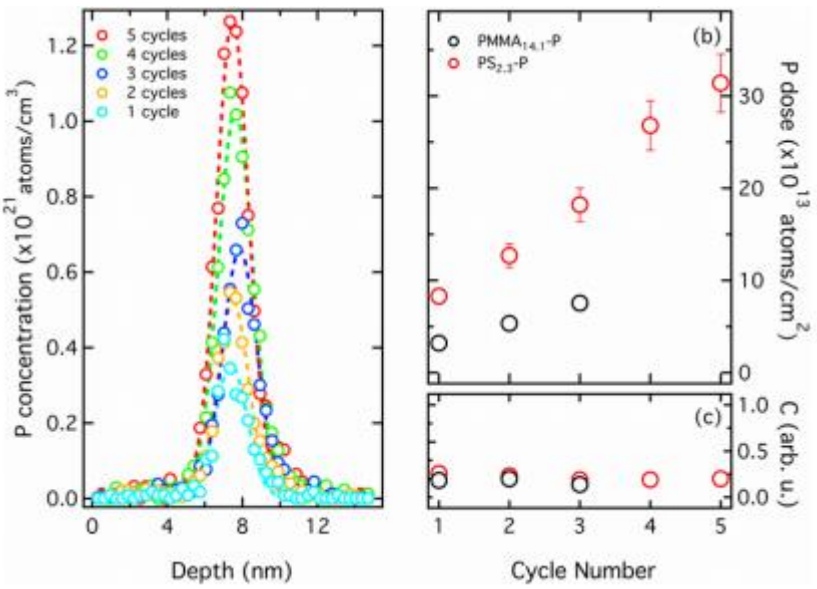

Figure 1.4: (a) SIMS analysis displays the increase in phosphorus concentration for the number of grafting-hashing cycles. (b) Phosphorus dose as a function of cycle number, with an increase in the dose for each cycle number. (c) Analysis of the carbon content of substrates subjected to grafting-hashing cycles. Reprinted from Perego, M. *et. al. ACS Nano* **2018**, *12* (1), 178–186. (16).

The continual scaling of device dimensions demands the increased precision of dopant atom placement. In addition to using the molecular footprint of the dopant precursor to tune the dose, precursors can also be designed to give increased lateral control of

dopant atom placement. Wu *et. al.*[4] synthesised dendrimer-like molecules containing a single P atom which allowed increased control of dopant atom placement due to the branched like structure of the synthesised phosphorus precursor. SIMS analysis showed doping resulted in a peak carrier concentration of ~ 10^{17} atoms/cm^3. Increased precision of lateral positioning of dopant molecules was also achieved by Voorthuijzen *et. al.*[17] using nanoimprint lithography. The Si substrate was functionalised using a hydrosilylation reaction followed by patterning, capping and an RTA. ToF-SIMS analysis revealed P concentrations of 2.3 × 10^{19} atoms/cm^3 and a decrease in sheet resistance was observed for unpatterned regions, indicative of successful doping in the desired regions.[17] Additionally, remote-MLD has been employed to create doped patterned regions on a substrate as shown in **Figure 1.5**.[18]

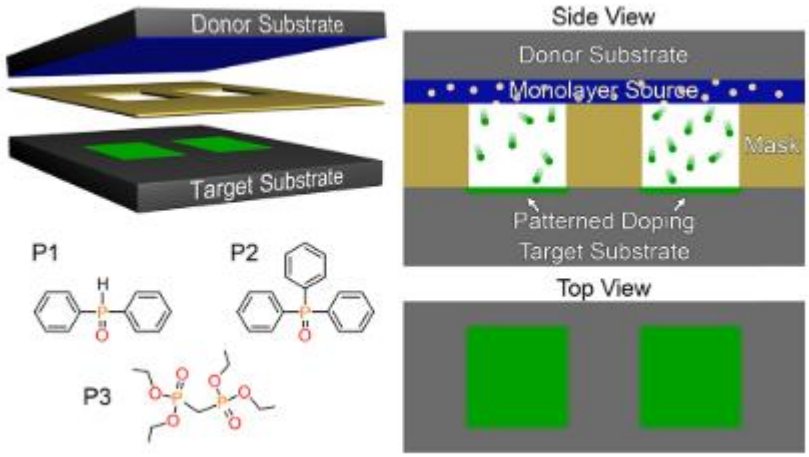

Figure 1.5: Remote-MLD is achieved using a mask which is placed in between the donor and target substrate. Dopant diffusion occurs through the gap during the rapid thermal anneal using three molecules: P1 (diphenylphosphine oxide), P2 (triphenylphosphine oxide) and P3 (tetraethylmethylene diphosphonate). Reprinted from Hazut, O. *et. al. Langmuir* **2017**, *33* (22), 5371–5377. (18).

A mask is used to avoid contact of certain areas, and dopant fragmentation during RTA results in volatilisation and diffusion of the dopant from the donor to the target

substrate without being in direct contact with the target substrate. Similarly, the use of a poly(methyl methacrylate) (PMMA) resist, which was patterned prior to surface reaction, allows the selective doping of certain areas as the PMMA can be lifted off before the RTA.[19] Following patterning, gas phase MLD where the gas-phase dopant precursor reacts with the substrate surface followed by an RTA was used to selectively dope certain areas.

MLD faces a number of challenges in its scale-up for industry application including the sensitivity of functionalised surfaces to ambient exposure and the use of hydrofluoric acid (HF), which is required for the removal of the native oxide before functionalisation and the capping layer after RTA.[20,21] MLD conventionally uses hydrosilylation reactions to attach dopant precursors through the reaction of alkene groups to the Si surface resulting in the formation of Si-C bonds. The surface chemistry of Si is quite sensitive to ambient conditions and hydrosilylated surfaces often display re-oxidation either during functionalisation or subsequent ambient exposure. O'Connell *et. al.*[22] functionalised the Si surface with a dialkyne and employed click chemistry to attach the dopant precursor to the remaining free alkyne group. The use of an alkyne molecule, which gives a closely packed monolayer, enhances the oxidation resistance of the Si substrate in between processing steps. Alternatively, SiO_2 surfaces can be employed for MLD which display enhanced oxidation resistance, while also eliminating the need for HF treatment.[11,15,21] Functionalisation of the SiO_2 layer using diethyl 1-propylphosphonate followed by annealing at low temperatures (100 or 165 °C) creates a P δ layer that can subsequently act as a dopant source.[20]

1.3.2 Monolayer Contact Doping and Application to Nanowires

Monolayer contact doping (MLCD) has been employed to enhance the level of doping in Si substrates and eliminate the need for a capping layer. The use of a capping layer has been shown to be incompatible with MLD of porous nanowires, as damage can occur during the etching step which is required to remove the capping layer.[23] MLCD employs a donor substrate which is functionalised with the dopant precursor and held in contact with the target substrate during an RTA, as shown in **Figure 1.6**. Repetition of doping cycles is used to achieve high carrier concentrations in the 5×10^{20} atom cm^{-3} range.[24] The MLCD method was also applied to chemical vapour deposition (CVD) grown Si nanowires which displayed a six fold increase in conductivity compared to undoped nanowires.

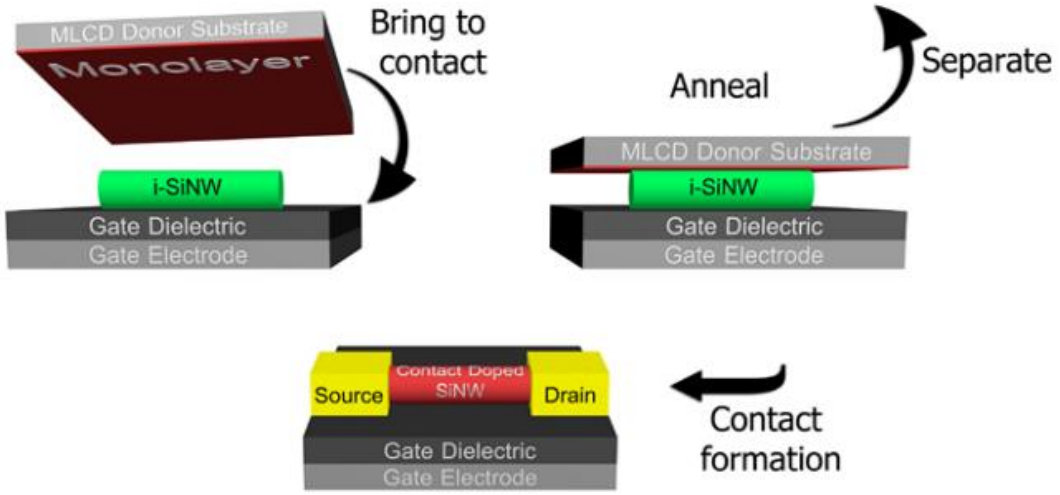

Figure 1.6: MLCD of Si nanowires by bringing a dopant functionalised donor substrate in contact with an acceptor substrates on which nanowires have been grown using CVD. Reprinted from Hazut, O. *et. al. ACS Nano* **2012**, *6* (11), 10311–10318. (24).

Additionally, Kelvin probe force microscopy (KPFM) revealed a linear surface potential indicating a constant electric field and uniform doping in the nanowire, which

is difficult to achieve using in-situ doping techniques. The dopant concentration was extracted to be $(1 \pm 0.5) \times 10^{19}$ atoms/cm^3 using KPFM and current measurements.[24]

The MLCD method has been optimised by using a donor substrate with a thicker SiO_2 layer which reduces dopant diffusion in the donor substrate and increases the dopant concentration in the target substrate through the use of alkoxysilane-functionalised carborane, a boron-rich molecule.[25] SIMS measurements showed MLCD provided a dose of 4.4×10^{13} cm^{-2} compared to 2.2×10^{13} cm^{-2} for MLD.[25] The contact doping approach was applied to the doping of nanowires for the formation of a p-n junction by Hazut and coworkers.[26] The target substrate contained Si NWs and acted as a boron source while donor substrate acted as the phosphorus source. **Figure 1.7** shows the resulting formation of a p-n junction. Scanning tunnelling microscopy and spectroscopy were used to assess the doping which showed a phosphorus concentration of 2.6×10^{19} atoms/cm^3, a boron concentration of 1×10^{20} atoms/cm^3 and low doping levels (~10^{17} atoms/cm^3) in the core.

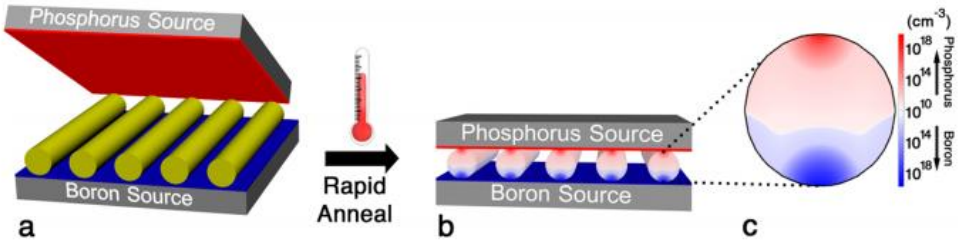

Figure 1.7: MLCD of nanowires results in the formation of a p-n junction. A boron functionalised substrate with NWs is brought into contact with a phosphorus functionalised donor substrate. Reprinted from Hazut, O. *et. al. ACS Nano* **2014**, *8* (8), 8357–8362. (26).

Detailed characterisation of the doping mechanism showed that in addition to contact doping, proximity doping also took place where thermally degraded precursors enter

the substrate during an RTA, even though they are not in direct contact with the nanowire.[26]

Current developments in the deterministic doping of Si have shown advances in the precise placement of doping which is critical for the future progression of doping technology during the scaling of device sizes. In particular, the use of MLD for the doping of nanowires has shown successful results which cannot be achieved using ion implantation. Ho *et. al.*[3] showed doping of Si nanowires using trioctylphosphine oxide resulted in p-doping as an I_{on}/I_{off} of 10^3 and resistance of 1 GΩ was obtained. O'Connell *et. al.*[12] doped Si nanowires using As which displayed a decreases of 7 orders of magnitude in resistivity compared to undoped nanowires, as displayed in **Figure 1.8**.

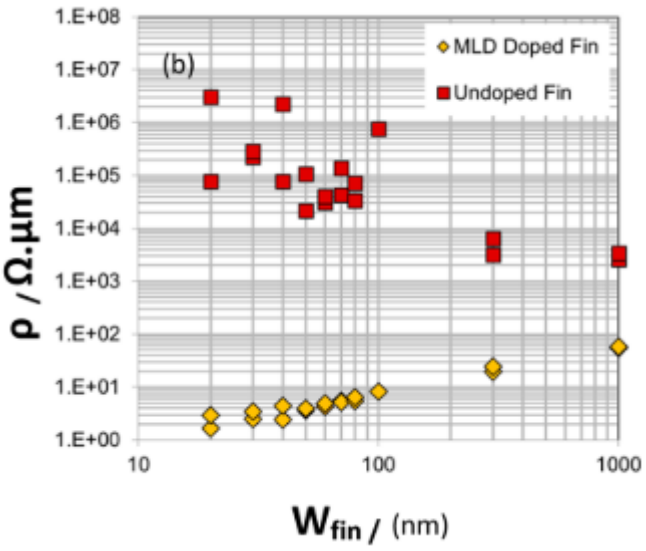

Figure 1.8: Resistivity of MLD doped and undoped Si NWs as a function of width. Reprinted from O'Connell, J. *et. al. ACS Appl. Mater. Interfaces* **2015**, *7* (28), 15514–15521. (12).

The doping of various sizes of nanowires was assessed, with nanowires that had a width <40 nm giving optimal resistivity, indicating that the MLD process is most

suitable for small feature sizes.[12] Veerbeek *et. al.*[23] employed 3 different approaches for the doping of nanowires: (1) MLD, (2) MLCD and (3) a combination of the two where the nanowires are functionalised but the capping layer is applied in a similar way to MLCD to avoid the harsh etching conditions of removing a deposited capping layer which can result in etching of the nanowires. MLCD was successfully applied to porous n++ nanowires without damaging the nanowires and achieving a carrier concentration of ~10^{20} atoms/cm^3, as measured by SIMS analysis. The combination of MLD and MLCD resulted in a higher dose of 1.9×10^{15} atoms/cm^3 compared to 5.9×10^{15} atoms/cm^3 for MLCD and 7.3×10^{14} atoms/cm^3 for MLD when applied to p-nanowires considering boron loading. The high dose for MLCD can be attributed to the use of a dopant-rich carborane molecule and the combined MLD and MLCD approach displayed the highest dose when boron loading is taken into account. SIMS analysis showed a carrier concentration of 2×10^{21} atoms/cm^3 for n++ nanowires and 4×10^{20} atoms/cm^3 for p-nanowires for the combined MLD and MLCD approach. The doping density was enhanced by combining MLD and MLCD, allowing application to porous nanowires which can be damaged during the MLD process.[23]

1.3.3 Carbon Contamination

Carbon contamination has been reported to be a major drawback of the MLD process.[13] The use of carbon-containing monolayers allows the unintentional carbon diffusion into the substrate during the RTA. Conflicting reports have been published suggesting the volatilisation of carbon during the RTA while other studies that discuss the extent of carbon contamination indicate that there is significant amount of diffusion into the substrate.

Theoretical studies indicate a breaking of the P-C bond at lower annealing temperature of 500 °C which would release the C chain rather diffusing into the Si substrate during the annealing step.[27] Further experimental studies suggest that capping layers are not required for the MLD of Si using oxide layers functionalised using phosphonic acids. XPS and ToF-SIMS analysis of samples doped without the use of a capping layer show the desorption of the carbon ligand and diffusion of the phosphorus through the SiO_2 layer into the underlying Si.[28] The capping layer ensures diffusion of the dopant precursor rather than volatilisation, although undesired atoms such as carbon are also incorporated into the substrate using this approach.

Further experimental studies have investigated the diffusion of contaminants during the MLD process. Carbon and oxygen diffusion have been reported to be limited to the first few monolayers, in contrast to phosphorus which diffuses deeper into the Si substrate.[29] Atom probe tomography (APT) indicated the formation of Si-C, which is limited by the carbon concentration, as displayed in **Figure 1.9**. Therefore, deep diffusion of carbon is hindered by bond formation with Si. Caccamo *et. al.*[30] also reported a lower than expected value of carbon in doped substrates when using MLD without the use of a capping layer. Additionally, an etching procedure was used to eliminate contaminants by removing the first 1.4-1.7 nm of the doped substrate.[30] The limited diffusion of carbon allows removal following doping, but 3D nanostructures will require minimal incorporation of contaminants as surface removal will not be applicable due to their small dimensions. Further analysis of the carbon diffusion during MLD displayed different behaviour.[31]

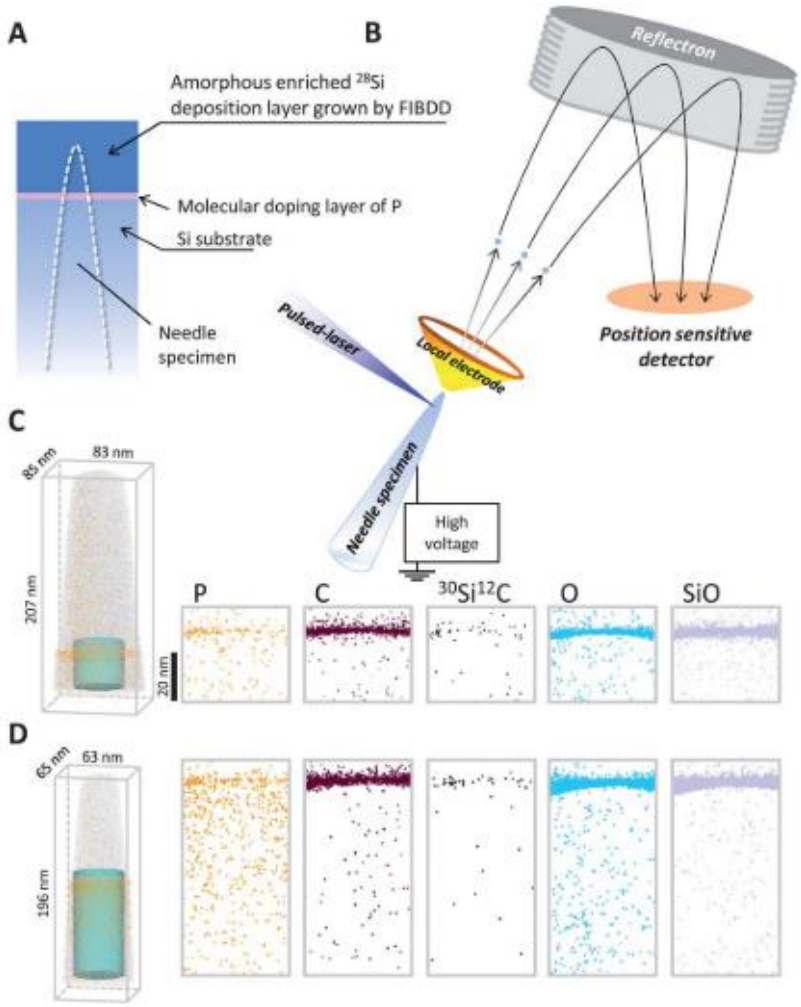

Figure 1.9: (a) Illustration of the preparation of a sample for APT. (b) Schematic of APT instrument setup. Elemental maps of P, C, Si-C O and SiO for samples annealed at (c) 800 °C and (d) 1025 °C. Reprinted from Shimizu, Y. *et. al. Nanoscale* **2014**, *6* (2), 706–710. (29).

Deep-level transient spectroscopy (DLTS) was used to evaluate the formation of defects during the MLD process.[31] DLTS analysis revealed ~20 % of phosphorus dopants were deactivated during annealing as a result of the formation of carbon defects, which were identified as interstitial-carbon-substitutional-phosphorus pairs.[31] Further experimental work demonstrated that the number of C_i-D_s defects can be reduced using a longer annealing period during which interstitial carbon defects turn into substitutional carbon atoms.[32]

The incorporation of carbon into doped substrates remains a challenge when using MLD and also results in dopant deactivation. Minimisation of carbon contamination has been accomplished through the use of self-capping molecules,[15,21] an ultra-thin oxide layer[11] or carbon-free precursors.[11] While studies suggest phosphorus MLD can be carried out without the use of a capping layer, the absence of a capping layer can also result in a decrease in the efficiency of the doping process.[3,11] The synthesis of tailored boron precursors with bulky ligands that also act as capping layers resulted in minimal incorporation of contaminants as analysed using SIMS analysis.[21] Similarly, self-capping polyhedral oligomeric silsesquioxane species containing phosphorus ensure minimal dopant volatilisation during the RTA. As surface binding occurs through silanol groups instead of the traditional hydrosilylation reaction, carbon contamination can be avoided.[15] The use of an ultrathin oxide layer provides a barrier to carbon contamination as the SiO_2 layer impedes carbon diffusion, with removal of the layer after annealing resulting in a contaminant-free doped substrate.[11] The use of an oxide layer also facilitates attachment of carbon-free precursors, eliminating the need for carbon in the dopant precursor as attachment occurs through the phosphonic acid groups.[11] Carbon contamination remains a critical challenge, although significant developments have been made in the minimisation of carbon incorporation during the MLD process.

1.4 Movement from Silicon to 2D Materials

While Si has been used extensively in electronic devices for the last 50 years, the physical limit of the material will eventually become a roadblock in the fabrication of devices. Recently, the movement to 3D architectures (e.g. FinFETs) and manipulation of Si (e.g. strain engineering)[33] has allowed the continual use of Si in transistor

devices. New materials, which have a higher carrier mobility than Si, have been investigated as potential replacements for Si, including Ge,[34] III-V materials[35] and more recently 2D materials. The isolation of graphene from graphite, which results in dramatic changes to the properties of the material compared to their bulk counterpart, has given rise to a new class of undiscovered materials with interesting properties.[36] Graphene's low bandgap (0-0.2 eV) makes it ineffective for electronic applications, however, many new 2D materials have been discovered which display more suitable, semiconducting properties.[37–39] TMDs, which consists of a transition metal atom layer (e.g. Mo) in between two layers of a chalcogen (e.g. S), have semiconducting character and display a bandgap in the 1-2 eV range when in monolayer form.[40–42] TMDs, including MoS_2 and WSe_2, display a mobility, an $I_{on/off}$ ratio and ambipolar behaviour that is comparable to Si, making them promising candidates for devices.[40] While group IV elemental 2D analogues have been predicted to be thermodynamically stable, their synthesis and the production of reliable devices remains limited, highlighting the difficulty in the fabrication of these few-layer materials.[43,44] The lack of silicene, germanane and stanane, the 2D counterparts of Si, Ge and Sn, in bulk layered form also inhibits their formation through mechanical or liquid exfoliation,[45] resulting in a reliance on the bottom-up synthesis of group IV 2D materials. Once the group IV analogues are synthesised the ambient instability also poses a challenge which has been overcome using capping layers[43] or covalent functionalisation with hydrogen or methyl groups.[46,47] The ambient instability of the group IV analogues has also created difficulties in the fabrication of devices.[44]

Recently, research into the 2D pnictogens, in particular phosphorene, has flourished. BP is a semiconductor that displays a layer tunable direct bandgap. The bandgap and

semiconducting properties are present in both mono- and few-layer form, unlike TMDs. While TMDs only display a direct bandgap in monolayer from, the indirect bandgap in few-layer TMDs can also be useful for other devices. Phosphorene can easily be isolated from bulk BP using mechanical or liquid exfoliation while the fabrication of devices using few-layer BP display excellent electrical characteristics, however, ambient degradation results in a loss of mobility. Other 2D pnictogens, such as arsenene, antimonene and bismuthene, which have only recently been isolated from their bulk counterparts, are a new group of promising materials that can also potentially be useful as a replacement for Si.[48,49]

1.5 Black Phosphorus

BP, a layered material, has a puckered honeycomb lattice structure with layers held together by van der Waals interactions.[50–52] The weak interlayer interactions in bulk 2D materials allows their smooth exfoliation into nanosheets, often resulting in dramatic changes to their properties. BP displays extraordinary properties in mono- and few-layer form and shows promise in electronic[52–54], energy storage,[55,56] catalysis[57], sensing[58] and medical[59–61] applications. Unlike graphene or TMDs, BP displays a layer tunable direct bandgap and exfoliation of bulk BP into phosphorene nanosheets changes its bandgap from ~0.3 eV in bulk BP, to ~1.5 eV for monolayer BP.[37,62] The high carrier mobility of BP, around 1000 $cm^2 V^{-1} S^{-1}$, makes it a potential replacement for Si in some electronic devices.[54,63] However, in ambient conditions BP reacts with oxygen and water resulting in rapid decomposition,[64] making processing of the material challenging and resulting in detrimental effects on its optical and electronic properties.[65–67] The ambient degradation of BP presents a significant hurdle to realising the full potential of BP in various applications. The successful

application of BP will rely either on its exclusion from the factors that contribute to its degradation or protection methods that prevent its degradation in ambient conditions. Literature reports that have studied the degradation chemistry of BP have revealed some conflicting results regarding the effect of water, oxygen and light, indicating that BP has a complex surface chemistry. The in-depth characterisation of BP degradation is critical for the development of new protection strategies and progress of the material and its applications. The role of the surface oxide as a passivation layer that stabilises BP has also created some debate between researchers. Although a stabilising oxide has been reported in theoretical studies,[68,69] experimental reports question the challenges of creating a self-limiting surface oxide on BP.[70] Protection of BP can also be accomplished by capping layers,[67,71,72] functionalisation,[73,74] solvent passivation[62] or the incorporation of polymers.[75,76] Ambient degradation can be suppressed by covalent functionalisation where chemical binding of molecules to the reactive lone pairs on the surface prevent decomposition.[73,74] Non-covalent functionalisation can also be employed which inhibits degradation by passivating BP nanoflakes through non-covalent interactions.[74] Solvent passivation forms a protective barrier against oxidants while polymer coatings, or the formation of BP-polymer hybrids enhances its oxidation resistance while also modifying its properties.

This chapter outlines factors that influence the oxidation of BP from a surface chemistry perspective, including the effect of water, oxygen and light on the degradation of BP, as well as elucidation of the oxidation mechanism through analysis of BP exposed to single oxidants and evaluation of the oxidation products.

Additionally, an overview of current advances in chemistry-based protection strategies for BP is presented.

1.5.1 Structure, Properties and Exfoliation of BP

BP has an orthorhombic crystal structure and consists of layers of phosphorene held together by van der Waals interactions, as depicted in **Figures 1.10**(a)-(c).[77] The individual layers of phosphorene consist of phosphorus atoms covalently bound to two intraplane atoms and one interplane phosphorus atom resulting in a puckered structure and sp^3 hybridisation. The reactivity under ambient conditions arises from the lone pairs present on each phosphorus atom which are susceptible to oxidation.

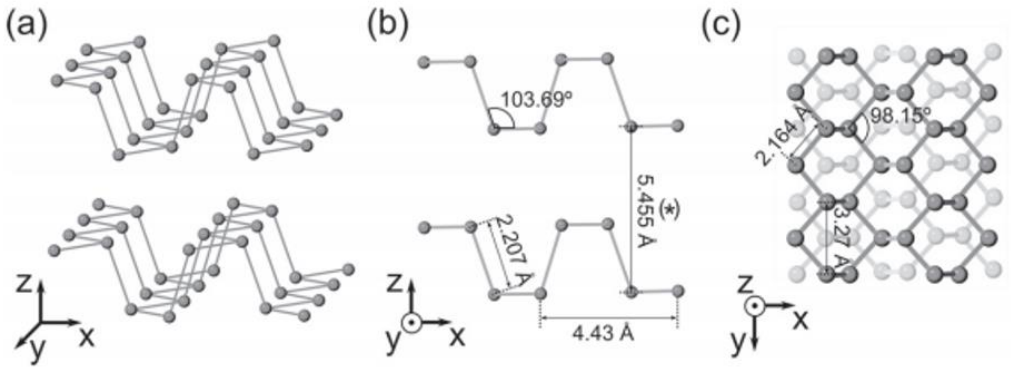

Figure 1.10: Structure of layered BP displayed in (a) 3D, (b) lateral view and (c) top view. Reprinted from Castellanos-Gomez, A. *et. al. 2D Mater.* **2014**, *1* (2), 025001. (77).

The semiconducting properties of BP were discovered in 1953 by Keyes *et. al.*[78] but research into BP did take off until 2014 when many research groups fabricated devices from the material.[37,53,63] BP displays a carrier mobility of 1000 $cm^2\ V^{-1}\ s^{-1}$ and hole and electron mobilities of 350 $cm^2\ V^{-1}\ s^{-1}$ and 220 $cm^2\ V^{-1}\ s^{-1}$, respectively.[54] BP has a direct bandgap, as displayed in **Figure 1.11**(a), which is tunable through layer thickness, as shown in **Figure 1.11**(b), making it favourable for electronic and

optoelectronic applications.[37] Additionally, the bandgap range of BP between 0.3-2 eV falls between the bandgap of graphene (0-0.2 eV) and TMDs (1-2 eV), opening up a new range of optical applications.[79]

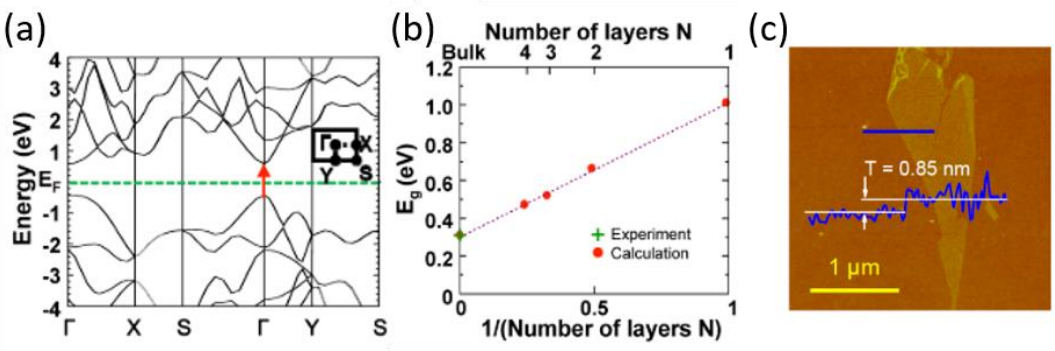

Figure 1.11: (a) DFT band structure of monolayer BP. (b) Layer-dependant bandgap of BP. (c) Atomic force microscopy analysis of a mechanically exfoliated BP nanosheet. Reprinted from Liu, H. *et. al. ACS Nano* **2014**, *8* (4), 4033–4041. (37).

Isolation of BP was first reported in 2014 through the Scotch tape exfoliation method,[37] where atomically thin sheets of a 2D material are peeled off from the bulk crystal and deposited on a substrate, as displayed in **Figure 1.11**(c). One of the main issues with mechanical exfoliation is the transfer of tape residues onto exfoliated flakes, which requires rinses to remove contaminants.[77] A modification to the Scotch tape procedure to minimise the transfer of tape residue has been developed where flakes are transferred to a poly-dimethylsiloxane (PDMS) substrate before transfer to the desired substrate.[77] However, the scalability of mechanical exfoliation remains a critical issue for the large scale application of BP. Liquid exfoliation of BP, which has been developed as a scalable production method of various 2D materials,[80] was reported by Brent *et. al.*,[81] Kang *et. al.*[82] and Hanlon *et. al.*[62] in 2015. N-cyclohexyl-2-pyrrolidone (CHP) or N-methylpyrrolidone (NMP) was used to produce high-quality phosphorene sheets. The high yield of BP nanosheets in CHP was attributed to a match between the surface energy of the solvent and the material which promotes

exfoliation and prevents reaggregation of exfoliated nanosheets.[62,83] Theoretical studies suggest NMP is particularly suitable for liquid exfoliation due to its planarity which allows the solvent to wedge and intercalate in between the layers, prying them apart.[84] Liquid exfoliation allows selection of flakes of the desired size through a number of centrifugation steps[85] rather than requiring manual selection of flakes that have been mechanically exfoliated onto a substrate. The lateral size and thickness of exfoliated sheets can also be tailored by varying the exfoliating medium. Dimethylformamide (DMF) and dimethyl sulfoxide (DMSO) have been used to tailor the thickness of BP flakes,[86] while choline chloride urea, an ionic liquid, was used for the production of flakes with large lateral dimensions in the micrometre range.[87] Liquid exfoliation has therefore been established as a scalable production strategy of high-quality BP nanosheets with minimal defects.[62]

1.5.2 Degradation of BP

1.5.2.1 BP Surface Chemistry

The surface chemistry of BP has been widely debated with many reports displaying conflicting results regarding the hydrophobicity of the BP surface. The instability of BP was first reported by Castellanos-Gomez *et. al.*[77] and Island *et. al.*[88] who characterised mechanically exfoliated BP. Optical microscopy revealed the presence of droplets on the surface which were ascribed to adsorbed water. The hydrophilic nature of BP was proposed which was in correlation with initial theoretical studies, as the droplets on the BP surface increased with higher levels of humidity.[77] Condensation of ambient water on the surface resulted in a layer-by-layer etching process and thinning of the BP flakes.[88] Theoretical studies by Ziletti *et. al.*[89] reported the increasing hydrophilicity of the BP surface after oxidation, as the binding energy of water physisorption was lowered due to surface polarisation after oxygen

chemisorption. Wang *et. al.*[90] first reported that the pristine BP surface was hydrophobic, which was later confirmed experimentally by Huang *et. al.*[91]. The hydrophobicity was verified by experimental studies where BP did not degrade when kept in deaerated solutions of water, indicative of a weak interaction of water with BP.[91,92] Additionally, contact angle studies displayed a hydrophobic surface that progressively turned hydrophilic after ambient exposure, as shown in **Figures 1.12**(a) and (b).[91]

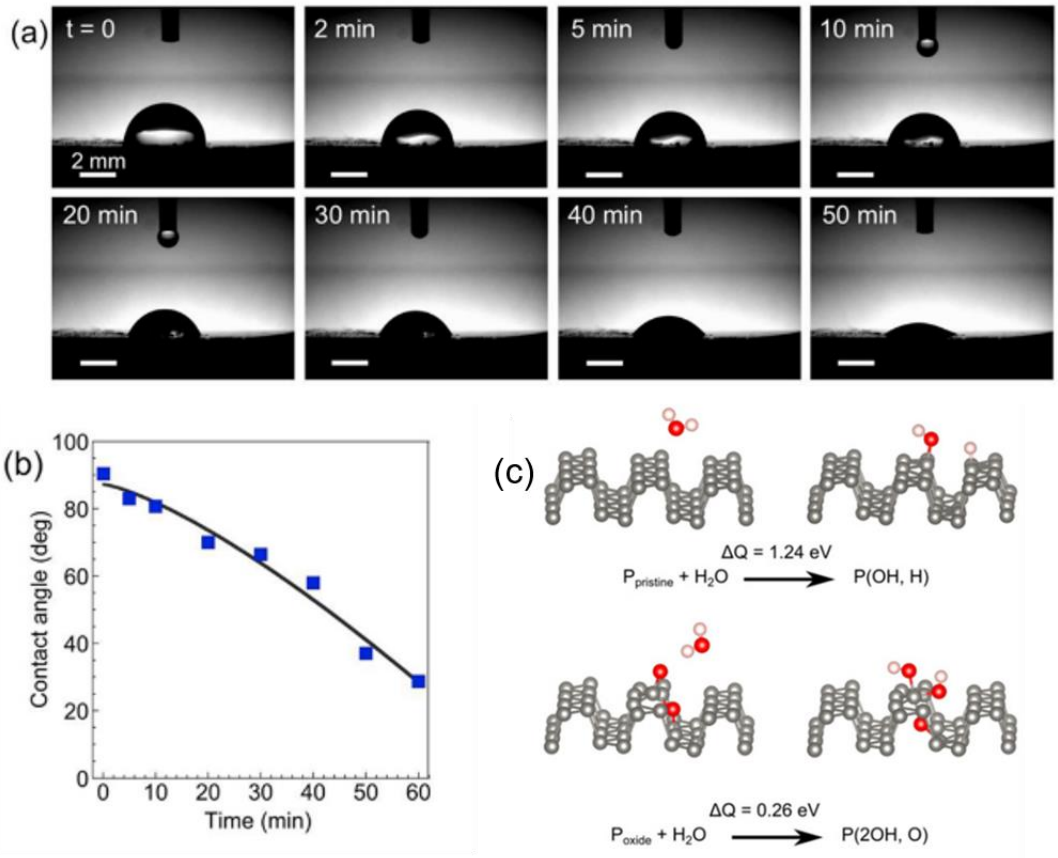

Figure 1.12: (a) Contact angle measurements display the progression of a hydrophobic to hydrophilic BP surface during ambient exposure as a result of surface oxidation. (b) Corresponding decrease in contact angle as a function of time. Reprinted from Huang, Y. *et. al. Chem. Mater.* **2016**, *28* (22), 8330–8339. (91). (c) Theoretical studies illustrating the exothermic energy (ΔQ) of the reaction of water with pristine and oxidised BP. Reprinted from Wang, G. *et. al. 2D Mater.* **2016**, *3* (2), 025011 (93).

Exfoliation of BP in aqueous solutions has also been reported to produce minimal oxidation of BP.[94–96] Therefore, initial reports suggesting that water adsorption occurred were likely carried out using BP surfaces with minor surface oxidation, where physisorption of water is favourable. **Figure 1.12**(c) shows the exothermic energy of water reacting with pristine and oxidised BP. The reaction with pristine BP was calculated to be endothermic but a decrease in the energy for the reaction with oxidised BP suggests dissociation occurs, as further analysis revealed the energy release of the reaction with oxygen and then water is exothermic.[93] Isotope labelling experiments confirmed the increased hydrophilicity of the oxidised BP surface, where water adsorbed predominantly on the oxidised areas while pristine areas remained hydrophobic.[91]

1.5.2.2 Role of Oxygen and Water

The initial studies on the effect of different oxidants used theoretical calculations to determine the likely pathways of degradation and interaction of BP with single oxidants. Ziletti *et. al.*[89] evaluated the favourable chemisorption of oxygen on phosphorene, supported by Wang *et. al.*[90] who reported on the effect of oxygen and water on BP oxidation. The exothermic chemisorption of oxygen was reported to be advantageous in a dangling and bridging configuration as displayed in **Figures 1.13**(a) and (b).[89] Wang *et. al.*[90] reported that water favours physisorption on the pristine BP surface rather than chemisorption due to the strong hydrogen bonds formed between hydrogen atoms and the lone pairs present on the BP surface.

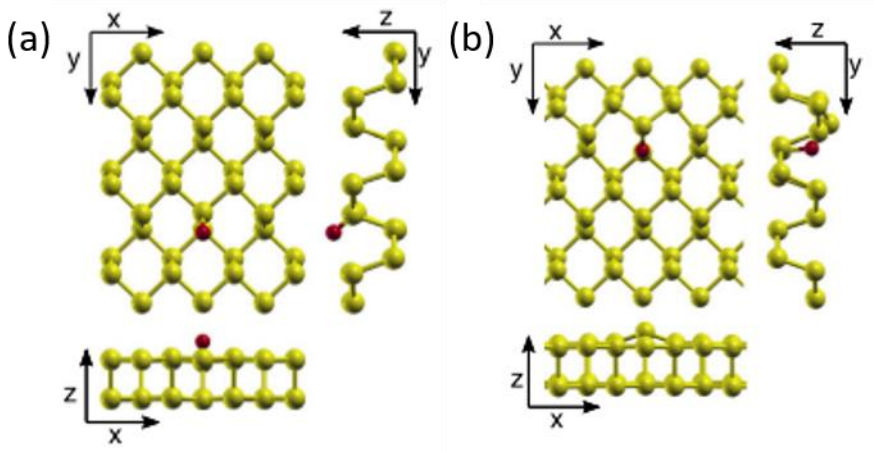

Figure 1.13: Exothermic chemisorption of oxygen in (a) a dangling and (b) a bridging configuration. Reprinted from Ziletti, A. *et. al. Phys. Rev. Lett.* **2015**, *114* (4), 26–29. (89).

Experimental studies by Huang *et. al.*[91] supported these findings by exposing BP flakes to deaerated and oxygen enriched solutions of DI water, as displayed in **Figures 1.14**(a)-(h).

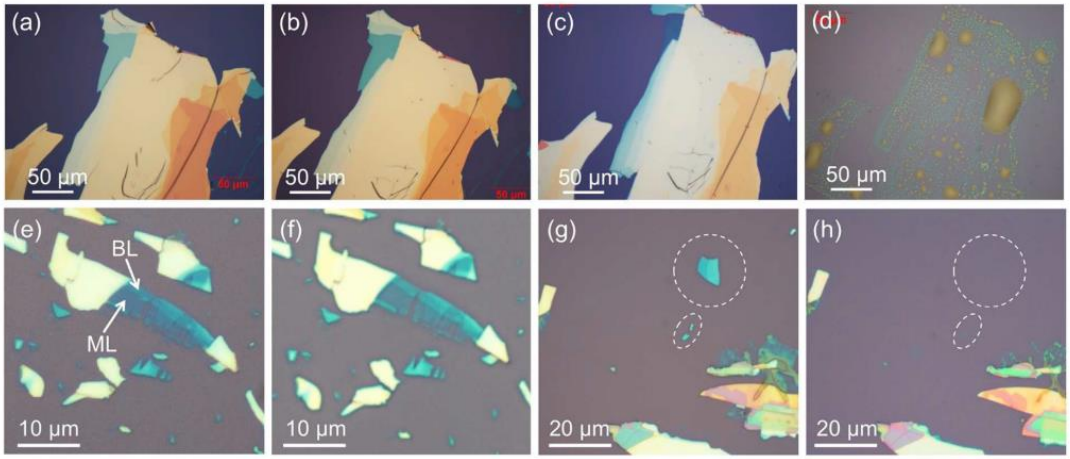

Figure 1.14:(a) Freshly exfoliated BP, after being exposed to DI water for (b) 1 week, (c) 2 weeks and (d) removal from water and exposure to air for 1 week. (e) Exfoliated flake with mono- and bilayer thickness exposed to (f) deaerated water for 2 days. (g) Freshly exfoliated flakes (h) exposed to oxygenated water for 2 days. Reprinted from Huang, Y. *et. al. Chem. Mater.* **2016**, *28* (22), 8330–8339 (91).

A significant difference in the oxidation behaviours was observed, with mono- and bilayer flakes exposed to deaerated solutions remaining stable for 2 days, while the flakes exposed to oxygen enriched solutions completely degraded. BP exposed to deaerated water displayed no signs of oxidation when analysed using X-ray photoelectron spectroscopy (XPS)[97] and no major formation of oxidation products was observed using anion-exchange chromatography[98] or nuclear magnetic resonance (NMR) analysis.[92] The mole fraction of oxidised BP has also been monitored in oxygenated and deoxygenated aqueous solutions, with a significant increase in oxidised BP observed in oxygenated solutions, as displayed in **Figures 1.15**(a)-(b).[98]

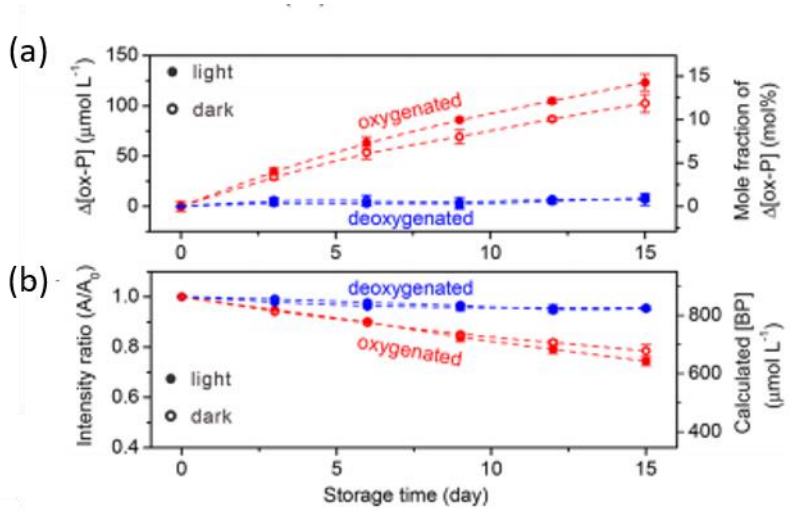

Figure 1.15: Evaluation of (a) the mole fraction and (b) the concentration of BP during exposure to oxygenated and deoxygenated solutions of water. Reprinted from Zhang, T. *et. al. J. Am. Chem. Soc.* **2018**, *140* (24), 7561–7567. (98).

Hanlon *et. al.*[62] demonstrated that dry and deoxygenated solutions produced BP flakes with increased stability, indicating oxygen and water have an effect on stability during exfoliation. Addition of water to exfoliated solutions also resulted in a large decrease in stability[62] suggesting water has a detrimental effect to BP solutions once initial oxidation has occurred. Water has been revealed to react exothermically with oxidised

BP once a surface oxide is formed, from theoretical studies.[93] Yang *et. al.*[99] first reported on the degradation of liquid exfoliated BP using combined theoretical and XPS studies. A number of oxide structures and their corresponding XPS binding energy shifts were proposed using density functional theory (DFT) studies. This was developed further by Kuntz *et. al.*[70] who studied the effect of oxidants on BP and oxidation at defect and non-defect sites. Exposure to oxygen resulted in the formation of a uniform oxide across the basal plane, while exposure to water oxidised defect sites which could be observed through the formation of surface pitting. When flakes were exposed to ambient conditions surface pitting occurred similarly to those exposed to water alone. However, flakes exposed to ambient conditions displayed more severe signs of oxidation with loss of edges and in some cases full layers. This oxidation at defect sites results in continual etching and degradation. Oxygen creates defects making BP more susceptible to oxidation by water, which reacts at defect sites.[70] Wu *et. al.*[100] used transmission electron microscopy (TEM) to demonstrate the evaporation of water from the surface, leaving behind a porous layer with visible surface pitting. High levels of oxygen were observed at the pit edges confirming the oxidation mechanism proposed by Kuntz *et. al.*[70]. These experimental studies suggest an initial oxidation pathway through reaction with oxygen, followed by further degradation through chemisorption of water at oxidised sites. Theoretical studies also suggest chemisorbed oxygen atoms facilitate physisorption of water[89,93,101] which promotes further reaction of surface oxidation products.[67,97,102] The low reactivity of BP in water can also be deduced by evaluation of the electrical characteristics of BP during exposure to water. While water alone does not have a significant effect on the degradation of the electrical characteristics of BP, it has been reported to result in n-doping of FETs.[91,97,103] An increase in the electron mobility from 4.5 to 17.4 $cm^2 V^{-1}$

s^{-1} is observed which can be attributed to electron transfer from water to BP.[97] No change was observed in the on-current and mobility was preserved during water exposure, indicating water has no detrimental effects on the electrical properties of BP. The deterioration of the electrical properties of BP in ambient conditions can be attributed to exposure to a combination of oxygen and water which diminishes the electron and hole mobility. Within 3 h of exposure a reduction of 163.7 to 1.3 $cm^2 V^{-1} s^{-1}$ for hole mobility and 5.7 to 0.2 $cm^2 V^{-1} s^{-1}$ electron mobility is observed. An I_{on}/I_{off} ratio of ~10^4 is observed initially[37,82] which decreases to <10 after 35 h of ambient exposure.[67] The loss of electrical characteristics in ambient conditions occurs as a result of exposure to both oxygen and water. In addition to this degradation mechanism, several other mechanisms have been proposed. Zhang *et. al.*[104] elucidated the role of OH^- and H_3O^+ ions on BP degradation by exposing BP to solutions of various pH values. The degradation rate was highest in an alkaline solution of pH 10 while decomposition slowed down in solutions of pH 4, indicating OH^- ions accelerated dissolution of surface oxides, formed due to initial oxygen exposure, and reacted exothermically with BP through P-P cleavage, while H_3O^+ passivated the surface protecting it from degradation.[104] Another alternative oxidation mechanism where BP degradation occurs in the absence of light has also been proposed. Hu *et. al.*[97] reported water enhances the charge transfer from BP to oxygen and allows formation the of $O_2^{-}H_2O$ superclusters which form without illumination. The formation of these superclusters reduces the energy barrier of the reaction of oxygen with BP. Therefore, the degradation is accelerated in the presence of water which initiates decomposition by enhancing the electron affinity of oxygen.[97] The complex surface chemistry of BP has given rise to many different mechanisms of oxidation which are all likely pathways of degradation.

1.5.2.3 Degradation Products

Assessment of the degradation products gives further insight into the degradation mechanism of BP, as the reaction of oxygen and water with BP would result in the production of phosphorus oxyacids due to hydrolysis. Literature reports have identified an oxide in the form of P_2O_5 on BP, [101,105] which was characterised as a stable surface oxide. Theoretical studies suggest a multistep oxidation process where PO_3 and PO_4 species convert to P_2O_5.[101] The use of P_2O_5 as a desiccant that has a high level of hygroscopicity contradicts the formation of a stable oxide in the form of P_2O_5,[67,70] especially since the reaction of water with oxidised BP is favourable.[93] Degradation products have also been identified as various phosphorus oxides and a decrease in pH was often observed for in-solution degradations studies,[62,106] indicating the formation of phosphorus oxyacids. The formation of H_3PO_4 was confirmed through electrochemical experiments[91], electron energy loss spectroscopy (EELS) analysis[91] and NMR analysis.[92] Zhang *et. al.*[98] identified 3 main oxidation products during the degradation of BP in oxygenated water: PO_2^{3-}, PO_3^{3-} and PO_4^{3-}. The disengagement of these 3 oxidation products to form the corresponding phosphorous acids was calculated to be exothermic. Luo *et. al.*[103] evaluated the oxidation products by exposing mechanically exfoliated BP to single oxidants. The study revealed different oxidation products were obtained for each oxidant and a combination of water and oxygen resulted in a higher oxidation rate. The major oxidation product after exposure to water was H_3PO_4 while dry oxygen exposure produced a surface oxide comprised mainly of P=O species. The higher degradation rate for water and oxygen was explained by reaction of surface oxides, in the form of P_4O_{10}, with water resulting in the formation of phosphoric acid which allows for further reaction with oxygen.[93,103] Plutnar *et. al.*[92] evaluated the degradation of BP in aqueous and

methanolic solutions, using NMR analysis to study the degradation products. Oxidation of BP in aqueous solutions containing oxygen resulted in the formation of mainly phosphoric (H_3PO_4) and phosphonic acid (H_3PO_3), as displayed in **Figure 1.16**. A high amount of oxidation products in the +5 oxidation state in the aqueous solution was attributed to the oxidation of lower oxidation state products (+1, +3) to phosphoric acids containing P in a +5 oxidation state. Wu *et. al.*[100] used Raman analysis to show the conversion of P^{3+} species to P^{5+} in the form of orthophosphoric and phosphorus acid.

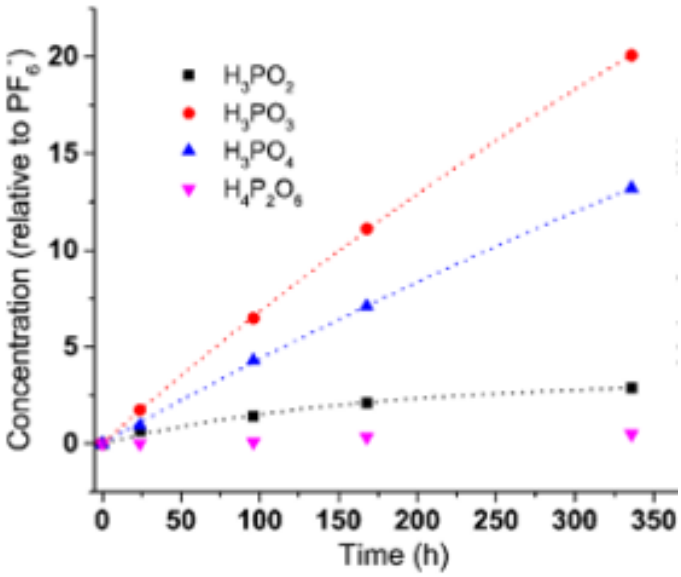

Figure 1.16: ^{31}P NMR spectroscopy of degradation products formed in the presence of water and oxygen. Reprinted from Plutnar, J. *et. al. ACS Nano* **2018**, *12* (8), 8390–8396. (92).

Figure 1.17 shows the conversion of P-O-P linkages to phosphorous oxyacids which was analysed using XPS and Fourier-transform infrared (FTIR) spectroscopy where the variation of P-O-P component was compared to other oxidation products.[100,102] The formation of P-O-P bridges was confirmed experimentally by Luo *et. al.*[103] after treatment with oxygen or a combination of oxygen and water.

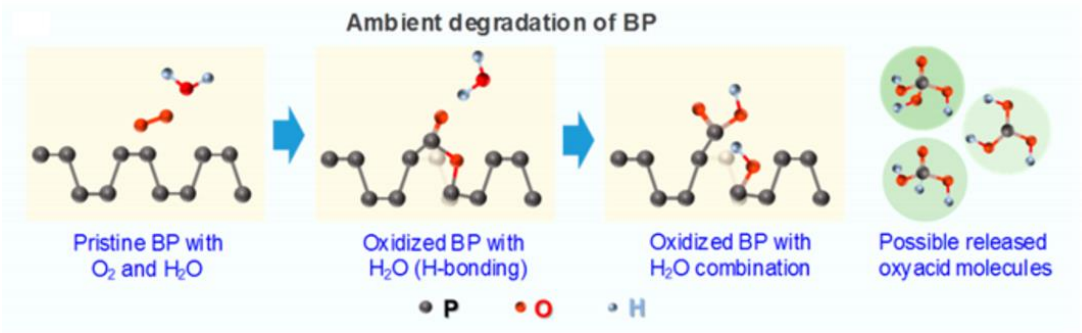

Figure 1.17: Reaction of BP with water and oxygen forming oxyacid reaction products. Reprinted from Wu, S. *et. al. Nano Lett.* **2018**, *18* (9), 5618–5627. (100).

While P-O-P species have been reported to act as a native oxide,[68,69] the formation of P-O-P species is likely to influence the hydrophobicity of the surface and induce deformation which makes them a starting point for further oxidation.[92,102] Therefore, initial degradation products in a low oxidation state convert to a +5 oxidation state after oxidation, followed by detachment from the surface.[98] This oxidation mechanism is supported by a subtle shift of the P 2p oxide shoulder in XPS to a higher BE during ambient exposure, suggesting conversion of low oxidation state P oxides to higher oxidation state oxides[70] and subsequent evaporation of phosphorus oxyacids which has been observed using FTIR analysis.[102]

1.5.2.4 Effect of Light on Degradation

While different oxidation mechanisms have been identified using single oxidants, light has been reported to play a significant role in BP degradation. Favron *et. al.*[107] demonstrated that exposure to single oxidants and a mixture of oxygen and water in the dark did not display significant degradation indicating all three factors must be present for oxidation to occur. **Figures 1.18**(a)-(d) show the effect of exposure to ambient conditions and light as characterised using TEM-EELS. A reaction mechanism was proposed where light induced excitons produce superoxide anions that

react with BP. The formation of superoxide species under light exposure was supported by theoretical studies[69] as displayed in **Figures 1.19**(a) and (b).

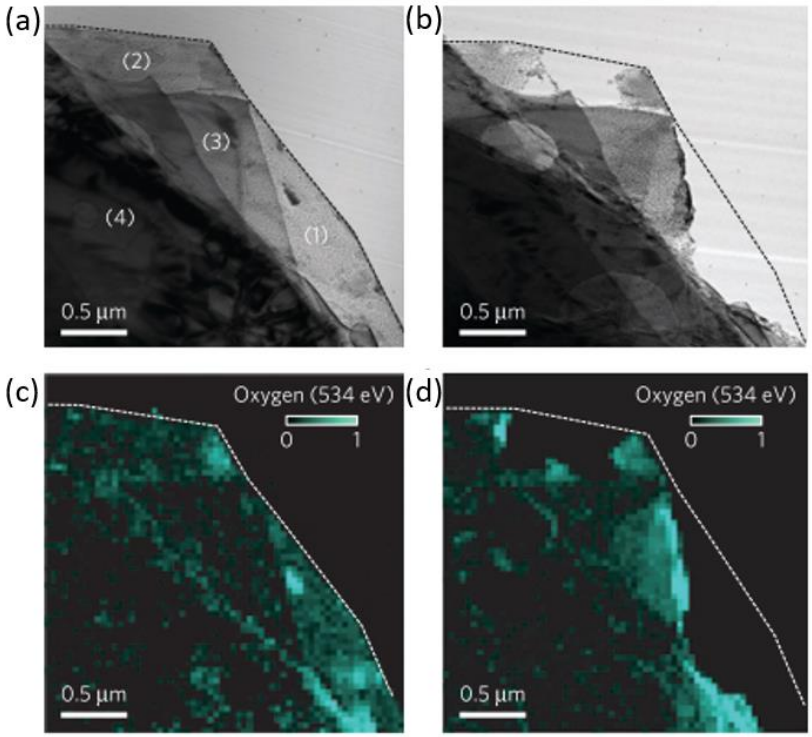

Figure 1.18: (a),(c) TEM-EELS analysis of freshly exfoliated BP and (b),(d) after 20 s of light exposure. Reprinted from Favron, A. *et. al. Nat. Mater.* **2015**, *14* (8), 826–832. (107).

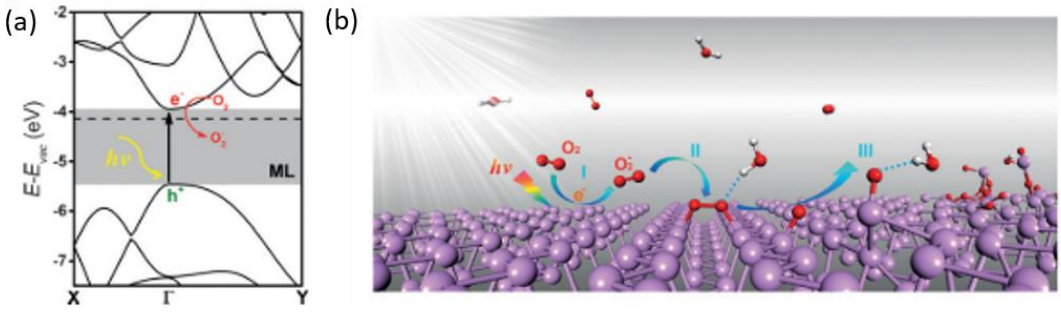

Figure 1.19: (a) HSE band structure of monolayer BP showing the reaction of oxygen in the presence of light. (b) Light induced ambient degradation mechanism involving the formation of O_2^- which dissociates forming P-O bonds. Reprinted from Zhou, Q. *et. al. Angew. Chemie Int. Ed.* **2016**, *55* (38), 11437–11441. (69).

The dissociation of the superoxide on the BP surface occurs more easily than standard oxygen, which is followed by the formation of dangling oxygen species creating a hydrophilic surface. Dissolution then occurs through physisorption of water which removes the P-O species through P-P cleavage resulting a layer-by-layer oxidation mechanism.[69] The normalised A^1_g peak has been used to evaluate the oxidation of BP and a significant decrease is seen for samples exposed to light compared to samples stored in the dark as displayed in **Figure 1.20**.[108]

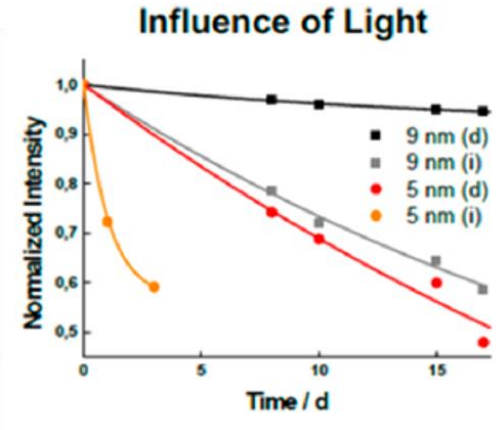

Figure 1.20: Influence of light on the intensity of the A^1_g peak. Reprinted from Abellán, G. *et. al. J. Am. Chem. Soc.* **2017**, *139* (30), 10432–10440. (108).

Hu *et. al.*[97] reported that degradation still occurs in dark conditions as superoxide species can form without the presence of light but experimental reports confirm that degradation occurs more slowly in dark conditions[98,108] suggesting light plays a catalytic role in the degradation of BP.

1.5.2.5 Stability of BP oxides

The formation of a stable oxide passivation layer has been proposed as a possible protection strategy using both theoretical and experimental studies.[69,105] Edmonds *et. al.*[105] found that bulk BP forms a surface oxide consisting mainly of P_2O_5 confined to

the first 0.4 nm of the surface, leaving the underlying bulk BP intact. After initial removal of surface layers, saturation of the oxide occurred, indicative of the formation of a stable oxide layer.[105] The formation of P-O-P species has also been proposed to act as a native oxide capping layer[69] and phosphorene oxide has been predicted to be stable.[68,109] However, other theoretical and experimental reports have demonstrated the instability of P-O-P species.[89,92,102] A factor contributing to the disagreement in the literature could be due to the variation in layer thickness between samples used in different studies. The experimental study verifying the stability of a native oxide layer was carried out exclusively on bulk BP[105] which has been shown to display a different oxidation behaviour to few-layer BP.[102,110] The experimental formation of a stable oxide was found to be quite challenging as the initial oxide formation can catalyse further oxidation and ambient conditions can result in degradation rather than the formation of a self-limiting oxide.[70] Additionally, the formation of a stable oxide on a bulk BP surface contradicts quite a few experimental reports that note rapid degradation of BP.

1.5.2.6 Effect of Layer Thickness and Reactivity of the BP Surface and Edge Sites

Few-layer BP will display a higher reactivity with decreasing layer numbers, due to the increased percentage of atoms at the surface[64] and therefore bulk and few-layer BP display different oxidation patterns.[102,110] Favron *et. al.*[107] noted a decrease in layer thickness of mechanically exfoliated flakes caused a bandgap shift to higher energies which increased the overlap with the band edge. The increasing reactivity with decreasing flake size was also confirmed by Abellán *et. al.*[108] who used the normalised A^1_g ratio to assess the extent of degradation, as shown in **Figure 1.20**. Liquid exfoliated flakes displayed a similar trend[62] where the absorbance displayed a more

significant decrease for smaller flake sizes. Zhou *et. al.*[69] reported that the formation of a superoxide was found to occur primarily for few-layer BP rather than bulk BP explaining the thickness dependant degradation behaviour and high reactivity of few-layer BP.

The reactivity of edge sites compared to the basal plane has also been investigated to further clarify the oxidation mechanism. Favron *et. al.*[107] reported that bumps form on the surface of BP flakes which grow after prolonged exposure, suggesting a nucleation step occurs prior to oxide formation. The formation of bubbles was attributed to the conversion of P_xO_y to phosphoric acid. Degradation of liquid exfoliated BP was proposed to occur at the edges while the basal plane remained protected by the solvation shell.[62] DFT calculations showed that water can react with edge sites removing P atoms in the form of phosphoric acids.[62] Zhang *et. al.*[98] reported that even though water dissociation is endothermic on the BP surface it becomes exothermic at edge sites although the energy barrier remains high. BP flakes stored in oxygenated water displayed degradation predominantly at edges in contrast to most studies which observed the formation of droplets on the BP surface.[98] Experimental work confirmed water prefers to react at edge sites or existing oxide defects[70] while Raman analysis suggests thick flakes display primarily edge degradation prior to degradation of the surface. Edge degradation also occurs at a faster rate than surface degradation.[110] In contrast, few-layer flakes displayed a higher reactivity as surface oxidation most likely occurred at the same time due to the increased reactivity of oxygen with the BP surface of few-layer flakes.[107] However, Zhu *et. al.*[111] showed C_{60} edge-protected few-layer BP shows an increased stability using ultraviolet-visible (uv-vis) spectroscopy, suggesting oxidation through edge sites could be a predominant

degradation pathway and the exact reactivity of edge sites compared to the surface oxidation remains unclear.

1.5.2.7 Characterisation Techniques Applied to Degradation Studies

A variety of techniques have been employed to evaluate the extent of BP oxidation. The stability is often evaluated using microscopic techniques such as TEM or Atomic Force Microscopy (AFM), making comparison between literature reports challenging, while some other commonly used techniques, such as Raman analysis, do not always adequately evaluate the degree of oxidation. Favron *et. al.*[107] first used the A^1_g/A^2_g ratio to characterise BP oxidation and a decrease in the ratio was observed after ambient exposure. Raman analysis can also be used to spectroscopically assess the crystal orientation,[112,113] thickness of flakes[108,110] and extent of degradation.[108] Although the A^1_g/A^2_g ratio has been used to assess the oxidation it is also highly dependent on crystal orientation, which must be considered when evaluating oxidation.[108] The A^1_g peak has been monitored instead of the A^1_g/A^2_g ratio to evaluate the extent of oxidation because the A^1_g/A^2_g ratio only displays changes for few-layer flakes with a thickness < 10 nm.[108,110] The reduction in intensity of the A^1_g peak was attributed to the oxidation of surface layers which would reduce the amount of BP present, while in thick BP flakes (> 10 nm) the oxidation is too low compared to the amount of BP present to have a significant effect on the A^1_g/A^2_g ratio.[89,108] Raman analysis is highly sensitive to the crystal orientation and thickness of the flakes[108] and is therefore most suitable for the analysis of single mechanically exfoliated flakes.

Gamage *et. al.*[114] used infrared scattering-type scanning near-field microscopy which allows chemical identification of surface degradation species giving detailed

characterisation. However, techniques such as Raman, AFM and TEM do not provide surface sensitive analysis such as other spectroscopic techniques, e.g. XPS. Additionally, Raman, AFM and TEM are time consuming as flakes must be imaged individually while spectroscopic techniques such as FTIR, NMR and XPS analysis allow a large amount of flakes to be characterised simultaneously. XPS has proven to be a useful technique in identifying specific surface oxide species and there has been good correlation between predicted DFT structures and experimental XPS studies.[70,99] However, one of the problems with XPS is the high vacuum environment which can facilitate the removal of oxidation products through a reduction in flake thickness.[105] Phosphoric acid has been reported as a major oxidation product[91,92] but it has not been observed as a final degradation product except when present in a high concentration.[102] The removal of these degradation products can make meaningful analysis challenging and can give an inaccurate representation of degradation products. This effect can be circumvented by combining XPS with other analysis techniques such as FTIR, electrochemical experiments or EELS.[91,102]

1.5.3 Protection Strategies

1.5.3.1 Capping Layers

Passivation layers such as Al_2O_3 or SiO_2 are often deposited to encapsulate BP, thereby preventing reaction with ambient oxidants. Similarly, other 2D materials such as boron nitride (BN), MoS_2 or graphene can also be used to form barriers which circumvent further degradation. The use of various protection strategies and their effect on the stability of BP is summarised in **Table 1.1**. Al_2O_3 is often deposited using ALD which involves the reaction of two precursors (trimethylaluminium and water) that react with the surface separately in a self-limiting reaction at a high

temperature. Alternatively, a layer of Al is deposited which is subsequently oxidised in ambient conditions first, to protect BP from the high-temperature oxidative environment and to avoid contact with oxygenated water before formation of the film.[67,103] Al_2O_3 passivated BP FETs can remain stable for periods up to 1-17 months,[67,115] although the effect of the ALD process on the stability has been debated and degradation of BP during the ALD process has also been observed.[103,116] Luo *et. al.*[117] reported passivated phosphorene transistors displayed a stability of 100 h, while Wood *et. al.*[67] used ALD to deposit a 30 nm Al_2O_3 layer which allowed BP to maintain its mobility and I_{on}/I_{off} ratio for 175 h, during which non-passivated BP FETs display significant deterioration. In contrast, some Al_2O_3 passivated devices have also been reported to lose their electrical properties.[103,116] Thin layers of Al_2O_3 passivation (~2-3 nm) have be reported to be inadequate at encapsulating BP while thicker layers (>25 nm) display superior passivating properties although degradation at edges remains an issue.[116] The additional coating of a fluoropolymer (DuPont Teflon AF) on Al_2O_3 passivated BP preserves its I_{on}/I_{off} ratio, on current and hysteresis in gate voltage due to the hydrophobicity of the polymer which repels oxidants. The degradation of BP flakes coated in a thin layer of Al_2O_3 suggests thicker layers are required which provide additional protection of edge sites while superior passivation can be obtained when employed in combination with a fluoropolymer.[116] An investigation into the effect the surface oxide has during the ALD process revealed the presence of surface oxides can cause further oxidation due to the reaction with adventitious contaminants or H_2O present in the ALD reactor environment.[118] The use of pristine BP is robust enough to be subjected to the ALD deposition of Al_2O_3, however, avoiding oxidation can be difficult and the oxidation of BP highlights the need for development of new moisture- and oxygen-free ALD processes.[103]

Table 1.1: Overview of the protection strategies employed to enhance the ambient stability with corresponding timeframes of BP stability.

Strategy	Stability	Characterisation method	Reference
Al_2O_3	100 h – 17 months	Electrical measurements	67,115,117
SiO_2	7 days	Electrical measurements	72
Boron Nitride	7 days	AFM, Raman	119
MoS_2	21 days	Raman	120
Graphene	100 h	Raman	121
Aryl diazonium salts	25 days	AFM	73
Azobisisobutyronitrile	10 days	XPS, Raman	122
Titanium Sulfonate	72 h	UV	123
Azide	21 days	UV	124
Fluorination	7 days	UV, AFM	125
Chlorosilanes	28 days	Raman, electrical measurements	126
Iodonium salts	2 days	XPS, STEM	127
C_{60}	7 days	UV	111
Perylene diimide	2 days	Raman	128
N-Methyl-2-pyrrolidone	30 days (dark), 11 days (light)	Raman, UV	108
1-butyl-3-methylimidazolium tetrafluoroborate	58 days	Raman, STEM-EELS	108
poly[(1 ,4-diethhynylbenzene)-alt-9,9-biss(4-diphenylaminophenyl)fluorene]	3 months	Electrical measurements	75
Poly(methyl methacrylate)	6 months	NMR, Raman, XRD	76
Polymer Ionic Liquids	120 h	Electrical measurements	129

The use of SiO_2 shows promise in prolonging the ambient lifetime of BP due to its widespread use in the semiconductor industry. SiO_2 passivation of BP allows preservation of the electrical characteristics with a minor change in the $I_{on/off}$ ratio from 810 to 600 while the mobility decreases from 524.3 $cm^2 V^{-1} s^{-1}$ to 470.4 $cm^2 V^{-1} s^{-1}$ over a 1 week period.[72] In comparison, unpassivated BP showed a drop in $I_{on/off}$ ratio from ~600 to ~50 $cm^2 V^{-1} s^{-1}$. Boron nitride has also been employed as a BP passivation layer which preserves its drain current and field effect mobility of 139 $cm^2 V^{-1} s^{-1}$ when stored in a dry N_2 environment while uncapped BP devices display a reduced mobility of 88 $cm^2 V^{-1} s^{-1}$.[103] AFM and Raman analysis reveal the formation of a BP-hBN heterostructure remains stable for a period of a 1 week.[119] MoS_2 passivation prolongs the ambient stability to 3 weeks while also enhancing the thermal stability and photoconductivity.[120] Additionally, a doping effect was observed in few-layer BP flakes which decreases as flake thickness increased. CVD deposited graphene has also been used to extend the ambient lifetime to 100 hours.[121] 1-3 layers of graphene were deposited with 2 or 3 layers displaying a higher stability than a single layer when analysed using Raman analysis. Passivation of BP both using Al_2O_3 or other 2D materials effectively prolongs the ambient lifetime of BP while maintaining its electrical properties as long as the capping layer encapsulates the flake surface as well as the edges. The ambient stability of thicker encapsulation layers (>25 nm) surpasses the lifetime of thinner passivation layers. The deposition of other 2D materials can however have a low yield, due to the physical deposition onto flakes which is completed manually. Although, the stacking of 2D materials to form van der Waals heterostructures, which allows the design of devices with selected properties based on their 2D counterparts, opens up a new range of promising hybrid materials.[130,131]

1.5.3.2 Covalent and Non-covalent Functionalisation

Covalent functionalisation is a promising strategy to enhance the ambient stability of BP by forming a protective layer on the BP surface and occupying the reactive lone pairs, thereby preventing reaction with ambient oxygen and water. Functionalisation has been proposed to occur by attachment directly to P-sites or through attachment to the surface oxide. Ryder *et. al.*[73] used diazonium salts to functionalise mechanically exfoliated BP through attachment of aryl radicals as shown in **Figure 1.21**.

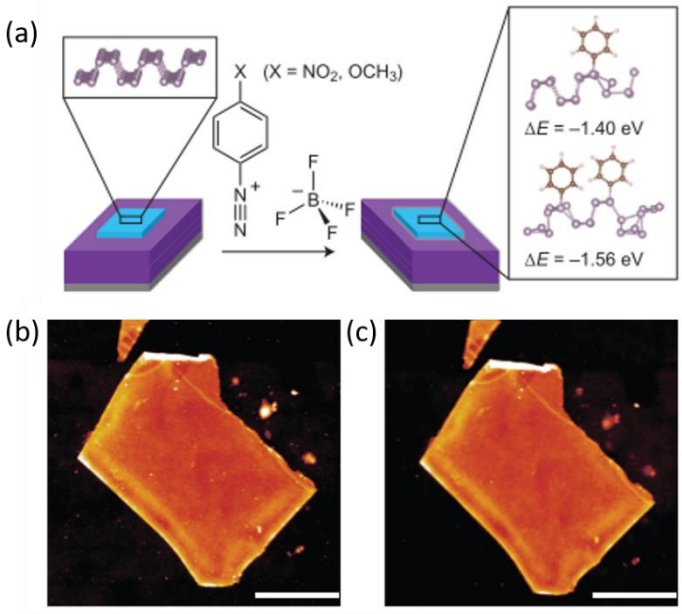

Figure 1.21: Covalent functionalisation of BP through (a) diazonium radicals which result in aryl passivation and (b) AFM analysis of 2-nitrobenzenediazonium functionalised BP directly after functionalisation and (c) after 10 days of ambient exposure. The scale bars correspond to 2 µm. Reprinted from Ryder, C. R. *et. al. Nat. Chem.* **2016**, *8* (6), 597–602. (73).

The use of various substituents on the aryl group tailored the reactivity of salts and therefore the extent of functionalisation which influenced the electrical properties of BP. Attachment was proposed to occur via P-C bonding by formation of four bonds to P which creates a lattice distortion as predicted by DFT calculations. A reduction

in both the P 2p peak and the A^1_g Raman mode indicated disruption of P-P bonding corresponding to arylation. The formation of P-C bonds was characterised using XPS analysis but the binding energy of P-C bonds occurs in close proximity to P-O bonds making accurate deconvolution difficult. Additionally, the P-O component was not assigned even though diazonium functionalisation has been reported to result in significant oxidation.[127] While further theoretical studies report the insertion of a P-C bond which replaces a P-P bond in the BP lattice[132,133] the exact binding of aryl groups remains unclear. Aryl diazonium functionalisation enhanced the stability of BP to 25 days, as characterised by the absence of morphological protrusions during AFM analysis which is displayed in **Figures 1.21**(b)-(c).[73] The use of radicals was also investigated by Hu *et. al.*[122] who used azodiisobutyronitrile (AIBN) to generate free radicals that react with BP through the formation of P-C bonds. AIBN modification resulted in a stability of 10 days in ambient conditions as assessed using XPS and Raman analysis. NMR analysis also revealed AIBN functionalised BP displayed superior aqueous stability compared to bare BP.[122]

Sofer *et. al.*[133] reported the attachment of nucleophilic, organometallic and radical based species with BP. Nucleophilic reagents, in particular (*S*)-bromomethyl ethanethiolate was found to be most effective, through both covalent and non-covalent attachment. Additionally, DFT calculations revealed Br elimination was required for covalent modification through P-C or P-O-C bond formation. Perfluorinated alkyl and aryl molecules were also investigated but were found to be less effective for functionalisation. The use of diazonium reagents did not show signs of chemical modification which was attributed to the use of DMF as a reaction solvent instead of water. Organometallic reagents also only showed subtle signs of covalent attachment

indicating nucleophilic reagents proved to be more successful. Modification of BP has also been achieved using a titanium sulfonate ligand which coordinated to P through Ti, giving stability in aqueous solutions of 72 h when assessed using extinction spectroscopy.[123] **Figure 1.22** shows azide passivation which resulted in the formation of P=N bonds through the in-situ creation of a nitrene intermediate.[124] The fulfilment of a full octet by reaction with a surface lone pair significantly increased the stability to 21 days as assessed using extinction spectroscopy.

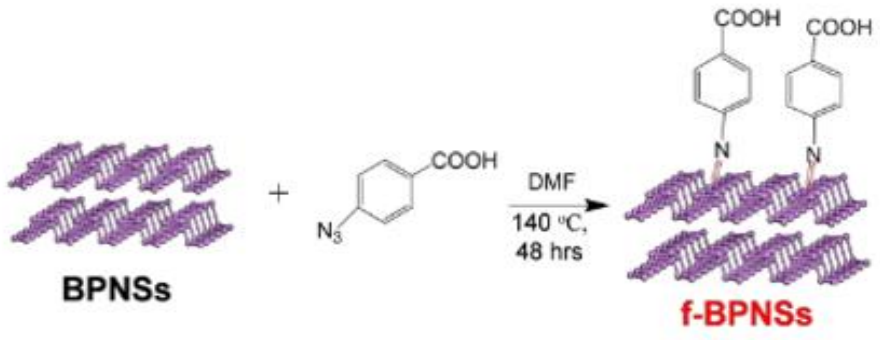

Figure 1.22: Azide passivation resulting in the formation of P=N bonds. Reprinted from Yajuan Liu. *et. al. Angew. Chemie Int. Ed.* **2019**, *58* (5), 1479–1483. (124).

Recently, fluorination of the BP surface has been investigated as a protection method similar to the fluorination of graphene which drastically modifies its properties.[134] Theoretical studies predict fluorinated BP to be energetically stable[135] but the high reactivity of fluorine could result in degradation. Fluorination has been realised through electrochemical exfoliation in an ionic liquid[125] and under a continuous flow of fluorine at various pressures and temperatures.[136] The fluorination of BP enhanced the ambient stability up to 1 week due the high electronegativity of fluorine which repels oxidants.[125] Additionally, control over fluorination has been predicted to allow tunability of the bandgap of BP,[125,135] which could be a more realistic strategy of stabilising and modifying the properties of BP compared to controlling the oxidation of BP.

Attachment through oxygen sites present on the BP surface has also been investigated as a protection strategy. Artel *et. al.*[126] used chlorosilanes to prevent ambient degradation of BP and preserve its electrical properties. Chlorosilanes form an ordered SAM by reduction of the surface oxide. The covalent attachment to oxide sites was confirmed by the absence of chlorine and a reduced oxide component of the P 2p core level in XPS. Coated flakes displayed a stability of 28 days using Raman analysis and BP devices also remained stable during this timeframe. The use of thiols as a protection strategy was investigated by Kwak *et. al.*[137]. Interestingly, surface oxides present on the BP surface were removed by thiol treatment. DFT calculations revealed a P-O-H chain is removed from the surface during the binding of a thiol molecule resulting in removal of surface oxide sites. XPS and Raman analysis indicated restoration of the pristine BP surface, which was also visible through the removal of surface bubbles using TEM analysis. Electron and hole mobility was also restored to the values of pristine BP after the thiol treatment and an annealing step.[137] Binding to surface oxides sites is accompanied by a reduction in the oxide component of the P 2p core level in XPS which was also observed for aryliodonium functionalisation of BP.[127] Furthermore, the attachment to surface oxides sites by aryl iodonium salts protects the surface by impeding reaction and decomposition of the oxides, as initial oxide formation promotes further oxidation.[127] Therefore, binding to P-sites only will likely give inferior stability as existing oxides present on the surface will lead to decomposition and a strategy that protects both P- and O-sites will result in optimal stability. Recently, edge selective functionalisation of BP using hydrophobic C_{60} molecules significantly enhanced its stability, by protecting edge sites from degradation while preserving the photoelectrochemical and photocatalytic properties

of BP.[111] UV-vis spectroscopy revealed that the BP-C_{60} hybrid maintained its absorbance peak, surpassing the stability of bare BP.

Covalent modification can lead to the formation of defects and can have a detrimental effect on the electrical properties of BP while non-covalent functionalisation exploits the weak van der Waals forces to protect the BP surface. Passivation of BP using non-covalent interactions enables tuning of its properties through the charge transfer induced by complexes that can be selected based on their electron-withdrawing capability. Abellan *et. al.*[128] reported the noncovalent functionalisation of liquid exfoliated BP using 7,7,8,8-tetra-cyano-p-quinodimethane (TCNQ) and perylene diimide (PDI) which displayed increased stability compared to bare BP. The use of TCNQ resulted in a large electron transfer from BP while PDI only created weak charge transfer. The non-covalent interactions of these complexes also played a facilitative role in the exfoliation of BP. Similarly, Anthraquinone was used by Gusmão *et. al.*[138] to enhance the storage capacity and prolong the ambient lifetime of BP due to its hydrophobicity.

1.5.3.3 Solvent-Based Protection Methods

The lifetime of liquid exfoliated flakes is higher than that observed for mechanically exfoliated flakes, indicating that the exfoliation procedure can influence degradation.[62] Solvent passivation plays a significant role in the stability of exfoliated flakes both in solution and after removal of the solvent, as certain solvents can form a protective barrier to oxidants. Mechanically exfoliated flakes have displayed bumps on the basal plane,[107] while liquid exfoliated flakes are predominantly degraded at edges sites as the exfoliating medium protects the basal plane during degradation.[62] The exfoliation

strategy therefore defines the oxidation mechanism and solvent passivation can be employed as a protection strategy. Hanlon *et. al.*[62] successfully obtained high yields of BP through liquid exfoliation in NMP. The flakes displayed a significantly higher stability than mechanically exfoliated flakes and those exfoliated using other solvents, such as isopropyl alcohol (IPA). The increased stability was attributed to the formation of a solvation shell both in solution and after deposition onto substrates. Abellan *et. al.*[108] confirmed solvents had an impact on the stability of various solvent passivated flakes, including tetrahydrofuran (THF), NMP and ionic liquids (ILs). While THF did not influence the lifetime of BP, NMP greatly enhanced the stability of flakes up to 30 days, especially when stored in dark conditions. However, solvent passivation can make fabrication of devices challenging[108] and can be detrimental to electrical performance.[139] Solvent passivation is also undesirable for the performance of energy storage devices.[139] Therefore, the use of ILs which can easily be removed by rinsing has been investigated as a protection strategy.[108] ILs facilitate efficient high-yield exfoliation of 2D materials[87,140–143] and provide a protective barrier to degradation.[142] Two ILs, 1-ethyl-3-methylimidazolium bis(trifluoromethylsulfonyl) imide and 1-butyl-3-methylimidazolium bis(trifluoromethylsulfonyl)imide, were used for the liquid exfoliation of BP. Both ILs resulted in the production of few-layer flakes and SIMS suggested the IL formed a thin passivation layer on the BP surface. Exfoliation in the IL resulted in minimal generation of surface oxide due to the passivation by the ILs through van der Waals interactions, however, long-term stability was not assessed.[141] Furthermore, Abellán *et. al.*[108] used 1-butyl-3-methylimidazolium tetrafluoroborate to protect BP, as displayed in **Figure 1.23**, which also resulted in a thin coverage and enhanced the ambient stability of BP flakes for up to 58 days. The increased oxidation resistance was attributed to a high surface

tension of the IL which creates a barrier to oxidants and the ability of the imidazole species to neutralise superoxide anions which play a key role in the degradation of BP.[108]

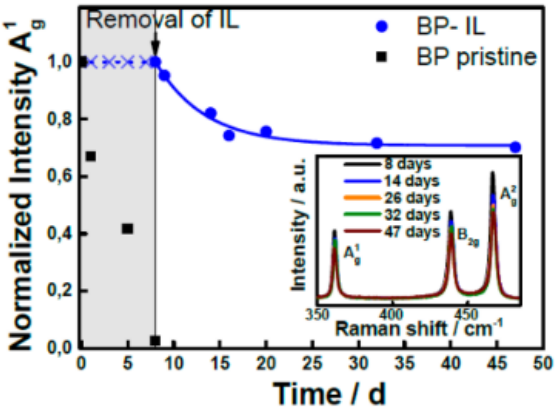

Figure 1.23: Normalised A^1_g intensity of IL-passivated and bare BP during ambient exposure. Reprinted from Abellán, G. *et. al. J. Am. Chem. Soc.* **2017**, *139* (30), 10432–10440. (108).

1.5.3.4 Polymer-Based Protection Methods

Addition of polymers during the exfoliation process has also become a popular method of tuning the properties of BP and enhancing its stability. The use of polymers with various electron withdrawing and donating groups can allow tailoring of the energy bands which can influence the ambient stability.[132] Additionally, BP-polymer composites have been predicted to maintain electron and hole mobilities.[132] Various polymers have been employed to create BP-hybrids for sensors,[144] photothermal agents[145] and enhance the performance of energy storage devices.[146,147] Poly (lactic-co-glycolic acid) (PLGA) was employed to enhance the stability of BP quantum dots to 8 days compared to unencapsulated BP when assessed using uv-vis analysis.[148] The use of poly[(1,4-diethynylbenzene)-alt-9,9-bis(4-diphenylaminophenyl)fluorene] to enhance the solubility in organic solvents and improve ambient stability has been reported by Cao *et. al.*[75]. Fluorescence spectroscopy revealed that electron transfer

occurred and memory devices remained stable for 3 months due to polymer incorporation. Poly(methyl methacrylate) (PMMA) has also been used to stabilise BP using 3 different strategies: (1) liquid exfoliated BP was added to a solution of PMMA, (2) BP was exfoliated in a PMMA solution and (3) in-situ polymerisation using methyl methacrylate and a radical initiator.[76] The polymerisation by addition of a radical initiator proved to be most effective and displayed a stability of 6 months, however, stability was only assessed using NMR, Raman and X-ray diffraction (XRD) analysis. Similarly, exfoliation of BP in a solution of polyvinylpyrrolidone (PVP) and ethanol prolonged the stability to 24 h as assessed using extinction spectroscopy and AFM analysis. XPS analysis also only showed a 3.9 % oxide component compared to the P 2p core level over a period of 1 week. The removal of PVP was achieved using ethanol rinses allowing for use of the exfoliated nanosheets in various applications.[149] Polymer ionic liquids (PILs) have been employed to enhance the ambient lifetime to 120 h and provide reliable electrical contact for devices. The use of conductive materials to protect BP overcomes the limitations of insulating capping materials such as AlO_x and SiO_2, while the formation of a BP-hybrid during sonication ensures scalability.[129] The use of PILs allows dilution of the IL while maintaining high exfoliation yields in contrast to the low yields obtained from diluted ILs.[129] Incorporation of BP with polymers appears to be a useful strategy for enhancement of the stability and full exploitation of its properties.

1.6 Antimonene

Among the 2D pnictogens, antimonene (AM) has recently gained interest within the 2D community. First isolated in 2015, AM displays a high carrier mobility and tunable bandgap, similar to BP, but exhibits a higher ambient stability which makes it more

practical for various applications. Theoretical studies predict an indirect bandgap in the 0-2.28 eV range which is tunable through layer thickness[150] or surface oxidation.[151] The use of strain[152,153] or oxidation[151] can be used to change AM to a direct bandgap material. AM shows promise in electronics,[154] energy storage,[155] solar cells,[150] optoelectronics,[152] catalysis,[156] medical applications[157–159] and as a saturable absorber.[160] Research on the production of AM has focused on the bottom-up growth while its mechanical and liquid exfoliation still remain limited. The strong interlayer binding of AM can hinder its smooth exfoliation which can impede the exfoliation of the material into sheets with large lateral sizes, and favours the formation of quantum dots.[48]

1.6.1 Structure and Properties

Sb has a rhombohedral layered structure, which is also known as the β-phase, and it displays semimetallic behaviour.[48] AM is most stable in buckled form corresponding to the β-phase, as illustrated in **Figure 1.24**, in contrast to the puckered structure or α-phase of BP.[49]

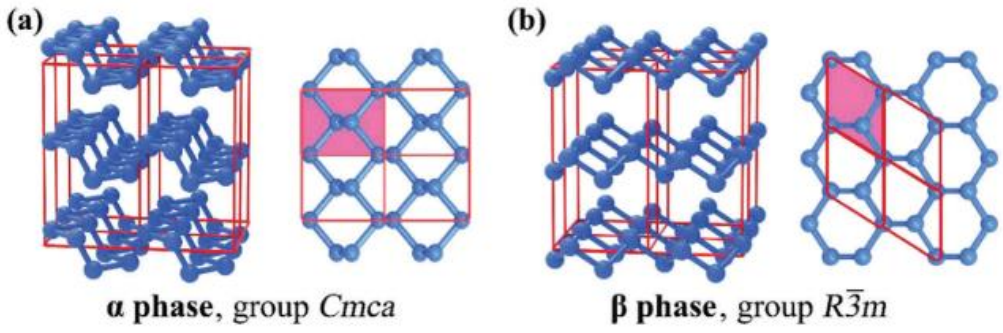

Figure 1.24: Comparison of the (a) α-phase or puckered honeycomb structure and the (b) β-phase which is also known as the buckled structure. Sb occurs in the β-phase while BP is most stable in the α-phase. Reprinted from Zhang, S. *et. al. Chem. Soc. Rev.* **2018**, *47* (3), 982–1021. (49).

AM displays semiconducting character, with electron and hole mobilities calculated to be 630 and 1737 cm2 V^{-1} s^{-1},[161] making it suitable for electronic applications.[150] AM flakes display good electrical conductivity of 10^4 S m^{-1} while also exhibiting optical transparency in the visible light range.[162] The theoretical bandgap of AM has been predicted to be in the 0-2.28 eV range. However, an experimental bandgap of 0.8-1.44 eV compared to the predicted 0-2.28 eV theoretical bandgap has been observed. The difference between the experimental and theoretical bandgap was attributed to surface oxidation.[150] Variation of the layer thickness resulted in a modification of the bandgap, similar to BP. While AM displays an indirect bandgap, the application of strain can allow transformation to a direct bandgap semiconductor. The resulting bandgap of 2.28 eV shows promise in optoelectronic applciations.[152,153] Tuning of the bandgap of AM has also allowed it to be employed as a more efficient hole transport layer in perovskite solar cells.[150]

1.6.2 Production

AM was first synthesised using van der Waals epitaxy growth. The growth of AM on both mica and flexible substrates resulted in monocrystalline few-layer (1-50 nm) rhombohedral AM, corresponding to the most stable β-phase.[162] Graphene has been used a substrate for the van der Waals epitaxy growth of Sb islands, sheets and thin-films which could be useful for the formation of van der Waals heterostrutures.[163] $PdTe_2$ has also been used as a substrate for the molecular beam epitaxial growth of AM due to its minimal lattice match and chemical surface stability.[164] AM also grows selectively on MoS_2 areas on a sapphire substrates, which could potentially be used as contacts for 2D material devices.[165] Additionally, Ge has been used as a substrate for the epitaxial growth of mono- and few-layer AM.[166] Chemical vapour deposition can

also be used for the production of AM on SiO_2 substrates, which results in the formation of large sheets in the 40 μm range.[167] The wet chemical synthesis of hexagonal antimonene nanosheets was carried out using various Sb precursors which were mixed with oleylamine. The layer thickness of AM sheets can be tuned through variation of the annealing time.[168]

While AM has been synthesised using various bottom-up approaches, literature reports on the production of AM by exfoliation remain limited. AM was mechanically exfoliated into few-layer flakes in 2016, which displayed good ambient stability of 2 months and did not show deterioration after exposure to water.[169] The liquid phase exfoliation of AM was reported by Gibaja *et. al.*[170], who used a mixture of isopropyl alcohol (IPA)/water (4:1) to produce stable few-layer flakes with high ambient stability. The use of a mixture of IPA and water was selected based on the surface tension of the solvents, as a match between the surface tension of the layered material and solvent promotes exfoliation and prevents reaggregation of flakes.[80,171] Liquid exfoliation in ethanol using combined probe sonication and ice-bath sonication resulted in the formation of antimonene quantum dots (AMQDs) with average dimensions of 3.9 nm in length and 2.6 nm in height.[157] Electrochemical exfoliation of Sb also resulted in the formation of AMQDs with an average thickness of 31.6 nm.[172] Similarly, shear exfoliation was used to create few-layer Sb, As and Bi nanosheets by Gusmão *et. al.*[156] which show promise in catalysis applications, in particular the hydrogen evolution reaction where the performance of AM surpasses other pnictogen nanosheets, such as arsenene and bismuthene.[156] The exfoliation of Sb into few-layer sheets with large lateral dimensions can be difficult due to the strong interlayer interactions. The pre-grinding of Sb results in the formation of Sb plates

which can subsequently be exfoliated into large Sb sheets using tip sonication, as shown in **Figure 1.25**.[150]

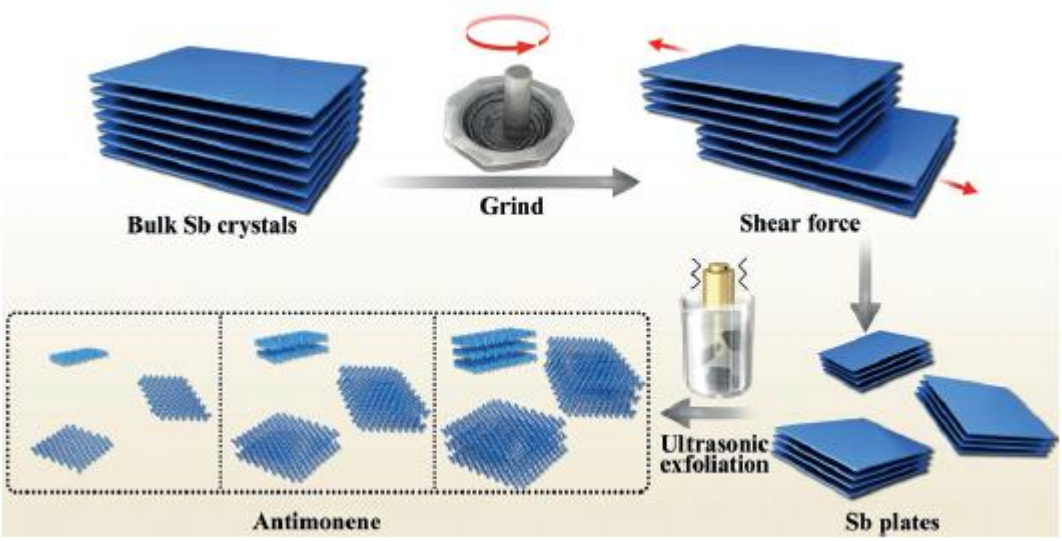

Figure 1.25: Grinding of Sb creates Sb plates which can be exfoliated into AM sheets using sonication. Reprinted from Wang, X. *et. al. Angew. Chemie* **2018**, *130* (28), 8804–8809. (150).

The AM nanosheets were separated using liquid cascade centrifugation, which successfully separated the flakes with various layer thicknesses and confirmed the production of large few-layer AM sheets, as displayed in **Figure 1.26**.

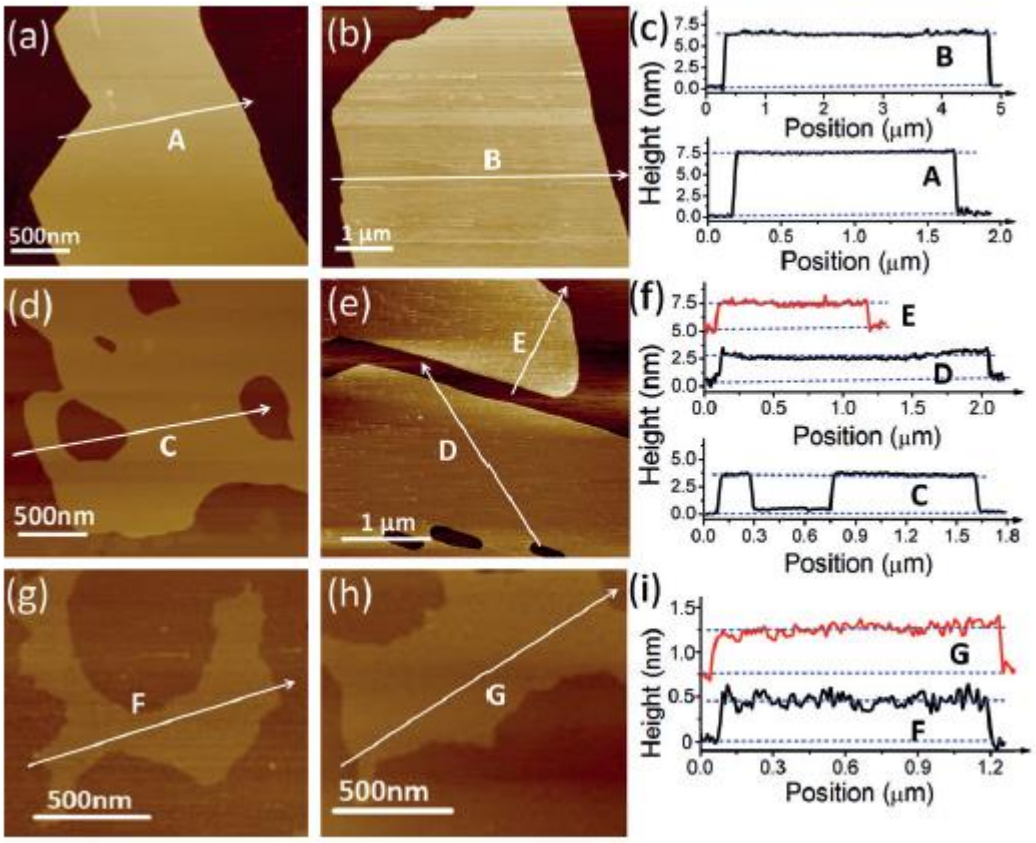

Figure 1.26: AFM analysis with corresponding height profiles for AM centrifuged at (a)-(c) 1000–2000 rpm, (d)–(f) 2000–5000 rpm, (g)–(i) 5000–9000 rpm. Reprinted from Wang, X. *et. al. Angew. Chemie* **2018**, *130* (28), 8804–8809. (150).

1.6.3 Ambient Stability of Antimonene

AM has been reported to display a significantly higher stability compared to BP. Flakes remain stable for at least a period of 1 month in ambient conditions.[150,162,164] AM flakes grown by van der Waals epitaxy did not show an increase in roughness using AFM measurements and did not display the appearance of antimony trioxide or pentoxide peaks, as assessed using Raman spectroscopy over a 1 month period.[162] XPS analysis also confirms the increased stability with no increase in the oxide content.[150] The high ambient stability of non-covalently functionalised AM flakes was investigated and the formation of a self-passivating oxide layer was discovered using

theoretical studies.[173] Theoretical calculations also reveal oxygen is more likely to react with BP compared to AM due to a more negative exothermic energy of the reaction of BP with oxygen.[162] However, a separate theoretical study attributes the increased ambient stability of AM compared to BP, to its strong interaction with oxygen but weak interaction with water,[174] as the rapid degradation of BP has often been attributed to the combined effect of oxygen and water.[102] While water acts as an electron acceptor for AM, it acts as an electron donor for BP which facilitates the formation of acids and subsequent degradation. The energy barrier of oxygen dissociation was also quite low which indicates oxidation of AM could occur under ambient conditions.[174] However, as the interaction with water does not result in deterioration of AM the formation of AM oxides may be easier to produce, compared to the formation of phosphorene oxides. AM oxides have been predicted to have tunable bandgap (0-2.28 eV) based on their oxygen content and have been predicted to be a 2D topological insulators.[151] The adsorption of oxygen on AM also alters the optical and electrical properties. Theoretical studies show the ease with which ambient contaminants, such as NO_2, H_2O, and O_2, adsorb on the AM surface, which highlights the need for a protective layer that preserves the electrical properties of AM during operation.[174]

1.6.5 Functionalisation

Although AM does not degrade rapidly in ambient conditions, functionalisation is still necessary for protection from ambient contaminants which allows preservation of its properties. Additionally, functionalisation can be used to tune the properties of AM. Theoretical studies indicate the use of tetrathiafulvalene (TTF) and tetracyanoquinodimethane (TCNQ) can induce doping, due to their electron-

withdrawing and -donating character, which can be used to modulate the bandgap and electrical properties of AM.[175] Non-covalent functionalisation was carried out using perylene bisimide (PBI) and TCNQ, resulting in charge transfer, which has also been observed during the non-covalent functionalisation of BP. The wet chemical synthesis of AM nanosheets resulted in the surface passivation of halide ions and coordination of thiol groups indicating functionalisation of the sheets.[168] Fluorination has become a popular method to tailor the properties of both graphene and BP,[176] and has also been applied to AM. Fluorinated AM displays ferromagnetic properties while its curie temperature at 717 K makes it suitable for magnetic devices.[177] The chemical modification of AM remains extremely limited and further investigation into the functionalisation is necessary.

1.7 Conclusions and Future Outlook

The 2D pnictogens show promising properties for electrical devices, although their implementation is still limited by certain roadblocks. While BP devices display excellent electrical properties their ambient degradation results in a loss of mobility. The key mechanisms of degradation indicate a general agreement that oxidation of BP is initiated by the reaction with oxygen followed by reaction with water, which promotes further decomposition. Despite its extraordinary properties, the ambient lifetime remains a significant hurdle of the material. The modification, either by physical capping layers or chemical protective layers, can significantly increase its ambient lifetime while preserving the electrical characteristics. Several protection strategies have been developed to enhance its ambient stability, although there is still room for further investigation. Covalent functionalisation using aryl diazonium salts or chlorosilanes has been reported to give superior oxidation resistance of BP. In

particular, recent developments, including the use of ILs or polymer incorporation show promise in protecting BP and additionally provide scalability. BP offers extraordinary properties and a wide range of potential applications once its ambient degradation has been fully addressed. Although the superior ambient stability of AM should facilitate the application of the material, its smooth exfoliation is a hurdle to the large scale production of nanosheets with large lateral dimensions. Additionally, the surface chemistry and functionalisation remain undiscovered and require further investigation.

1.8 References

(1) International Roadmap for Devices and Systems (https://irds.ieee.org/images/files/pdf/2017/2017IRDS_MM.pdf).

(2) Peercy, P. S. The Drive to Miniaturization. *Nature* **2000**, *406* (6799), 1023–1026.

(3) Ho, J. C.; Yerushalmi, R.; Jacobson, Z. a; Fan, Z.; Alley, R. L.; Javey, A. Controlled Nanoscale Doping of Semiconductors via Molecular Monolayers. *Nat. Mater.* **2008**, *7* (1), 62–67.

(4) Wu, H.; Guan, B.; Sun, Y.; Zhu, Y.; Dan, Y. Controlled Doping by Self-Assembled Dendrimer-like Macromolecules. *Sci. Rep.* **2017**, *7*, 41299.

(5) Alphazan, T.; Adrian, A. D.; Martin, F.; Grampeix, H.; Enyedi, V.; Martinez, E.; Rochat, N.; Veillerot, M.; Dewitte, M.; Nys, J.-P.; Berthe, M.; Stiévenard, D.; Thieuleux, C.; Grandidier, B. Shallow Heavily Doped N++ Germanium by Organo-Antimony Monolayer Doping. *ACS Appl. Mater. Interfaces* **2017**, *9* (23), 20179–20187.

(6) Long, B.; Alessio Verni, G.; O'Connell, J.; Holmes, J.; Shayesteh, M.; O'Connell, D.; Duffy, R. Molecular Layer Doping: Non-Destructive Doping of Silicon and Germanium. In *2014 20th International Conference on Ion Implantation Technology (IIT)*; Portland, 2014; pp 1–4.

(7) Cho, K.; Ruebusch, D. J.; Lee, M. H.; Moon, J. H.; Ford, A. C.; Kapadia, R.; Takei, K.; Ergen, O.; Javey, A. Molecular Monolayers for Conformal, Nanoscale Doping of InP Nanopillar Photovoltaics. *Appl. Phys. Lett.* **2011**, *98* (20), 203101.

(8) Ho, J. C.; Ford, A. C.; Chueh, Y.-L.; Leu, P. W.; Ergen, O.; Takei, K.; Smith, G.; Majhi, P.; Bennett, J.; Javey, A. Nanoscale Doping of InAs via Sulfur

Monolayers. *Appl. Phys. Lett.* **2009**, *95* (7), 72108.

(9) O'Connell, J.; Napolitani, E.; Impellizzeri, G.; Glynn, C.; McGlacken, G. P.; O'Dwyer, C.; Duffy, R.; Holmes, J. D. Liquid-Phase Monolayer Doping of InGaAs with Si-, S-, and Sn-Containing Organic Molecular Layers. *ACS Omega* **2017**, *2* (5), 1750–1759.

(10) Ho, J. C.; Yerushalmi, R.; Smith, G.; Majhi, P.; Bennett, J.; Halim, J.; Faifer, V. N.; Javey, A. Wafer-Scale, Sub-5 Nm Junction Formation by Monolayer Doping and Conventional Spike Annealing. *Nano Lett.* **2009**, *9* (2), 725–730.

(11) Van Druenen, M.; Collins, G.; Glynn, C.; O'Dwyer, C.; Holmes, J. D. Functionalization of SiO2 Surfaces for Si Monolayer Doping with Minimal Carbon Contamination. *ACS Appl. Mater. Interfaces* **2018**, *10* (2), 2191–2201.

(12) O'Connell, J.; Verni, G. A.; Gangnaik, A.; Shayesteh, M.; Long, B.; Georgiev, Y. M.; Petkov, N.; McGlacken, G. P.; Morris, M. A.; Duffy, R.; Holmes, J. D. Organo-Arsenic Molecular Layers on Silicon for High-Density Doping. *ACS Appl. Mater. Interfaces* **2015**, *7* (28), 15514–15521.

(13) Ye, L.; Pujari, S. P.; Zuilhof, H.; Kudernac, T.; de Jong, M. P.; van der Wiel, W. G.; Huskens, J. Controlling the Dopant Dose in Silicon by Mixed-Monolayer Doping. *ACS Appl. Mater. Interfaces* **2015**, *7* (5), 3231–3236.

(14) Ye, L.; González-Campo, A.; Nuñez, R.; de Jong, M. P.; Kudernac, T.; van der Wiel, W. G.; Huskens, J. Boosting the Boron Dopant Level in Monolayer Doping by Carboranes. *ACS Appl. Mater. Interfaces* **2015**, *7* (49), 27357–27361.

(15) Alphazan, T.; Mathey, L.; Schwarzwälder, M.; Lin, T.-H.; Rossini, A. J.; Wischert, R.; Enyedi, V.; Fontaine, H.; Veillerot, M.; Lesage, A.; Emsley, L.; Veyre, L.; Martin, F.; Thieuleux, C.; Copéret, C. Monolayer Doping of Silicon

through Grafting a Tailored Molecular Phosphorus Precursor onto Oxide-Passivated Silicon Surfaces. *Chem. Mater.* **2016**, *28* (11), 3634–3640.

(16) Perego, M.; Seguini, G.; Arduca, E.; Nomellini, A.; Sparnacci, K.; Antonioli, D.; Gianotti, V.; Laus, M. Control of Doping Level in Semiconductors via Self-Limted Grafting of Phosphorus End-Terminated Polymers. *ACS Nano* **2018**, *12* (1), 178–186.

(17) Voorthuijzen, W. P.; Yilmaz, M. D.; Naber, W. J. M.; Huskens, J.; van der Wiel, W. G. Local Doping of Silicon Using Nanoimprint Lithography and Molecular Monolayers. *Adv. Mater.* **2011**, *23* (11), 1346–1350.

(18) Hazut, O.; Yerushalmi, R. Direct Dopant Patterning by a Remote Monolayer Doping Enabled by a Monolayer Fragmentation Study. *Langmuir* **2017**, *33* (22), 5371–5377.

(19) Taheri, P.; Fahad, H. M.; Tosun, M.; Hettick, M.; Kiriya, D.; Chen, K.; Javey, A. Nanoscale Junction Formation by Gas-Phase Monolayer Doping. *ACS Appl. Mater. Interfaces* **2017**, *9* (24), 20648–20655.

(20) Arduca, E.; Mastromatteo, M.; Salvador, D. De; Seguini, G.; Lenardi, C.; Napolitani, E. Synthesis and Characterization of P δ -Layer in SiO 2 by Monolayer Doping. *Nanotechnology* **2016**, *27* (7), 75606.

(21) Mathey, L.; Alphazan, T.; Valla, M.; Veyre, L.; Fontaine, H.; Enyedi, V.; Yckache, K.; Danielou, M.; Kerdiles, S.; Guerrero, J.; Barnes, J.-P.; Veillerot, M.; Chevalier, N.; Mariolle, D.; Bertin, F.; Durand, C.; Berthe, M.; Dendooven, J.; Martin, F.; Thieuleux, C.; Grandidier, B.; Copéret, C. Functionalization of Silica Nanoparticles and Native Silicon Oxide with Tailored Boron-Molecular Precursors for Efficient and Predictive p -Doping of Silicon. *J. Phys. Chem. C* **2015**, *119* (24), 13750–13757.

(22) O'Connell, J.; Collins, G.; McGlacken, G. P.; Duffy, R.; Holmes, J. D. Monolayer Doping of Si with Improved Oxidation Resistance. *ACS Appl. Mater. Interfaces* **2016**, *8* (6), 4101–4108.

(23) Veerbeek, J.; Ye, L.; Vijselaar, W.; Kudernac, T.; van der Wiel, W. G.; Huskens, J. Highly Doped Silicon Nanowires by Monolayer Doping. *Nanoscale* **2017**, *9* (8), 2836–2844.

(24) Hazut, O.; Agarwala, A.; Amit, I.; Subramani, T.; Zaidiner, S.; Rosenwaks, Y.; Yerushalmi, R. Contact Doping of Silicon Wafers and Nanostructures with Phosphine Oxide Monolayers. *ACS Nano* **2012**, *6* (11), 10311–10318.

(25) Ye, L.; Gonzalez-Campo, A.; Kudernac, T.; Nuñez, R.; Jong, M. De; Wiel, W. G. Van Der; Huskens, J. Monolayer Contact Doping from a Silicon Oxide Source Substrate. *Langmuir* **2017**, *33* (15), 3635–3638.

(26) Hazut, O.; Huang, B.; Pantzer, A.; Amit, I.; Rosenwaks, Y.; Kohn, A.; Chang, C.; Chiu, Y.-P.; Yerushalmi, R. Parallel p–n Junctions across Nanowires by One-Step Ex Situ Doping. *ACS Nano* **2014**, *8* (8), 8357–8362.

(27) Longo, R. C.; Cho, K.; Schmidt, W. G.; Chabal, Y. J.; Thissen, P. Monolayer Doping via Phosphonic Acid Grafting on Silicon: Microscopic Insight from Infrared Spectroscopy and Density Functional Theory Calculations. *Adv. Funct. Mater.* **2013**, *23* (27), 3471–3477.

(28) Longo, R. C.; Cho, K.; Hohmann, S.; Thissen, P. Mechanism of Phosphorus Transport Through Silicon Oxide During Phosphonic Acid Monolayer Doping. *J. Phys. Chem. C* **2018**, *122* (18), 10088–10095.

(29) Shimizu, Y.; Takamizawa, H.; Inoue, K.; Yano, F.; Nagai, Y.; Lamagna, L.; Mazzeo, G.; Perego, M.; Prati, E. Behavior of Phosphorous and Contaminants from Molecular Doping Combined with a Conventional Spike Annealing

Method. *Nanoscale* **2014**, *6* (2), 706–710.

(30) Caccamo, S.; Puglisi, R. A.; Di Franco, S.; D'Urso, L.; Indelicato, V.; Italia, M.; Pannitteri, S.; La Magna, A. Silicon Doped by Molecular Doping Technique: Role of the Surface Layers of Doped Si on the Electrical Characteristics. *Mater. Sci. Semicond. Process.* **2016**, *42*, 200–203.

(31) Gao, X.; Guan, B.; Mesli, A.; Chen, K.; Dan, Y. Deep Level Transient Spectroscopic Investigation of Phosphorus-Doped Silicon by Self-Assembled Molecular Monolayers. *Nat. Commun.* **2018**, *9* (1), 118.

(32) Gao, X.; Guan, B.; Mesli, A.; Chen, K.; Sun, L.; Dan, Y. Toward Defect-Free Doping by Self-Assembled Molecular Monolayers: The Evolution of Interstitial Carbon-Related Defects in Phosphorus-Doped Silicon. *ACS Omega* **2019**, *4* (2), 3539–3545.

(33) Chidambaram, P. R.; Bowen, C.; Chakravarthi, S.; Machala, C.; Member, S.; Wise, R. Fundamentals of Silicon Material Properties for Successful Exploitation of Strain Engineering in Modern CMOS Manufacturing. *IEEE Trans. Electron Devices* **2006**, *53* (5), 944–964.

(34) Pillarisetty, R. Academic and Industry Research Progress in Germanium Nanodevices. *Nature* **2011**, *479* (7373), 324–328.

(35) Alamo, J. A. Nanometre-Scale Electronics with III – V Compound Semiconductors. *Nature* **2011**, *479* (7373), 317.

(36) Novoselov, K. S.; Geim, A. K.; Morozov, S. V; Jiang, D.; Zhang, Y.; Dubonos, S. V; Grigorieva, I. V; Firsov, a a. Electric Field Effect in Atomically Thin Carbon Films. *Science (80-.).* **2004**, *306* (2004), 666–669.

(37) Liu, H., Neal, A. T., Zhu, Z., Luo, Z., Xu, X., Tománek, D., & Peide, D. Y. Phosphorene : An Unexplored 2D Semiconductor with a High Hole Mobility.

ACS Nano **2014**, *8* (4), 4033–4041.

(38) Roy, T.; Tosun, M.; Kang, J. S.; Sachid, A. B.; Desai, S. B.; Hettick, M.; Hu, C. C.; Javey, A. Field-Effect Transistors Built from All Two-Dimensional Material Components. *ACS Nano* **2014**, *8* (6), 6259–6264.

(39) Chhowalla, M.; Jena, D.; Zhang, H. Two-Dimensional Semiconductors for Transistors. *Nat. Rev. Mater.* **2016**, *1* (11), 16052.

(40) Wang, Q. H.; Kalantar-zadeh, K.; Kis, A.; Coleman, J. N.; Strano, M. S. Electronics and Optoelectronics of Two-Dimensional Transition Metal Dichalcogenides. *Nat. Nanotechnol.* **2012**, *7* (11), 699–712.

(41) Manzeli, S.; Ovchinnikov, D.; Pasquier, D.; Yazyev, O. V; Kis, A. 2D Transition Metal Dichalcogenides. *Nat. Rev.* **2017**, *2* (8), 17033.

(42) Chhowalla, M.; Shin, H. S.; Eda, G.; Li, L.; Loh, K. P.; Zhang, H. The Chemistry of Two-Dimensional Layered Transition Metal Dichalcogenide Nanosheets. *Nat. Chem.* **2013**, *5* (4), 263–275.

(43) Molle, A.; Goldberger, J.; Houssa, M.; Xu, Y.; Zhang, S. Buckled Two-Dimensional Xene Sheets. *Nat. Mater.* **2017**, *16* (2), 163.

(44) Molle, A., Grazianetti, C., Tao, L., Taneja, D., Alam, M. H., & Akinwande, D. Silicene, Silicene Derivatives, and Their Device Applications. *Chem. Soc. Rev.* **2018**, *47* (16), 6370–6387.

(45) Balendhran, S.; Walia, S.; Nili, H.; Sriram, S.; Bhaskaran, M. Elemental Analogues of Graphene: Silicene, Germanene, Stanene, and Phosphorene. *Small* **2015**, *11* (6), 640–652.

(46) Huey, W. L. B.; Goldberger, J. E.; Goldberger, J. E. Covalent Functionalization of Two-Dimensional Group 14 Graphane Analogues. *Chem. Soc. Rev.* **2018**, *47* (16), 6201–6223.

(47) Bianco, E.; Butler, S.; Jiang, S.; Restrepo, O. D.; Windl, W.; Goldberger, J. E. Stability and Exfoliation of Germanane : A Germanium Graphane Analogue. *ACS Nano* **2013**, *7* (5), 4414–4421.

(48) Pumera, M.; Sofer, Z. 2D Monoelemental Arsenene, Antimonene, and Bismuthene: Beyond Black Phosphorus. *Adv. Mater.* **2017**, *29* (21), 1605299.

(49) Zhang, S.; Guo, S.; Chen, Z.; Wang, Y.; Gao, H.; Gómez-Herrero, J.; Ares, P.; Zamora, F.; Zhu, Z.; Zeng, H. Recent Progress in 2D Group-VA Semiconductors : From Theory to Experiment. *Chem. Soc. Rev.* **2018**, *47* (3), 982–1021.

(50) Ling, X.; Wang, H.; Huang, S.; Xia, F.; Dresselhaus, M. S. The Renaissance of Black Phosphorus. *Proc. Natl. Acad. Sci.* **2015**, *112* (15), 4523–4530.

(51) Gusmao, R.; Sofer, Z.; Pumera, M. Black Phosphorus Rediscovered: From Bulk to Monolayer. *Angew. Chemie Int. Ed.* **2017**, *56* (28), 8052–8072.

(52) Chen, P.; Li, N.; Chen, X.; Ong, W.; Zhao, X. The Rising Star of 2D Black Phosphorus beyond Graphene : Synthesis , Properties and Electronic Applications The Rising Star of 2D Black Phosphorus beyond Graphene : Synthesis , Properties and Electronic Applications. *2D Mater.* **2017**, *5* (1), 014002.

(53) Koenig, S. P.; Doganov, R. A.; Schmidt, H.; Castro Neto, A. H.; Özyilmaz, B. Electric Field Effect in Ultrathin Black Phosphorus. *Appl. Phys. Lett.* **2014**, *104* (10), 103–106.

(54) Liu, H.; Du, Y.; Deng, Y.; Ye, P. D. Semiconducting Black Phosphorus: Synthesis, Transport Properties and Electronic Applications. *Chem. Soc. Rev.* **2732**, *44* (44), 2732–2743.

(55) Xue, Y.; Zhang, Q.; Zhang, T.; Fu, L. Black Phosphorus: Properties, Synthesis,

and Applications in Energy Conversion and Storage. *ChemNanoMat* **2017**, *3* (6), 352–361.

(56) Zhang, Y.; Zheng, Y.; Rui, K.; Hng, H. H.; Hippalgaonkar, K.; Xu, J.; Sun, W.; Zhu, J.; Yan, Q.; Huang, W. 2D Black Phosphorus for Energy Storage and Thermoelectric Applications. *Small* **2017**, *13* (28), 1700661.

(57) Pang, J.; Bachmatiuk, A.; Yin, Y.; Trzebicka, B.; Zhao, L.; Fu, L.; Mendes, R. G.; Gemming, T.; Liu, Z.; Rummeli, M. H. Applications of Phosphorene and Black Phosphorus in Energy Conversion and Storage Devices. *Adv. Energy Mater.* **2018**, *8* (8), 1702093.

(58) Mao, S.; Chang, J.; Pu, H.; Lu, G.; He, Q.; Zhang, H.; Chen, J. Two-Dimensional Nanomaterial-Based Field-Effect Transistors for Chemical and Biological Sensing. *Chem. Soc. Rev.* **2017**, *46* (22), 6872–6904.

(59) Choi, J. R.; Yong, K. W.; Choi, J. Y.; Nilghaz, A.; Lin, Y.; Xu, J.; Lu, X. Black Phosphorus and Its Biomedical Applications. *Theranostics* **2018**, *8* (4), 1005.

(60) Ge, X.; Xia, Z.; Guo, S. Recent Advances on Black Phosphorus for Biomedicine and Biosensing. *Adv. Funct. Mater.* **2019**, 1900318.

(61) Luo, M.; Fan, T.; Zhou, Y.; Zhang, H.; Mei, L. 2D Black Phosphorus – Based Biomedical Applications. *Adv. Funct. Mater.* **2019**, 1808306.

(62) Hanlon, D.; Backes, C.; Doherty, E.; Cucinotta, C. S.; Berner, N. C.; Boland, C.; Lee, K.; Harvey, A.; Lynch, P.; Gholamvand, Z.; Zhang, S.; Wang, K.; Moynihan, G.; Pokle, A.; Ramasse, Q. M.; McEvoy, N.; Blau, W. J.; Wang, J.; Abellan, G.; Hauke, F.; Hirsch, A.; Sanvito, S.; O'Regan, D. D.; Duesberg, G. S.; Nicolosi, V.; Coleman, J. N. Liquid Exfoliation of Solvent-Stabilized Few-Layer Black Phosphorus for Applications beyond Electronics. *Nat. Commun.* **2015**, *6*, 8563.

(63) Li, L.; Yu, Y.; Ye, G. J.; Ge, Q.; Ou, X.; Wu, H.; Feng, D.; Chen, X. H.; Zhang, Y. Black Phosphorus Field-Effect Transistors. *Nat. Nanotechnol.* **2014**, *9* (5), 372–377.

(64) Kuriakose, S.; Ahmed, T.; Balendhran, S.; Bansal, V.; Sriram, S.; Bhaskaran, M.; Walia, S. Black Phosphorus : Ambient Degradation and Strategies for Protection. *2D Mater.* **2018**, *5* (3), 032001.

(65) Ma, X.; Lu, W.; Chen, B.; Zhong, D.; Huang, L.; Dong, L.; Jin, C.; Zhang, Z. Performance Change of Few Layer Black Phosphorus Transistors in Ambient. *AIP Adv.* **2015**, *5* (10), 107112.

(66) Yi, Z.; Ma, Y.; Zheng, Y.; Duan, Y.; Li, H. Fundamental Insights into the Performance Deterioration of Phosphorene Due to Oxidation : A GW Method Investigation. *Adv. Mater. Interfaces* **2019**, *6* (1), 1801175.

(67) Wood, J. D.; Wells, S. A.; Jariwala, D.; Chen, K. S.; Cho, E.; Sangwan, V. K.; Liu, X.; Lauhon, L. J.; Marks, T. J.; Hersam, M. C. Effective Passivation of Exfoliated Black Phosphorus Transistors against Ambient Degradation. *Nano Lett.* **2014**, *14* (12), 6964–6970.

(68) Ziletti, A.; Carvalho, A.; Trevisanutto, P. E.; Campbell, D. K.; Coker, D. F.; Neto, A. H. C. Phosphorene Oxides : Bandgap Engineering of Phosphorene by Oxidation. *Phys. Rev. B* **2015**, *91* (8), 085407.

(69) Zhou, Q.; Chen, Q.; Tong, Y.; Wang, J. Light-Induced Ambient Degradation of Few-Layer Black Phosphorus: Mechanism and Protection. *Angew. Chemie Int. Ed.* **2016**, *55* (38), 11437–11441.

(70) Kuntz, K. L.; Wells, R. A.; Hu, J.; Yang, T.; Dong, B.; Guo, H.; Woomer, A. H.; Druffel, D. L.; Alabanza, A.; Tománek, D.; Warren, S. C. Control of Surface and Edge Oxidation on Phosphorene. *ACS Appl. Mater. Interfaces* **2017**, *9* (10),

9126–9135.

(71) Avsar, Ahmet Ivan J. Vera-Marun, Jun You Tan, Kenji Watanabe, T. T.; Antonio H. Castro Neto, and B. O. Air-Stable Transport in Graphene-Contacted, Fully Encapsulated Ultrathin Black Phosphorus-Based Field-Effect Transistors. *ACS Nano* **2015**, *9* (4), 4138–4145.

(72) Wan, B.; Yang, B.; Wang, Y.; Zhang, J.; Zeng, Zhongming, Z. L. and W. W. Enhanced Stability of Black Phosphorus Field-Effect Transistors with SiO2 Passivation. *Nanotechnology* **2015**, *26* (43), 435702.

(73) Ryder, C. R.; Wood, J. D.; Wells, S. A.; Yang, Y.; Jariwala, D.; Marks, T. J.; Schatz, G. C.; Hersam, M. C. Covalent Functionalization and Passivation of Exfoliated Black Phosphorus via Aryl Diazonium Chemistry. *Nat. Chem.* **2016**, *8* (6), 597–602.

(74) Hirsch, A.; Hauke, F. Post- Graphene 2D Chemistry: The Emerging Field of Molybdenum Disulfide and Black Phosphorus Functionalization. *Angew. Chemie Int. Ed.* **2018**, *57* (16), 4338–4354.

(75) Cao, Y.; Tian, X.; Gu, J.; Liu, B.; Zhang, B.; Song, S.; Fan, F.; Chen, Y.; Yaming Cao, Xiangyu Tian, Junwei Gu, Bo Liu, Bin Zhang, Sannian Song, Fei Fan, A.; Chen, Y. Covalent Functionalization of Black Phosphorus with Conjugated Polymer for Information Storage. *Angew. Chemie Int. Ed.* **2018**, *57* (17), 4543–4548.

(76) Passaglia, E.; Cicogna, F.; Costantino, F.; Coiai, S.; Legnaioli, S.; Lorenzetti, G.; Borsacchi, S.; Geppi, M.; Telesio, F.; Heun, S.; Ienco, A.; Serrano-ruiz, M.; Peruzzini, M. Polymer-Based Black Phosphorus (BP) Hybrid Materials by in Situ Radical Polymerization: An Effective Tool To Exfoliate BP and Stabilize BP Nanoflakes. *Chem. Mater.* **2018**, *30* (6), 2036–2048.

(77) Castellanos-Gomez, A.; Vicarelli, L.; Prada, E.; Island, J. O.; Narasimha-Acharya, K. L.; Blanter, S. I.; Groenendijk, D. J.; Buscema, M.; Steele, G. a.; Alvarez, J. V.; Zandbergen, H. W.; Palacios, J. J.; van der Zant, H. S. J. Isolation and Characterization of Few-Layer Black Phosphorus. *2D Mater.* **2014**, *1* (2), 025001.

(78) Keyes, R. The Electrical Properties of Black Phosphorus. **1953**, *92* (3), 580.

(79) Castellanos-Gomez, A. Black Phosphorus: Narrow Gap, Wide Applications. *J. Phys. Chem. Lett.* **2015**, *6* (21), 4280–4291.

(80) Coleman, J. N.; Lotya, M.; O'Neill, A.; Bergin, S. D.; King, P. J.; Khan, U.; Young, K.; Gaucher, A.; De, S.; Smith, R. J.; Shvets, I. V.; Arora, S. K.; Stanton, G.; Kim, H.-Y.; Lee, K.; Kim, G. T.; Duesberg, G. S.; Hallam, T.; Boland, J. J.; Wang, J. J.; Donegan, J. F.; Grunlan, J. C.; Moriarty, G.; Shmeliov, A.; Nicholls, R. J.; Perkins, J. M.; Grieveson, E. M.; Theuwissen, K.; McComb, D. W.; Nellist, P. D.; Nicolosi, V. Two-Dimensional Nanosheets Produced by Liquid Exfoliation of Layered Materials. *Science (80-.).* **2011**, *331* (6017), 568–571.

(81) Brent, J. R.; Savjani, N.; Lewis, E. A.; Haigh, S. J.; Lewis, D. J.; O'Brien, P. Production of Few-Layer Phosphorene by Liquid Exfoliation of Black Phosphorus. *Chem. Commun.* **2014**, *50* (87), 13338–13341.

(82) Kang, J.; Wood, J. D.; Wells, S. A.; Lee, J.-H. H.; Liu, X.; Chen, K.-S. S.; Hersam, M. C. Solvent Exfoliation of Electronic-Grade, Two-Dimensional Black Phosphorus. *ACS Nano* **2015**, *9* (4), 3596–3604.

(83) Shen, J.; He, Y.; Wu, J.; Gao, C.; Keyshar, K.; Zhang, X. Liquid Phase Exfoliation of Two-Dimensional Materials by Directly Probing and Matching Surface Tension Components. *Nano Lett.* **2015**, *15* (8), 5449–5454.

(84) Sresht, V.; Pádua, A. A. H.; Blankschtein, D. Liquid-Phase Exfoliation of Phosphorene: Design Rules from Molecular Dynamics Simulations. *ACS Nano* **2015**, *9* (8), 8255–8268.

(85) Backes, C.; Szydlowska, B. M.; Harvey, A.; Yuan, S.; Vega-Mayoral, V.; Davies, B. R.; Zhao, P. L.; Hanlon, D.; Santos, E. J. G.; Katsnelson, M. I.; Blau, W. J.; Gadermaier, C.; Coleman, J. N. Production of Highly Monolayer Enriched Dispersions of Liquid-Exfoliated Nanosheets by Liquid Cascade Centrifugation. *ACS Nano* **2016**, *10* (1), 1589–1601.

(86) Yasaei, P.; Kumar, B.; Foroozan, T.; Wang, C.; Asadi, M.; Tuschel, D.; Indacochea, J. E.; Klie, R. F.; Salehi-Khojin, A. High-Quality Black Phosphorus Atomic Layers by Liquid-Phase Exfoliation. *Adv. Mater.* **2015**, *27* (11), 1887–1892.

(87) Ng, A.; Sutto, T. E.; Matis, B. R.; Deng, Y.; Ye, P. D.; Stroud, R. M.; Brintlinger, T. H.; Bassim, N. D. Chemically Exfoliating Large Sheets of Phosphorene via Choline Chloride Urea Viscosity-Tuning. *Nanotechnology* **2017**, *28* (15), 155601.

(88) Island, J. O.; Steele, G. A.; Zant, H. S. J. van der; Castellanos-Gomez, A. Environmental Instability of Few-Layer Black Phosphorus. *2D Mater.* **2015**, *2* (1), 011002.

(89) Ziletti, A.; Carvalho, A.; Campbell, D. K.; Coker, D. F.; Castro Neto, A. H. Oxygen Defects in Phosphorene. *Phys. Rev. Lett.* **2015**, *114* (4), 26–29.

(90) Wang, G.; Slough, W. J.; Pandey, R.; Karna, S. P. Degradation of Phosphorene in Air: Understanding at Atomic Level. *2D Mater.* **2016**, *3* (2), 025011.

(91) Huang, Y.; Qiao, J.; He, K.; Bliznakov, S.; Sutter, E.; Chen, X.; Luo, D.; Meng, F.; Su, D.; Decker, J.; Ji, W.; Ruoff, R. S.; Sutter, P. Interaction of Black

Phosphorus with Oxygen and Water. *Chem. Mater.* **2016**, *28* (22), 8330–8339.

(92) Plutnar, J.; Sofer, Z.; Pumera, M. Products of Degradation of Black Phosphorus. *ACS Nano* **2018**, *12* (8), 8390–8396.

(93) Wang, G.; Slough, W. J.; Pandey, R.; Karna, S. P. Degradation of Phosphorene in Air: Understanding at Atomic Level. *2D Mater.* **2016**, *3* (2), 025011.

(94) Wang, H.; Yang, X.; Shao, W.; Chen, S.; Xie, J.; Zhang, X.; Wang, J.; Xie, Y. Ultrathin Black Phosphorus Nanosheets for Efficient Singlet Oxygen Generation. *J. Am. Chem. Soc.* **2015**, *137* (35), 11376–11382.

(95) Kang, J.; Wells, S. A.; Wood, J. D.; Lee, J.-H.; Liu, X.; Ryder, C. R.; Zhu, J.; Guest, J. R.; Husko, C. A.; Hersam, M. C. Stable Aqueous Dispersions of Optically and Electronically Active Phosphorene. *Proceeding Natl. Acad. Sci.* **2016**, *113* (42), 11688–11693.

(96) Serrano-ruiz, M.; Caporali, M.; Ienco, A.; Piazza, V.; Heun, S.; Peruzzini, M. The Role of Water in the Preparation and Stabilization of High-Quality Phosphorene Flakes. *Adv. Mater. Interfaces* **2016**, *3* (3), 1500441.

(97) Hu, Z.; Li, Q.; Lei, B.; Zhou, Q.; Xiang, D.; Lyu, Z.; Hu, F.; Wang, J.; Ren, Y.; Guo, R.; Goki, E.; Wang, L.; Han, C.; Wang, J.; Chen, W. Water-Catalyzed Oxidation of Few-Layer Black Phosphorous in a Dark Environment. *Angew. Chemie - Int. Ed.* **2017**, *129* (31), 9259–9263.

(98) Zhang, T.; Wan, Y.; Xie, H.; Mu, Y.; Du, P.; Wang, D.; Wu, X.; Ji, H.; Wan, L. Degradation Chemistry and Stabilization of Exfoliated Few-Layer Black Phosphorus in Water. *J. Am. Chem. Soc.* **2018**, *140* (24), 7561–7567.

(99) Yang, T.; Dong, B.; Wang, J.; Zhang, Z.; Guan, J.; Kuntz, K.; Warren, S. C.; Tománek, D. Interpreting Core-Level Spectra of Oxidizing Phosphorene: Theory and Experiment. *Phys. Rev. B - Condens. Matter Mater. Phys.* **2015**, *92*

(12), 125412.

(100) Wu, S.; He, F.; Xie, G.; Bian, Z.; Luo, J.; Wen, S. Black Phosphorus: Degradation Favors Lubrication. *Nano Lett.* **2018**, *18* (9), 5618–5627.

(101) Eslamibidgoli, M. J.; Eikerling, M. H. Mechanical and Chemical Stability of Monolayer Black Phosphorous Studied by Density Functional Theory Simulations. *J. Phys. Chem. C* **2018**, *122* (39), 22366–22373.

(102) Van Druenen, M.; Davitt, F.; Collins, T.; Glynn, C.; O'Dwyer, C.; Holmes, J. D.; Collins, G. Evaluating the Surface Chemistry of Black Phosphorus during Ambient Degradation′. *Langmuir* **2019**, *35* (6), 2172–2178.

(103) Luo, W.; Zemlyanov, D. Y.; Milligan, C. A.; Du, Y.; Yang, L.; Wu, Y.; Ye, P. D. Surface Chemistry of Black Phosphorus under a Controlled Oxidative Environment. *Nanotechnology* **2016**, *27* (43), 434002.

(104) Zhang, S.; Zhang, X.; Lei, L.; Yu, X.; Chen, J.; Ma, C.; Wu, F.; Zhao, Q.; Xing, B. PH-Dependent Degradation of Layered Black Phosphorus : Essential Role of Hydroxide Ions. *Angew. Chemie* **2019**, *131* (2), 477–481.

(105) Edmonds, M. T.; Tadich, A.; Carvalho, A.; Ziletti, A.; O'Donnell, K. M.; Koenig, S. P.; Coker, D. F.; Ozyilmaz, B.; Neto, A. H. C.; Fuhrer, M. S. Creating a Stable Oxide at the Surface of Black Phosphorus. *ACS Appl. Mater. Interfaces* **2015**, *7* (27), 14557–14562.

(106) Woomer, A. H.; Farnsworth, T. W.; Hu, J.; Wells, R. A.; Donley, C. L.; Warren, S. C. Phosphorene: Synthesis, Scale-Up, and Quantitative Optical Spectroscopy. *ACS Nano* **2015**, *9* (9), 8869–8884.

(107) Favron, A.; Gaufrès, E.; Fossard, F.; Phaneuf-L'Heureux, A.-L.; Tang, N. Y.-W.; Lévesque, P. L.; Loiseau, A.; Leonelli, R.; Francoeur, S.; Martel, R. Photooxidation and Quantum Confinement Effects in Exfoliated Black

Phosphorus. *Nat. Mater.* **2015**, *14* (8), 826–832.

(108) Abellán, G.; Wild, S.; Lloret, V.; Scheuschner, N.; Gillen, R.; Mundloch, U.; Maultzsch, J.; Varela, M.; Hauke, F.; Hirsch, A. Fundamental Insights into the Degradation and Stabilization of Thin Layer Black Phosphorus. *J. Am. Chem. Soc.* **2017**, *139* (30), 10432–10440.

(109) Wang, G.; Pandey, R.; Karna, S. P. Phosphorene Oxide: Stability and Electronic Properties of a Novel Two-Dimensional Material. *Nanoscale* **2015**, *7* (2), 524–531.

(110) Alsaffar, F.; Alodan, S.; Alrasheed, A.; Alhussain, A.; Alrubaiq, N.; Abbas, A.; Amer, M. R. Raman Sensitive Degradation and Etching Dynamics of Exfoliated Black Phosphorus. *Sci. Rep.* **2017**, *7*, 44540.

(111) Zhu, X.; Zhang, T.; Jiang, D.; Duan, H.; Sun, Z.; Zhang, M.; Jin, H.; Guan, R.; Liu, Y.; Chen, M.; Ji, H.; Du, P.; Yan, W.; Wei, S.; Lu, Y.; Yang, S. Stabilizing Black Phosphorus Nanosheets via Edge-Selective Bonding of Sacrificial C60 Molecules. *Nat. Commun.* **2018**, *9* (1), 4177.

(112) Zhang, S.; Yang, J.; Xu, R.; Wang, F.; Li, W.; Ghufran, M.; Zhang, Y. W.; Yu, Z.; Zhang, G.; Qin, Q.; Lu, Y. Extraordinary Photoluminescence and Strong Temperature/Angle-Dependent Raman Responses in Few-Layer Phosphorene. *ACS Nano* **2014**, *8* (9), 9590–9596.

(113) Ling, X.; Huang, S.; Hasdeo, E. H.; Liang, L.; Parkin, W. M.; Tatsumi, Y.; Nugraha, A. R. T.; Puretzky, A. A.; Das, P. M.; Sumpter, B. G.; Geohegan, D. B.; Kong, J.; Saito, R.; Drndic, M.; Meunier, V.; Dresselhaus, M. S. Anisotropic Electron-Photon and Electron-Phonon Interactions in Black Phosphorus. *Nano Lett.* **2016**, *16* (4), 2260–2267.

(114) Gamage, S.; Li, Z.; Yakovlev, V. S.; Lewis, C.; Wang, H.; Cronin, S. B.; Abate,

Y. Nanoscopy of Black Phosphorus Degradation. *Adv. Mater. Interfaces* **2016**, *3* (12), 1600121.

(115) Illarionov, Y. Y.; Waltl, M.; Rzepa, G.; Knobloch, T.; Kim, J. Highly-Stable Black Phosphorus Fi Eld-Effect Transistors with Low Density of Oxide Traps. *npj 2D Mater. Appl.* **2017**, *1* (1), 23.

(116) Kim, J.; Liu, Y.; Zhu, W.; Kim, S.; Wu, D.; Tao, L.; Dodabalapur, A.; Lai, K.; Akinwande, D. Toward Air-Stable Multilayer Phosphorene Thin-Films and Transistors. *Sci. Rep.* **2015**, *5*, 8989.

(117) Luo, X.; Rahbarihagh, Y.; Hwang, J. C. M.; Liu, H.; Du, Y.; Ye, P. D. Temporal and Thermal Stability of Al2O3-Passivated Phosphorene MOSFETs. *IEEE* **2014**, *35* (12), 1314–1316.

(118) Zhu, H.; Mcdonnell, S.; Qin, X.; Azcatl, A.; Cheng, L.; Kim, J.; Ye, P. D.; Wallace, R. M. Al 2 O 3 on Black Phosphorus by Atomic Layer Deposition : An in Situ Interface Study. *ACS Appl. Mater. Interfaces* **2015**, *7* (23), 13038–13043.

(119) Sinha, S.; Takabayashi, Y.; Shinohara, H.; Kitaura, R. Simple Fabrication of Air-Stable Black Phosphorus Heterostructures with Large-Area HBN Sheets Grown by Chemical Vapor Deposition Method Simple Fabrication of Air-Stable Black Phosphorus Heterostructures with Large-Area HBN Sheets Grown by Chemical Vapor D. *2D Mater.* **2016**, *3* (3), 035010.

(120) Son, Y.; Kozawa, D.; Liu, A. T.; Koman, V. B.; Wang, Q. H.; Strano, M. S. A Study of Bilayer Phosphorene Stability under MoS_2 -Passivation. *2D Mater.* **2017**, *4* (2), 025091.

(121) Kim, J.; Baek, S. K.; Kim, K. S.; Chang, Y. J.; Choi, E. J. Long-Term Stability Study of Graphene-Passivated Black Phosphorus under Air Exposure. *Curr.*

Appl. Phys. **2016**, *16* (2), 165–169.

(122) Haiguo Hu, Hong Gao, Lili Gao, Feng Li, Na Xu, Xuefeng Long, Yi Ping Hu, J. J. and J. M. Covalent Functionalization of Black Phosphorus Nanoflakes by Carbon Free Radicals for Durable Air and Water Stability. *Nanoscale* **2018**, *10* (13), 5834–5839.

(123) Zhao, Y.; Wang, H.; Huang, H.; Xiao, Q.; Xu, Y.; Guo, Z.; Xie, H.; Shao, J.; Sun, Z.; Han, W.; Yu, X. F.; Li, P.; Chu, P. K. Surface Coordination of Black Phosphorus for Robust Air and Water Stability. *Angew. Chemie Int. Ed.* **2016**, *55* (16), 5003–5007.

(124) Yajuan Liu, Pengfei Gao, Taiming Zhang, Xianjun Zhu, Mengmeng Zhang, Muqing Chen, P.; Du, Guan-Wu Wang, Hengxing Ji, Jinlong Yang, and S. Y. Azide Passivation of Black Phosphorus Nanosheets: Covalent Functionalization Affords Ambient Stability Enhancement. *Angew. Chemie Int. Ed.* **2019**, *58* (5), 1479–1483.

(125) Tang, X.; Liang, W.; Zhao, J.; Li, Z.; Qiu, M.; Fan, T. Fluorinated Phosphorene: Electrochemical Synthesis, Atomistic Fluorination, and Enhanced Stability. *Small* **2017**, *13* (47), 1702739.

(126) Artel, V.; Guo, Q.; Cohen, H.; Gasper, R.; Ramasubramaniam, A.; Xia, F. Protective Molecular Passivation of Black Phosphorus. *npj 2D Mater. Appl.* **2017**, *1* (1), 6.

(127) Van Druenen, M.; Davitt, F.; Collins, T.; Glynn, C.; O'Dwyer, C.; Holmes, J. D.; Collins, G. Covalent Functionalization of Few-Layer Black Phosphorus Using Iodonium Salts and Comparison to Diazonium Modified Black Phosphorus. *Chem. Mater.* **2018**, *30* (14), 4667–4674.

(128) Abellán, G.; Lloret, V.; Mundloch, U.; Marcia, M.; Neiss, C.; Görling, A.;

Varela, M.; Hauke, F.; Hirsch, A. Noncovalent Functionalization of Black Phosphorus. *Angew. Chemie Int. Ed.* **2016**, *55* (47), 14557–14562.

(129) Hu, C.; Xiao, Q.; Ren, Y.; Zhao, M.; Dun, G.; Wu, H.; Li, X.; Yang, Q.; Sun, B.; Peng, Y.; Yan, F.; Wang, Q.; Hao-li, Z. Polymer Ionic Liquid Stabilized Black Phosphorus for Environmental Robust Flexible Optoelectronics. *Adv. Funct. Mater.* **2018**, *28* (51), 1805311.

(130) Novoselov, K.S., Mishchenko, A., Carvalho, A. and Neto, A. C. 2D Materials and van Der Waals Heterostructures. *Science (80-.).* **2016**, *353* (6298), aac9439.

(131) Geim, A. K.; Grigorieva, I. V. Van Der Waals Heterostructures. *Nature* **2013**, *499* (7459), 419–425.

(132) Li, Q.; Zhou, Q.; Niu, X.; Zhao, Y.; Chen, Q.; Wang, J. Covalent Functionalization of Black Phosphorus from First-Principles. *J. Phys. Chem. Lett.* **2016**, *7* (22), 4540–4546.

(133) Sofer, Z.; Luxa, J.; Bouša, D.; Sedmidubský, D.; Lazar, P.; Hartman, T.; Hardtdegen, H.; Pumera, M. The Covalent Functionalization of Layered Black Phosphorus by Nucleophilic Reagents. *Angew. Chemie Int. Ed.* **2017**, *56* (33), 9891–9896.

(134) Georgakilas, V.; Otyepka, M.; Bourlinos, A. B.; Chandra, V.; Kim, N.; Kemp, K. C.; Hobza, P.; Zboril, R.; Kim, K. S. Functionalization of Graphene: Covalent and Non-Covalent Approaches, Derivatives and Applications. *Chem. Rev.* **2012**, *112* (11), 6156–6214.

(135) Nahas, S.; Ghosh, B.; Bhowmick, S.; Agarwal, A. First-Principles Cluster Expansion Study of Functionalization of Black Phosphorene via Fluorination and Oxidation. *Phys. Rev. B* **2016**, *93* (16), 165413.

(136) Jan Plutnar, Jirí Šturala, Vlastimil Mazánek, Zdenek Sofer, and M. P. Fluorination of Black Phosphorus — Will Black Phosphorus Burn Down in the Elemental Fluorine ? *Adv. Funct. Mater.* **2018**, *28* (35), 1801438.

(137) Kwak, D. H.; Ra, H. S.; Yang, J.; Jeong, M. H.; Lee, A. Y.; Lee, W.; Hwang, J. Y.; Lee, J. H.; Lee, J. S. Recovery Mechanism of Degraded Black Phosphorus Field-Effect Transistors by 1,2-Ethanedithiol Chemistry and Extended Device Stability. *Small* **2018**, *14* (6), 1703194.

(138) Gusmão, R.; Sofer, Z.; Pumera, M. Functional Protection of Exfoliated Black Phosphorus by Noncovalent Modification with Anthraquinone. *ACS Nano* **2018**, *12* (6), 5666–5673.

(139) Del Rio Castillo, A. E.; Pellegrini, V.; Sun, H.; Buha, J.; Dinh, D. A.; Lago, E.; Ansaldo, A.; Capasso, A.; Manna, L.; Bonaccorso, F. Exfoliation of Few-Layer Black Phosphorus in Low Boiling Point Solvents and Its Application in Li-Ion Batteries. *Chem. Mater.* **2018**, *30* (2), 506–516.

(140) Sudhir Ravula, Sheila N. Baker, G. K. and G. A. B. Ionic Liquid-Assisted Exfoliation and Dispersion: Stripping Graphene and Its Two-Dimensional Layered Inorganic Counterparts of Their Inhibitions. *Nanoscale* **2015**, *7* (10), 4338–4353.

(141) Lee, M.; Roy, A. K.; Jo, S.; Choi, Y.; Chae, A.; Kim, B.; Park, S. Y.; In, I. Exfoliation of Black Phosphorus in Ionic Liquids. *Nanotechnology* **2017**, *28* (12), 125603.

(142) Chaban, V. V.; Fileti, E. E.; Prezhdo, O. V. Imidazolium Ionic Liquid Mediates Black Phosphorus Exfoliation While Preventing Phosphorene Decomposition. *ACS Nano* **2017**, *11* (6), 6459–6466.

(143) Zhao, W.; Xue, Z.; Wang, J.; Jiang, J.; Zhao, X.; Mu, T. Large-Scale, Highly

Efficient, and Green Liquid-Exfoliation of Black Phosphorus in Ionic Liquids. *ACS Appl. Mater. Interfaces* **2015**, *7* (50), 27608–27612.

(144) Kumar, V.; Brent, J. R.; Shorie, M.; Kaur, H.; Chadha, G.; Thomas, A. G.; Lewis, E. A.; Rooney, A. P.; Nguyen, L.; Zhong, X. L.; Burke, M. G.; Haigh, S. J.; Walton, A.; McNaughter, P. D.; Tedstone, A. A.; Savjani, N.; Muryn, C. A.; O'Brien, P.; Ganguli, A. K.; Lewis, D. J.; Sabherwal, P. Nanostructured Aptamer-Functionalized Black Phosphorus Sensing Platform for Label-Free Detection of Myoglobin, a Cardiovascular Disease Biomarker. *ACS Appl. Mater. Interfaces* **2016**, *8* (35), 22860–22868.

(145) Sun, Z.; Xie, H.; Tang, S.; Yu, X.; Guo, Z.; Shao, J.; Zhang, H.; Huang, H.; Wang, H.; Chu, P. K. Ultrasmall Black Phosphorus Quantum Dots : Synthesis and Use as Photothermal Agents. *Angew. Chemie Int. Ed.* **2015**, *127* (39), 11688–11692.

(146) Sajedi-moghaddam, A.; Mayorga-martinez, C. C.; Sofer, Z.; Bousa, D.; Saievar-iranizad, E.; Pumera, M. Black Phosphorus Nanoflakes/Polyaniline Hybrid Material for High- Performance Pseudocapacitors. *J. Phys. Chem. C* **2017**, *121* (37), 20532–20538.

(147) Luo, S.; Zhao, J.; Zou, J.; He, Z.; Xu, C.; Liu, F.; Huang, Y.; Dong, L.; Wang, L.; Zhang, H. Self-Standing Polypyrrole/Black Phosphorus Laminated Film: Promising Electrode for Flexible Supercapacitor with Enhanced Capacitance and Cycling Stability. *ACS Appl. Mater. Interfaces* **2018**, *10* (4), 3538–3548.

(148) Shao, J.; Xie, H.; Huang, H.; Li, Z.; Sun, Z.; Xu, Y.; Xiao, Q.; Yu, X.; Zhao, Y.; Zhang, H.; Wang, H.; Chu, P. K. Biodegradable Black Phosphorus-Based Nanospheres for in Vivo Photothermal Cancer Therapy. *Nat. Commun.* **2016**, *7*, 12967.

(149) Zhang, Y.; Dong, N.; Tao, H.; Yan, C.; Huang, J.; Liu, T.; Robertson, A. W.; Texter, J.; Wang, J.; Sun, Z. Exfoliation of Stable 2D Black Phosphorus for Device Fabrication. *Chem. Mater.* **2017**, *29* (15), 6445–6456.

(150) Wang, X.; He, J.; Zhou, B.; Zhang, Y.; Wu, J.; Hu, R.; Liu, L. Bandgap-Tunable Preparation of Smooth and Large Two-Dimensional Antimonene. *Angew. Chemie* **2018**, *130* (28), 8804–8809.

(151) Zhang, S.; Zhou, W.; Ma, Y.; Ji, J.; Cai, B.; Yang, S. A.; Zhu, Z.; Chen, Z.; Zeng, H. Antimonene Oxides: Emerging Tunable Direct Bandgap Semiconductor and Novel Topological Insulator. *Nano Lett.* **2017**, *17* (6), 3434–3440.

(152) Zhang, S.; Yan, Z.; Li, Y.; Chen, Z.; Zeng, H. Atomically Thin Arsenene and Antimonene: Semimetal-Semiconductor and Indirect-Direct Band-Gap Transitions. *Angew. Chemie - Int. Ed.* **2015**, *54* (10), 3112–3115.

(153) Wang, G.; Pandey, R.; Karna, S. P. Atomically Thin Group V Elemental Films: Theoretical Investigations of Antimonene Allotropes. *ACS Appl. Mater. Interfaces* **2015**, *7* (21), 11490-11496.

(154) Sun, X.; Song, Z.; Liu, S.; Wang, Y.; Li, Y.; Wang, W.; Lu, J. Sub‐5 Nm Monolayer Arsenene and Antimonene Transistors. *ACS Appl. Mater. Interfaces* **2018**, *10* (26), 22363–22371.

(155) Tian, W.; Zhang, S.; Huo, C.; Zhu, D.; Li, Q.; Wang, L.; Ren, X.; Xie, L.; Guo, S.; Chu, P. K.; Zeng, H.; Huo, K. Few-Layer Antimonene: Anisotropic Expansion and Reversible Crystalline-Phase Evolution Enable Large-Capacity and Long-Life Na-Ion Batteries. *ACS Nano* **2018**, *12* (2), 1887–1893.

(156) Gusmão, R.; Sofer, Z.; Bouša, D.; Pumera, M. Pnictogen (As, Sb, Bi) Nanosheets for Electrochemical Applications Are Produced by Shear

Exfoliation Using Kitchen Blenders. *Angew. Chemie* **2017**, *129* (46), 14609–14614.

(157) Tao, W.; Ji, X.; Xu, X.; Islam, M. A.; Li, Z.; Chen, S.; Saw, P. E.; Zhang, H.; Bharwani, Z.; Guo, Z.; Shi, J.; Farokhzad, O. C. Cancer Therapy Antimonene Quantum Dots : Synthesis and Application as Near- Infrared Photothermal Agents for Effective Cancer Therapy Angewandte. *Angew. Chemie Int. Ed.* **2017**, *56* (39), 11896–11900.

(158) Tao, W.; Ji, X.; Zhu, X.; Li, L.; Wang, J.; Zhang, Y.; Saw, P. E.; Li, W.; Kong, N.; Islam, M. A.; Gan, T.; Zeng, X.; Zhang, H.; Mahmoudi, M.; Tearney, G. J.; Farokhzad, O. C. Two-Dimensional Antimonene-Based Photonic Nanomedicine for Cancer Theranostics. *Adv. Mater.* **2018**, *30* (38), 1802061.

(159) Lu, G.; Lv, C.; Bao, W.; Li, F.; Zhang, F.; Zhang, L.; Wang, S.; Gao, X.; Zhao, D.; Wei, W.; Xie, H. Antimonene with Two-Orders-of-Magnitude Improved Stability for High-Performance Cancer Theranostics. *Chem. Sci.* **2019**, *10* (18), 4847–4853.

(160) Zhang, F., Wang, M., Wang, Z., Han, K., Liu, X., & Xu, X. Excellent Nonlinear Absorption Properties of B-Antimonene Nanosheets. *J. Mater. Chem. C* **2018**, *6* (11), 2848–2853.

(161) Pizzi, G.; Gibertini, M.; Dib, E.; Marzari, N.; Iannaccone, G.; Fiori, G. Performance of Arsenene and Antimonene Double-Gate MOSFETs from First Principles. *Nat. Commun.* **2016**, *7*, 12585.

(162) Ji, J.; Song, X.; Liu, J.; Yan, Z.; Huo, C.; Zhang, S.; Su, M.; Liao, L.; Wang, W.; Ni, Z.; Hao, Y.; Zeng, H. Two-Dimensional Antimonene Single Crystals Grown by van Der Waals Epitaxy. *Nat. Commun.* **2016**, *7*, 13352.

(163) Sun, X., Lu, Z., Xiang, Y., Wang, Y., Shi, J., Wang, G.C., Washington, M.A.

and Lu, T.M., . Van Der Waals Epitaxy of Antimony Islands, Sheets, and Thin Films on Single-Crystalline Graphene. *ACS Nano* **2018**, *12* (6), 6100–6108.

(164) Wu, X.; Shao, Y.; Liu, H.; Feng, Z.; Wang, Y.; Sun, J.; Liu, C.; Wang, J.; Liu, Z.; Zhu, S.; Wang, Y.; Du, S.; Shi, Y.; Ibrahim, K.; Gao, H. Epitaxial Growth and Air-Stability of Monolayer Antimonene on PdTe2. *Adv. Mater.* **2017**, *29* (11), 1605407.

(165) Chen, Hsuan-An, Hsu Sun, Chong-Rong Wu, Yu-Xuan Wang, Po-Hsiang Lee, Chun-Wei Pao, and S.-Y. L. Single-Crystal Antimonene Films Prepared by Molecular Beam Epitaxy: Selective Growth and Contact Resistance Reduction of the 2D Material Heterostructure. *ACS Appl. Mater. Interfaces* **2018**, *10* (17), 15058–15064.

(166) Fortin-Deschênes, M., Waller, O., Mentes, T.O., Locatelli, A., Mukherjee, S., Genuzio, F., Levesque, P.L., Hébert, A., Martel, R. and Moutanabbir, O. Synthesis of Antimonene on Germanium. *Nano Lett.* **2017**, *17* (8), 4970–4975.

(167) Wu, Q.; Song, Y. J. The Environmental Stability of Large-Size and Single-Crystalline Antimony Flakes Grown by Chemical Vapor Deposition on SiO2 Substrates. *Chem. Commun.* **2018**, *54* (69), 9671-9674.

(168) Lucheng Peng, Shuai Ye, Jun Song, and J. Q. Solution-Phase Synthesis of Few-Layer AM Nanosheets via Anisotropic Growth. *Angew. Chemie* **2019**.

(169) Ares, P.; Aguilar-galindo, F.; Rodríguez-san-miguel, D.; Aldave, D. A.; Díaz-tendero, S.; Alcamí, M.; Martín, F.; Gómez-herrero, J. Mechanical Isolation of Highly Stable Antimonene under Ambient Conditions. *Adv. Mater.* **2016**, *28* (30), 6332–6336.

(170) Gibaja, C.; Rodriguez-San-Miguel, D.; Ares, P.; Gómez-Herrero, J.; Varela, M.; Gillen, R.; Maultzsch, J.; Hauke, F.; Hirsch, A.; Abellán, G.; Zamora, F.

Few-Layer Antimonene by Liquid-Phase Exfoliation. *Angew. Chemie - Int. Ed.* **2016**, *55* (46), 14345–14349.

(171) Hernandez, Y.; Nicolosi, V.; Lotya, M.; Blighe, F. M.; Sun, Z.; De, S.; McGovern, I. T.; Holland, B.; Byrne, M.; Gun'Ko, Y. K.; Boland, J. J.; Niraj, P.; Duesberg, G.; Krishnamurthy, S.; Goodhue, R.; Hutchison, J.; Scardaci, V.; Ferrari, A. C.; Coleman, J. N. High-Yield Production of Graphene by Liquid-Phase Exfoliation of Graphite. *Nat. Nanotechnol.* **2008**, *3* (9), 563–568.

(172) Lu, L.; Tang, X.; Cao, R.; Wu, L.; Li, Z.; Jing, G.; Dong, B.; Lu, S.; Li, Y.; Xiang, Y.; Li, J.; Fan, D.; Zhang, H. Broadband Nonlinear Optical Response in Few-Layer Antimonene and Antimonene Quantum Dots : A Promising Optical Kerr Media with Enhanced Stability. *Adv. Opt. Mater.* **2017**, *5* (17), 1700301.

(173) Abellan, G.; Ares, P.; Wild, S.; Nuin, E.; Neiss, C.; Rodriguez-, D.; Miguel, S.; Segovia, P.; Gibaja, C.; Michel, E. G.; Gçrling, A.; Hauke, F.; Julio, G.; Hirsch, A.; Zamora, F. Ø. Noncovalent Functionalization and Charge Transfer in Antimonene Angewandte. *Angew. Chemie* **2017**, *56* (46), 14389–14394.

(174) Kistanov, A. A.; Cai, Y.; Kripalani, D. R.; Zhou, K.; Dmitriev, S. V; Zhang, Y. A First-Principles Study on the Adsorption of Small Molecules on Antimonene : Oxidation Tendency and Stability. *J. Mater. Chem. C* **2018**, *6* (15), 4308–4317.

(175) Xie, M. Q.; Zhang, S. L.; Cai, B.; Zou, Y. S.; Zeng, H. B. N- and p-Type Doping of Antimonene. *RSC Adv.* **2016**, *6* (18), 14620–14625.

(176) Robinson, J. T.; Burgess, J. S.; Junkermeier, C. E.; Badescu, S. C.; Reinecke, T. L.; Perkins, F. K.; Zalalutdniov, M. K.; Baldwin, J. W.; Culbertson, J. C.; Sheehan, P. E.; Snow, E. S. Properties of Fluorinated Graphene Films. *Nano Lett.* **2010**, *10* (8), 3001–3005.

(177) Tang, X.; Hu, L.; Fan, T.; Zhang, L.; Zhu, L.; Li, H.; Liu, H.; Liang, J.; Wang, K.; Li, Z.; Ruan, S.; Zhang, Y.; Fan, D.; Chen, W.; Zeng, Y.; Zhang, H. Robust Above-Room-Temperature Ferromagnetism in Few-Layer Antimonene Triggered by Nonmagnetic Adatoms. *Adv. Funct. Mater.* **2019**, *29*, 1808746.

Chapter 2

Functionalisation of SiO_2 Surfaces for Monolayer Doping with Minimal Carbon Contamination

This chapter has been published in ACS Applied Materials & Interfaces and therefore sections may contain repeating concepts and paragraphs.

Van Druenen, M.; Collins, G.; Glynn, C.; O'Dwyer, C.; Holmes, J. D. Functionalization of SiO_2 Surfaces for Si Monolayer Doping with Minimal Carbon Contamination. *ACS Appl. Mater. Interfaces* 2018, *10* (2), 2191–2201.

2. Functionalisation of SiO_2 Surfaces for Monolayer Doping with Minimal Carbon Contamination

2.1 Abstract

MLD conventionally employs hydrosilylation to attach dopant precursors to the Si surface. However, hydrosilylation reactions are air and moisture sensitive, requiring inert conditions along with drying of solvents and precursors. Oxide functionalisation is more compatible with ambient conditions as it can be carried out without drying precursors or solvents. Similar doping concentrations can be achieved using oxide functionalised surfaces compared to hydrosilylated surfaces (~2×10^{20} atoms/cm^3). Oxide functionalised surfaces display excellent ambient stability and the use of oxide functionalisation allows selection of a large range of inexpensive p- and n-dopant precursors. The oxide layer facilitates attachment of carbon-free precursors due to attachment of precursors through the phosphonic acid head group instead of an alkene group, hence eliminating carbon contamination, an issue arising from using MLD as a doping method. Additionally, the oxide layer impedes carbon diffusion into the substrate by trapping carbon at the SiO_2 side of the SiO_2-Si interface. Oxide functionalised surfaces are characterised in detail using x-ray photoelectron spectroscopy (XPS), attenuated total reflectance Fourier infrared (ATR-FTIR) spectroscopy and contact angle (CA) measurements to assess the formation and binding of monolayers to the SiO_2 surface. Electrochemical capacitance voltage (ECV) profiling, Hall measurements and secondary ion mass spectrometry (SIMS) were used to assess doping and demonstrate carbon diffusion is limited to the capping layer.

2.2 Introduction

As device dimensions are scaled down to keep up with Moore's law, doping of non-planar structures is becoming more challenging. MLD has been employed to overcome the problems associated with current doping techniques such as ion implantation, which suffers from crystal damage and does not allow the application to nanostructures or the formation of shallow junctions.[1] MLD involves the functionalisation of the semiconductor surface followed by an annealing step, which diffuses the dopant into the substrate. The functionalisation of the semiconductor surface allows the application to nanostructures and avoids shadowing effects due to the uniform coverage of device surfaces, whereas 3D architectures can block dopant ions when using ion implantation. Additionally, the functionalisation step allows tailoring of precursors and optimisation of the desired dopant profile.[2–5] Hydrosilylation, where an alkene group reacts with the Si surface, is typically used as a functionalisation method for attaching p- or n-containing dopant precursors.[6–9] Hydrosilylation reactions are air-sensitive requiring purification of solvents while precursors are often not compatible with ambient conditions. While the surface chemistry of Si has been widely studied for MLD applications, the SiO_2 surface has only recently been used for MLD.[4,5,10] The functionalisation of various surfaces using phosphonic acids has been researched for electronic, sensing and solar cell applications.[11–14] The phosphonic acid functionalisation route offers a number of advantages over hydrosilylation chemistry including the formation of robust self-assembled monolayers (SAMs) which display superior ambient stability[15] and elimination of inert reaction conditions.

This chapter focuses on the functionalisation of SiO_2 surfaces with phosphonic acids[16]

as an alternative doping strategy, oxide-MLD, as displayed in **Figure 2.1**.

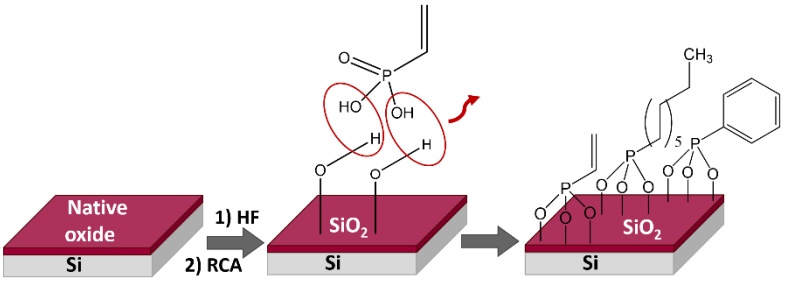

Figure 2.1: Oxide functionalisation involves the removal of the native SiO_2 using a HF dip and re-oxidation of the surface using an RCA clean. Phosphonic acid attachment occurs through a condensation reaction with surface hydroxyl groups.

The surface chemistry of phosphonic acid functionalised surfaces was studied in detail to allow optimisation of the doping profile. While phosphonic acids only physisorb on the SiO_2 surface, chemisorption can take place when heated in a low humidity environment.[17] A temperature of 140 °C is needed to form a covalently bound layer on the SiO_2 surface through a condensation reaction with surface hydroxyl groups.[17] Oxide functionalised surfaces do not display re-oxidation during the reaction and the functionalised substrates display excellent ambient stability. A lower reaction temperature of 140 °C compared to 160 °C required for hydrosilylation is less harsh on the Si surface and the presence of an oxide layer protects the Si interface.[17] Physisorbed species present after annealing can be removed using a combination of rinses and sonication. A controlled monolayer coverage without the presence of physisorbed species is crucial for obtaining reproducible doping profiles. Doping of substrates using a larger doping source by including physisorbed species resulted in a larger junction depth rather than a significant increase in peak carrier concentration, in agreement with literature reports.[3] The use of molecules with varying molecular footprints to tailor peak carrier concentration was successfully demonstrated, while

oxide-MLD also shows potential to tune junction depth through variation of the oxide spacer layer thickness. The oxide layer thickness can be increased chemically or electrochemically.[18–20] A thicker oxide layer slows diffusion of phosphorus dopant atoms during the RTA creating a shallower junction depth.

Carbon contamination has been reported to lead to the formation of defects which results in dopant deactivation.[21] MLD of oxide functionalised surfaces using self-capping silanol dopant precursors that can act as a capping layer have been reported to minimise carbon contamination.[4,10] The requirement of capping layers during oxide-MLD has been debated, as theoretical studies suggest the release of the carbon ligand at a lower temperature prior to phosphorus diffusion.[22] In order to further minimise carbon contamination, the oxide layer facilitates attachment of carbon-free precursors, in comparison to hydrosilylation where alkene functionality is necessary for reaction with the Si surface. Characterisation of the binding mechanism suggests phosphonic acids preferentially form a tridentate configuration on the Si surface and therefore reaction of the P=O group occurs. Binding through the P=O group also results in the successful attachment of phosphorus pentoxide, a major advantage due to the carbon-free nature of the molecule which can reduce carbon contamination in doped substrates. Additionally, literature reports suggest carbon segregates at the SiO_2-Si interface. SIMS studies have shown a carbon peak on the SiO_2 side of the interface in samples subjected to high dose carbon ion implants.[23] The effect of oxide-MLD on carbon levels has been studied in detail using SIMS analysis, with negligible changes in carbon levels in doped Si substrates obtained after the oxide-MLD process compared to a reference Si substrate. Therefore, oxide-MLD ensures carbon-free

doped substrates either through the use of carbon-free precursors or by trapping of carbon in the oxide layer, as displayed in **Figure 2.2**.

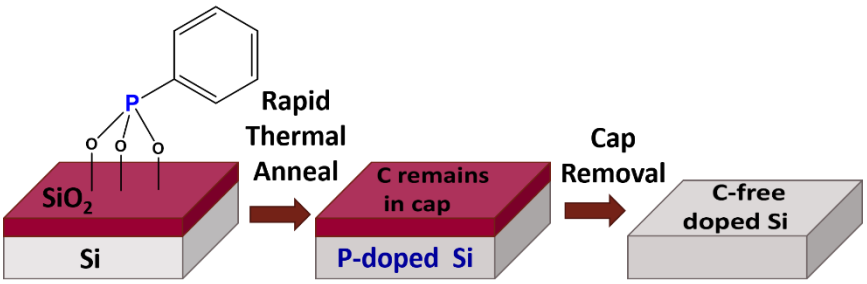

Figure 2.2: Carbon present in the dopant precursor is trapped in the SiO_2 layer during the RTA. The removal of the capping layer ensures the formation of a carbon free doped Si substrate.

2.3 Experimental

Sulfuric acid (95-97 %), hydrogen peroxide (30 % w/w), nitric acid (64-66 %), ammonium hydroxide (30-33 %) and all other chemicals were purchased from Sigma-Aldrich. Glassware was cleaned using a Piranha solution followed by rinsing in water and stored overnight in a 140 °C oven.

2.3.1 Hydrosilylation

Functionalisation of oxide-free surfaces was carried out using conventional hydrosilylation of H-terminated Si surfaces. Mesitylene (98 %) was dried overnight using CaH_2 (95 %) and distilled under reduced pressure onto molecular sieves (4 Å). Vinyl phosphonic acid (97 %) (VPA) was dried using P_2O_5 (99 %) and subsequently filtered through alumina onto molecular sieves. Diethylvinyl phosphonate (97 %) (DVP) was dried using CaH_2 and distilled under reduced pressure or dried using the same procedure as VPA. Allyldiphenylphosphine oxide (ADPO) was dried under vacuum on a Schlenk line for 24 h. Allyldiphenylphosphine (ADP) was dried using

CaH_2 or dried using molecular sieves and distilled under reduced pressure. Diethyl allylphosphonate (DAP) was dried using P_2O_5. Substrates of 1 × 1 cm were cut from a (100) Si wafer and degreased by 2 min of sonication in IPA (99.9 %). A Piranha (3:1 H_2SO_4:H_2O_2) solution was used to clean the samples followed by copious rinsing with water. Oxide removal and H-termination was achieved using a 10 % HF (≥40 %) dip for 2 min. The samples were dried under a stream of nitrogen and placed in a 100 ml round-bottomed flask, previously cooled under an inert environment, under vacuum for 30 min (refilling with argon every 10 min). Ten freeze-pump thaw cycles were used to degas the precursor solution prior to use (0.13 mM for VPA, 0.5 mM for diethyl DVP). Optimal precursor concentrations were determined using XPS analysis. The mixture was added to the reaction flask using cannula transfer and refluxed under argon at 160 °C for 2 h. After the reaction cooled to room temperature the samples were sonicated in anhydrous toluene (≥99.8 %) for 10 min with subsequent rinsing in anhydrous ethanol (≥99.5 %), anhydrous dichloromethane (≥99.8) (DCM) and toluene to remove physi-adsorbed material. Samples were stored under nitrogen to prevent oxidation before analysis took place.

2.3.2 Oxide Functionalisation

Ultra-thin SiO_2 layers were prepared using conventional RCA cleaning procedures. Si substrates were degreased by sonicating in IPA for 2 min and cleaned using a Piranha solution. H-termination was achieved using a 5 % HF dip for 2 min followed by an RCA clean (NH_4OH:H_2O_2:H_2O in a 1:1:5 ratio) to re-oxidise the surface for oxide functionalisation. Samples were placed in a solution of the phosphonic acid dissolved in 10 ml of anhydrous THF (≥99.9 %) for 24 hr or 1 week to form a physisorbed self-assembled monolayer (SAM). The optimal phosphonic acid concentrations were

determined by evaluating the WCA and XPS analysis of the functionalised surfaces (34 mM for VPA, 63 mM for phenylphosphonic acid (98 %) (PPA), 8 mM for n-dodecylphosphosphonic acid (≥89.5 %) (DPA), 12 mM for 1H,1H,2H,2H–perfluorooctanephosphonic acid (95 %) (FOPA), 12 mM for octadecylphosphonic acid (97 %) (OPA), 80 mM for boric acid (≥99.5 %) (BA), a 25 mM phenylboronic acid (≥97 %) (PBA)). A carbon-free precursor, phosphorus pentoxide (P_2O_5), was also used with two different concentrations: 7 mM and 14 mM. The substrates were removed from solution and dried under a stream of nitrogen before annealing at 140 °C for 1 or 24 hr in an ambient environment (oven) or moisture-free environment (vacuum oven or on Schlenk line under argon). Following annealing, physisorbed material was removed using one of two rinses: sonication in THF and then ethanol for 10 min each or sonication in a base rinse (10:3:1 water: THF: trimethylamine (99 %)) and ethanol for 10 min each. Samples were stored under nitrogen before analysis was carried out.

2.3.3 Oxide Growth for Oxide Spacers of Different Thicknesses

A previously published procedure was used to electrochemically and chemically grow thin oxide layers (5-20 nm) on Si in a 1M HNO_3 electrolyte[18]. Anodic oxidation occurred at the Si working electrode (WE) with a Pt counter electrode (CE) and a calomel reference electrode with potentials of 10 to 20 V applied using a potentiostat or using only WE, CE and a power source to provide voltages greater than 10 V. Nitric acid oxidation of Si (NAOS) was employed to chemically grow oxide layers using a 40 wt. % solution of nitric acid which was heated to 108 °C for ~1.5 h until the azeotropic point was reached[19]. After which the solution was added to a round-bottomed flask and refluxed at 121 °C for 14 h.

2.3.4 Surface Characterisation

X-Ray photoelectron spectroscopy (XPS) analysis was carried out on an Oxford Applied Research Escabase XPS system with a unmonochromated Al Kα X-Ray source at 200 W with a base pressure of 5×10^{-10} mbar. Survey spectra were acquired at 0-1000 eV using a step size of 0.7 eV, a dwell time of 0.3 s and a pass energy of 100 eV. Core level scans were averaged over 20-40 scans at a step size of 0.1 eV, a dwell time of 0.1 s and a pass energy of 50 eV. Spectra were recorded normal to the surface direction and also at a grazing angle of 165 ° from the axis of recording. XPS was also carried out using a Kratos AXIS-ULTRA XPS using monochromated Al X-rays at 150 W. Survey spectra were recorded at a pass energy of 160 eV with a step size of 1 eV and a dwell time of 50 ms. Core level scans were acquired at 20 eV with a step size of 0.05 eV and a dwell time of 100 ms. These measurements were recorded normal to the surface direction. Scans were averaged over 12 scans for the survey scans and 5-40 for core level scans. CasaXPS software was used to process the spectra with Shirley background correction and peaks fitted to Voigt profiles. Peaks were charge corrected to the C 1s peak at 285 eV. SiO_2 thicknesses were calculated using the thickogram[24] and measurements were averaged over 3 samples. Attenuated total reflectance infrared (ATR-FTIR) spectra were recorded using a Nicolet 6700 Infrared Spectrometer with a VariGATR and a liquid cooled HgCdTe detector using 3000 scans at a resolution of 2 cm^{-1}. Spectra were collected under p-polarisation in an ambient atmosphere. ATR-FTIR spectra were also collected using a Bruker Platinum ATR using 1000 scans. Contact angle measurements were recorded using deionised water on a Data Physics Contact Angle instrument using a minimum of 8 measurements per sample.

2.3.5 Dopant Profiling

Samples were capped with 50 nm of sputtered SiO_2 and samples were placed in a rapid thermal anneal furnace for 5 seconds at 950, 1000, 1050 or 1100 °C. A WEP Control CVP21 Wafer Profiler was used for ECV analysis. A 0.1 M ammonium hydrogen difluoride (≥98.5 %) solution was used as an etchant. SIMS analysis was carried out on an ION TOF TOF-SIMS 5. Sputtering was carried out with a Cs^+ ion beam and analysis was completed using a 25 keV Bi^+ ion beam incident at 45° of a 40 µm × 40 µm area. ECV and SIMS measurements were carried out in duplicate and analysis displayed is an average of the two measurements. Hall Effect measurements were acquired using a LakeShore® 8600 series instrument, with an excitation field of 1.7 T and an excitation current from 10 µA to 100 µA. Errors in measurements can occur due to the approximation of samples to the van der Pauw geometry.

2.4 Results and Discussion

2.4.1 Functionalisation of Oxide-Free Silicon

Si surfaces can be functionalised using hydrosilylation reactions, where an alkene group reacts with a H-terminated Si surface. Hydrosilylation reactions are sensitive to air and moisture and therefore must be carried out under inert conditions. All precursors must be dried prior to functionalisation as trace amounts of water can cause significant oxidation of the Si surface. A number of phosphorus-containing molecules were used for hydrosilylation reactions as depicted in **Figure 2.3**.

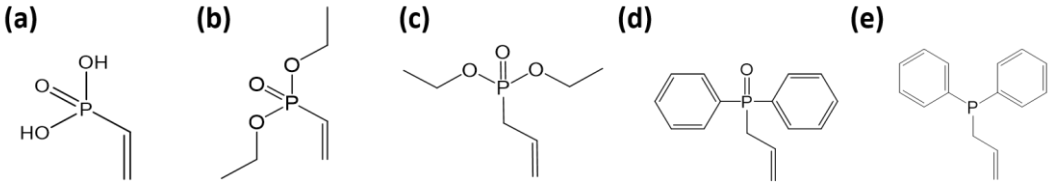

Figure 2.3: P-containing dopant precursors used for hydrosilylation reactions with the Si surface. (a) vinylphosphonic acid (b) diethylvinyl phosphonate (c) diethyl allylphosphonate (d) allyldiphenylphosphine oxide (e) allyldiphenylphosphine.

Figure 2.4 shows the Si 2p core levels of Si surfaces functionalised using vinylphosphonic acid (VPA) through a hydrosilylation reaction.

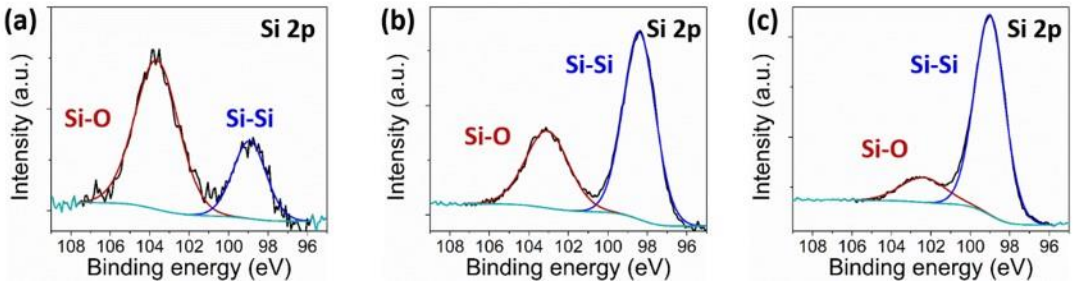

Figure 2.4: Si 2p XPS spectrum showing the Si 2p peak at 99 eV and oxide shoulder at 103 eV. The Si 2p spectrum when VPA is used (a) without drying, (b) dried over molecular sieves and (c) after drying with P_2O_5 and molecular sieves.

Hydrosilylation reactions attempted using vinylphosphonic acid (VPA) resulted in a large amount of oxidation which occurred during the reaction, as displayed in **Figure 2.4**(a). A reduction in oxide growth was observed when VPA was purified with molecular sieves, as displayed in **Figure 2.4**(b), and an even more significant reduction was seen when pre-dried using P_2O_5, filtered through alumina and subsequently dried over molecular sieves for a week, as seen in **Figure 2.4**(c). Diethyl vinylphosphonate (DVP) was used, as its viscosity was more suitable for distillation. After drying overnight in CaH_2, DVP was distilled and the reaction was repeated resulting in ~0.5 nm of oxide growth during the reaction. DVP was analysed using ATR-FTIR showing a broad absorption at ~3650 cm^{-1}, as displayed in **Figure 2.5**, indicative of the presence of water suggesting CaH_2 is an unsuitable drying agent. Drying was attempted using Na and molecular sieves but both resulted in a similar peak at 3500 cm^{-1}.

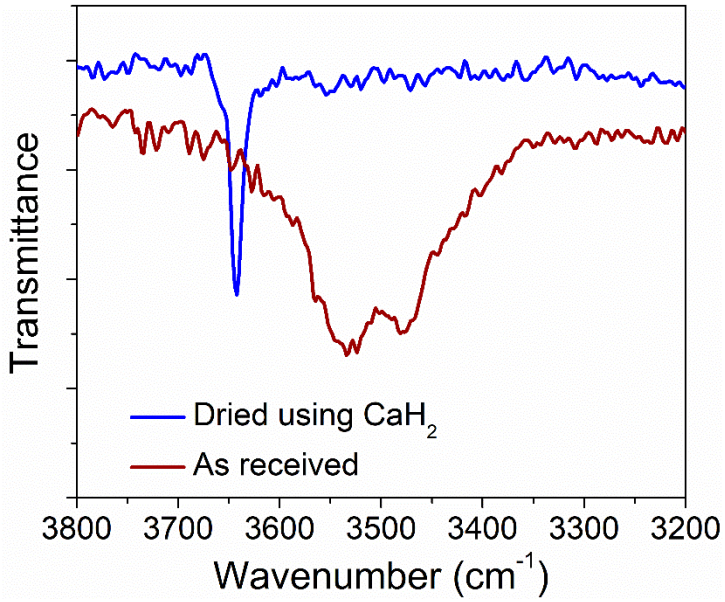

Figure 2.5: IR analysis of DVP as received and after drying using CaH_2.

As DVP is air, light and moisture sensitive it could not be dried completely without being chemically changed and the oxide thickness of hydrosilylated substrates could

not be reduced below 0.5 nm. Allyldiphenylphosphine oxide (ADPO) did not display OH absorptions when analysed using IR and therefore could be more suitable for functionalisation. Oxide growth (0.4 nm) was estimated to be similar to DVP and purified VPA even after drying ADPO under vacuum. Allyldiphenylphosphine was distilled under reduced pressure but high temperatures (~300 °C) were needed to achieve reflux which can induce polymerisation, in correlation with a higher amount of phosphorus present when samples were analysed using XPS. The molecule reacted when dried using molecular sieves resulting in a grease-like consistency. When dried using CaH_2 the clear liquid turned into yellow crystals overnight. When used unpurified a lower amount of oxide (0.2 nm) was attained which could not be improved due to the reactive nature of the molecule with drying agents. Diethyl allylphosphonate (DAP) was used due to its lower light and moisture sensitivity. Drying with P_2O_5 with filtration through alumina resulted in an OH-free spectrum when compared to unpurified DAP indicating an effective drying agent was selected. A similar oxide thickness was obtained (0.5 nm) when compared to other molecules.

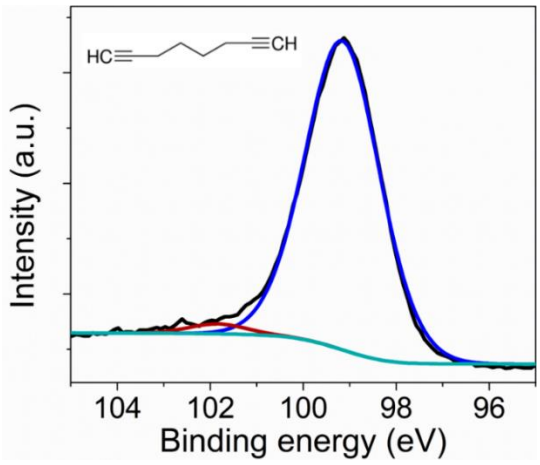

Figure 2.6: Si 2p spectrum of an alkyne functionalised Si surface.

Consistent growth of underlying SiO_2 for all 5 molecules is indicative of the presence of water in the dopant precursor molecules. As some molecules used for hydrosilylation reactions contain oxygen functionality, water could be originating from the precursor. To confirm the origin of water, the reaction was repeated using a molecule with no hydrophilic groups (1,7-dialkyne) under the same reaction conditions. The Si 2p spectrum is displayed in **Figure 2.6** showing a negligible amount of oxidation, confirming oxidation must be caused by the inability to completely dry phosphorus precursors.

2.4.2 Functionalisation of SiO_2

Oxide functionalisation was investigated due to its more robust nature and compatibility with ambient conditions. A large range of inexpensive precursors can be selected without the need for purification of precursors and solvents. VPA was selected to give an accurate comparison between hydrosilylation and oxide functionalisation.

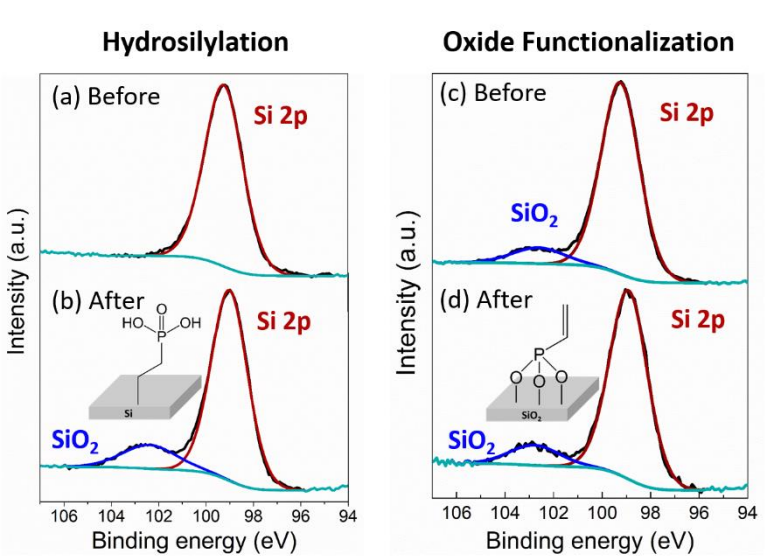

Figure 2.7: The Si 2p peak is illustrated (a) before and (b) after a hydrosilylation reaction and (c) before and (d) after the oxide functionalisation process.

The oxide layer used for oxide functionalisation was grown using an RCA clean which oxidises the Si surfaces to form 0.4 nm of SiO_2. The self-limiting nature of the process ensures a reproducible oxide thickness is achieved.[25] **Figure 2.7** compares the Si 2p core levels of the Si substrates before and after hydrosilylation and oxide functionalisation. The appearance of an oxide shoulder at 103 eV can be seen by comparison of **Figures 2.7**(a) and (b), with an estimated oxide growth of 0.5 nm. **Figures 2.7**(c) and (d) show the negligible changes in the oxide shoulder (0.1 nm) as a result of oxide functionalisation. Three molecules were selected for oxide functionalisation: vinylphosphonic acid (VPA), phenylphosphonic acid (PPA) and n-dodecylphosphosphonic acid (DPA), as displayed in **Figure 2.8**.

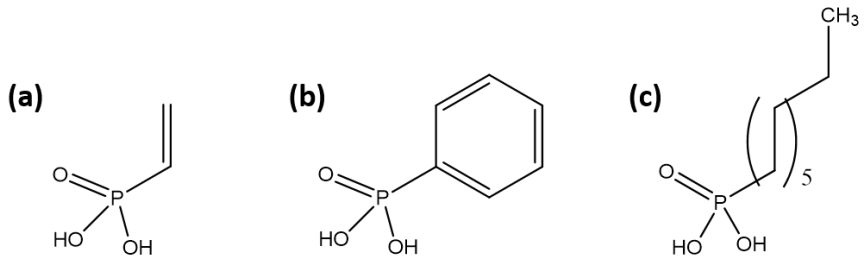

Figure 2.8: Molecules used for oxide functionalisation. (a) vinylphosphonic acid (VPA), (b) phenylphosphonic acid (PPA) and (c) n-dodecylphosphosphonic acid (DPA).

All molecules displayed negligible oxidation during the oxide functionalisation reaction, with an oxide thickness of 0.5 nm obtained after functionalisation. Successful attachment of VPA was confirmed using the XPS P 2s and P 2p signals after prolonged sonication in THF and ethanol, ensuring signals are largely due to chemisorbed rather than physisorbed species. Due to the overlap of phosphorus signals with Si plasmons, grazing angle XPS was carried out to resolve the phosphorus and Si signals. **Figure 2.9** shows the Si 2p spectrum acquired at an angle of 0-75°. As the substrate is tilted the sampling area increases and the penetration depth of the

beam decreases resulting in a lower intensity Si peak. A reduction in the Si peak at 99 eV and increase in the oxide shoulder displays the enhanced surface sensitivity acquired at 75 °.

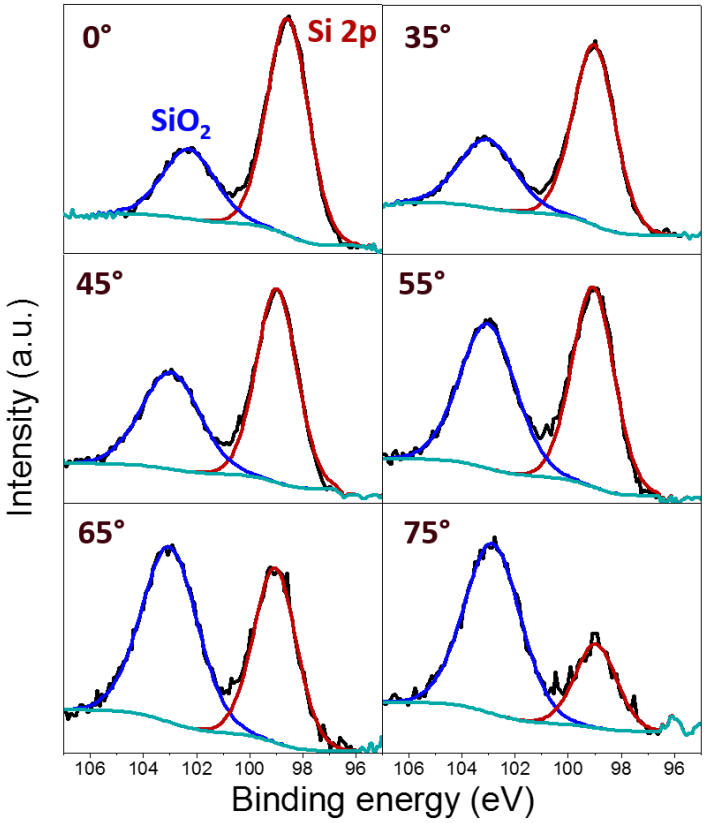

Figure 2.9: The changes of the Si 2p peak can be seen as the tilt angle of the substrate is varied in order to increase surface sensitivity during XPS analysis.

Figures 2.10(a)-(b) show the P 2p peak acquired at 0 ° and 75 °. A reduction in the Si plasmon is observed at 75 ° with a remaining P 2s peak observed confirming successful attachment of VPA.

Surface attachment was also investigated using a fluorinated phosphonic acid (1H,1H,2H,2H–perfluorooctanephosphonic acid) giving a characteristic shift in the C 1s due to fluorine's high electronegativity. The C 1s peak can be seen in **Figure 2.10**(c).

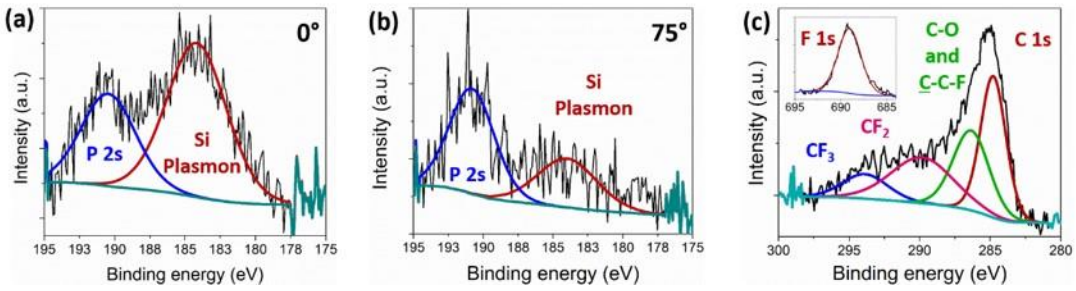

Figure 2.10: The P 2s peak acquired at (a) 0° and (b) a more surface sensitive angle of 75°. (c) The C 1s peak displays attachment of a fluorinated phosphonic acid with deconvoluted carbon environments and the inset showing the F 1s peak.

CF_3 groups can be seen at a BE of 293.9 eV while CF_2 groups can be observed at 289.8 eV. The contribution at 286.4 corresponds to C-C-F and C-O, as the shift in BE is too small to be deconvoluted. A F 1s peak was also seen further confirming surface attachment.

The attachment of boron-containing precursors was also investigated to allow application of oxide-MLD to both p- and n-doping. Boronic acid (BA) and phenyl boronic acid (PBA) were selected as precursors. The B 1s spectra for a boronic acid SiO_2 functionalised sample is shown is **Figure 2.11**, which overlaps with the Si plasmon.

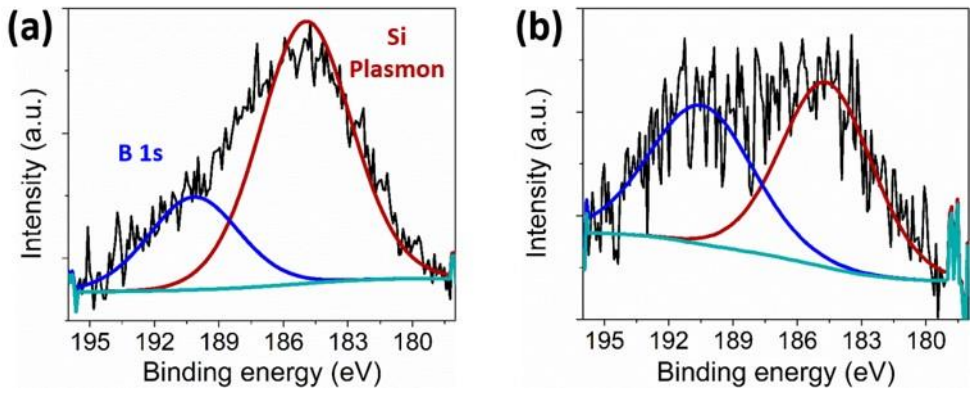

Figure 2.11: B 1s spectrum of a boronic acid SiO_2 functionalised sample acquired at (a) 0 ° and (b) 75 °.

Angle resolved XPS displays a B 1s peak is present which is accompanied with a reduction in the Si plasmon intensity, hence demonstrating successful application to of boron-containing precursors to oxide-MLD

2.4.3 Optimisation of Monolayer Attachment of Phosphonic Acids

Reproducibility of doping profiles is highly dependent on monolayer coverage obtained through controlled functionalisation of substrates. Investigation of phosphonic acid attachment was carried out to optimise the packing and assess the extent of physisorption on the Si surface. The changes in BE of the P 2s peak allow differentiation between physisorption and chemisorption. The P 2s peak for PPA functionalised SiO_2 surfaces is compared before annealing (pre-anneal), after annealing without rinsing (post-anneal) and after prolonged sonication (post-sonication) as shown in **Figure 2.12**.

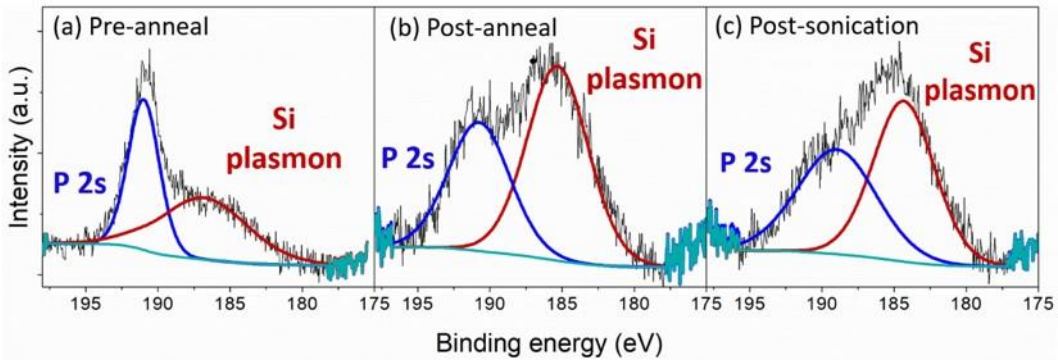

Figure 2.12: Changes in the P 2s spectra can be evaluated at different stages of the functionalisation process to characterise physisorption and chemisorption.

A shift can be seen from 191.4 eV (pre-anneal), to 190.8 eV (post-anneal), to 189 eV (post sonication) consistent with the conversion of a physisorbed multilayer to a covalently bound monolayer after sonication. The shift in the P 2s BE is associated

with conversion of P-O-H bonds in physisorbed phosphonic acid molecules to covalently bound P-O-Si bonds.[26]

The O 1s was also evaluated at different stages of the monolayer formation process. A broadening of the full width at half maximum (FWHM) from 2.22 eV (pre-anneal), to 2.58 eV (post-anneal) to 2.37 eV (post-sonication) can be attributed to the incorporation of a P-O-Si component in the main O 1s peak.[26] The combined shift in P 2s peak and broadening of O 1s peak indicate covalent binding of phosphonic acids and a reduction in physisorbed species. ATR-FTIR was used to assess conditions that contribute to optimal monolayer coverage. Immersion time was varied to determine optimal self-assembled monolayer (SAM) formation and assess the extent of oxidation as a result of longer immersion times. A 7 day immersion time did not result in residual oxide growth, most likely due to the protection of the phosphonic acid SAM that passivates the surface. Similar surface coverages are obtained for both immersion times (7 days or 24 hours) as determined by similar intensities in P 2s peaks. Therefore, a thermodynamically stable SAM is formed after 24 hours that is physisorbed on the SiO_2 surface. Alkyl phosphonates were also investigated for SiO_2 functionalisation. However, a growth in oxide thickness was observed from 0.4 nm to 1.3 nm during functionalisation. Phosphonates typically have a large molecular footprint due to the R groups which can hinder monolayer formation and result in a less tightly packed monolayer. The formation of SAMs is influenced by substituents, such as H-bonding in the phosphonate head-group and π-π interactions between aryl substituents which can facilitate monolayer formation.[27] Incompletely passivated surfaces are more susceptible to re-oxidation especially during the annealing step. Phosphonic acids typically have a less sterically hindered head group compared to

phosphonates and therefore phosphonic acids are more compatible with SiO_2 functionalisation.

A growth in the oxide layer was observed with an anneal time of 24 hours[26,28–30] accompanied with surface stains that could not be removed by sonication. Attachment of phosphonic acids to SiO_2 occurs within seconds of reaching 140 °C but only in a low humidity environment (<16 %).[17] A P 2s peak was observed for samples annealed under ambient humidity levels, indicating a low amount of surface binding occurs, however, a P-O-Si signal was not observed when substrates were analysed using ATR-FTIR. When annealed in a humidity level below 16 % (under nitrogen or vacuum) a P-O-Si feature appeared at 1100 cm^{-1}, displaying improved coverage. At high humidity levels the hydroxyl network does not allow reaction but when humidity levels are lowered the network is broken which facilitates attachment of phosphonic acids.[17] The presence of P 2s peaks for substrates annealed under both humidity conditions (<16 % and >16 %) indicates functionalisation occurs but optimal coverage is achieved in low humidity environments. Phosphonic acid attachment occurs through a condensation reaction with loss of water and therefore low humidity environments will drive this reaction and provide optimal coverage.

Covalent attachment has been established using XPS and ATR-FTIR on the SiO_2 surface. However, the extent of physisorption must be characterised to confirm reproducible monolayer coverage is obtained through oxide functionalisation. Contact angle measurements can provide insight into the physisorption of phosphonic acid species, as the presence of physisorbed species can lower contact angles.

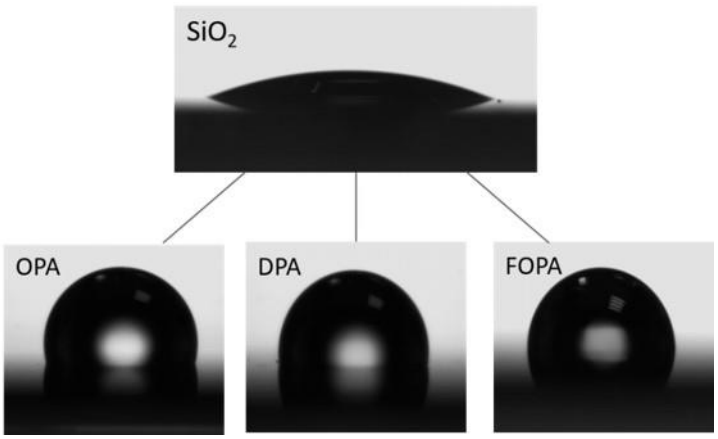

Figure 2.13: Contact angle displayed for an RCA-cleaned SiO_2 surface, OPA, DPA and FOPA functionalised SiO_2 surfaces.

Table 2.1: Contact angles obtained for SiO_2 and phosphonic acid functionalised surfaces.

Molecule	Contact angle (°)
SiO_2 Surface	22
DPA	97
OPA	105
FOPA	92

Figure 2.13 and **Table 2.1** display the changes in contact angle from 22 ° for an RCA cleaned SiO_2 surface to a contact angle >90 ° for functionalised surfaces. The hydrophobicity of oxide functionalised surfaces confirms well-ordered covalently bound monolayers are formed through oxide functionalisation.

Oxide functionalisation has been demonstrated to be more suitable to ambient conditions than hydrosilylation, as reactions can be carried out under ambient conditions without an increase in the oxide shoulder of the Si 2p core level. The

stability of oxide functionalised samples was assessed over a period of 24 hours, 1 week and 1 month and compared to hydrosilylated surfaces using XPS analysis. Hydrosilylated samples displayed significant re-oxidation of the surface, while oxide functionalised surfaces remained stable over a period of a month. **Figure 2.14** displays the SiO_2:Si ratio over a period of a month clearly showing the increase in SiO_2 for hydrosilylated substrates. Hydrosilylated surfaces displayed a decrease in the P 2s signal indicating loss of coverage which was not observed for oxide functionalised substrates demonstrating the increased passivation properties of oxide functionalisation.

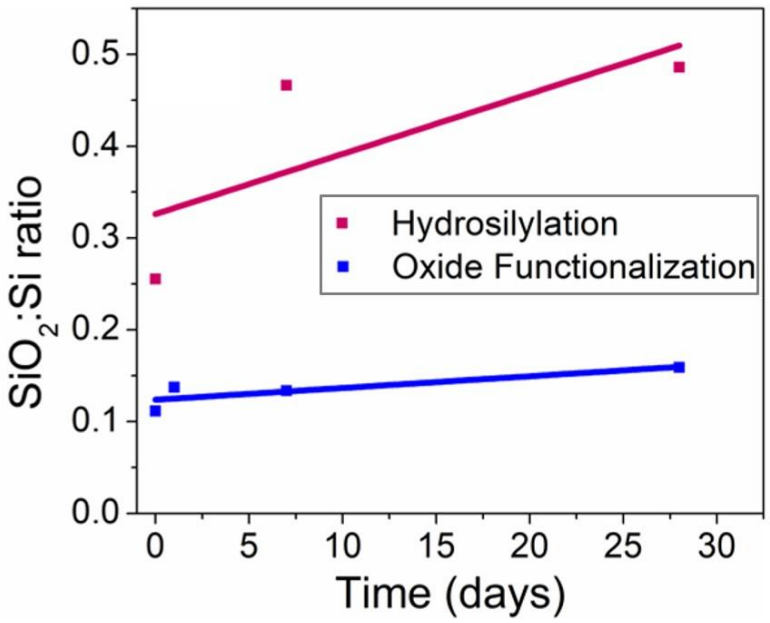

Figure 2.14: SiO_2:Si ratio over a period of a month for hydrosilylated and oxide functionalised substrates

2.4.4 Binding Mechanism of Phosphonic Acids to SiO_2

Phosphonic acid binding mechanism can occur through three main binding modes: monodentate, bidentate or tridentate, as displayed in **Figure 2.15**.[16,17,26,31,32]

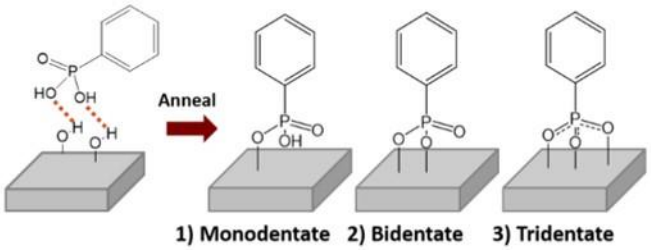

Figure 2.15: Surface attachment changes from physisorbed to chemisorbed attachement after annealing. Attachment can occur in a monodentate, bidentate or tridentate configuration.

By evaluating the XPS and ATR-FTIR spectra at different stages of the functionalisation process the binding mechanism can be determined. A physisorbed overlayer is formed first which is converted to chemisorbed layer with physisorbed species after annealing. Rinsing and sonication removes physisorbed species leaving a covalently bound monolayer. Comparison of a physisorbed multiayer (Pre-anneal) to a chemisorbed multilayer (Post-anneal) to a chemisorbed monolayer (Post-sonication) allows determination of the binding mechanism.

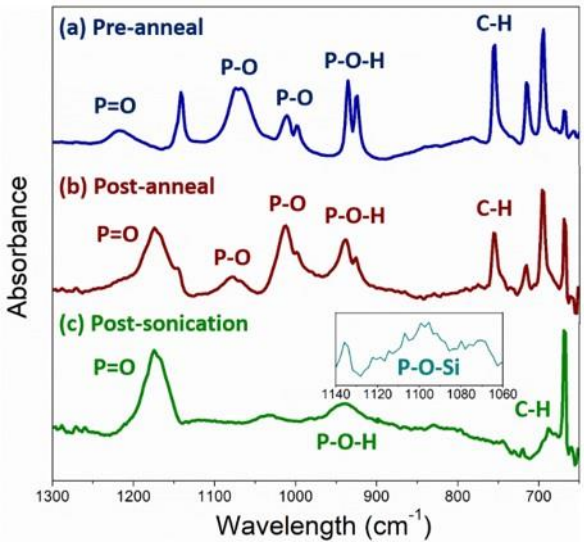

Figure 2.16: ATR-FTIR spectrum of pre-anneal, post-anneal and post-sonication substrates used to investigate the surface binding mechanism.

Figure 2.16 displays the ATR-FTIR spectra of the three stages of the functionalisation process. The presence of PPA was determined by symmetric and asymmetric P-O stretches which were observed at 1025-975 cm^{-1} and 1070 cm^{-1} as seen in **Figure 2.16**(a). Aromatic C-H absorptions were seen at 760-650 cm^{-1} as well as aromatics overtones at 1750 cm^{-1} supporting the presence of PPA. The split peak at 940-930 cm^{-1} can be attributed to P-O-H which characteristically appears at 950-900 cm^{-1}. A decrease in P-O-H peak intensity can be observed after annealing by comparison of **Figures 2.16**(a) and (b), indicative of reaction of P-O-H bonds with the SiO_2 surface. A decrease in peak intensity can be seen in **Figures 2.16**(b) and (c) along with a broadening of the absorption due to removal of physisorbed species. The P=O feature can be identified at 1220 cm^{-1} as it usually occurs in the 1250-1200 cm^{-1} region. Annealing results in an increase in P=O intensity and a shift to 1180 cm^{-1} which can be attributed to a change in environment with P-O-H bonds becoming bound to the surface. ATR-FTIR does not identify bonding of P=O groups due to the remaining peak but XPS allows more detailed characterisation. ATR-FTIR shows surface binding of P-O-H groups due to the reduction in intensity of the P-O-H peak.

By comparing the (P-O-H)/O 1s and (P=O)/O 1s XPS ratios the conclusions drawn from ATR-FTIR can be confirmed and the binding mechanism can be characterised further. **Figures 2.17**(a)-(c) displays the deconvoluted O 1s environments with the main O 1s peak at ~533 eV, P-O-H at ~531 eV and P=O at ~534 eV. Annealing creates a reduction in ~30 % of the P=O and ~60 % of the P-O-H component suggesting reaction of these components. P=O surface binding could not be distinguished using ATR-FTIR, however, a clear reduction can be observed in the XPS O 1s core level indicating reaction of P=O with the SiO_2 surface. Rinsing and sonicating results in a

30 % decrease in both P-O- H and P=O components, as shown by comparison of **Figures 2.17**(b) and (c). This reduction can be attributed to removal of physisorbed material.

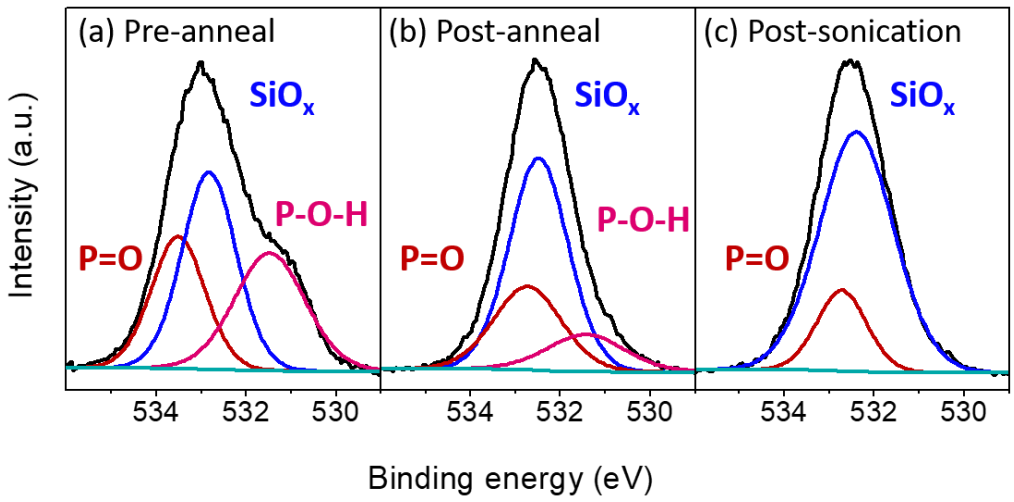

Figure 2.17: O 1s XPS spectra showing changes in P=O and P-O-H components during the oxide functionalisation process.

No P-O-H was observed after sonication suggesting reaction of most P-O-H groups with the SiO_2 surface. The remaining P-O-H group can therefore be attributed to a resonance structure where one P-O-H and one P=O group binds to the surface leaving one free P-O-H bond. A similar structure has been observed on indium tin oxide (ITO) surfaces.[31] A remaining P=O peak was observed to be ~30 % compared to a pre-anneal sample, suggesting not all P=O groups react with the surface. No P-O-H peak was observed after sonication as most P-O-H will have either bonded to the surface or be rinsed away. Therefore, most P-O-H bonds and ~60 % of P=O bonds will react with the surface resulting in a combination of bidentate and tridentate attachment. The remaining P-O-H peak observed through ATR-FTIR can be attributed to a resonance structure formed, however, to quantify the remaining P-O-H bonds a base rinse (containing triethylamine) was carried out. Triethylamine will coordinate to free acid

groups (P-O-H) and can be discerned using the XPS N 1s peak.[31] No clear peak could be identified using XPS as shown in **Figure 2.18** confirming the presence of a negligible amount of P-O-H.

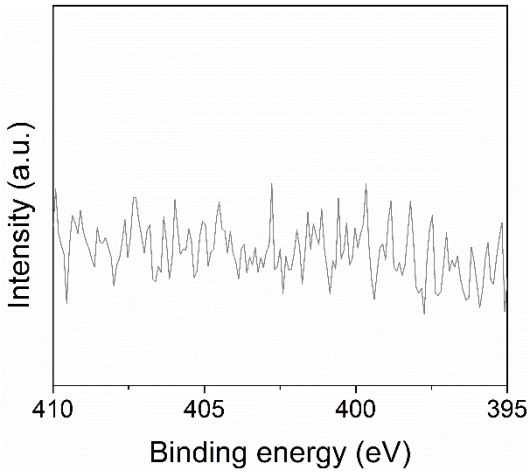

Figure 2.18: N 1s core level after a VPA functionalised substrate was rinsed with trimethylamine which binds to free P-O-H groups.

Consequently, monodentate attachment can be ruled out. Bidentate attachment can be confirmed due to a remaining P=O peak observed using ATR-FTIR and XPS. Tridentate attachment can also be confirmed due to the reduction of the P=O component as seen by XPS analysis which is in agreement with literature reports of phosphonic acid binding to the surface.[26] Tridentate attachment is the most stable configuration due to the resonance delocalisation that occurs when all 3 O atoms bind to the surface. [33]

2.4.5 Doping of SiO_2 Functionalised Surfaces using Phosphonic Acids and comparison to Si-doped Substrates

Oxide functionalisation was compared to hydrosilylation in terms of doping concentration using VPA, a phosphonic acid that can attach to the Si surface through

its alkene group and to the SiO_2 surface through its phosphonic acid head group. Therefore, VPA provides an accurate comparison between the two doping profiles resulting from both functionalisation strategies. **Figure 2.19** displays similar doping profiles are obtained for hydrosilylated (2.59×10^{20} atoms/cm^3) and oxide functionalised (2.36×10^{20} atoms/cm^3) surfaces. The high peak carrier concentration obtained for oxide functionalised surfaces indicates no loss of dopant occurs when an oxide layer is incorporated in the monolayer doping process. The solubility of phosphorus in SiO_2 is lower compared to Si resulting in rejection of phosphorus by the oxide and a high presence of phosphorus in the underlying Si substrate. Therefore, oxide layers can successfully be used for doping applications. Similar oxide thicknesses were obtained for oxide functionalised and hydrosilylated substrates, but as hydrosilylated surfaces are not stable the oxide thickness can grow in between processing steps giving unreliable doping profiles. The stability of the oxide functionalised samples ensures no extra oxide forms between fabrication and doping steps.

A range of different phosphonic acids were selected to influence the dopant dose which can be tailored by selecting molecules with varying steric sizes. **Figure 2.19**(b) illustrates the ECV doping profiles for VPA, DPA and PPA.The highest peak carrier concentration was obtained using VPA at 4×10^{19} atoms/cm^3, while a decrease was observed for PPA to 1×10^{19} atoms/cm^3 and the lowest peak carrier concentration was DPA at 7×10^{18} atoms/cm^3. VPA has the smallest molecular footprint as illustrated in **Figure 2.19**.

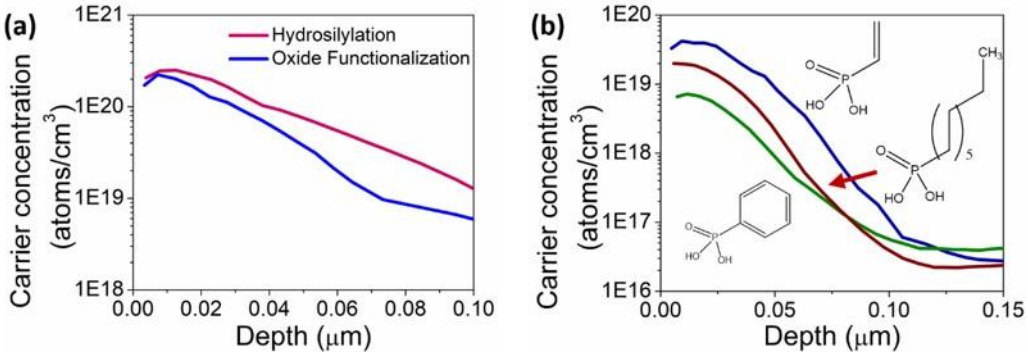

Figure 2.19: (a) Comparison of doping profiles obtained for hydrosilylated and oxide functionalised surfaces. (b) Variation in peak carrier concentration achieved through use of different phosphonic acids.

A slight decrease in carrier concentration is observed for DPA due to the more favourable tilted configuration formed when long-chain structures attach to surfaces. The large increase in peak carrier concentration seen for VPA could also be attributed to the formation of multilayers due to the high viscosity of the molecule which made removal of physisorbed species difficult. Peak carrier concentrations have successfully been tailored by employing different sterically sized phosphonic acids.

The accuracy of ECV measurements was evaluated using Hall and SIMS measurements. SOI substrates were used for Hall measurements to create an insulating layer necessary for Hall measurements. Comparison between the two techniques was made by taking the peak carrier concentration at the same depth of the doping profile as the thickness of the Si on the SOI substrate. The Hall measurement for VPA at 3×10^{18} atoms/cm^3 was in good agreement with 4.5×10^{18} atoms/cm^3 as determined by ECV measurements. PPA doped substrates had a carrier concentration of 7×10^{17} atoms/cm^3 at 66 nm as determined by ECV, comparable to 7×10^{17} atoms/cm^3 obtained by the Hall measurement.

2.4.6 Modification of Dopant Profile in SiO_2 substrates

The RTA temperature has been used to influence the doping profile in terms of peak carrier concentration and junction depth. Lower temperatures result in a shallower junction depth but are accompanied with a reduction in peak carrier concentration. The optimal doping profile was found by annealing substrates at temperatures from 950-1100 °C, as displayed in **Figure 2.20**. The highest peak carrier concentration was obtained at an RTA temperature of 1000 °C at 7.87×10^{19} atoms/cm^3. A slight decrease in peak carrier concentration to 3.09×10^{19} atoms/cm^3 occurred when substrates were annealed at 1100 °C. Optimal RTA temperature has been established at 1050 °C for hydrosilylated substrates while we report a slightly lower temperature of 1000 °C resulting in a higher peak carrier concentration when doping oxide functionalised substrates.[6] As expected, an increase in junction depth was observed to 100 nm taken at 1.36×10^{18} atoms/cm^3 substrates annealed at 1100 °C while a decrease to 22 nm at 1.72×10^{18} atoms/cm^3 was observed for substrates annealed at 950 °C. Annealing below 950 °C was also investigated to further reduce junction depth, however, no doping was observed at RTA temperatures of 750 and 850 °C indicating these temperatures are not high enough for doping oxide functionalised substrates.

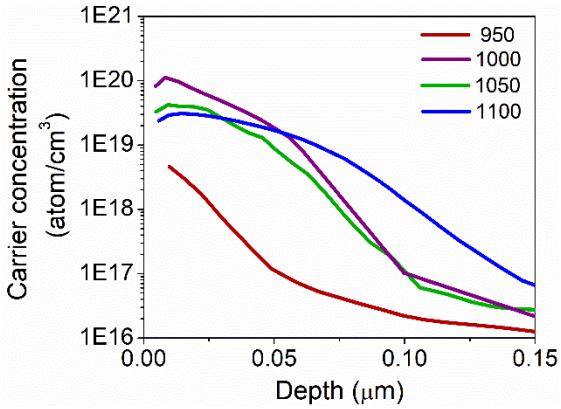

Figure 2.20: Doping profiles showing the influence of temperature on peak carrier concentration and junction depth.

While temperature provides a way of reducing junction depth it also reduces active carrier concentration. In order to maintain high peak carrier concentrations the dopant source was increased by using a physisorbed multilayer layer which will contain a higher amount of phosphorus compared to a chemisorbed monolayer. Physisorbed samples were prepared using the oxide functionalisation process but substrates were not sonicated or rinsed hence leaving a large amount of physisorbed material on the surface. **Figure 2.21** displays the ECV profiles for PPA, DPA and VPA. An increase in peak carrier concentration was seen from 5.74×10^{18} atoms/cm^3 to 2.36×10^{19} atoms/cm^3 for physisorbed PPA to chemisorbed PPA. Therefore, a larger dopant source does lead to a higher peak carrier concentration but physisorbed samples did not display good reproducibility as physisorbed layers do not provide a fixed dopant source unlike the consistent coverage obtained for chemisorbed monolayer substrates after rinsing. DPA displayed similar results to PPA. Similar peak carrier concentrations were obtained for physisorbed and chemisorbed VPA at 4.39×10^{19} atoms/cm^3 and 3.42×10^{19} atoms/cm^3, respectively. A high viscosity can lead to the formation of multilayers and removal of physisorbed species can be difficult.

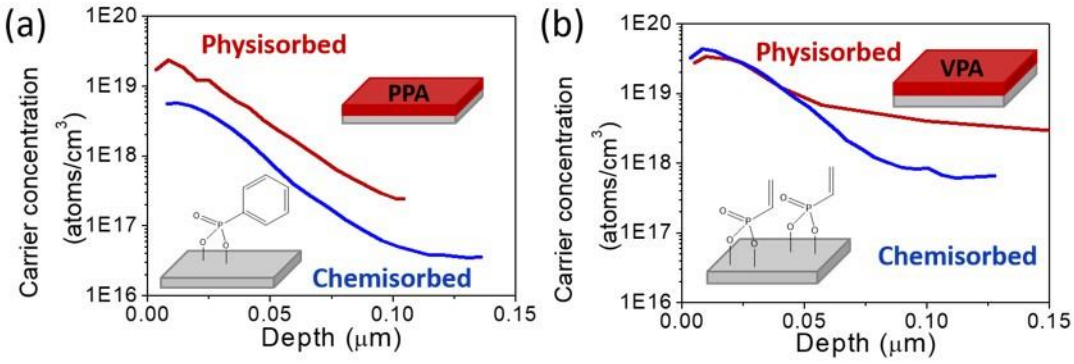

Figure 2.21: Comparison of physisorbed and chemisorbed samples for (a) PPA and (b) VPA.

Variation of rinsing procedures was used to remove physisorbed species from the chemisorbed layer. An ethanol rinse was used initially with 10 minutes of sonication in THF followed by ethanol and compared to a base rinse, 10 minutes of sonication in triethylamine followed by ethanol. Similar doping profile obtained for both PPA and DPA using an ethanol and a base rinse suggests an ethanol rinse allows successful removal of physisorbed species. However, phyisorbed samples show a large increase in junction depth without a significant increase in carrier concentration, as previously reported.[3] An increase in dopant source has resulted in an increase in junction depth without leading to a higher peak carrier concentration. As a result, functionalisation of semiconductor surfaces provides a reproducible method of doping with a shallower junction depth compared to physisorbed substrates.

2.4.7 Modification of Oxide Layer Thickness to Modify Junction Depth

In order to modify junction depth while providing a fixed dopant source and maintaining high peak carrier concentrations the thickness of the oxide layer was varied to slow diffusion and subsequently give shallower junction depths. The oxide layer was grown electrochemically using anodic oxidation of silicon by variation of current densities from 10 to 30 $\mu A/cm^2$ for times of 0-60 minutes which resulted in growth of 3-8 nm. Oxide thicknesses obtained using ellipsometry were inconsistent and ellipsometry was found not to give an accurate measurement of oxide layers under 10 nm. XPS analysis is more reliable when characterising oxide films below 10 nm in thickness.[34] The Si 2p XPS peak was used to calculate oxide thicknesses using the thickogram.[24] **Figure 2.22**(a) shows a promising effect in reducing junction depth from 45 nm at 1.31×10^{18} atoms/cm^3 to 19 nm at 1.58×10^{18} atoms/cm^3 for a 20 nm oxide layer, with no reduction in peak carrier concentration of 4.65×10^{18} atoms/cm^3.

A chemically grown spacer was also investigated as reports suggest chemically grown oxides have a higher density compared to electrochemically grown oxides.[35]

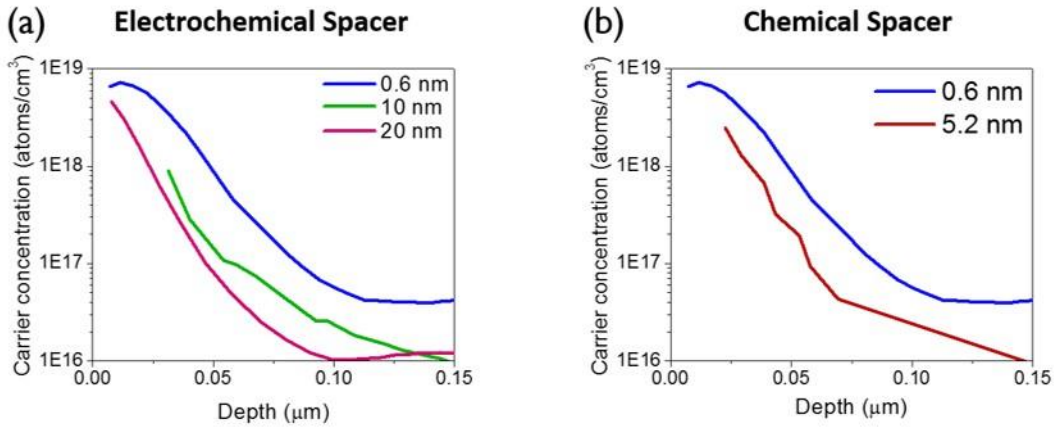

Figure 2.22: Comparison of a chemically and electrochemically grown SiO_2 layer that acts as a spacer to slow dopant diffusion.

The NAOS procedure was used to grow a 5.2 nm oxide layer and showed a similar effect to the 10 nm electrochemically grown oxide with a reduction in junction depth from 45 nm at 1.31×10^{18} atoms/cm^3 to 29 nm at 1.31×10^{18} atoms/cm^3. Optimisation of the oxide growth procedure must be carried out to successfully give consistent oxide thicknesses. However, preliminary experiments show promise in achieving a shallower junction depth while maintaining high peak carrier concentrations.

2.4.8 Minimisation of Carbon Contamination when Doping SiO_2 Substrates

Carbon contamination is a key challenge when using MLD as a doping method, which leads to dopant deactivation.[21,22] While carbon contamination has been reported to be limited to the first few monolayers of doped substrates,[36] the removal of the top layer is not feasible for 3D architectures. The use of hydrosilylation to attach dopant precursors results in use of carbon-rich dopant precursors. Oxide functionalisation allows attachment of precursors through the phosphonic acid head group and hence do not require carbon in the precursor. Functionalisation using carbon-free precursors

was investigated as an alternative doping method that eliminates carbon contamination.

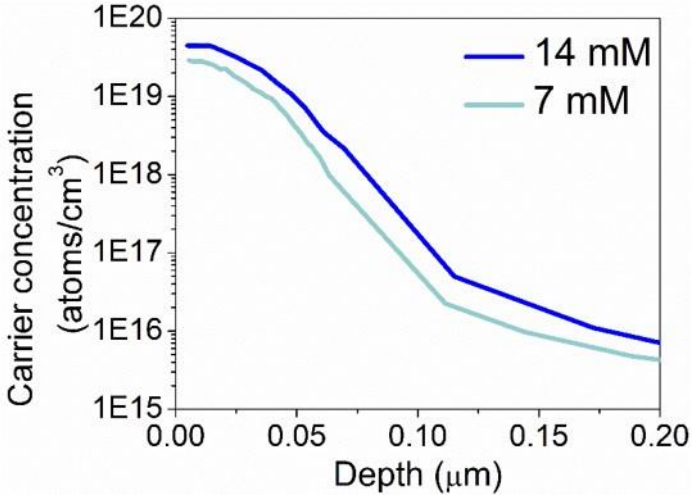

Figure 2.23: ECV doping profile of a carbon-free precursor, phosphorus pentoxide (P_2O_5).

Figure 2.23 shows the ECV profile of a P_2O_5 functionalised substrate with a high peak carrier concentration obtained at 4.49×10^{19} atoms/cm^3 for a P_2O_5 concentration of 14 mM and 2.79×10^{19} atoms/cm^3 for a concentration of 7 mM. An increase in P_2O_5 concentration increases the doping concentration, showing the peak carrier concentration can be varied through functionalisation of oxide surfaces with P_2O_5.

Theoretical studies have suggested capping layers are not required for phosphonic acid oxide functionalised surfaces, with the release of the carbon ligand occurring before the dopant enters the substrate.[22,37] When samples were not capped no dopant entered the substrate, as shown by the high contact resistance which did not allow measurement of a doping profile, suggesting capping layers are necessary for reproducible results even when phosphonic acids are used as dopant precursors.

While carbon-free precursors can be selected when using oxide functionalisation, the effect of carbon-containing precursors has also been investigated when using oxide-MLD. Literature reports have demonstrated segregation of carbon at the SiO_2-Si interface while carbon remains on the SiO_2 side of the interface.[23] **Figure 2.24** shows the SIMS data extracted from a substrate doped using PPA, a dopant precursor containing a phenyl ring. An increase in carbon can be seen at the SiO_2-Si interface, with the peak occurring at the SiO_2 side of the interface. Additionally, the concentration of carbon remains low considering the dopant precursor contains a phenyl ring, as a Si reference substrate contains the same amount of carbon as seen in the doped substrate (~1×10^{18} atoms/cm^3). Another indication of low carbon levels is the Hall mobility which was measured to be 217 and 129 cm^2/Vs for PPA and VPA, respectively. In conclusion, oxide-MLD is a suitable method of eliminating carbon contamination from doped substrates through trapping of carbon in the oxide layer or by selection of carbon-free precursors.

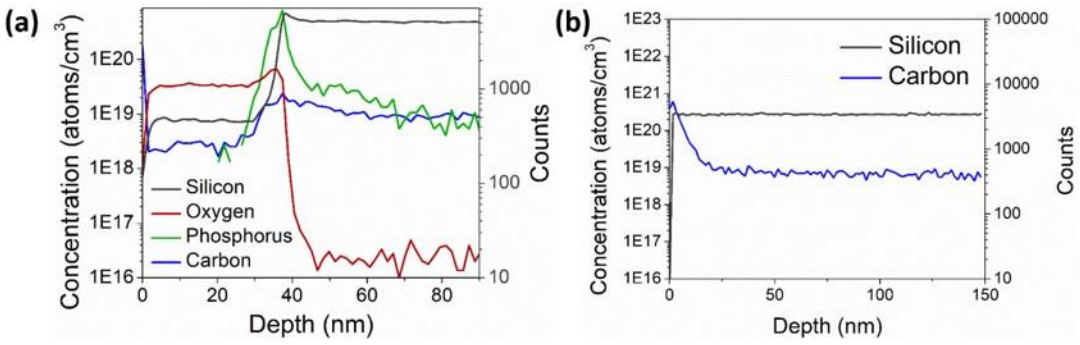

Figure 2.24: (a) SIMS analysis of a PPA-doped substrate without cap removal and (b) a reference Si substrate.

2.5 Conclusions

Oxide functionalisation has proven to be an effective functionalisation strategy for MLD applications, with similar peak carrier concentrations achieved when compared to hydrosilylated surfaces. Oxide functionalised surfaces display excellent ambient stability compared to hydrosilylated samples while reactions do not need to be carried out under inert conditions. The detailed characterisation of SiO_2 functionalised surfaces revealed the binding of the phosphonic acid group occurred mainly through a tridentate configuration without the presence of physisorbed species. Monolayer chemisorbed samples have produced optimal results in terms of doping profiles with high peak carrier concentrations and low junction depths. The variation of the molecular footprint of the phosphorus precursor also allowed variation of the peak carrier concentration. Modification of the oxide layer thickness allows reduction in junction depths while maintaining high peak carrier concentrations, although oxide growth must be optimised to obtain reproducible oxide layer thickness. The oxide layer facilitates attachment of a large range of carbon-free n-dopants through the attachment of the phosphonate group, thereby eliminating carbon contamination. The presence of the SiO_2 layer traps carbon present in carbon-containing dopant precursors during the RTA, eliminating carbon contamination for optimal dopant activation.

2.6 References

(1) Ho, J. C.; Yerushalmi, R.; Jacobson, Z. a; Fan, Z.; Alley, R. L.; Javey, A. Controlled Nanoscale Doping of Semiconductors via Molecular Monolayers. *Nat. Mater.* **2008**, *7* (1), 62–67.

(2) Ye, L.; Pujari, S. P.; Zuilhof, H.; Kudernac, T.; de Jong, M. P.; van der Wiel, W. G.; Huskens, J. Controlling the Dopant Dose in Silicon by Mixed-Monolayer Doping. *ACS Appl. Mater. Interfaces* **2015**, *7* (5), 3231–3236.

(3) Ye, L.; González-Campo, A.; Nuñez, R.; de Jong, M. P.; Kudernac, T.; van der Wiel, W. G.; Huskens, J. Boosting the Boron Dopant Level in Monolayer Doping by Carboranes. *ACS Appl. Mater. Interfaces* **2015**, *7* (49), 27357–27361.

(4) Alphazan, T.; Mathey, L.; Schwarzwälder, M.; Lin, T.-H.; Rossini, A. J.; Wischert, R.; Enyedi, V.; Fontaine, H.; Veillerot, M.; Lesage, A.; Emsley, L.; Veyre, L.; Martin, F.; Thieuleux, C.; Copéret, C. Monolayer Doping of Silicon through Grafting a Tailored Molecular Phosphorus Precursor onto Oxide-Passivated Silicon Surfaces. *Chem. Mater.* **2016**, *28* (11), 3634–3640.

(5) Perego, M.; Seguini, G.; Arduca, E.; Nomellini, A.; Sparnacci, K.; Antonioli, D.; Gianotti, V.; Laus, M. Control of Doping Level in Semiconductors via Self-Limted Grafting of Phosphorus End-Terminated Polymers. *ACS Nano* **2018**, *12* (1), 178–186.

(6) O'Connell, J.; Verni, G. A.; Gangnaik, A.; Shayesteh, M.; Long, B.; Georgiev, Y. M.; Petkov, N.; McGlacken, G. P.; Morris, M. A.; Duffy, R.; Holmes, J. D. Organo-Arsenic Molecular Layers on Silicon for High-Density Doping. *ACS Appl. Mater. Interfaces* **2015**, *7* (28), 15514–15521.

(7) O'Connell, J.; Collins, G.; McGlacken, G. P.; Duffy, R.; Holmes, J. D. Monolayer Doping of Si with Improved Oxidation Resistance. *ACS Appl. Mater. Interfaces* **2016**, *8* (6), 4101–4108.

(8) Bent, S. F. Attaching Organic Layers to Semiconductor Surfaces. *J. Phys. Chem. B* **2002**, *106* (11), 2830–2842.

(9) Bent, S. F. Organic Functionalization of Group IV Semiconductor Surfaces: Principles, Examples, Applications, and Prospects. *Surf. Sci.* **2002**, *500* (1–3), 879–903.

(10) Mathey, L.; Alphazan, T.; Valla, M.; Veyre, L.; Fontaine, H.; Enyedi, V.; Yckache, K.; Danielou, M.; Kerdiles, S.; Guerrero, J.; Barnes, J.-P.; Veillerot, M.; Chevalier, N.; Mariolle, D.; Bertin, F.; Durand, C.; Berthe, M.; Dendooven, J.; Martin, F.; Thieuleux, C.; Grandidier, B.; Copéret, C. Functionalization of Silica Nanoparticles and Native Silicon Oxide with Tailored Boron-Molecular Precursors for Efficient and Predictive p -Doping of Silicon. *J. Phys. Chem. C* **2015**, *119* (24), 13750–13757.

(11) Hotchkiss, P. J.; Jones, S. C.; Paniagua, S. a; Sharma, A.; Kippelen, B.; Armstrong, N. R.; Marder, S. R. The Modification of Indium Tin Oxide with Phosphonic Acids: Mechanism of Binding, Tuning of Surface Properties, and Potential for Use in Organic Electronic Applications. *modAccounts Chem. Res.* **2011**, *45* (3), 337–346.

(12) Curreli, M.; Li, C.; Sun, Y.; Lei, B.; Gundersen, M. A.; Thompson, M. E.; Zhou, C. Selective Functionalization of In2O3 Nanowire Mat Devices for Biosensing Applications. *J. Am. Chem. Soc.* **2005**, *127* (127), 6922–6923.

(13) Clemence Que´ffelec; Petit, M.; Janvier, P.; Knight, D. A.; Bujoli, B. Surface

Modification Using Phosphonic Acids and Esters. *Chem. Rev.* **2012**, *112* (7), 3777–3807.

(14) Cattani-Scholz, A.; Pedone, D.; Dubey, M.; Neppl, S.; Nickel, B.; Feulner, P.; Schwartz, J.; Absteiter, G.; Tornow, M. Organophosphonate-Based PNA-Functionalization of Silicon Nanowires for Label-Free DNA Detection. *ACS Nano* **2008**, *2* (8), 1653–1660.

(15) Cattani-Scholz, A. Functional Organophosphonate Interfaces for Nanotechnology : A Review. *ACS Appl. Mater. Interfaces* **2017**, *9* (31), 25643–25655.

(16) Pujari, S. P.; Scheres, L.; Marcelis, A. T. M.; Zuilhof, H. Covalent Surface Modification of Oxide Surfaces. *Angew. Chemie Int. Ed.* **2014**, *53* (25), 6322–6356.

(17) Vega, A.; Thissen, P.; Chabal, Y. J. Environment-Controlled Tethering by Aggregation and Growth of Phosphonic Acid Monolayers on Silicon Oxide. *Langmuir* **2012**, *28* (21), 8046–8051.

(18) S. Imai, M. Takahashi, K. Matsuba, Asuha, Y. Ishikawa, H. Kobayashi, S. Formation and Electrical Characteristics of Silicon Dioxide Layers by Use of Nitric Acid Oxidation Method. *Acta Phys. slovaca* **2005**, *55* (3), 305–313.

(19) Asuha; Im, S.-S.; Tanaka, M.; Imai, S.; Takahashi, M.; Kobayashi, H. Formation of 10–30nm SiO2/Si Structure with a Uniform Thickness at ~120°C by Nitric Acid Oxidation Method. *Surf. Sci.* **2006**, *600* (12), 2523–2527.

(20) Kim, M.; Kim, K.; Kim, S. Y.; Kim, Y.; Won, Y. H. In-Situ Monitoring of Anodic Oxidation of p-Type Si (100) by Electrochemical Impedance

Techniques in Nonaqueous and Aqueous Solutions. *Bull. Korean Chem. Soc.* **1999**, *20* (9), 1049–1055.

(21) Gao, X.; Guan, B.; Mesli, A.; Chen, K.; Dan, Y. Deep Level Transient Spectroscopic Investigation of Phosphorus-Doped Silicon by Self-Assembled Molecular Monolayers. *Nat. Commun.* **2018**, *9* (1), 118.

(22) Longo, R. C.; Cho, K.; Schmidt, W. G.; Chabal, Y. J.; Thissen, P. Monolayer Doping via Phosphonic Acid Grafting on Silicon: Microscopic Insight from Infrared Spectroscopy and Density Functional Theory Calculations. *Adv. Funct. Mater.* **2013**, *23* (27), 3471–3477.

(23) Ichiro, M.; Eiji, K.; Norihisa, A.; Masahisa, S.; Masahiko, Y.; Shin-ichi, T.; Mikio, W.; Shigeru, K.; Yuichi, M.; Sei-ichi, M.; Masahiro, K. Diffusion and Segregation of Carbon in SiO2 Films. *Jpn. J. Appl. Phys.* **1997**, *36* (3S), 1465.

(24) Cumpson, P. J.; Zalm, P. C. Thickogram: A Method for Easy Film Thickness Measurement in XPS. *Surf. Interface Anal.* **2000**, *29*, 403–406.

(25) Celler, G. K.; Barr, D. L.; Rosamilia, J. M. Etching of Silicon by the RCA Standard Clean 1. *Electrochem. Solid-State Lett.* **2000**, *3* (1), 47–49.

(26) Gouzman, I.; Dubey, M.; Carolus, M. D.; Schwartz, J.; Bernasek, S. L. Monolayer vs. Multilayer Self-Assembled Alkylphosphonate Films: X-Ray Photoelectron Spectroscopy Studies. *Surf. Sci.* **2006**, *600* (4), 773–781.

(27) Yerushalmi, R.; Ho, J. C.; Fan, Z.; Javey, A. Phosphine Oxide Monolayers on SiO2 Surfaces. *Angew. Chem. Int. Ed. Engl.* **2008**, *47* (23), 4440–4442.

(28) Branch, B.; Dubey, M.; Anderson, A. S.; Artyushkova, K.; Baldwin, J. K.; Petsev, D.; Dattelbaum, A. M. Investigating Phosphonate Monolayer Stability

on ALD Oxide Surfaces. *Appl. Surf. Sci.* **2014**, *288*, 98–108.

(29) Dubey, M.; Weidner, T.; Gamble, L. J.; Castner, D. G. Structure and Order of Phosphonic Acid-Based Self-Assembled Monolayers on Si(100). *Langmuir* **2010**, *26* (18), 14747–14754.

(30) Hanson, E. L.; Schwartz, J.; Nickel, B.; Koch, N.; Danisman, M. F. Bonding Self-Assembled, Compact Organophosphonate Monolayers to the Native Oxide Surface of Silicon. *J. Am. Chem. Soc.* **2003**, *125* (51), 16074–16080.

(31) Paniagua, S. a; Hotchkiss, P. J.; Jones, S. C.; Marder, S. R.; Mudalige, A.; Marrikar, F. S.; Pemberton, J. E.; Armstrong, N. R. Phosphonic Acid Modification of ITO Electrodes - Combined XPS - UPS - Contact Angle Studies. *J. Phys. Chem. C* **2008**, *112* (21), 7809–7817.

(32) Thissen, P.; Vega, A.; Peixoto, T.; Chabal, Y. J. Controlled, Low-Coverage Metal Oxide Activation of Silicon for Organic Functionalization: Unraveling the Phosphonate Bond. *Langmuir* **2012**, *28* (50), 17494–17505.

(33) Hector, L. G.; Opalka, S. M.; Nitowski, G. A.; Wieserman, L.; Siegel, D. J.; Yu, H.; Adams, J. B. Investigation of Vinyl Phosphonic Acid/Hydroxylated - Al2O3(0001) Reaction Enthalpies. *Surf. Sci.* **2001**, *494* (1), 1–20.

(34) Cole, D. A.; Shallenberger, J. R.; Novak, S. W.; Moore, R. L.; Edgell, M. J.; Smith, S. P.; Hitzman, C. J.; Kirchhoff, J. F.; Principe, E.; Nieveen, W.; Huang, F. K.; Biswas, S.; Bleiler, R. J.; Jones, K. SiO2 Thickness Determination by X-Ray Photoelectron Spectroscopy, Auger Electron Spectroscopy, Secondary Ion Mass Spectrometry, Rutherford Backscattering, Transmission Electron Microscopy, and Ellipsometry. *J. Vac. Sci. Technol.* **2000**, *18* (1), 440.

(35) Philipsen, H. G. G.; Kelly, J. J. Anisotropy in the Anodic Oxidation of Silicon in KOH Solution. *J. Phys. Chem. B* **2005**, *109* (36), 17245–17253.

(36) Shimizu, Y.; Takamizawa, H.; Inoue, K.; Yano, F.; Nagai, Y.; Lamagna, L.; Mazzeo, G.; Perego, M.; Prati, E. Behavior of Phosphorous and Contaminants from Molecular Doping Combined with a Conventional Spike Annealing Method. *Nanoscale* **2014**, *6* (2), 706–710.

(37) Longo, R. C.; Cho, K.; Hohmann, S.; Thissen, P. Mechanism of Phosphorus Transport Through Silicon Oxide During Phosphonic Acid Monolayer Doping. *J. Phys. Chem. C* **2018**, *122* (18), 10088–10095.

Chapter 3

Evaluation of the Surface Chemistry of Black Phosphorus during Ambient Degradation

This chapter has been published in Langmuir and therefore sections may contain repeating concepts and paragraphs.

Van Druenen, M.; Davitt, F.; Collins, T.; Glynn, C.; O'Dwyer, C.; Holmes, J. D.; Collins, G. Evaluating the Surface Chemistry of Black Phosphorus during Ambient Degradatioń. *Langmuir* 2019, *35* (6), 2172–2178.

3. Evaluation of the Surface Chemistry of Black Phosphorus during Ambient Degradation

3.1 Abstract

BP shows promise in a range of applications, including electrical and energy storage devices, due to its high carrier mobility and tunable bandgap. However, a major challenge is its ambient instability which results in degradation within hours of ambient exposure. Several methods have been used to circumvent its degradation including functionalisation, capping layers or other protective coatings; however, the surface chemistry through which BP degrades remains to be elucidated. Literature reports have been contradictory with respect to the degradation products and the factors that influence degradation. Here, complementary X-ray photoelectron spectroscopy (XPS) and attenuated total reflectance Fourier transform infrared (ATR-FTIR) spectroscopy are used to monitor the stages of degradation and give an insight into the BP surface chemistry. The degradation was observed to occur through the formation of non-bridging oxide species (P=O) that convert to bridged oxygen (P-O-P) species, which is in correlation with theoretical studies. Bridged oxygen species are highly unstable and react with ambient water to form liquid oxidation products such as phosphoric acid which were characterised using ATR-FTIR and scanning transmission electron microscopy (STEM) analysis. The higher instability of few-layer BP compared to bulk BP can be explained due to the absence of the formation of P-O-P species for bulk BP, as characterised by XPS analysis. The characterisation of the degradation chemistry of BP will facilitate the discovery of targeted protection methods.

3.2 Introduction

One of the key challenges of processing BP is its ambient instability which results in rapid degradation. Degradation occurs within days for solvent exfoliated[1] and hours for mechanically exfoliated[2,1,3] BP. Initial degradation studies used microscopic techniques to qualitatively evaluate oxidation by monitoring bubble formation.[3,4] The formation of droplets on the surface was proposed to occur as a result of water adsorption on the hydrophilic BP surface.[4] However, theoretical studies reported a hydrophobic BP surface which became increasingly hydrophilic as a result of oxidation.[5] Additionally, physisorption of water was found to be more favourable than chemisorption on the pristine BP surface.[5] Experimental studies confirmed these findings by monitoring deaerated solutions of BP which remained stable while oxygenated solutions displayed an increased degradation rate.[6,7] Contact angle studies also showed a hydrophobic surface that became progressively hydrophilic after ambient exposure.[6] The reaction of various oxidants with BP displayed different oxidation products and therefore occurred through different oxidation mechanisms. Oxygen was found to form a uniform layer at the basal plane[8] and attachment was proposed to occur through a dangling or bridging species.[9] Water was suggested to be more reactive towards edge sites, defect sites[8] and the oxide layer present from initial oxidation by oxygen. The higher amount of degradation for BP exposed to both O_2 and H_2O was explained by the catalytic effect of the oxide present which promoted further oxidation by water.[8]

While many reports have observed the formation of liquid droplets on the BP surface using atomic force microscopy (AFM) and transmission electron microscopy (TEM) analysis when exposed to ambient conditions,[3,10] quantification of the oxide formation

and subsequent degradation can be difficult using these techniques. The droplets that appear as a result of degradation have been identified as phosphoric acid[11,12] which is consistent with the decrease in pH observed during oxidation of BP in solution.[13] Recently, Abellán *et. al.*[14] developed a reliable method to characterise oxidation using AFM and Scanning Raman Microscopy by showing how thickness and crystal orientation affect the A^1_g/A^2_g ratio, which is used to monitor the degree of oxidation.[14] However, assignment of the degradation products is often conflicting due to the lack of chemical identification and therefore liquid formation has been ascribed to adsorbed water[3,4] or various phosphorus oxides (P_xO_y).[10,15] XPS analysis is a surface sensitive technique that can provide a more accurate description of BP surface degradation products.[8,12,16,17] The oxide shoulder of the P 2p core level can consist of several phosphorus oxides occurring in the 132-136 eV binding energy (BE) range.[8] Theoretical studies have predicted various oxide structures that form on the BP surface which can be observed using XPS analysis.[16]

Initially, oxidation was often evaluated using microscopic techniques such as AFM or TEM. Yang e*t. al.*[16] and Kuntz *et. al.*[8] have reported on the different phosphorus oxide structures that form during BP oxidation both theoretically using DFT studies and experimentally using XPS analysis, a more surface sensitive technique. Here, we used complementary XPS and ATR-FTIR to monitor the degradation product formed during ambient degradation. Additionally, the use of the O 1s core level can also supplement the P 2p core level when assigning degradation products by identification of the P-O-P component.[12] XPS analysis has displayed a reduction in flake thickness after analysis[17] and volatile degradation products are not observed due to the high vacuum environment of the instrument.[8] By employing ATR-FTIR in addition to XPS

analysis, we have demonstrated the production of phosphoric acid which is not observed during the initial stages of oxidation using XPS analysis, but can be seen clearly using STEM and AFM analysis. The evaporation of volatile oxides was also confirmed using ATR-FTIR analysis. Initial oxide formation was a result of O_2 chemisorption while further oxidation was a result of interaction of water with the oxidised BP surface, as displayed in **Figure 3.1**.

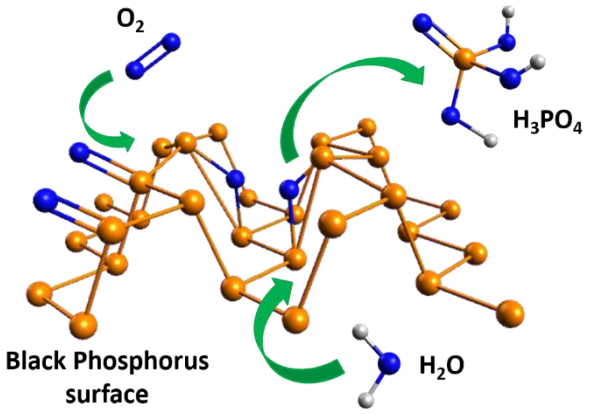

Figure 3.1: Interaction of BP with ambient oxidants (*e.g.* oxygen and water) to form phosphoric acid.

The formation of P-O-P species have been proposed to produce a native oxide on the BP surface which creates a protective layer against degradation.[18,19] However, these theoretical predictions have only been achieved using bulk BP crystals.[17] The formation of bridging oxide species formed after oxygen insertion into the lattice resulted in significant deformation causing instability in the BP lattice.[9] Plutnar *et. al.*[20] revealed a likely mechanism for degradation occurred through the formation of P-O-P species which undergo solvolysis in aqueous solutions. Additionally, Wu *et. al.*[21] proposed the conversion of P-O-P linkages to phosphorous oxyacid degradation products using Raman analysis. Here, the instability of P-O-P species is confirmed which is in correlation with theoretical[9] and experimental studies.[20,21] P-O-P species

are susceptible to hydrolysis[22] and therefore act as a starting point for further oxidation. The conversion of bridging oxide species to phosphoric acids is also shown using ATR-FTIR analysis which results in a continuous oxidation process. The comparison of the degradation patterns of few-layer and multilayer BP are compared, revealing the higher reactivity of few-layer BP that originates from the formation of P-O-P species. The elucidation of the degradation chemistry of BP can facilitate the discovery of new stabilisation strategies.

3.3 Experimental Section

3.3.1 Black Phosphorus Exfoliation

BP was purchased from Smart Elements (purity 99.998 %) and anhydrous N-metyl-2-pyrrolidone (NMP) and acetonitrile (ACN) were purchased from Sigma-Aldrich. BP was stored in a glovebox prior to use. Exfoliation of BP in degassed and Ar saturated NMP using a bath sonicator (Branson 1800) for 20 h with cooling (< 25 ºC) was carried out under inert conditions using a Schlenk line. The exfoliated solution was left to settle overnight. An exfoliated BP sample was obtained by centrifuging at 2000 rpm for 30 min and discarding the sediment, followed by centrifugation at 14500 rpm for 1 h. The discarded sediment was used as a multilayer sample. The exfoliated sample was purified using 3 × ACN washes and was subsequently dropcast on Ti substrates or Si wafers for XPS analysis. Samples were exposed to light during degradation, humidity varied from 68-99 % and temperature was kept constant at 19 °C.

3.3.2 Characterisation

X-Ray photoelectron spectroscopy (XPS) analysis was carried out on an Oxford Applied Research Escabase XPS system with a base pressure of 5 x 10^{-10} mbar and a

nonmonochromated Al Kα X-Ray source at 200 W. Survey spectra were recorded at 0-1000 eV at a step size of 0.7 eV, a dwell time of 0.3 s and a pass energy of 100 eV. Core levels scans were acquired at a step size of 0.1 eV, a dwell time of 0.1 s and a pass energy of 20 eV. CasaXPS software was used for spectra processing with peaks corrected to a Shirley background and fitted to Voigt profiles. Charge correction was applied to the C 1s peak at 285 eV. Attenuated total reflectance Fourier transform infrared (ATR-FTIR) spectra were acquired using a Nicolet 6700 Infrared Spectrometer, with a liquid cooled HgCdTe detector and Smart iTR accessory. Spectra were collected under ambient conditions at a resolution of 2 cm^{-1} and averaged over 300 scans. Raman scattering spectra were collected using a QE65PRO OceanOptics spectrometer with a 50 μm width slit and a microscope with a 40 × objective to focus on the surface of substrates. A Laser Quantum GEM DPSS 532 nm laser was used for excitation. AFM analysis was performed on a Park XE-100 AFM system in non-contact mode with SSS-NCHR enhanced resolution tips, the XY and Z resolution are ~ 2 nm and 0.05 nm. Scanning transmission electron microscopy (STEM) analysis was acquired on an FEI Helios NanoLab 600i scanning electron microscope operating at 20 kV. Transmission electron microscopy (TEM) analysis was acquired on a Jeol 2100 at an operating accelerating voltage of 200 kV.

3.4 Results and Discussion

3.4.1 Liquid Exfoliation of Black Phosphorus

Liquid phase exfoliation has been used for the production of many 2D materials, including graphene, due to its scalability.[23,24] BP has been exfoliated in CHP,[1] NMP,[25] aqueous solutions[7,26] and ionic liquids.[27,28] Here, NMP was used for the production of few-layer BP flakes, as exfoliation in NMP results in a high-yield. **Figure 3.2** displays STEM and TEM analysis of few-layer flakes where the layers can be clearly seen. The flake morphology remains defined after exfoliation, suggesting no damage is induced during the exfoliation process.

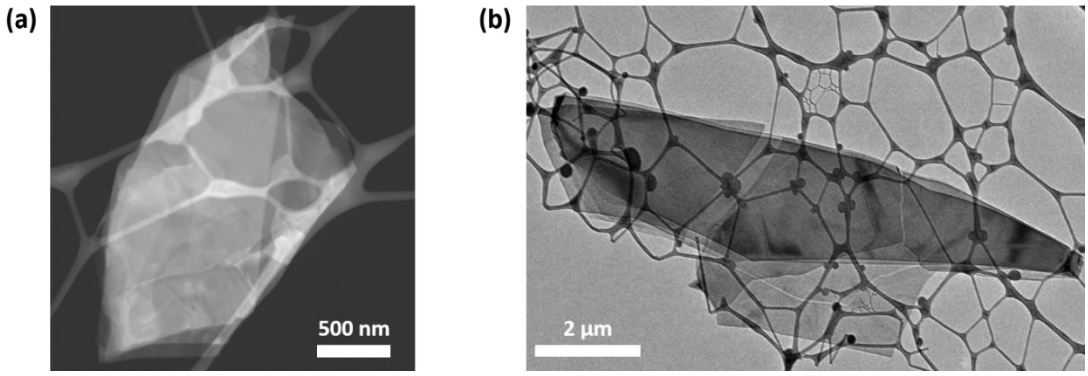

Figure 3.2: (a) STEM and (b) TEM analysis of liquid exfoliated BP flakes.

AFM analysis in **Figure 3.3** shows the formation of few-layer flakes with line profiles showing a height of ~1 nm and ~ 2nm. As the height of a monolayer is estimated to be ~1 nm,[1,29] the exfoliation and centrifugation steps resulted in the formation of mono- and bilayer flakes. **Figure 3.3**(c) displays the range of flake heights obtained from a liquid exfoliated sample after centrifuging steps were used to remove unexfoliated material. The distribution of flake heights confirms ~80 % of flakes are less than 10 nm in height, indicating the formation of a large proportion of few-layer flakes.

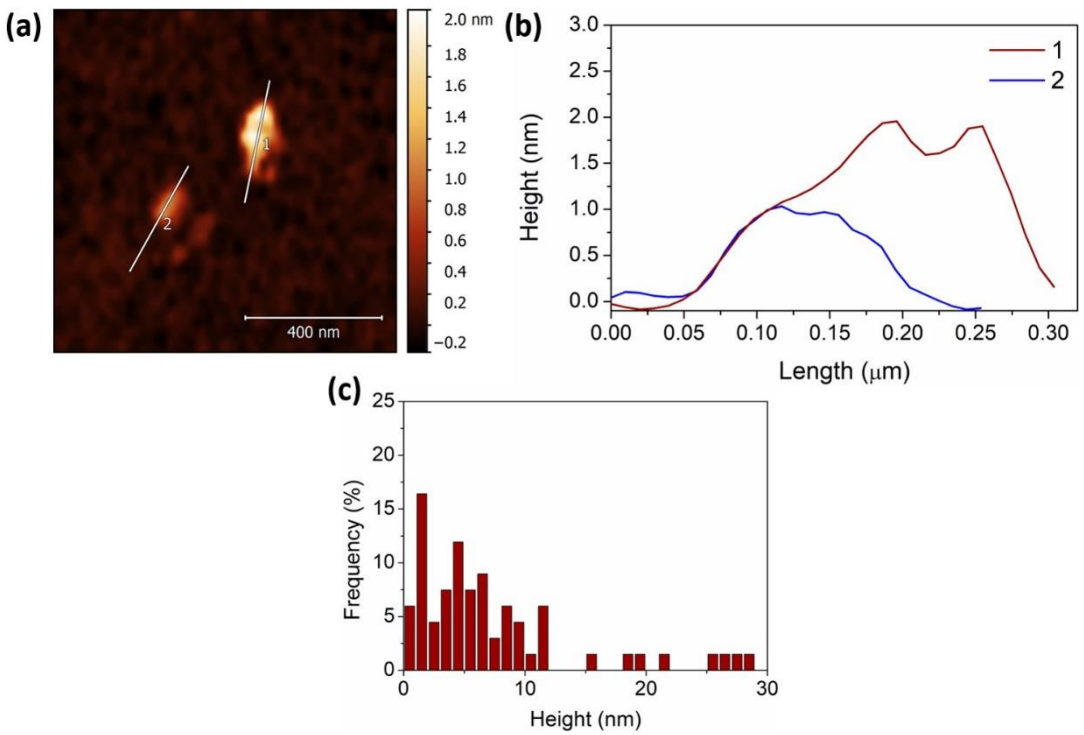

Figure 3.3: (a) AFM analysis of few-layer liquid exfoliated BP with (b) line profiles displaying a height of ~1 and ~2 nm. (c) The histogram shows the distribution of the heights of flakes in a liquid exfoliated sample.

Figure 3.4 shows the TEM analysis of liquid exfoliated few-layer BP flakes. TEM analysis shows d-spacings of 0.33 and 0.44 nm corresponding to the (010) and (100) planes,[30] indicating BP maintains its crystallinity during the exfoliation process.

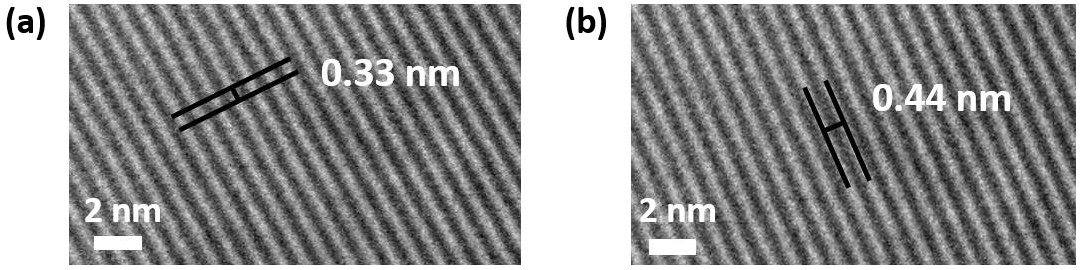

Figure 3.4: TEM analysis shows d-spacinga of (a) 0.33 nm and (b) 0.44 nm.

Raman analysis in **Figure 3.5**(a) shows the A^1_g, A^2_g and B^2_g modes at 367, 444 and 472 cm^{-1} also confirming no damage is induced during the exfoliation process. The

peak at 520 cm^{-1} can be attributed to the Si substrate. **Figure 3.5**(b) displays photoluminescence (PL) analysis of exfoliated BP with two peaks at 600 and 900 nm corresponding to mono- and bilayer BP.[1] The appearance of PL peaks associated with few-layer BP and AFM analysis confirm successful exfoliation of BP into few-layer flakes.

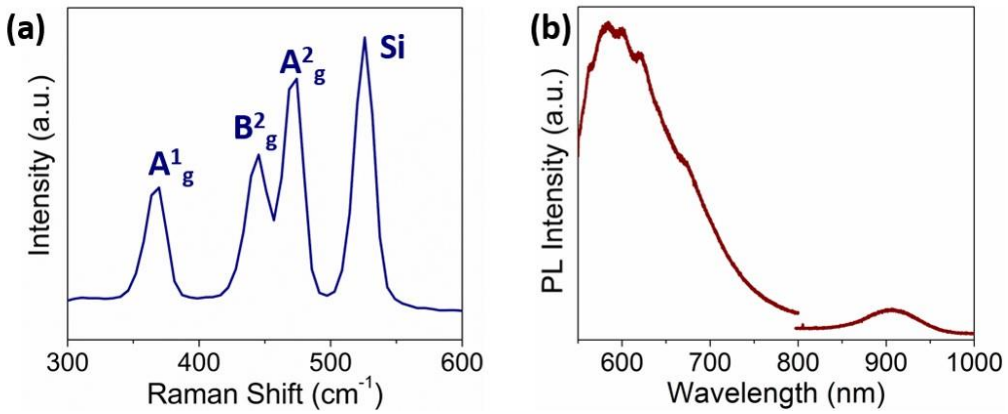

Figure 3.5: (a) Raman and (b) PL analysis of liquid exfoliated BP.

3.4.2 Characterisation of Black Phosphorus Degradation

The ATR-FTIR spectra and the P 2p and O 1s core levels were monitored during ambient degradation to characterise degradation products. **Figure 3.6**(a) displays the P 2p core level for exfoliated BP, with the main P 2p doublet at 129.5 and 130.4 eV and an oxide shoulder located at 133.2 eV. The oxide shoulder amounts to 20 % of the P 2p peak, consistent with literature reports of liquid exfoliated BP.[1] The oxide content of liquid exfoliated BP can be reduced further by purging the exfoliation solvents with Ar following freeze-pump-thaw degassing. The reduction in the oxide shoulder to 13 % after purging with Ar suggests dissolved gases cause BP oxidation during exfoliation. The broad oxide peak consists of a range of oxide structures in the 131-136 eV range which cannot be deconvoluted. **Figures 3.6**(b)-(d) show the P 2p core level during degradation in ambient conditions over a period of 2 weeks. A slight increase of 3 % is observed after 40 h of ambient exposure along with a downward

shift of 0.2 eV, indicating an increase in phosphorus oxides with a lower oxidation state. Another increase of 3 % is seen after 1 week of ambient exposure with an upshift to 133.7 eV. The P 2p core level showed a total increase to 37 % after 2 weeks, shifting from 133.7 eV to 134.3 eV.

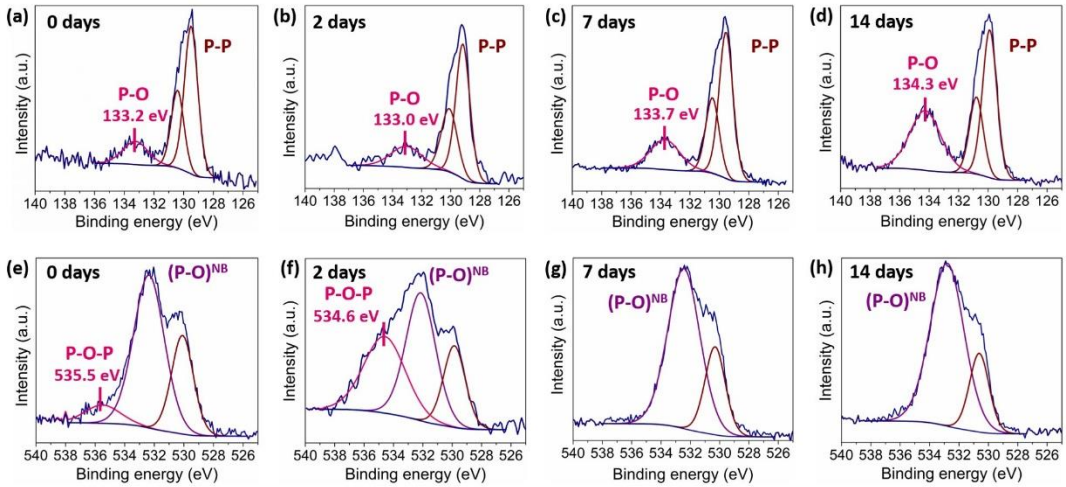

Figure 3.6: P 2p core levels during (a) 0 days, (b) 2 days, (c) 7 days and (d) 14 days of ambient exposure. O 1s core levels during (e) 0 days, (f) 2 days, (g) 7 days and (h) 14 days of ambient exposure.

The O 1s peak can be deconvoluted into 3 components which reveal additional changes in the presence of different phosphorus oxide species. **Figure 3.6**(e) displays the O 1s spectrum with a peak at 530 eV which can be assigned to $P^{<5+}$ species[12] and TiO_2 due to the titanium used as a substrate for XPS analysis. The peak at ~532 eV corresponds to nonbridging P-O environments ($(P\text{-}O)^{NB}$) including P-O-H and P=O groups.[12] The component at ~535 eV can be attributed to bridging oxide species (P-O-P).[12] The O 1s spectrum of freshly exfoliated BP can be observed in **Figure 3.6**(e), which displays 9 % bridging and 63 % nonbridging oxide species compared to the total O 1s core level. After 2 days of ambient exposure, the intensity of the bridging oxide component increases to 36 % at the expense of the nonbridging which decreases to 42 %, as displayed in **Figure 3.6**(f). The changes in the O 1s spectra indicate the

conversion of nonbridging to bridging oxide species which is in correlation which the peak shift of the P 2p core level. The shift of the P 2p core level would correspond to the conversion of nonbridging to bridging oxide species. After 7 days of ambient exposure the P-O-P component disappears, as seen by comparison of **Figures 3.6**(f)-(g). The oxidation of BP has been reported to result in the formation of volatile liquid oxidation products.[8,17] The liquid oxidation products that form during BP oxidation have also been reported to evaporate under the high vacuum environment of the XPS chamber.[16,17] After 2 weeks of ambient exposure, the peak intensity of the nonbridging oxide species increases, in correlation with the increase of the P 2p oxide shoulder.

The variation of the P 2p and O 1s core levels after 2 days of ambient exposure indicate the initial formation of a surface oxide consisting mostly of non-bridging P-O species, which convert to bridging oxide species after further ambient exposure, as displayed in **Figure 3.7**. Theoretical studies[9] reported the exothermic chemisorption of oxygen both as a dangling and bridging configuration. The bridging oxide configuration, where oxygen replaces a phosphorus atom in the lattice, induces deformation that reduces the stability of the BP lattice.

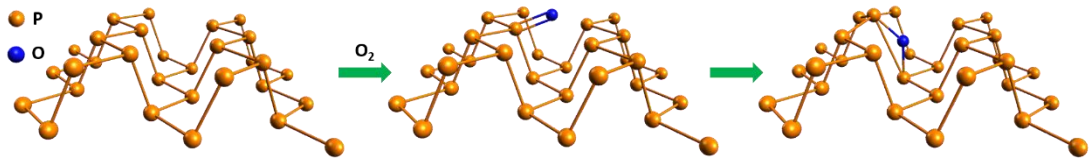

Figure 3.7: BP oxidation is initiated by the formation of P=O species which react further to form P-O-P species which are highly unstable.

The formation of a stable oxide, in the form of phosphorus pentoxide, has been reported on bulk BP surfaces.[17] However, mono- and few-layer BP can display different oxidation mechanisms to bulk BP due to an increase in surface area and a

larger contribution of edge effects. The characteristic BE for phosphorus pentoxide is 135 eV[31] which cannot be readily deconvoluted from the oxide shoulder in BP. Additionally, liquid oxidation products such as phosphoric acid occur at a similar BE of 134.5 eV[17] and are difficult to analyze using XPS analysis due to their volatility under vacuum conditions. ATR-FTIR analysis was used to distinguish between the formation of phosphorus pentoxide and phosphoric acid. The appearance of a peak associated with P-O-P species in the 850-900 cm^{-1} range[32–34] can allow identification of bridging oxide species while the formation of phosphoric acid can be confirmed by the presence of PO_3 absorptions.[34]

Table 3.1: IR frequencies of few-layer BP over a period of 0 days to 1 week.

IR Frequencies of Black Phosphorus Surface Species				
Phosphorus Group	**0 days (cm^{-1})**	**1 day (cm^{-1})**	**3 days (cm^{-1})**	**7 days (cm^{-1})**
O=P-OH	1655	1655	1665	-
P=O	1406	1430	1450	-
P=O	1302	-	-	-
$(PO_2)_s$	-	1196	1194	1197
$(PO_2)_{as}$	1263	1272	1272	1272
$(PO_3)_s$	1115	1165	1163	1165
$(PO_3)_{as}$	985	995	992	-
$(P\text{-}O\text{-}P)_s$	-	850	850	850
$(P\text{-}O\text{-}P)_{as}$	-	770, 700	773, 706	770, 710

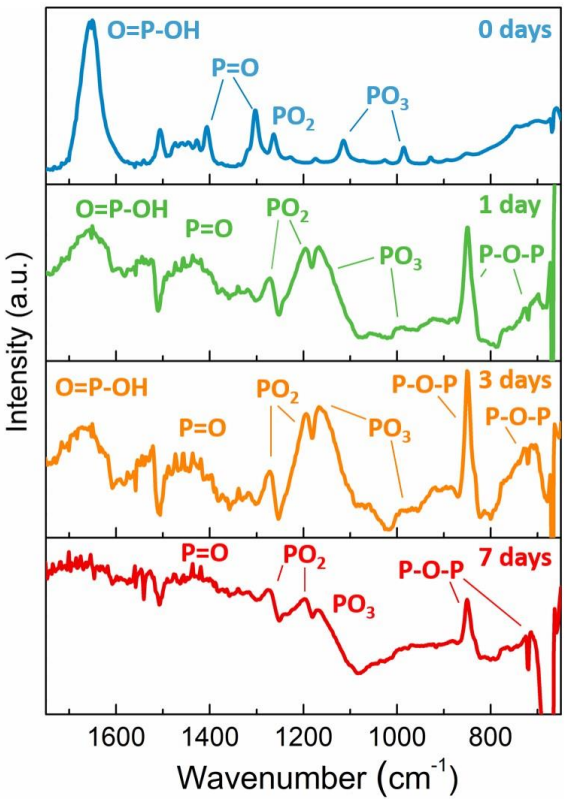

Figure 3.8: ATR-FTIR analysis of BP degradation over a period of 1 week.

Table 3.1 and **Figure 3.8** display the ATR-FTIR analysis of liquid exfoliated few-layer BP over a 1 week period of ambient exposure. ATR-FTIR analysis of freshly exfoliated BP displays a large absorption peak at 1650 cm^{-1} which can be attributed to O=P-OH species,[35] as well as two stretches at 1400 and 1300 cm^{-1} which can be assigned to P=O groups.[35,36] An asymmetric PO_2 stretch was observed at 1260 cm^{-1} while symmetric and asymmetric PO_3 stretches occurred at 1115 and 985 cm^{-1}.[34] The presence of absorptions associated with P=O during the initial exposure period indicates a dissociative reaction of oxygen with the BP surface, in correlation with DFT calculations as reported by Huang *et. al.*[6].

Following 1 day of ambient exposure, the ATR-FTIR spectrum changes considerably with the appearance of new absorptions associated with significant oxidation of BP

after ambient exposure. **Figure 3.8** shows the appearance of symmetric P-O-P vibrations at 850 cm^{-1} and asymmetric P-O-P stretches[34,37] at 710 and 770 cm^{-1}, indicating the formation of bridging oxide species, which is in excellent agreement with the O 1s core level. Additionally, a reduction in the O=P-OH peak intensity at 1650 cm^{-1} further supports conversion of non-bridging P-O species to bridging oxide species. The broadening of the P=O absorption and shift to 1430 cm^{-1} often occur as a result of the incorporation of hydrogen bonding[38] due to physisorption prior to chemical reaction with ambient water. An increase in the intensity of asymmetric PO_2 stretches at 1270 cm^{-1} and appearance of symmetric PO_2 stretches[37] at 1190 cm^{-1} also occur as BP oxidises. Furthermore, the PO_3 stretches shift to 993 cm^{-1} and 1170 cm^{-1} which can be attributed to protonation of P-O species[33,39] to form P-OH groups. Bridging oxide species are highly reactive and readily react under ambient conditions as demonstrated by the reaction of phosphorus pentoxide which forms phosphoric acid after ambient exposure.[8] Protonation of P-O species suggests ambient water interacts with BP surface oxides to produce phosphoric acid. The shift and increase in intensity of PO_3 absorptions to form P-OH groups and a reduction in P=O peak intensity, as shown in **Figure 3.8**, also support the conversion of P=O groups to H_3PO_4 through reaction with water. This experimental observation is also in agreement with DFT studies.[5] Additionally, XPS analysis of the final product of degradation is displayed in **Figure 3.9** with a peak at 134.3 eV corresponding to the BE of phosphoric acid.[17] Initial formation of phosphoric acid cannot be deconvoluted from the oxide shoulder and when present in low concentrations, liquid oxidation products may be removed under the vacuum of the XPS instrument.[8,17] After 3 days of ambient exposure the intensity of the PO_2 and the P-O-P absorption peaks increase as a result of further oxidation of BP. However, after a 1 week period in ambient conditions a large

decrease is observed in all signals associated with phosphorus oxides. The reduction of all P-O peaks and protonated PO_3 absorptions is consistent with evaporation of volatile oxide species such as phosphoric acid from the surface of BP.

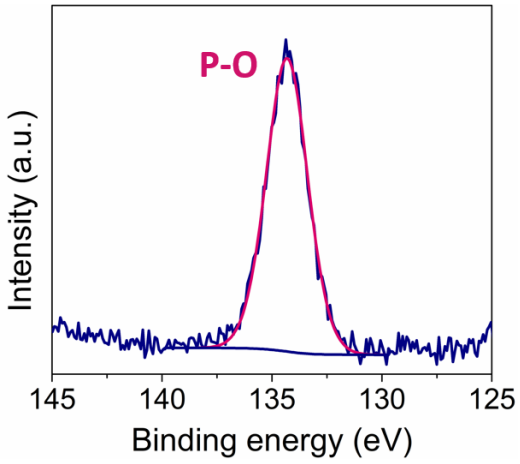

Figure 3.9: XPS analysis of the final product of degradation.

The presence of absorption peaks associated with O=P-OH and P-O species and the absence of P-O-P species both indicate that freshly exfoliated BP is characterised by the presence of primarily non-bridging oxide species, which is in excellent agreement with XPS analysis of the O 1s core level. Therefore, the BP lattice oxidises through the formation of bridging P-O-P species which are highly unstable and susceptible to hydrolysis.[22] The reduction of the P-O-P component observed in both XPS and ATR-FTIR analysis indicate conversion of bridging oxide species to phosphoric acid which suggests an oxidation cycle occurs. This continuous cycle results in the removal of the surface layers from the BP surface.[3,4,8,17] Literature reports vary in their discussion of the effect of water on the degradation of BP, but when combined with oxygen and light, water often facilitates oxidation.[15] Theoretical studies predict a hydrophobic BP surface that interacts more favorably with oxygen rather than water.[5] Therefore, the initial oxidation is most likely a result of the reaction of oxygen with the BP surface.[6]

Theoretical calculations have shown that oxidised few-layer BP reacts exothermically with water,[5] in agreement with our results where surface oxides react to form phosphoric acid through interaction with ambient water, which is also in correlation with studies on mechanically exfoliated few-layer BP by Favron *et. al.*[11] A key difference in our study is the use of liquid exfoliated BP rather than mechanically exfoliated BP which displays a shorter lifetime in ambient conditions. Solvent passivation has been reported to contribute to a higher stability in solution for liquid exfoliated BP in N-cyclohexyl-2-pyrrolidone, where a solvation shell protects flakes from oxidation.[1] The N 1s:P 2p ratios are displayed in **Figure 3.10** and can be used as an indication of the amount of solvent passivating the surface after removal from solution. The N 1s:P 2p ratio for freshly exfoliated BP at 0.38 decreases to 0.18 after 1 week which further decreases to 0.13 after 2 weeks of ambient exposure.

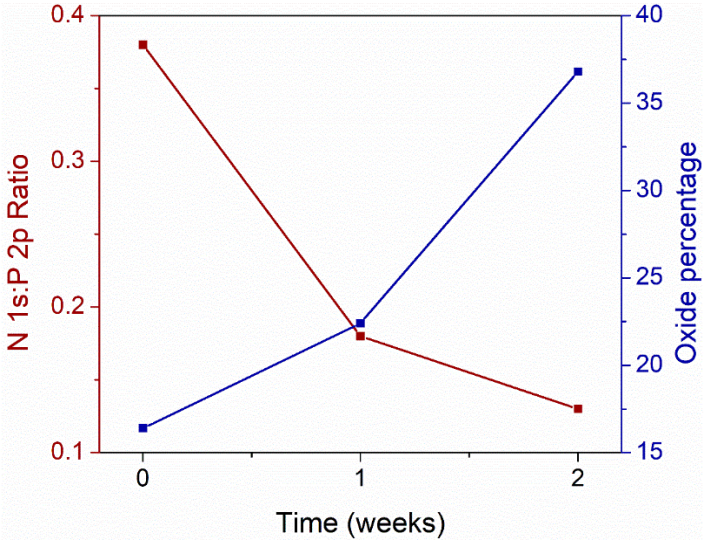

Figure 3.10: N 1s:P 2p ratios and comparison to the percentage of PO_x of the P 2p core level during ambient exposure.

Comparison of the N 1s:P 2p ratio to the percentage of oxide determined from the P 2p core level shows a more significant increase in the oxide component as the solvent

is removed, as displayed in **Figure 3.10**. The increased stability of solvent passivated flakes is in correlation with experimental studies by Abellán *et. al.*[14] where NMP-passivated BP displays a longer lifetime compared to THF-passivated or pristine BP. Therefore, solvent passivation also contributes to the stability of BP when flakes are removed from solution.

The stability of few-layer BP was monitored by STEM, TEM and AFM to give a visual representation of BP degradation. Freshly exfoliated flakes display well-defined edges as shown in **Figure 3.11**(a). After 1 week of ambient exposure, surface protrusions can be seen clearly in **Figure 3.11**(b) and **Figure 3.12**.

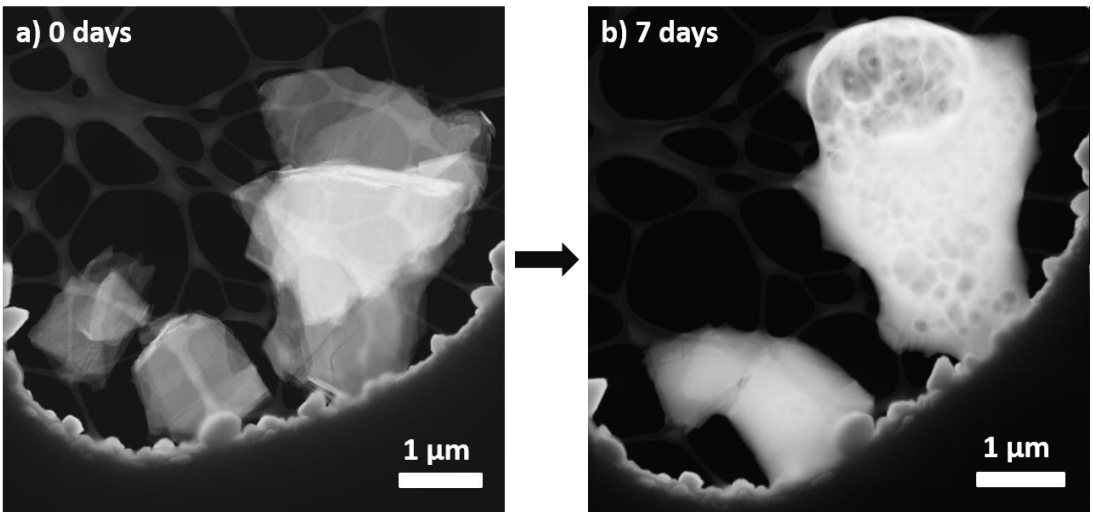

Figure 3.11: STEM analysis of (a) freshly exfoliated BP and (b) after 1 week of ambient exposure.

The formation of liquid oxidation products can be seen more clearly with STEM and TEM analysis in **Figure 3.12**. TEM analysis in **Figure 3.12**(b) also displayed a loss of crystallinity after ambient exposure.

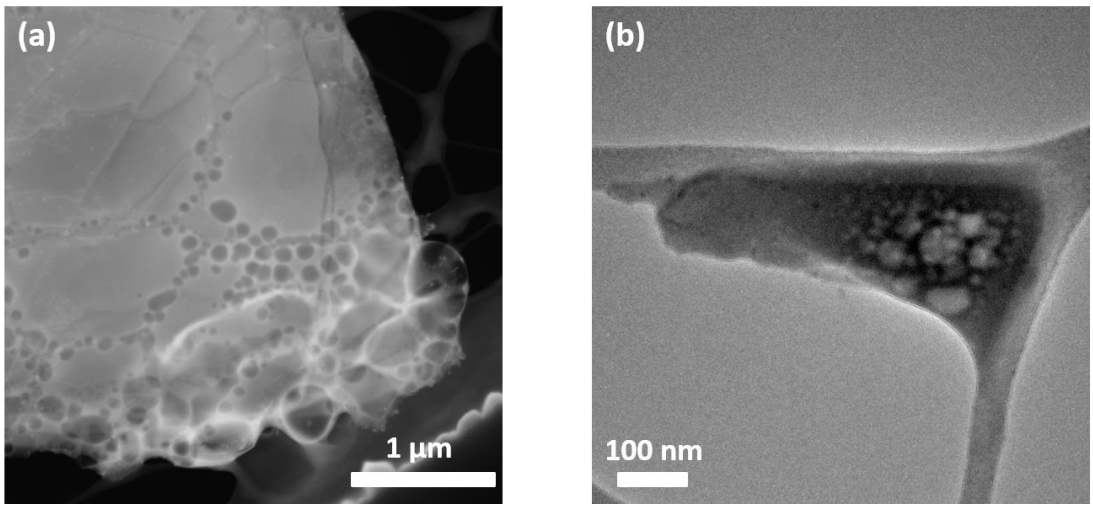

Figure 3.12: (a) STEM and (b) TEM analysis of BP after 1 week of ambient exposure.

AFM analysis in **Figure 3.13**(a)-(b) shows a similar loss of defined edges after 1 week of ambient exposure for few-layer BP flakes. As a comparison, a multilayer sample which is obtained from the sediment of the centrifuge cycle includes thicker flakes that were analysed as well.

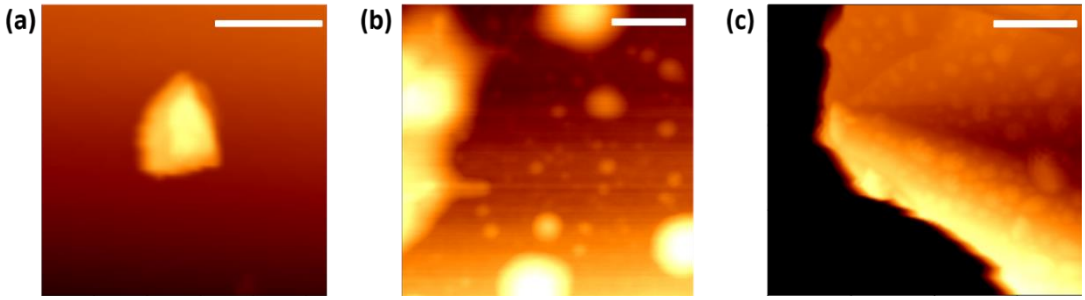

Figure 3.13: AFM analysis of (a) freshly exfoliated BP which was not exposed to ambient conditions. (b) Few-layer BP and (c) bulk BP exposed to ambient conditions for 1 week. The scale bars correspond to 0.5, 0.25 and 1 micron.

The AFM analysis shows the defined edges of the multilayer flake after 1 week of ambient exposure, although surface protrusions similar to those found on few-layer BP are visible. AFM and STEM analysis both corroborate the formation of liquid oxidation products (e.g. phosphoric acid), due to the appearance of liquid droplets on

the surface of few-layer BP flakes. The rapid deterioration contradicts the formation of a stable oxide and demonstrates the different oxidation chemistry of few-layer and multilayer BP.

The different degradation chemistries can also be observed by comparison of the O 1s and P 2p peaks after ambient exposure. **Figure 3.14** displays the P 2p core level of bulk BP during 1 week of ambient exposure showing the oxide component increases from 20.3 % to 40.1 %.

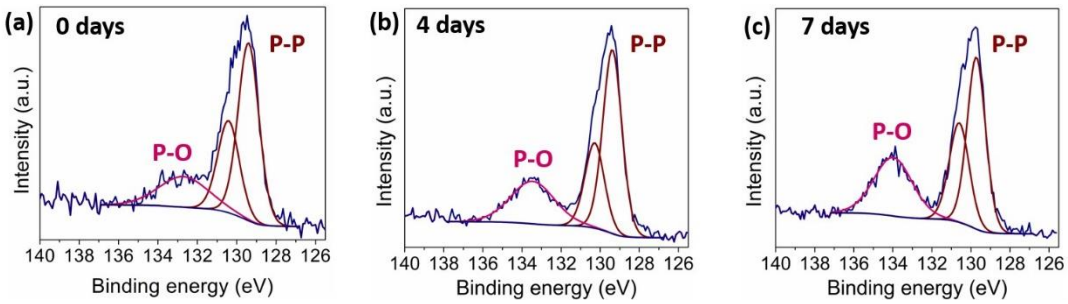

Figure 3.14: P 2p core levels displaying the oxidation of multilayer BP over a period of 1 week.

The O 1s core levels displayed in **Figure 3.15** did not show the formation of a P-O-P component as in the case of few-layer BP, suggesting the formation of a surface oxide but no major oxidation of the BP lattice structure. In comparison, few-layer flakes only displayed an increase of 6 % in the P 2p oxide shoulder, as seen in **Figures 3.6**(a)-(c), and additionally oxidation occurred through the formation of volatile oxidation products which were removed under vacuum conditions. The difference in degradation chemistry of few-layer flakes stems from the formation of P-O-P species which facilitates more significant degradation. The absence of P-O-P formation for multilayer BP allows the preservation of the crystal structure while the formation of a

surface oxide is in correlation with experimental studies by Edmonds *et. al.*[17]. Higher reactivity for decreasing layer thickness was also observed by Favron *et. al.*[11] which was attributed to greater overlap between the band edge as a result of the shift in band gap for lower flake thicknesses. Therefore, few-layer BP shows much more significant oxidation due to the formation of P-O-P species while multilayer BP displays minor oxidation, in correlation with the formation of a surface oxide.

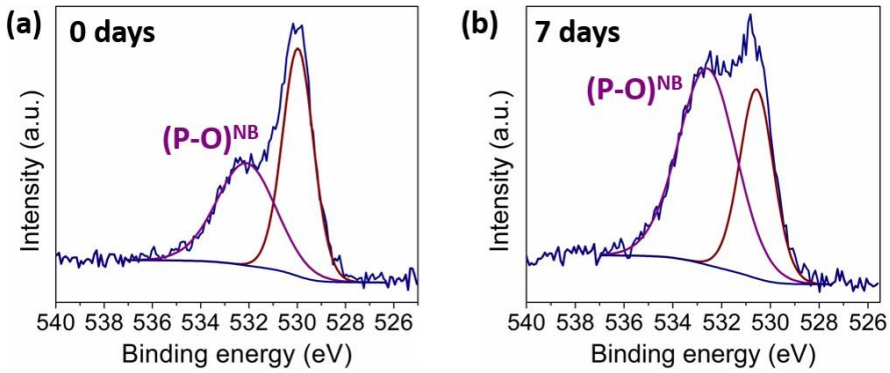

Figure 3.15: O 1s core levels for multilayer BP during (a) 0 days and (b) 7 days of ambient exposure.

3.5 Conclusions

The degradation chemistry of liquid exfoliated few-layer BP exposed to ambient conditions has been investigated using XPS and ATR-FTIR spectroscopy. Oxidation of BP initially occurs through the formation of non-bridging oxide species which convert to bridging oxide species (P-O-P) within 48 h of ambient exposure. The appearance of P-O-P species was monitored through XPS and ATR-FTIR analysis showing further oxidation leads to the conversion of bridging oxide species to phosphoric acid which subsequently evaporates from the BP surface. The differences in degradation behavior between multilayer and few-layer BP are demonstrated, with multilayer BP displaying higher stability due to the absence of bridging oxide species formation during ambient exposure. The successful determination of the degradation chemistry can assist in the discovery of targeted protection methods of BP.

3.6 References

(1) Hanlon, D.; Backes, C.; Doherty, E.; Cucinotta, C. S.; Berner, N. C.; Boland, C.; Lee, K.; Harvey, A.; Lynch, P.; Gholamvand, Z.; Zhang, S.; Wang, K.; Moynihan, G.; Pokle, A.; Ramasse, Q. M.; McEvoy, N.; Blau, W. J.; Wang, J.; Abellan, G.; Hauke, F.; Hirsch, A.; Sanvito, S.; O'Regan, D. D.; Duesberg, G. S.; Nicolosi, V.; Coleman, J. N. Liquid Exfoliation of Solvent-Stabilized Few-Layer Black Phosphorus for Applications beyond Electronics. *Nat. Commun.* **2015**, *6*, 8563.

(2) Koenig, S. P.; Doganov, R. A.; Schmidt, H.; Castro Neto, A. H.; Özyilmaz, B. Electric Field Effect in Ultrathin Black Phosphorus. *Appl. Phys. Lett.* **2014**, *104* (10), 103–106.

(3) Castellanos-Gomez, A.; Vicarelli, L.; Prada, E.; Island, J. O.; Narasimha-Acharya, K. L.; Blanter, S. I.; Groenendijk, D. J.; Buscema, M.; Steele, G. a.; Alvarez, J. V.; Zandbergen, H. W.; Palacios, J. J.; van der Zant, H. S. J. Isolation and Characterization of Few-Layer Black Phosphorus. *2D Mater.* **2014**, *1* (2), 025001.

(4) Island, J. O.; Steele, G. A.; Zant, H. S. J. van der; Castellanos-Gomez, A. Environmental Instability of Few-Layer Black Phosphorus. *2D Mater.* **2015**, *2* (1), 011002.

(5) Wang, G.; Slough, W. J.; Pandey, R.; Karna, S. P. Degradation of Phosphorene in Air: Understanding at Atomic Level. *2D Mater.* **2016**, *3* (2), 025011.

(6) Huang, Y.; Qiao, J.; He, K.; Bliznakov, S.; Sutter, E.; Chen, X.; Luo, D.; Meng, F.; Su, D.; Decker, J.; Ji, W.; Ruoff, R. S.; Sutter, P. Interaction of Black Phosphorus with Oxygen and Water. *Chem. Mater.* **2016**, *28* (22), 8330–8339.

(7) Chen, L.; Zhou, G.; Liu, Z.; Ma, X.; Chen, J.; Zhang, Z.; Ma, X.; Li, F.; Cheng, H. M.; Ren, W. Scalable Clean Exfoliation of High-Quality Few-Layer Black Phosphorus for a Flexible Lithium Ion Battery. *Adv. Mater.* **2016**, *28* (3), 510–517.

(8) Kuntz, K. L.; Wells, R. A.; Hu, J.; Yang, T.; Dong, B.; Guo, H.; Woomer, A. H.; Druffel, D. L.; Alabanza, A.; Tománek, D.; Warren, S. C. Control of Surface and Edge Oxidation on Phosphorene. *ACS Appl. Mater. Interfaces* **2017**, *9* (10), 9126–9135.

(9) Ziletti, A.; Carvalho, A.; Campbell, D. K.; Coker, D. F.; Castro Neto, A. H. Oxygen Defects in Phosphorene. *Phys. Rev. Lett.* **2015**, *114* (4), 26–29.

(10) Wood, J. D.; Wells, S. A.; Jariwala, D.; Chen, K. S.; Cho, E.; Sangwan, V. K.; Liu, X.; Lauhon, L. J.; Marks, T. J.; Hersam, M. C. Effective Passivation of Exfoliated Black Phosphorus Transistors against Ambient Degradation. *Nano Lett.* **2014**, *14* (12), 6964–6970.

(11) Favron, A.; Gaufrès, E.; Fossard, F.; Phaneuf-L'Heureux, A.-L.; Tang, N. Y.-W.; Lévesque, P. L.; Loiseau, A.; Leonelli, R.; Francoeur, S.; Martel, R. Photooxidation and Quantum Confinement Effects in Exfoliated Black Phosphorus. *Nat. Mater.* **2015**, *14* (8), 826–832.

(12) Luo, W.; Zemlyanov, D. Y.; Milligan, C. A.; Du, Y.; Yang, L.; Wu, Y.; Ye, P. D. Surface Chemistry of Black Phosphorus under a Controlled Oxidative Environment. *Nanotechnology* **2016**, *27* (43), 434002.

(13) Woomer, A. H.; Farnsworth, T. W.; Hu, J.; Wells, R. A.; Donley, C. L.; Warren, S. C. Phosphorene: Synthesis, Scale-Up, and Quantitative Optical Spectroscopy. *ACS Nano* **2015**, *9* (9), 8869–8884.

(14) Abellán, G.; Wild, S.; Lloret, V.; Scheuschner, N.; Gillen, R.; Mundloch, U.; Maultzsch, J.; Varela, M.; Hauke, F.; Hirsch, A. Fundamental Insights into the Degradation and Stabilization of Thin Layer Black Phosphorus. *J. Am. Chem. Soc.* **2017**, *139* (30), 10432–10440.

(15) Hu, Z.; Li, Q.; Lei, B.; Zhou, Q.; Xiang, D.; Lyu, Z.; Hu, F.; Wang, J.; Ren, Y.; Guo, R.; Goki, E.; Wang, L.; Han, C.; Wang, J.; Chen, W. Water-Catalyzed Oxidation of Few-Layer Black Phosphorous in a Dark Environment. *Angew. Chemie - Int. Ed.* **2017**, *129* (31), 9259–9263.

(16) Yang, T.; Dong, B.; Wang, J.; Zhang, Z.; Guan, J.; Kuntz, K.; Warren, S. C.; Tománek, D. Interpreting Core-Level Spectra of Oxidizing Phosphorene: Theory and Experiment. *Phys. Rev. B - Condens. Matter Mater. Phys.* **2015**, *92* (12), 125412.

(17) Edmonds, M. T.; Tadich, A.; Carvalho, A.; Ziletti, A.; O'Donnell, K. M.; Koenig, S. P.; Coker, D. F.; Ozyilmaz, B.; Neto, A. H. C.; Fuhrer, M. S. Creating a Stable Oxide at the Surface of Black Phosphorus. *ACS Appl. Mater. Interfaces* **2015**, *7* (27), 14557–14562.

(18) Zhou, Q.; Chen, Q.; Tong, Y.; Wang, J. Light-Induced Ambient Degradation of Few-Layer Black Phosphorus: Mechanism and Protection. *Angew. Chemie Int. Ed.* **2016**, *55* (38), 11437–11441.

(19) Ziletti, A.; Carvalho, A.; Trevisanutto, P. E.; Campbell, D. K.; Coker, D. F.; Neto, A. H. C. Phosphorene Oxides : Bandgap Engineering of Phosphorene by Oxidation. *Phys. Rev. B* **2015**, *91* (8), 085407.

(20) Plutnar, J.; Sofer, Z.; Pumera, M. Products of Degradation of Black Phosphorus. *ACS Nano* **2018**, *12* (8), 8390–8396.

(21) Wu, S.; He, F.; Xie, G.; Bian, Z.; Luo, J.; Wen, S. Black Phosphorus: Degradation Favors Lubrication. *Nano Lett.* **2018**, *18* (9), 5618–5627.

(22) Ewig, C. S.; Van Wazer, J. R. Ab Initio Structures of Phosphorus Acids and Esters. 3. The P-O-P Bridged Compounds H4P2O2n-1 for n = 1 to 4. *J. Am. Chem. Soc.* **1988**, *110* (1), 79–86.

(23) Hernandez, Y.; Nicolosi, V.; Lotya, M.; Blighe, F. M.; Sun, Z.; De, S.; McGovern, I. T.; Holland, B.; Byrne, M.; Gun'Ko, Y. K.; Boland, J. J.; Niraj, P.; Duesberg, G.; Krishnamurthy, S.; Goodhue, R.; Hutchison, J.; Scardaci, V.; Ferrari, A. C.; Coleman, J. N. High-Yield Production of Graphene by Liquid-Phase Exfoliation of Graphite. *Nat. Nanotechnol.* **2008**, *3* (9), 563–568.

(24) Ciesielski, A.; Samorı, P. Graphene via Sonication Assisted Liquid-Phase Exfoliation. *Chem. Soc. Rev.* **2014**, *43* (1), 381–398.

(25) Brent, J. R.; Savjani, N.; Lewis, E. A.; Haigh, S. J.; Lewis, D. J.; O'Brien, P. Production of Few-Layer Phosphorene by Liquid Exfoliation of Black Phosphorus. *Chem Commun* **2014**, *50* (87), 13338–13341.

(26) Kang, J.; Wells, S. A.; Wood, J. D.; Lee, J.-H.; Liu, X.; Ryder, C. R.; Zhu, J.; Guest, J. R.; Husko, C. A.; Hersam, M. C. Stable Aqueous Dispersions of Optically and Electronically Active Phosphorene. *Proceeding Natl. Acad. Sci.* **2016**, *113* (42), 11688–11693.

(27) Zhao, W.; Xue, Z.; Wang, J.; Jiang, J.; Zhao, X.; Mu, T. Large-Scale, Highly Efficient, and Green Liquid-Exfoliation of Black Phosphorus in Ionic Liquids. *ACS Appl. Mater. Interfaces* **2015**, *7* (50), 27608–27612.

(28) Ng, A.; Sutto, T. E.; Matis, B. R.; Deng, Y.; Ye, P. D.; Stroud, R. M.;

Brintlinger, T. H.; Bassim, N. D. Chemically Exfoliating Large Sheets of Phosphorene via Choline Chloride Urea Viscosity-Tuning. *Nanotechnology* **2017**, *28* (15), 155601.

(29) Liu, H., Neal, A. T., Zhu, Z., Luo, Z., Xu, X., Tománek, D., & Peide, D. Y. Phosphorene : An Unexplored 2D Semiconductor with a High Hole Mobility. *ACS Nano* **2014**, *8* (4), 4033–4041.

(30) Liu, H.; Du, Y.; Deng, Y.; Ye, P. D. Semiconducting Black Phosphorus: Synthesis, Transport Properties and Electronic Applications. *Chem. Soc. Rev.* **2732**, *44* (44), 2732–2743.

(31) Wang, Y.; Sherwood, P. M. A. Phosphorus Pentoxide (P2O5) by XPS. *Surf. Sci. Spectra* **2002**, *9* (1), 159.

(32) Colthup, N. *Introduction to Infrared and Raman Spectroscopy*; Elsevier, 2012.

(33) Gong, W. A Real Time in Situ ATR-FTIR Spectroscopic Study of Linear Phosphate Adsorption on Titania Surfaces. *Int. J. Miner. Process.* **2001**, *63* (3), 147–165.

(34) Omrani, R. O.; Krimi, S.; Videau, J. J.; Khattech, I.; El Jazouli, A.; Jemal, M. Structural and Thermochemical Study of Na2O–ZnO–P2O5 Glasses. *J. Non. Cryst. Solids* **2014**, *390*, 5–12.

(35) Nogami, M. Proton Conductivity in Sol–Gel-Derived P2O5–TiO2–SiO2 Glasses. *Solid State Ionics* **2004**, *166* (1–2), 39–43.

(36) Ahsan, M. R.; Uddin, M. A.; Mortuza, M. G. Infrared Study of the Effect of P 2 O 5 in the Structure of Lead Silicate Glasses. *Indian J. Pure Appl. Phys.* **2005**, *43*, 89–99.

(37) Chahine, A.; Et-tabirou, M. Structural Study of (50-x)Na2O-CuO-10Bi2O3-40P2O5 Glasses. **2002**, *37*, 1973–1979.

(38) Paniagua, S. a; Hotchkiss, P. J.; Jones, S. C.; Marder, S. R.; Mudalige, A.; Marrikar, F. S.; Pemberton, J. E.; Armstrong, N. R. Phosphonic Acid Modification of ITO Electrodes - Combined XPS - UPS - Contact Angle Studies. *J. Phys. Chem. C* **2008**, *112* (21), 7809–7817.

(39) Robinson, E. a. Characteristic Vibrational Frequencies of Oxygen Compounds of Silicon, Phosphorus, and Chlorine: Correlation of Stretching Frequencies and Force Constants With Bond Lengths and Bond Orders. *Can. J. Chem.* **1963**, *41* (12), 3021–3033.

Chapter 4

Covalent Functionalisation of Few-Layer Black Phosphorus using Aryl Iodonium Salts and Comparison to Diazonium Modified Black Phosphorus

This chapter has been published in Chemistry of Materials and therefore sections may contain repeating concepts and paragraphs.

Van Druenen, M.; Davitt, F.; Collins, T.; Glynn, C.; O'Dwyer, C.; Holmes, J. D.; Collins, G. Covalent Functionalization of Few-Layer Black Phosphorus Using Iodonium Salts and Comparison to Diazonium Modified Black Phosphorus. *Chem. Mater*. 2018, *30* (14), 4667–4674

4. Covalent Functionalisation of Few-Layer Black Phosphorus using Aryl Iodonium Salts and Comparison to Diazonium Modified Black Phosphorus

4.1 Abstract

The ambient instability of BP is a key roadblock that hinders its use in various applications. Functionalisation using diazonium salts has been reported to enhance the ambient instability of BP, although its surface chemistry and stability has not been characterised using surface sensitive techniques. Here, we demonstrate that diazonium functionalisation leads to oxidation of liquid exfoliated BP. Furthermore, reactive diazonium radicals can react with surface bound molecules resulting in the formation of uncontrolled multilayers. The presence of noncovalent solvent passivation was observed on diazonium functionalised BP surfaces indicating functionalisation does not disrupt the solvent passivation layer. Iodonium salts were used as an alternative strategy to functionalise BP without inducing oxidation during the functionalisation reaction. Additionally, iodonium salts prevent the formation of unstable P-O-P species through attachment to surface oxygen sites, significantly enhancing the oxidation resistance of BP in ambient conditions, as characterised using X-ray photoelectron spectroscopy (XPS) and scanning transmission electron microscopy (STEM) analysis. Iodonium functionalisation allows the attachment of various alkyl and aryl groups, potentially allowing the tuning of electronic properties of BP. Comparison of the stability of iodonium and diazonium functionalised BP using XPS and STEM shows the increased stability of iodonium functionalised BP due to the attachment to surface oxygen sites.

4.2 Introduction

The ambient instability of BP remains a challenge to its implementation in various applications such as electrical,[1,2] sensing[3] and energy storage devices.[4,5] Functionalisation has been a leading strategy in enhancing its oxidation resistance. Diazonium functionalisation was used by Ryder *et. al.*[6] for the covalent modification of BP to enhance its oxidation resistance in ambient conditions.[6] A variety of diazonium salts were used to tailor the extent of functionalisation and the electronic properties through the use of various electron-withdrawing substituents. However, this strategy was carried out on mechanically exfoliated BP and the ambient instability was characterised using AFM analysis to monitor bubble formation rather than using a surface sensitive technique such as XPS analysis. We have investigated diazonium functionalisation of liquid exfoliated BP and discovered that reactions often lead to surface oxidation. Additionally, diazonium functionalisation does not adequately disrupt solvent passivation suggesting a low extent of functionalisation, while the high reactivity of diazonium radicals results in uncontrolled multilayer formation.

Abellan *et. al.*[7] reported the noncovalent modification of BP using 7,7,8,8-tetracyano-*p*-quinodimethane as a protection strategy that additionally enhances electron transfer from BP. Zhao *et. al.*[8] used a titanium sulfonate ligand that coordinates to BP enhancing its ambient stability and dispersibility in solution. Sofer *et. al.* [9] carried out functionalisation of liquid exfoliated BP using a range of different precursors, but reported that diazonium reagents, alkyl lithium and Grignard functionalisation can lead to oxidation of the surface. Furthermore, the most successful routes to functionalisation were nucleophilic substitution reactions with alkyl bromides, iodides or (*S*)-bromomethyl ethanethiolate that lead to the formation of P-C and P-O-C bonds.

We have investigated the use of aryl iodonium salts for the ambient protection of BP which also attach through surface O sites forming P-O-C bonds as displayed in **Figure 4.1**.

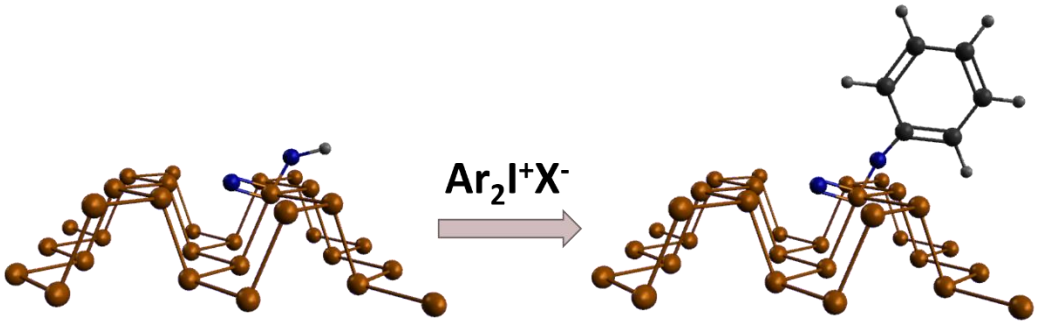

Figure 4.1: Aryl iodonium functionalisation of BP through surface oxygen sites resulting in attachment of aryl groups.

Molecular passivation of black phosphorus using silanes has been reported to functionalise a thin oxide layer present on the BP surface giving superior ambient stability to uncoated BP.[10] Additionally, silane functionalised BP maintained its original electronic properties which could be a result of the functionalisation of surface oxygen sites, rather than the formation of P-C bonds which has been shown to tailor electronic properties of BP by Ryder *et. al.*[6], therefore preserving the fundamental electrical properties of BP. Thiol functionalisation by Kwak *et. al.*[11] has also been reported to occur through surface oxygen sites where a removal of the oxide layer was observed, resulting in the recovery of degraded BP.[11] Oxide functionalisation of BP shows promise as a strategy in the ambient protection against surface oxidation. Iodonium salts have been used for the functionalisation of carbon surfaces such as carbon nanotubes and graphene.[12–14] Functionalisation using iodonium salts does not induce oxidation and aryliodonium salts permit greater control of functionalisation compared to diazonium salts, as observed on carbon surfaces.[14,15] The excellent leaving group ability of the aryl iodide allows reaction at room temperature with the

BP surface.[16] Aryl iodonium salts have been well-studied for functionalisation, including P-arylation.[17] The attachment of aryl groups to oxygen sites inhibits the formation of reactive P-O-P species, which is the main route of BP degradation.[18] The functionalisation through oxygen sites therefore greatly enhances its ambient stability. Additionally, the surface chemistry of arylated BP displays a low amount of solvent passivation indicating that iodonium salts result in a higher degree of functionalisation which gives superior oxidation resistance, possibly due to the attachment to O- and P-sites rather than just P sites. The functionalisation of liquid-exfoliated few-layer BP is challenging due to its rapid degradation and therefore a protection strategy that does not induce oxidation is critical to enhancing its oxidation resistance. Iodonium functionalised BP shows superior ambient stability compared to unfunctionalised and diazonium functionalised BP, as characterised using the XPS P 2p and O 1s core levels and STEM analysis. Functionalisation using iodonium salts provides a new and versatile method to covalent modification of BP

4.3 Experimental

4.3.1 Materials

Black phosphorus (BP) was purchased from Smart Elements (purity 99.998 %) and all chemicals were purchased from Sigma- Aldrich. Anhydrous N-methyl pyrrolidone (NMP) and acetonitrile (ACN) were stored in a glovebox and transfer of solvents and precursors was carried out in a glovebox while purification after functionalisation reactions and centrifugation steps were carried out in ambient conditions.

4.3.2 Exfoliation and Functionalisation

Anhydrous NMP and ACN were degassed using at least 7 freeze-pump-thaw cycles and subsequently purged using Ar gas for 1 h. BP was exfoliated in NMP in a Schlenk flask submersed in a bath sonicator (Branson 1800) under a constant flow of Ar for ~20 h. After exfoliation, the solution was left to settle overnight and subsequently centrifuged at 2000 rpm for 30 min. The sediment was discarded to exclude unexfoliated material. The supernatant was centrifuged at 14500 rpm for 40 min to obtain an exfoliated BP sample. The BP was functionalised using a 10 mM solution of methoxybenzenediazonium tetrafluoroborate (MBD), 3,5-bis(trifluoromethyl)benzenediazonium tetrafluoroborate (FBD), 4-nitrobenzenediazonium tetrafluoroborate (NBD), Bis(4-fluorophenyl)iodonium trifluoromethanesulfonate (FPI), (perfluoro-n-propyl)phenyliodonium trifluoromethanesulfonate (PPI) or bis(4-methylphenyl)iodonium hexfluorophosphate (MPI) and 100 mM tetrabutylammonium hexafluorophosphate in ACN for 3-24 h under flow of Ar. Iodonium precursor solutions were dried for 24 h prior to functionalisation. After functionalisation the BP was purified using 3 washes with ACN. The concentrated solution was drop cast onto a Si wafer or Si coated in a Ti layer to minimise Si contributions during the XPS analysis.

4.3.2 Characterisation

X-Ray photoelectron spectroscopy (XPS) analysis was carried out on an Oxford Applied Research Escabase XPS system with a nonmonochromated Al Kα X-Ray source at 200 W with a base pressure of 5×10^{-10} mbar. Survey spectra were acquired at 0-1000 eV using a step size of 0.7 eV, a dwell time of 0.3 s and a pass energy of 50 eV. Core level scans were averaged over 20-40 scans at a step size of 0.1 eV, a dwell

time of 0.1 s and a pass energy of 20 eV. CasaXPS software was used to process the spectra with Shirley background correction and peaks fitted to Voigt profiles. Peaks were charge corrected to the C 1s peak at 285 eV. Attenuated total reflectance Fourier transform infrared (ATR-FTIR) spectra were recorded using a Nicolet 6700 Infrared Spectrometer with a VariGATR, a liquid cooled HgCdTe detector and Smart ITR accessory. Spectra were collected under ambient atmosphere and averaged over 300 scans at a resolution of 2 cm^{-1}. Raman scattering spectra were acquired using a QE65PRO OceanOptics spectrometer with a 50 μm width slit coupled to a microscope with a 40× objective for focusing on the surface of substrates. A Laser Quantum GEM DPSS 532 nm laser was used for excitation. Photoluminescence spectroscopy was used to probe the electronic structure of the samples. Testing was carried out at room temperature using a 532 nm Laser Quantum GEM DPSS excitation source. Photoluminescence spectra were recorded using a Horiba iHR320 spectrometer equipped with a thermoelectrically cooled Syncerity CCD matrix. Scanning transmission electron microscopy (STEM) analysis was undertaken on an FEI Helios NanoLab 600i scanning electron microscope operating at 20 kV. Transmission electron microscopy (TEM) analysis was acquired on a Jeol 2100 at an operating accelerating voltage of 200 kV.

4.4 Results and Discussion

4.4.1 Covalent Functionalisation using Diazonium Salts

Aryldiazonium salts were used for the covalent functionalisation of BP, as displayed in **Figure 4.2**.

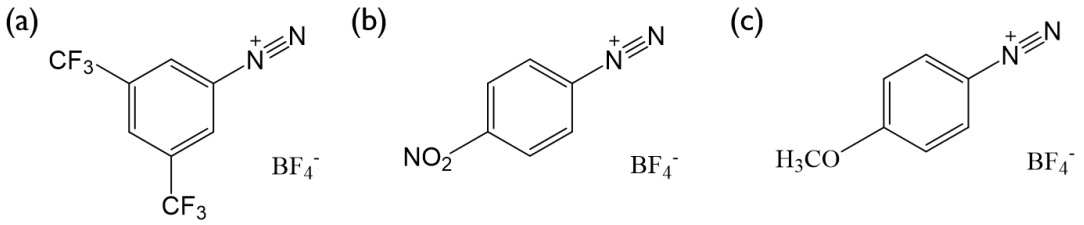

Figure 4.2: Three diazonium molecules were used for BP functionalisation: (a) 3,5-bis(trifluoromethyl)benzenediazonium tetrafluoroborate, (b) 4-nitrobenzenediazonium tetrafluoroborate, (c) methoxybenzenediazonium tetrafluoroborate.

ATR-FTIR analysis was used to confirm successful aryl functionalisation using aryldiazonium salts. **Figure 4.3** displays the ATR-FTIR spectrum of the 3,5-bis(trifluoromethyl)benzenediazonium tetrafluoroborate (FBD) bulk salt (bottom) and BP functionalised using FBD (top). FBD displays a peak associated with $N{=}N^+$ at 2310 cm^{-1}, BF_4^- peak at ~ 1030 cm^{-1}, C-F and C-H stretches and bends in the 1300-800 cm^{-1} region. The disappearance of the $N{=}N^+$ peak and a reduction in the BF_4^- peak indicates dissociation of the diazonium group and counterion.[19] The CF_3 asymmetric stretches were observed at 1260 and 1280 cm^{-1}, while the CF_3 symmetric stretch occurred at 1136 cm^{-1}.[20] A C-C stretch can also be seen at 1385 cm^{-1}.[20]

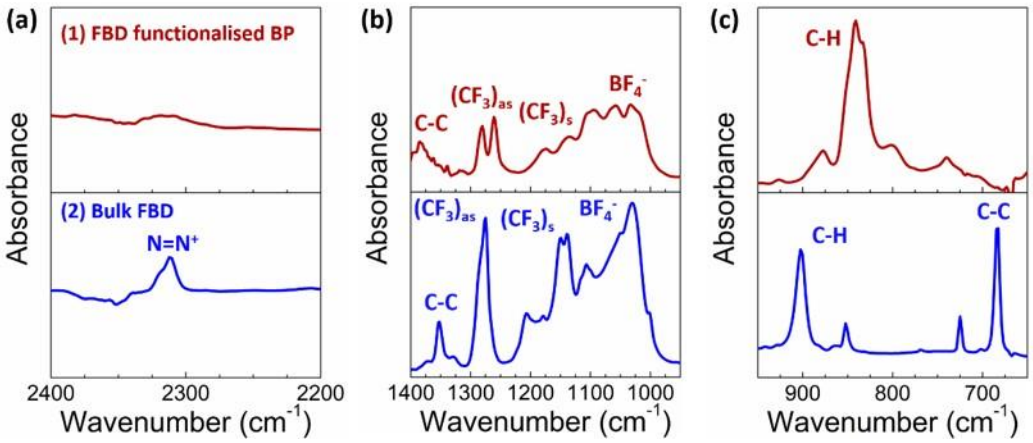

Figure 4.3: ATR-FTIR analysis of (1) 3,5-bis(trifluoromethyl)benzenediazonium tetrafluoroborate (FBD) functionalised BP and (2) the FBD salt.

The absence of the features associated with the counterion and presence of the CF_3 stretches confirm covalent attachment of FBD to BP, as the diazonium salt must dissociate to become surface bound.[14] Additionally, the C-H bend shifted from 903 cm^{-1} for the bulk diazonium salt to 842 cm^{-1} as a result of cleavage of the diazonium group, which has been reported to induce a shift in the C-H peak.[19] Functionalisation of BP using 4-nitrobenzenediazonium tetrafluoroborate (NBD) also resulted in the disappearance of the $N{=}N^+$ peak at 2307 cm^{-1}, as displayed in **Figure 4.4**(a). The asymmetric and symmetric stretches of the NO_2 group occurred at 1508 and 1300 cm^{-1}.[21] Stretches associated with the C-N group occur at 858 cm^{-1} for the bulk NBD salt; however, in the functionalised spectrum this peak overlaps with the C-H peak which has shifted to a lower wavenumber as a result of the cleavage of the diazonium group.[21] A peak was seen at 1262 cm^{-1}, which can be attributed to aromatic C-N vibration[22] and a C-N bend was also observed at 739 cm^{-1}. The presence of stretches associated with the amino group, the C-H bend at 835 cm^{-1} and reduction in the BF_4^- peak at 1032 cm^{-1} confirm successful attachment nitro-aryl group.

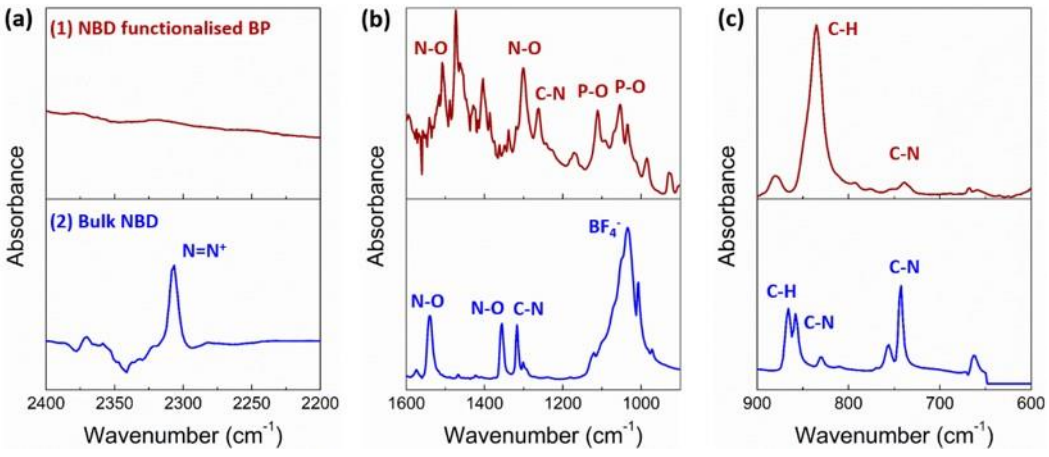

Figure 4.4: ATR-FTIR analysis of (1) 4-nitrobenzenediazonium tetrafluoroborate (NBD) functionalised BP and (2) the NBD salt.

Peaks in the 900-1200 cm^{-1} range are associated phosphorus oxides and indicates NBD functionalisation results in significant surface oxidation which is in correlation with XPS analysis which is discussed later.

ATR-FTIR analysis of methoxybenzenediazonium tetrafluoroborate (MBD) also displayed the disappearance of the $N{=}N^{+}$ peak at 2250 cm^{-1}, as shown in **Figure 4.5**(a). The remaining C-O stretches at 1260 and 1175 cm^{-1} are indicative of successful attachment of the methoxy-aryl group.[23] The reduction in the BF_4^- peak also suggests dissociation of the diazonium salt. The C-H bend and C-C out-of-plane bend were observed at 843 and 668 cm^{-1} in **Figure 4.5**(c), further confirming successful attachment.[19]

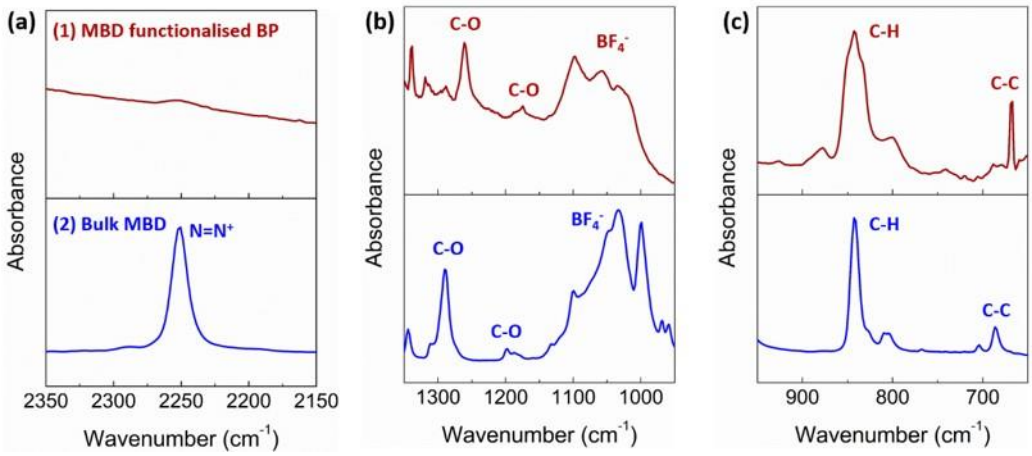

Figure 4.5: ATR-FTIR analysis of (1) methoxybenzenediazonium tetrafuoroborate (MBD) functionalised BP and (2) the MBD salt.

XPS analysis was used to provide additional confirmation of successful functionalisation and characterise the extent of surface oxidation. Diazonium functionalisation always resulted in an increase in the oxide shoulder at 133 eV compared to the main P 2p peak at 130 eV. Freshly exfoliated BP displays an average

oxide shoulder of ~20 % before functionalisation while MBD functionalisation increased the oxide shoulder to 28.5 %, NBD displayed an increase to 31.4 % and FBD resulted in a total oxide peak of 29.2 %, as displayed in **Figure 4.6**. The P 2p core level for FBD functionalised BP shows two oxide environments at 133.7 eV and 136.6 eV which can be attributed to phosphorus oxides in two different oxidation states.[24,25] The formation of two different oxide environments suggests significant oxidation of BP induced by the diazonium salt. While Ryder e*t. al.*[6] reported a low extent of BP surface oxidation during diazonium functionalisation, these results are in correlation with results by Sofer e*t. al.*[9] who also reported diazonium functionalisation resulted in oxidation.

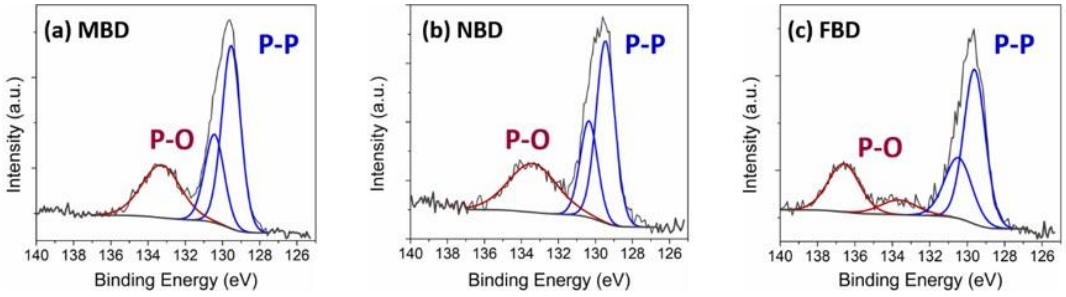

Figure 4.6: The P 2p core levels for (a) MBD, (b) NBD and (c) FBD functionalised BP.

The presence of a F 1s peak at ~687 eV displayed in **Figure 4.7**(a) for FBD functionalised BP, indicates successful attachment of the fluorinated aryl group.[26] Additionally, the C 1s core level can be deconvoluted into three components: C-C at 284.9 eV, C-O at 286.5 eV and CF_3 at 290.7 eV.[27] The presence of a peak at 290.7 eV due to the CF_3 group also indicates the presence of the fluorinated aryl group suggesting it has attached to the surface.

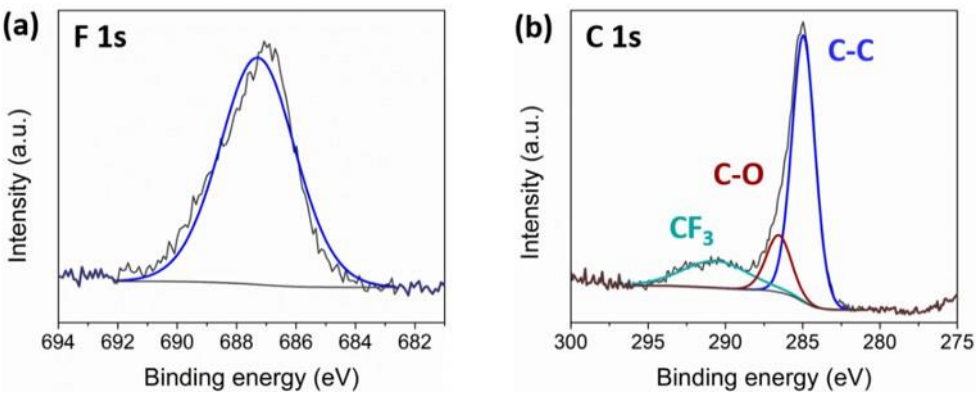

Figure 4.7: The XPS a) F 1s and b) C 1s core levels for FBD functionalised BP.

The N 1s peak, displayed in **Figure 4.8**(a), can be deconvoluted into three contributions. The NO_2 group can be observed at a BE of 406.4 eV which can be attributed to the aryl-NO_2 molecule on the surface.[26] A peak at 401.9 eV is also seen which is due to azo linkages (N=N) suggesting the formation of multilayers on the BP surface, which occurs as a result of diazonium radicals reacting with surface bound aryl groups, as displayed in **Figure 4.8**(b).[26] Diazonium multilayer formation is an uncontrolled process which has been studied on metallic[26] and graphene[28] surfaces and is undesirable for the stabilisation of BP.

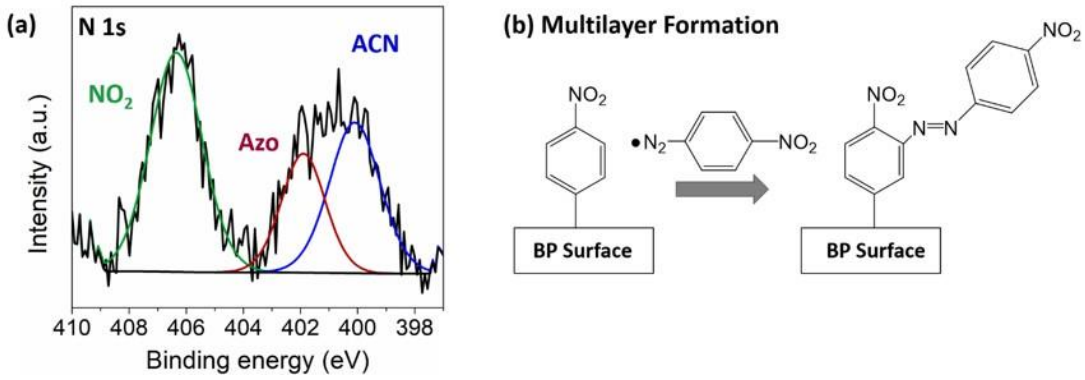

Figure 4.8: (a) N 1s peak for NBD functionalised BP showing the presence of NO_2 groups, azo linkages and the reaction solvent (ACN). (b) Scheme illustrating the multilayer formation as a result of the reaction of diazonium radicals with surface bound aryl groups.

The peak at 400.1 eV can be assigned to the reaction solvent (ACN) indicative of the presence of non-covalent solvent passivation.[29] The N 1s:P 2p ratio of unfunctionalised BP is 0.38 while diazonium functionalisation results in an increase for all three contributions and 32 % for ACN passivation specifically. Successful functionalisation should result in the removal of the solvent passivation layer while no change or an increase in the ratio suggests a low extent of functionalisation. The increase in the N 1s:P 2p ratio could also indicate trapping of reaction solvent in diazonium multilayers which is likely to influence stability of the BP.

4.4.2 Covalent Functionalisation using Iodonium Salts

Iodonium salts were used as an alternative functionalisation strategy to diazonium salts due to their lower reactivity which provides greater control over the passivation layer.[14]

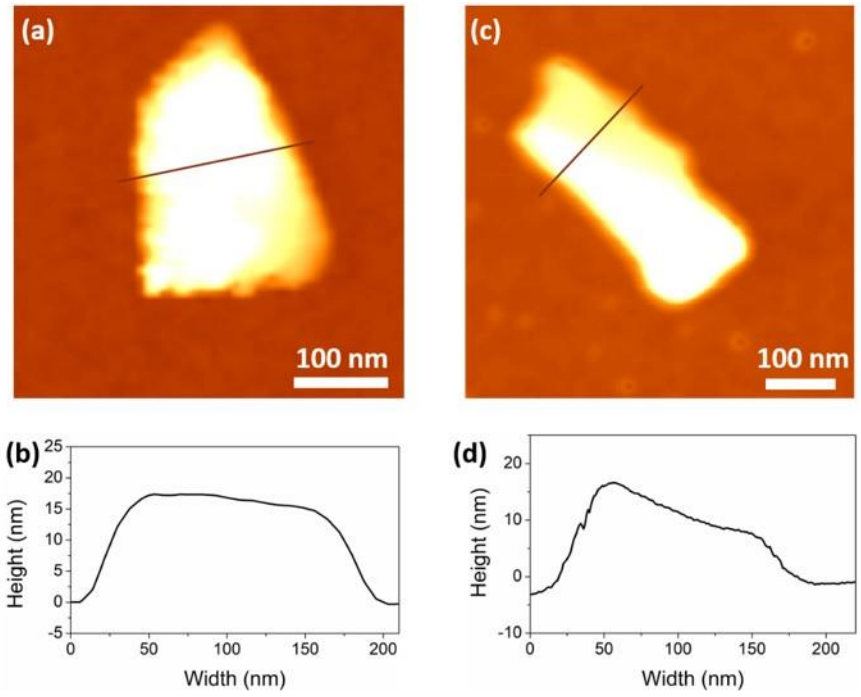

Figure 4.9: (a) AFM analysis of bare BP with a (b) height profile of 17 nm. (c) AFM analysis after FPI functionalisation with a height profile is displayed in (d).

AFM analysis before iodonium functionalisation, as displayed in **Figure 4.9**, was used to confirm the presence of few-layer BP and assess the effect of functionalisation on the flake morphology. The height profile of an unfunctionalised BP flake in **Figure 4.9**(b) shows a height of ~17 nm, confirming liquid exfoliation and centrifugation steps resulted in the extraction of few-layer BP. **Figure 4.9**(c) shows an iodonium functionalised BP flake with clear defined edges, indicating the functionalisation process does not induce degradation.

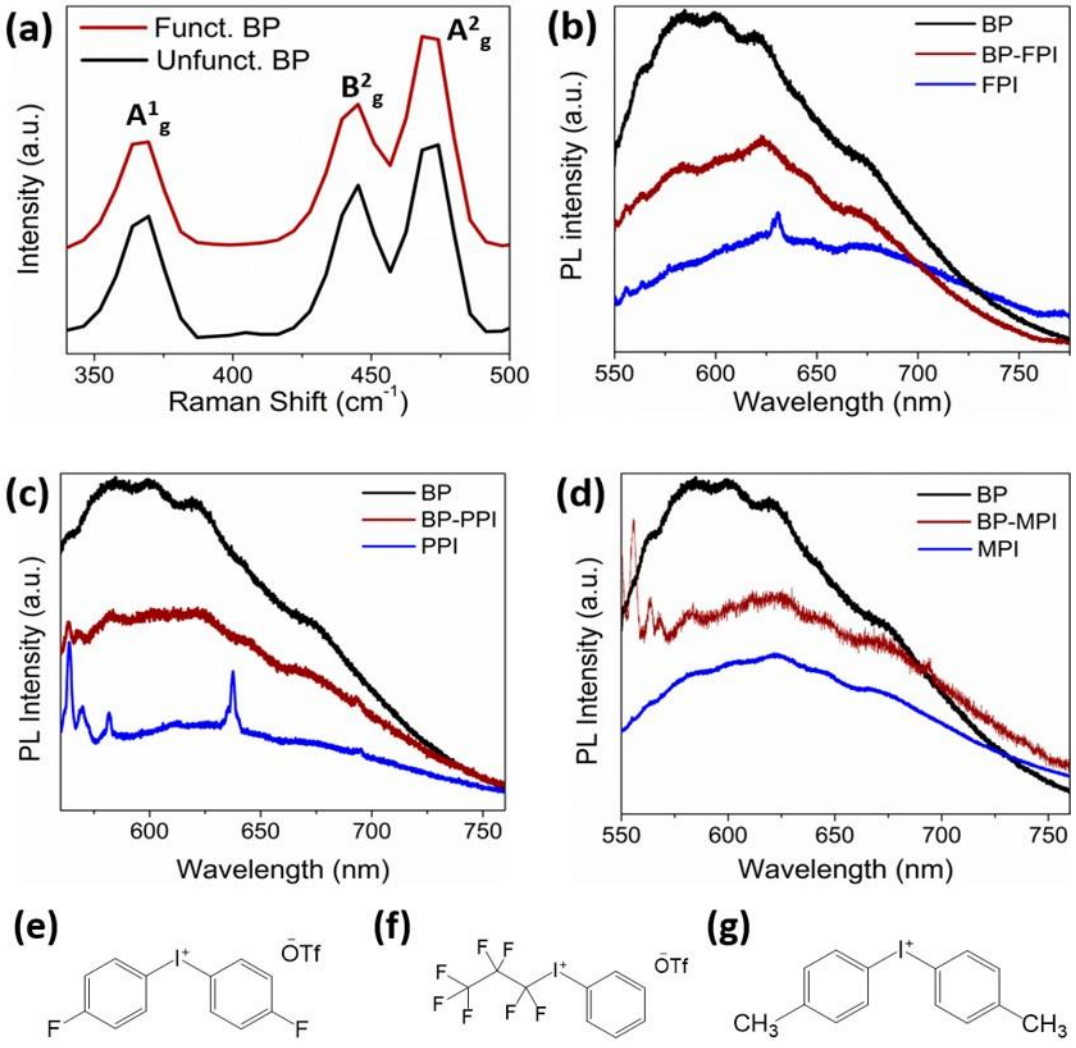

Figure 4.10: Raman analysis before (bottom) and after (top) FPI functionalisation. Photoluminescence analysis of (a) FPI, (b) PPI and (c) MPI functionalised BP. Schematic illustration of (e) FPI, (f) PPI and (c) MPI.

Raman analysis was used to assess the crystallinity of BP flakes after functionalisation. **Figure 4.10**(a) shows the presence of A^1_g, B^2_g, A^2_g modes before and after functionalisation confirming no damage is induced after FPI functionalisation.[30,31] PL analysis can be used to assess the formation of few-layer flakes, as peaks in the 600-1400 nm range can be assigned to few-layer BP.[31] **Figure 4.10**(b) displays a peak at 600 nm which can be attributed to mono-layer BP.[31] After functionalisation the peak is retained but shifts to 625 nm which could be caused due to strain or the electron withdrawing effects of the FPI aryl substituent, as observed for functionalised germanane.[32] A similar shift in the peak at 600 nm was also seen for PPI and MPI as shown in **Figures 4.10**(c) and (d).

Iodonium functionalisation was assessed using ATR-FTIR analysis for a variety of aryl and alkyl iodonium salts. Iodonium salts react through cleavage of the C-I bond with the formation of an aryl iodide leaving group, as displayed in **Figure 4.11**. After dissociation of the C-I bond the fluorinated aryl group reacts with the BP surface. The use of marker atoms on the aryl and alkyl groups allows functionalisation to be assessed more easily using ATR-FTIR analysis.

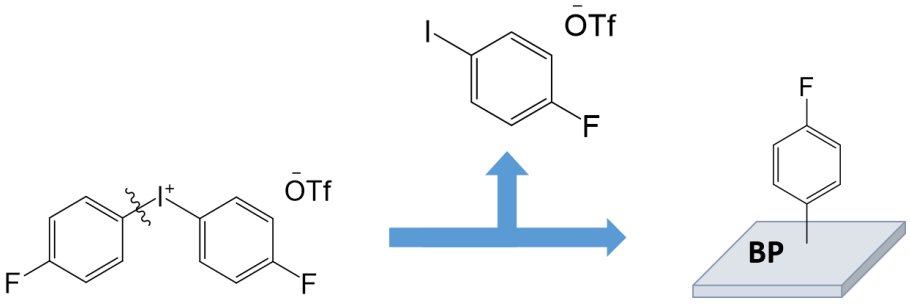

Figure 4.11: Reaction of aryliodonium salts through the formation of an aryl iodide leaving group, resulting in attachment of the fluorinated aryl group to the BP surface.

Figure 4.12 displays the ATR-FTIR spectrum before and after functionalisation with bis(4-fluorophenyl)iodonium triflate (FPI).

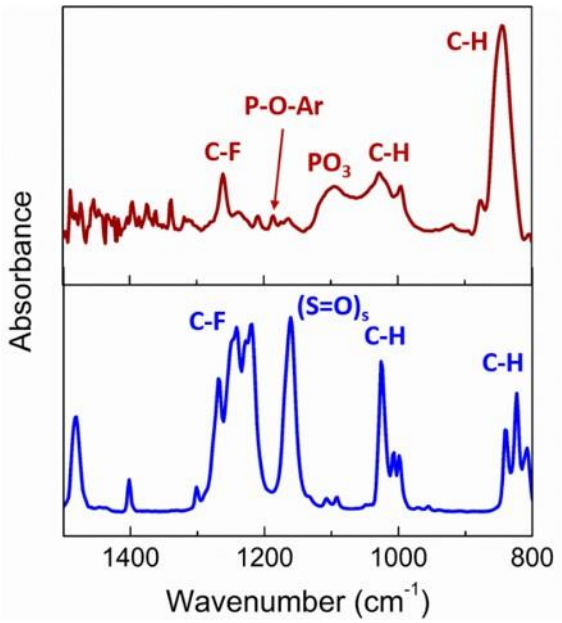

Figure 4.12: ATR-FTIR analysis of bis(4-fluorophenyl)iodonium triflate (FPI) functionalised BP (top) and the FPI salt (bottom).

The retention of the aromatic C-F stretch at 1260 cm^{-1}, the aromatic C-H in-plane bend at 1025 cm^{-1} and the aromatic C-H out-of-plane bend at 845 cm^{-1} indicate the presence of the Ar-F group on the surface.[19] A reduction in the $(S=O)_s$ peak at 1163 cm^{-1} associated with the triflate counterion suggests dissociation of the aryliodonium salt and functionalisation of BP.[33] Additionally, a P-O-Ar peak at 1186 cm^{-1} could indicate attachment of Ar groups through surface oxygen sites as has been reported for silanes functionalisation of BP, [10] although other P-O peaks associated with phosphorus oxides also occur in this region.[34,35]

Figure 4.13 shows the ATR-FTIR spectrum for the bulk bis(4-methylphenyl)iodonium hexafluorophosphate (MPI) salt and MPI functionalised BP.

The peak at 841 cm^{-1} can be attributed to both aromatic C-H bends and the PF_6^- counter ion.[36]

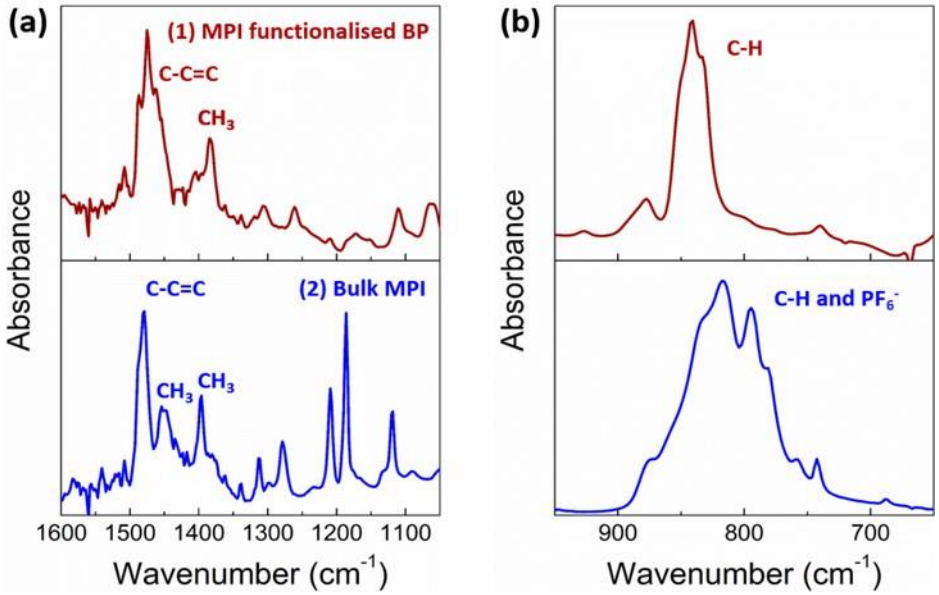

Figure 4.13: ATR-FTIR analysis of bis(4-methylphenyl)iodonium hexafluorophosphate (MPI) functionalised BP (top) and the MPI salt (bottom).

The reduction in broadness and retention of the peak suggests successful dissociation of the salt and functionalisation of BP. **Figure 4.13**(a) displays a peak at 1475 cm^{-1} which can be attributed to an asymmetric C-C=C stretch and a peak at 1384 cm^{-1} due to CH_3 stretches, indicating attachment of the aryl group. The XPS survey spectrum did not display the presence of a F 1s peak at 687 eV, also supporting the dissociation of the salt and subsequent reaction with BP.

An advantage of using iodonium salts is the potential to attach alkyl groups to the BP surface, as the excellent leaving group ability of aryl iodides favours alkyl rather than aryl functionalisation. The use of an asymmetrical iodonium salt resulted in the preferential attachment of the alkyl group as seen on carbon surfaces.[37] The FTIR

spectrum of (perfluoro-*n*-propyl)phenyliodonium triflate (PPI) is displayed in **Figure 4.14**(a), with the retention of CF_3 and C-F stretches at 1260 and 1316 cm^{-1}.

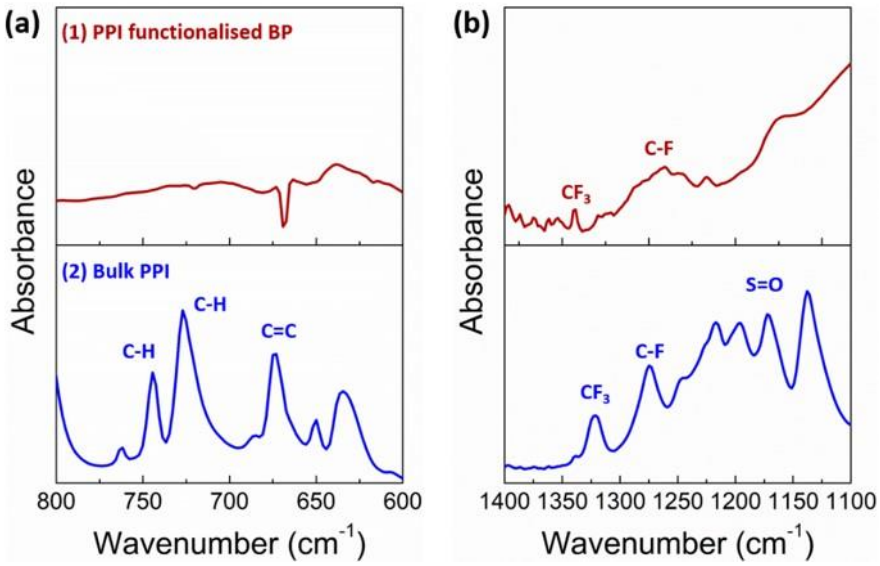

Figure 4.14: ATR-FTIR analysis of (perfluoro-n-propyl)phenyliodonium triflate (PPI) functionalised BP (top) and the PPI salt (bottom).

The reduction in the S=O peak suggests successful functionalisation of BP. The absence of aromatic C-H stretches at 744 and 727 cm^{-1} and C=C stretches at 673 cm^{-1} were also observed in **Figure 4.14**(b), suggesting preferential attachment of the alkyl group due to the excellent leaving group ability of aryl iodides.

Iodonium functionalised BP was assessed using XPS analysis to confirm reaction of the iodonium salt and characterise BP oxidation using the P 2p core levels. **Figure 4.15** displays the C 1s spectrum which can be deconvoluted into three components: C-C at 284.5 eV, C-O, C-O-P and C-C-F at 285.5 eV and C-F at 287 eV.[27] The presence of the C-P component has been reported to occur at ~284 eV but could not be analysed, as it cannot be deconvoluted accurately from the C-C component.[6] The presence of

C-F and C-O components in the C 1s core level suggest the successful attachment of the aryl group on the surface.

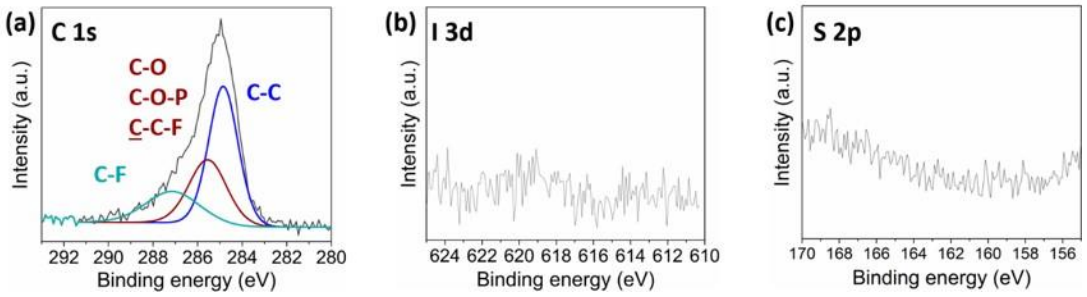

Figure 4.15: (a) C 1s, (b) I 3d and (c) S 2p core levels are displayed for FPI functionalised BP.

The absence of the I 3d and S 2p peaks, as displayed in **Figures 4.15**(b) and (c), indicates dissociation of the iodonium salt. Additionally, a F 1s peak was seen at 687 eV for both alkyl and aryl iodonium salts, as shown in **Figure 4.16**. The absence of I 3d and the presence of the F 1s peak suggests the aryl group has covalently reacted with the BP surface rather than the physisorption of the iodonium salt.

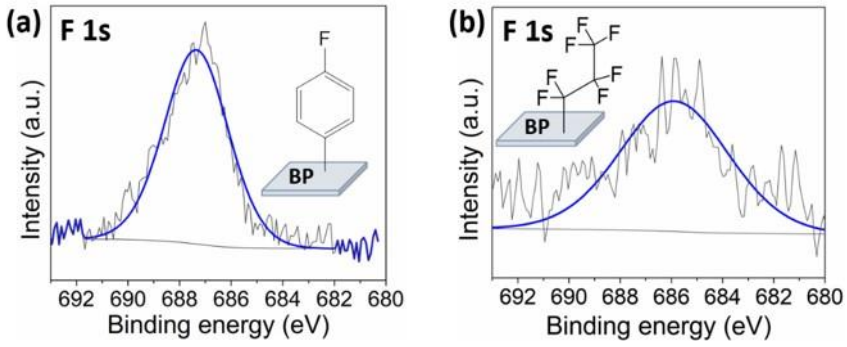

Figure 4.16: F 1s core levels for (a) FPI and (b) PPI functionalised BP.

XPS analysis was also used to monitor the extent of oxidation before and after functionalisation, as displayed in **Figure 4.17**. No increase in the P 2p oxide shoulder at 133 eV was observed after functionalisation confirming the gentle nature of iodonium salts as mild arylating agents.[38,39]

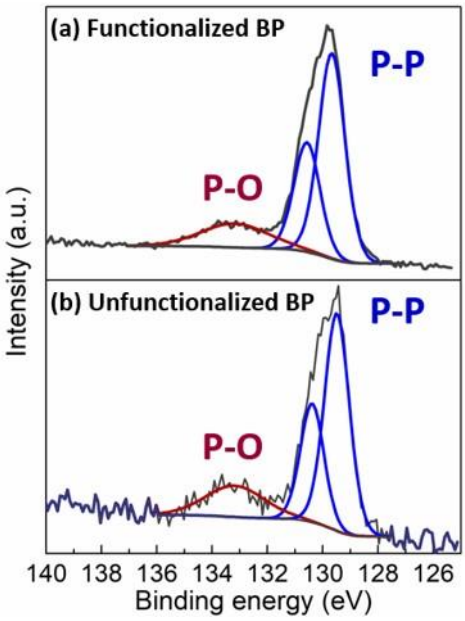

Figure 4.17: XPS analysis of (a) FPI functionalised and (b) unfunctionalised BP.

The extent of functionalisation for FPI and PPI was estimated using the F 1s:P 2p ratio which indicated PPI has a ~40 % lower fluorine content than FPI. Optimisation of the iodonium reaction conditions was carried out by varying the reaction length and temperature and assessing the F 1s:P 2p ratio. Heating the reaction mixture to 45 °C resulted in an increase in the oxide shoulder to 34.1 % and the formation of two oxide environments. The formation of two oxide environments is associated with significant oxidation of the surface.[25] The P 2p core level of BP functionalised for a reaction time of 24 h is displayed in **Figure 4.18** where an increase to 45.5 % was also observed. **Figure 4.18**(c) shows the increase in the F 1s:P 2p ratio for both reaction conditions, suggesting an increased degree of functionalisation although the formation of two oxide environments for both reaction conditions indicates major oxidation of the BP surface.

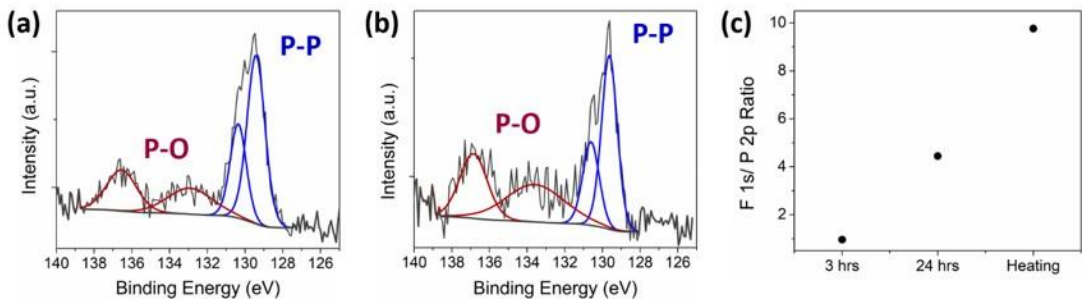

Figure 4.18: P 2p core levels for FPI functionalised BP using a) a 3 h reaction at 45 C or b) a 24 h reaction at room temperature. c) The F 1s: P 2p ratio is used to give an indication of the extent of functionalisation for the extended reaction time and the use of heat.

Figure 4.19 shows the attachment of aryl groups to BP. Binding to P sites has been proposed to occur through the cleavage of a P-P bond.[9,40] The exact binding of aryl groups to BP is difficult to evaluate; the P-C component in the P 2p core levels overlaps with the P-O peak making deconvolution difficult. The C 1s core level also displays an overlap of the C-C and C-P components.

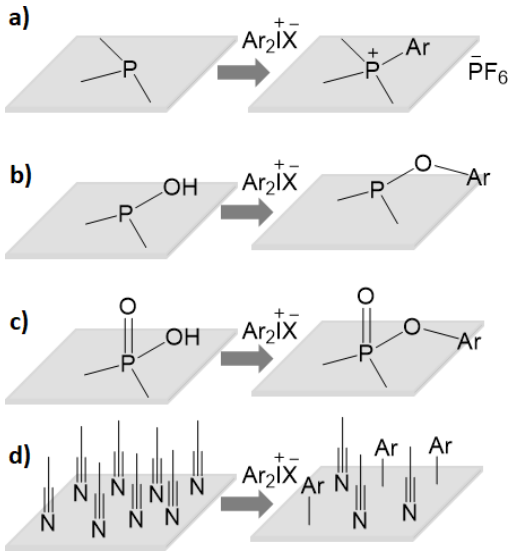

Figure 4.19: Attachment of aryl groups to BP through (a) P-sites, (b)-(c) O sites and (d) the presence of solvent passivation.

The attachment of aryl groups to BP without the cleavage of a P-P bond leads to the formation of a 4 coordinate phosphorus with a positive charge which may be stabilised by the aryl iodonium counterion. The ATR-FTIR analysis suggests the presence of a remaining S=O vibration indicating the presence of the counterion on BP functionalised surfaces.

The attachment of aryl group could also occur through O sites which has been reported previously.[9,10] Sofer *et. al.*[9] reported the reaction of alkyl halides with BP oxide sites resulted in the covalent attachment. Additionally, diaryliodonium salts have been reported to react with O nucleophiles.[41] The attachment to surface P-OH and O=P-OH groups is illustrated in **Figure 4.19**. The reduction in intensity of the O=P-OH peak during FPI functionalisation may be indicative of binding to the oxide site, as shown in **Figure 4.20**.

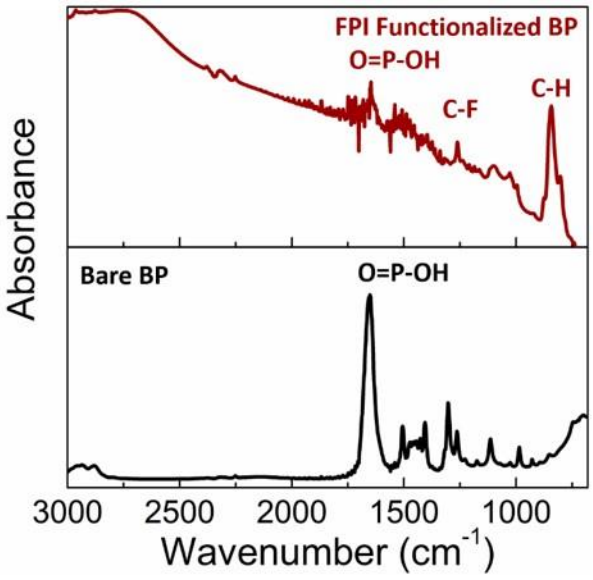

Figure 4.20: ATR-FTIR analysis of (a) FPI functionalised BP and (b) unfunctionalised BP.

The inhibition of the P-O-P component during ambient exposure of FPI functionalised

BP also suggests binding to the oxide sites. **Figure 4.19** (d) also shows the non-covalent passivation of ACN which occurs during the FPI functionalisation.

4.4.3 Comparison of Iodonium and Diazonium Functionalisation – Solvent Passivation and Stability

As previously discussed the diazonium functionalisation process results in non-covalent passivation of reaction solvent. Non-covalent solvent passivation can be detrimental to device performance as it can hinder contact formation[42] and therefore the extent of solvent passivation must be minimised, which can be achieved through covalent functionalisation.[43] An unfunctionalised BP sample displayed a N 1s:P 2p ratio of 0.4, demonstrating that the diazonium process results in a 33 % increase in solvent passivation. The increase in the N 1s:P 2p ratio indicates that diazonium functionalisation does not remove the passivation layer and solvent molecules are likely to be trapped within the multilayers that form on the BP surface. In contrast, iodonium functionalisation resulted in a ~70 % decrease in the N 1s: P 2p ratio as a result of the removal of the solvent passivation layer through covalent functionalisation of the surface. The decrease in the N 1s: P 2p ratio for iodonium functionalised BP and the increase for diazonium functionalised BP indicates functionalisation using iodonium salts results in a higher degree of functionalisation than diazonium functionalisation.

The stability of unfunctionalised and iodonium- and diazonium-functionalised BP was assessed using the P 2p and O 1s core levels. The O 1s core levels for unfunctionalised and iodonium functionalised BP are displayed in **Figure 4.21**. After 40 hours of ambient exposure of unfunctionalised BP, the P-O-P component at 534.6 eV increases and a reduction is seen in the non-bridging oxide species at 532.2 eV.[44] In comparison,

iodonium functionalisation inhibits the increase in the P-O-P component for the first 40 h of ambient exposure. The inhibition of the P-O-P component is crucial in enhancing the ambient stability of BP, as it prevents further oxide formation.[18]

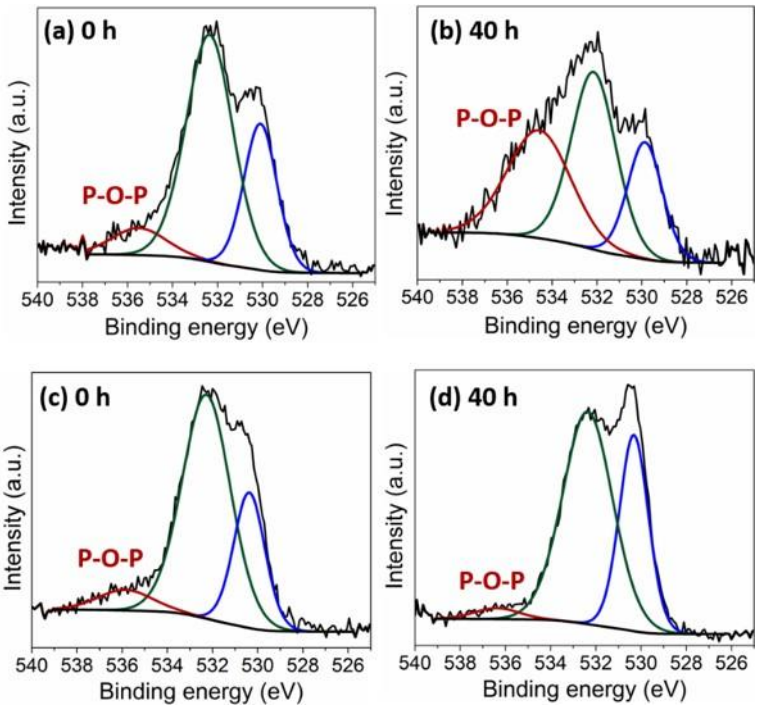

Figure 4.21: The O 1s core levels for unfunctionalised BP a) before and b) after 40 h of ambient exposure. The iodonium functionalised BP was assessed a) before and b) after 40 h of ambient exposure.

The corresponding STEM analysis in **Figure 4.22** shows the appearance of topographic protrusions on the surface of unfunctionalised BP after 48 h in ambient conditions. The formation of droplets on the BP surface is associated with the formation of phosphorus oxides as degradation products which react further to form liquid oxidation products.[18,24,25,44] In comparison, iodonium functionalised BP does not display the formation of liquid droplets on the surface and after 48 h demonstrating enhanced ambient stability.

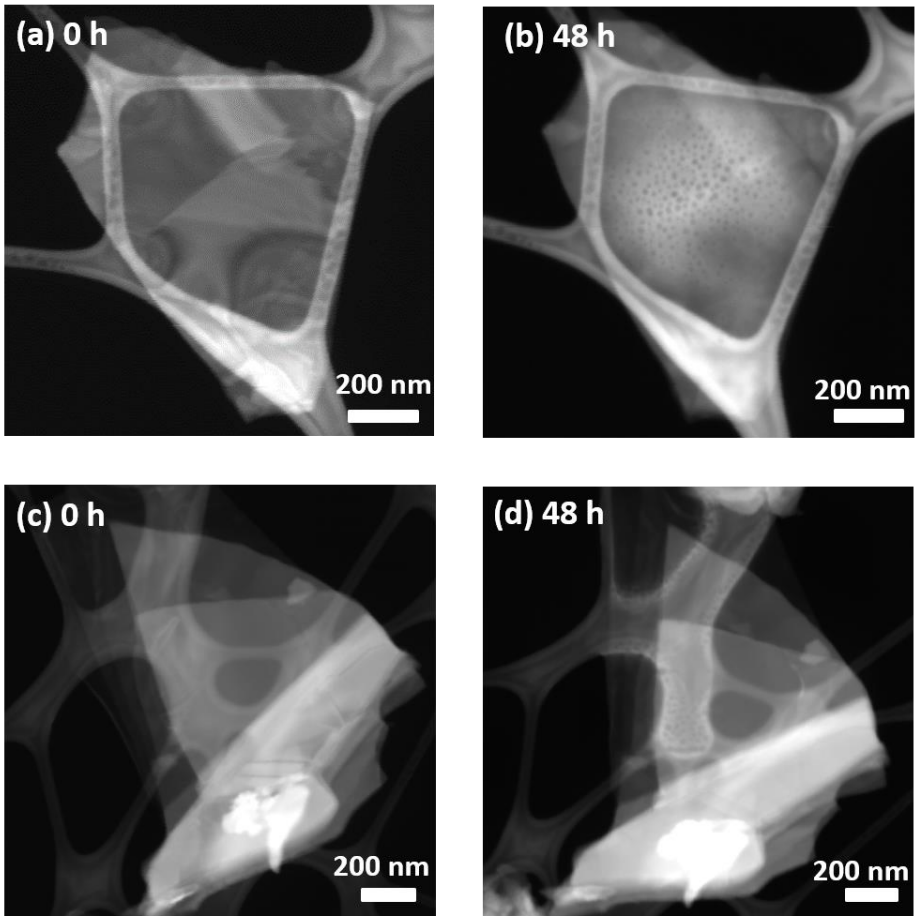

Figure 4.22: STEM analysis of unfunctionalised BP during (a) 0 h and (b) 48 h of ambient exposure and FPI functionalised BP at (c) 0 h and (d) 48 h of ambient exposure.

The P 2p core levels for iodonium functionalised BP are displayed in **Figure 4.23** which show the increased oxidation resistance of FPI functionalised BP. The oxide shoulder decreases from 16.3 % initially to 10.1 %, as seen by comparison of **Figures 4.23**(a) and (b). The reduction in the oxide shoulder, which suggests removal of surface oxides, has been reported during functionalisation of BP using both silanes and thiols where surface oxygen sites react with the precursors.[10,11] A further increase to 25.2 % is observed after 1 week of exposure, amounting to a total increase of 8.9 %.

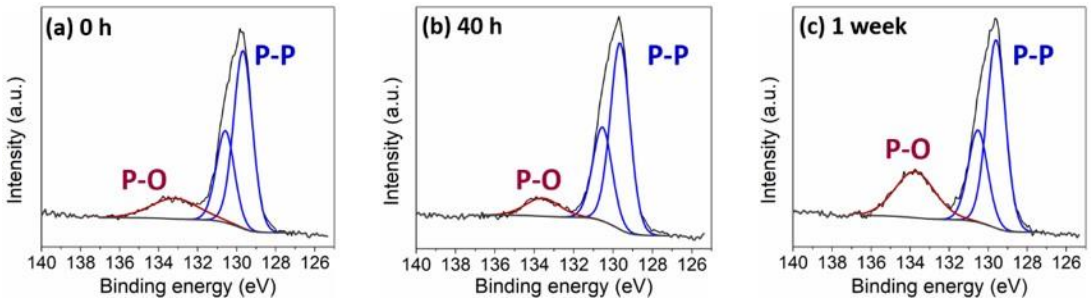

Figure 4.23: P 2p core levels displaying the increase in the oxide shoulder for iodonium functionalised BP at (a) 16.3 % at 0 h, (b) 10.1 % at 40 h and (c) 25.2 % at 1 week.

In comparison, diazonium functionalised BP displayed a larger increase of the oxide shoulder over a period of a week as displayed in **Figure 4.24**.

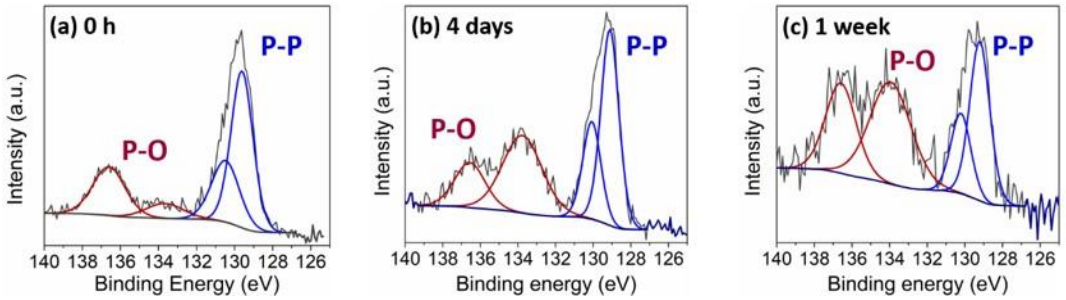

Figure 4.24: P 2p core level for diazonium functionalised BP exposed to ambient conditions for (a) 0 h, (b) 4 days and (c) 1 week.

The oxide shoulder increases from 29.2 % to 45.5 % over a period of 4 days. A further increase in the P 2p oxide shoulder to 59 % occurs after a period of a week. The formation of 2 oxide environments suggests a higher amount of oxidation occurred. Comparison between the stability of diazonium and iodonium functionalised BP is displayed in **Figure 4.25** where a more significant increase in oxidation is observed for diazonium functionalised BP.

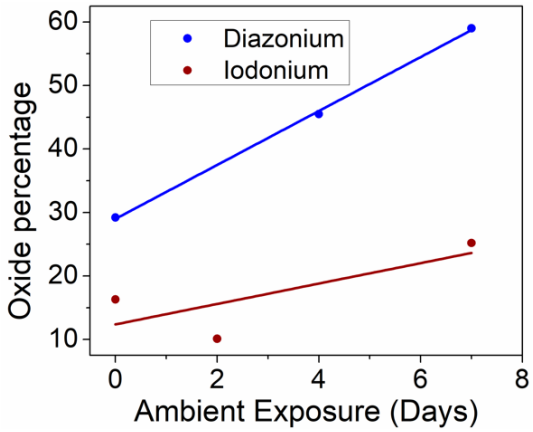

Figure 4.25: The stability of iodonium and diazonium functionalised BP is compared using the percentage of P_xO_y compared to the main P 2p peak.

The stability of diazonium functionalised BP is likely to be influenced by multilayer formation and non-covalent solvent passivation. The higher increase in the oxide shoulder for diazonium functionalisation is likely to stem from the oxidation induced during the reaction. Initial oxide formation has been reported to facilitate further degradation by increasing the hydophilicity of the surface.[25] In comparison, the iodonium functionalised BP displays a higher stability due to the removal of surface oxides during functionalisation and inhibition of further oxidation by attachment to existing oxide sites.

4.5 Conclusions

A new method for surface modification of BP using iodonium salts was investigated and compared to the previously established diazonium strategy. The detailed characterisation of surface chemistry of diazonium and iodonium functionalised BP flakes allows comparison between the two functionalisation strategies. While diazonium modification resulted in oxidation, multilayer formation and non-covalent solvent passivation, iodonium salts did not induce any oxidation. Iodonium salts display a greater compatibility with BP due to their lower reactivity which provides more control during functionalisation and prevents the formation of multilayers. The attachment of aryl groups to surface oxygen sites in addition to P-sites, resulted in a greater extent of functionalisation. Furthermore, iodonium functionalisation resulted in the inhibition of P-O-P formation, a key sign of major BP degradation, greatly enhancing its ambient stability compared to unfunctionalised and diazonium modified BP. Successful functionalisation of BP using a variety of aryl and alkyl groups shows potential to tune its electrical properties through variation of the aryl substituents. The investigation of electrical properties will provide further characterisation of the effect of functionalisation using different aryl and alkyl substituents.

4.6 References

(1) Koenig, S. P.; Doganov, R. A.; Schmidt, H.; Castro Neto, A. H.; Özyilmaz, B. Electric Field Effect in Ultrathin Black Phosphorus. *Appl. Phys. Lett.* **2014**, *104* (10), 103–106.

(2) Buscema, M.; Groenendijk, D. J.; Blanter, S. I.; Steele, G. A.; Van Der Zant, H. S. J.; Castellanos-Gomez, A. Fast and Broadband Photoresponse of Few-Layer Black Phosphorus Field-Effect Transistors. *Nano Lett.* **2014**, *14* (6), 3347–3352.

(3) Gusmao, R.; Sofer, Z.; Pumera, M. Black Phosphorus Rediscovered: From Bulk to Monolayer. *Angew. Chemie Int. Ed.* **2017**, *56* (28), 8052–8072.

(4) Pang, J.; Bachmatiuk, A.; Yin, Y.; Trzebicka, B.; Zhao, L.; Fu, L.; Mendes, R. G.; Gemming, T.; Liu, Z.; Rummeli, M. H. Applications of Phosphorene and Black Phosphorus in Energy Conversion and Storage Devices. *Adv. Energy Mater.* **2018**, *8* (8), 1702093.

(5) Zhang, Y.; Zheng, Y.; Rui, K.; Hng, H. H.; Hippalgaonkar, K.; Xu, J.; Sun, W.; Zhu, J.; Yan, Q.; Huang, W. 2D Black Phosphorus for Energy Storage and Thermoelectric Applications. *Small* **2017**, *13* (28), 1700661.

(6) Ryder, C. R.; Wood, J. D.; Wells, S. A.; Yang, Y.; Jariwala, D.; Marks, T. J.; Schatz, G. C.; Hersam, M. C. Covalent Functionalization and Passivation of Exfoliated Black Phosphorus via Aryl Diazonium Chemistry. *Nat. Chem.* **2016**, *8* (6), 597–602.

(7) Abellán, G.; Lloret, V.; Mundloch, U.; Marcia, M.; Neiss, C.; Görling, A.; Varela, M.; Hauke, F.; Hirsch, A. Noncovalent Functionalization of Black Phosphorus. *Angew. Chemie Int. Ed.* **2016**, *55* (47), 14557–14562.

(8) Zhao, Y.; Wang, H.; Huang, H.; Xiao, Q.; Xu, Y.; Guo, Z.; Xie, H.; Shao, J.; Sun, Z.; Han, W.; Yu, X. F.; Li, P.; Chu, P. K. Surface Coordination of Black Phosphorus for Robust Air and Water Stability. *Angew. Chemie Int. Ed.* **2016**, *55* (16), 5003–5007.

(9) Sofer, Z.; Luxa, J.; Bouša, D.; Sedmidubský, D.; Lazar, P.; Hartman, T.; Hardtdegen, H.; Pumera, M. The Covalent Functionalization of Layered Black Phosphorus by Nucleophilic Reagents. *Angew. Chemie Int. Ed.* **2017**, *56* (33), 9891–9896.

(10) Artel, V.; Guo, Q.; Cohen, H.; Gasper, R.; Ramasubramaniam, A.; Xia, F. Protective Molecular Passivation of Black Phosphorus. *npj 2D Mater. Appl.* **2017**, *1* (1), 6.

(11) Kwak, D. H.; Ra, H. S.; Yang, J.; Jeong, M. H.; Lee, A. Y.; Lee, W.; Hwang, J. Y.; Lee, J. H.; Lee, J. S. Recovery Mechanism of Degraded Black Phosphorus Field-Effect Transistors by 1,2-Ethanedithiol Chemistry and Extended Device Stability. *Small* **2018**, *14* (6), 1703194.

(12) Vase, K. H.; Holm, A. H.; Norrman, K.; Pedersen, S. U.; Daasbjerg, K. Covalent Graftin of Glassy Carbon Electrodes With Diaryliodomium Salts: New Aspects. *Langmuir* **2007**, *23* (8), 3786–3793.

(13) He, M.; Swager, T. M. Covalent Functionalization of Carbon Nanomaterials with Iodonium Salts. *Chem. Mater.* **2016**, *28* (23), 8542–8549.

(14) Chan, C. K.; Beechem, T. E.; Ohta, T.; Brumbach, M. T.; Wheeler, D. R.; Stevenson, K. J. Electrochemically Driven Covalent Functionalization of Graphene from Fluorinated Aryl Iodonium Salts. *J. Phys. Chem. C* **2013**, *117* (23), 12038–12044.

(15) Koefoed, L.; Pedersen, S. U.; Daasbjerg, K. Covalent Modification of Glassy Carbon Surfaces by Electrochemical Grafting of Aryl Iodides. *Langmuir* **2017**, *33* (13), 3217–3222.

(16) Bonin, H.; Fouquet, E.; Felpin, F. X. Aryl Diazonium versus Iodonium Salts: Preparation, Applications and Mechanisms for the Suzuki-Miyaura Cross-Coupling Reaction. *Adv. Synth. Catal.* **2011**, *353* (17), 3063–3084.

(17) Xu, J.; Zhang, P.; Gao, Y.; Chen, Y.; Tang, G.; Zhao, Y. Copper-Catalyzed P-Arylation via Direct Coupling of Diaryliodonium Salts with Phosphorus Nucleophiles at Room Temperature. *J. Org. Chem.* **2013**, *78* (16), 8176–8183.

(18) Van Druenen, M.; Davitt, F.; Collins, T.; Glynn, C.; O'Dwyer, C.; Holmes, J. D.; Collins, G. Evaluating the Surface Chemistry of Black Phosphorus during Ambient Degradatioń. *Langmuir* **2019**, *35* (6), 2172–2178.

(19) Collins, G.; Fleming, P.; O'Dwyer, C.; Morris, M. A.; Holmes, J. D.; O'Dwyer, C.; Morris, M. A.; Holmes, J. D. Organic Functionalization of Germanium Nanowires Using Arenediazonium Salts. *Chem. Mater.* **2011**, *23* (7), 1883–1891.

(20) Hermann, A.; Mora Valdez, M. I.; Cutin, E. H.; Della Vedova, C. O.; Oberhammer, H. Structures and Conformations of ((Trifluoroacetyl)Imido)(Trifluoromethyl)Sulfur Fluoride, CF3C(O)N=S(F)CF3. *J. Phys. Chem. A* **2003**, *107* (39), 7874–7878.

(21) Lomeda, J. R.; Doyle, C. D.; Kosynkin, D. V.; Hwang, W. F.; Tour, J. M. Diazonium Functionalization of Surfactant-Wrapped Chemically Converted Graphene Sheets. *J. Am. Chem. Soc.* **2008**, *130* (48), 16201–16206.

(22) Lyskawa, J.; Bélanger, D. Direct Modification of a Gold Electrode with Aminophenyl Groups by Electrochemical Reduction of in Situ Generated Aminophenyl Monodiazonium Cations. *Chem. Mater.* **2006**, *18* (20), 4755–4763.

(23) Mahouche, S.; Mekni, N.; Abbassi, L.; Lang, P.; Perruchot, C.; Jouini, M.; Mammeri, F.; Turmine, M.; Romdhane, H. Ben; Chehimi, M. M. Tandem Diazonium Salt Electroreduction and Click Chemistry as a Novel, Efficient Route for Grafting Macromolecules to Gold Surface. *Surf. Sci.* **2009**, *603* (21), 3205–3211.

(24) Yang, T.; Dong, B.; Wang, J.; Zhang, Z.; Guan, J.; Kuntz, K.; Warren, S. C.; Tománek, D. Interpreting Core-Level Spectra of Oxidizing Phosphorene: Theory and Experiment. *Phys. Rev. B - Condens. Matter Mater. Phys.* **2015**, *92* (12), 125412.

(25) Kuntz, K. L.; Wells, R. A.; Hu, J.; Yang, T.; Dong, B.; Guo, H.; Woomer, A. H.; Druffel, D. L.; Alabanza, A.; Tománek, D.; Warren, S. C. Control of Surface and Edge Oxidation on Phosphorene. *ACS Appl. Mater. Interfaces* **2017**, *9* (10), 9126–9135.

(26) Mesnage, A.; Lefèvre, X.; Jégou, P.; Deniau, G.; Palacin, S. Spontaneous Grafting of Diazonium Salts: Chemical Mechanism on Metallic Surfaces. *Langmuir* **2012**, *28* (32), 11767–11778.

(27) Robinson, J. T.; Burgess, J. S.; Junkermeier, C. E.; Badescu, S. C.; Reinecke, T. L.; Perkins, F. K.; Zalalutdniov, M. K.; Baldwin, J. W.; Culbertson, J. C.; Sheehan, P. E.; Snow, E. S. Properties of Fluorinated Graphene Films. *Nano Lett.* **2010**, *10* (8), 3001–3005.

(28) Barrière, F.; Downard, A. J. Covalent Modification of Graphitic Carbon Substrates by Non-Electrochemical Methods. *J. Solid State Electrochem.* **2008**, *12* (10), 1231–1244.

(29) Graf, N.; Yegen, E.; Gross, T.; Lippitz, A.; Weigel, W.; Krakert, S.; Terfort, A.; Unger, W. E. S. XPS and NEXAFS Studies of Aliphatic and Aromatic Amine Species on Functionalized Surfaces. *Surf. Sci.* **2009**, *603* (18), 2849–2860.

(30) Brent, J. R.; Savjani, N.; Lewis, E. A.; Haigh, S. J.; Lewis, D. J.; O'Brien, P. Production of Few-Layer Phosphorene by Liquid Exfoliation of Black Phosphorus. *Chem. Commun.* **2014**, *50* (87), 13338–13341.

(31) Hanlon, D.; Backes, C.; Doherty, E.; Cucinotta, C. S.; Berner, N. C.; Boland, C.; Lee, K.; Harvey, A.; Lynch, P.; Gholamvand, Z.; Zhang, S.; Wang, K.; Moynihan, G.; Pokle, A.; Ramasse, Q. M.; McEvoy, N.; Blau, W. J.; Wang, J.; Abellan, G.; Hauke, F.; Hirsch, A.; Sanvito, S.; O'Regan, D. D.; Duesberg, G. S.; Nicolosi, V.; Coleman, J. N. Liquid Exfoliation of Solvent-Stabilized Few-Layer Black Phosphorus for Applications beyond Electronics. *Nat. Commun.* **2015**, *6*, 8563.

(32) Jiang, S.; Krymowski, K.; Asel, T.; Arguilla, M. Q.; Cultrara, N. D.; Yanchenko, E.; Yang, X.; Brillson, L. J.; Windl, W.; Goldberger, J. E. Tailoring the Electronic Structure of Covalently Functionalized Germanane via the Interplay of Ligand Strain and Electronegativity. *Chem. Mater.* **2016**, *28* (21), 8071–8077.

(33) Miles, M. G.; Doyle, G.; Cooney, R. P.; Tobias, R. S. Raman and Infrared Spectra and Normal Coordinates of the Trifluoromethanesulfonate and

Trichloromethanesulfonate Anions. *Spectrochim. Acta Part A Mol. Spectrosc.* **1969**, *25* (9), 1515–1526.

(34) Nogami, M. Proton Conductivity in Sol–Gel-Derived P2O5–TiO2–SiO2 Glasses. *Solid State Ionics* **2004**, *166* (1–2), 39–43.

(35) Ahsan, M. R.; Uddin, M. A.; Mortuza, M. G. Infrared Study of the Effect of P 2 O 5 in the Structure of Lead Silicate Glasses. *Indian J. Pure Appl. Phys.* **2005**, *43*, 89–99.

(36) Sharma, J. P.; Yamada, K.; Sekhon, S. S. Conductivity Study on PEO Based Polymer Electrolytes Containing Hexafluorophosphate Anion : Effect of Plasticizer. **2012**, 188–197.

(37) Vase, K. H.; Holm, A. H.; Pedersen, S. U.; Daasbjerg, K. Immobilization of Aryl and Alkynyl Groups onto Glassy Carbon Surfaces by Electrochemical Reduction of Iodonium Salts. *Langmuir* **2005**, *21* (18), 8085–8089.

(38) Fañanás-Mastral, M.; Feringa, B. L. Copper-Catalyzed Synthesis of Mixed Alkyl Aryl Phosphonates. *J. Am. Chem. Soc.* **2014**, *136* (28), 9894–9897.

(39) Aradi, K.; Tóth, B. L.; Tolnai, G. L.; Novák, Z. Diaryliodonium Salts in Organic Syntheses: A Useful Compound Class for Novel Arylation Strategies. *Synlett* **2016**, *27* (10), 1456–1485.

(40) Wild, S.; Fickert, M.; Mitrovic, A.; Lloret, V.; Neiss, C.; Vidal-moya, J. Ø. A.; Rivero-crespo, M.; Ø, A. L.; Werbach, K.; Peterlik, H.; Grabau, M.; Wittk, H.; Papp, C.; Steinruck, H.; Pichler, T.; Gçrling, A.; Hauke, F.; Abellan, G.; Hirsch, A. Lattice Opening upon Bulk Reductive Covalent Functionalization of Black Phosphorus. *Angew. Chemie - Int. Ed.* **2019**, *58*

(17), 5763–5768.

(41) Jalalian, N.; Petersen, T. B.; Olofsson, B. Metal-Free Arylation of Oxygen Nucleophiles with Diaryliodonium Salts. *Chem. - A Eur. J.* **2012**, *18* (44), 14140–14149.

(42) Abellán, G.; Wild, S.; Lloret, V.; Scheuschner, N.; Gillen, R.; Mundloch, U.; Maultzsch, J.; Varela, M.; Hauke, F.; Hirsch, A. Fundamental Insights into the Degradation and Stabilization of Thin Layer Black Phosphorus. *J. Am. Chem. Soc.* **2017**, *139* (30), 10432–10440.

(43) Del Rio Castillo, A. E.; Pellegrini, V.; Sun, H.; Buha, J.; Dinh, D. A.; Lago, E.; Ansaldo, A.; Capasso, A.; Manna, L.; Bonaccorso, F. Exfoliation of Few-Layer Black Phosphorus in Low Boiling Point Solvents and Its Application in Li-Ion Batteries. *Chem. Mater.* **2018**, *30* (2), 506–516.

(44) Luo, W.; Zemlyanov, D. Y.; Milligan, C. A.; Du, Y.; Yang, L.; Wu, Y.; Ye, P. D. Surface Chemistry of Black Phosphorus under a Controlled Oxidative Environment. *Nanotechnology* **2016**, *27* (43), 434002.

Chapter 5

Stabilisation of Black Phosphorus using Sonication-Assisted Simultaneous Exfoliation-Functionalisation

5. Stabilisation of Black Phosphorus using Sonication-Assisted Simultaneous Exfoliation-Functionalisation

5.1 Abstract

Black Phosphorus (BP) displays extraordinary properties but its ambient instability remains a critical challenge. Functionalisation has been employed to overcome the sensitivity of BP to ambient conditions while preserving its properties. Here, we report a simultaneous exfoliation-functionalisation process that functionalises BP flakes during exfoliation, therefore providing increased protection which can be attributed to the minimal exposure of flakes to ambient oxygen and water. A tetrabutylammonium salt was employed for the intercalation of BP resulting in the formation of flakes with large lateral dimensions. The addition of an aryl iodide or an aryl iodonium salt to the exfoliation solvent creates a scalable strategy for the production of functionalised few-layer BP flakes. Aryl functionalisation was characterised using x-ray photoelectron spectroscopy (XPS) and attenuated total reflectance Fourier transform infrared (ATR-FTIR) spectroscopy. The ambient stability of functionalised BP was prolonged to a period of 1 week compared to unfunctionalised BP, as characterised using Scanning transmission electron microscopy (STEM), atomic force microscopy (AFM) and XPS.

5.2 Introduction

The last few years have seen an immense interest in BP, a promising new 2D material, which displays exceptional properties.[1,2] The high carrier mobility and layer tunable bandgap range (0.3-2 eV) that falls in between graphene and transition metal dichalcogenides (TMDs) make it ideal for a range of applications including electrical,[3,4] energy storage[5,6] and optical devices.[7] While BP shows extraordinary properties, its application is hindered by its degradation under ambient conditions.[8–10] The lifetime of BP has been extended using covalent functionalisation,[11–14] non-covalent functionalisation,[15,16] solvents,[17,18] polymers[19–21] and fluorination[22,23] which protect BP from reaction with ambient water and oxygen, and can also enhance its properties for various applications. While the study of the surface chemistry and covalent modification is crucial for future application of the material, it remains largely undiscovered.

Covalent functionalisation has been achieved using nucleophilic reagents,[12] azide modification,[24] iodonium salts[13] and diazonium salts[11] which enhanced the stability up to 25 days. Wild *et. al.*[14] used K and Na intercalation compounds to exfoliate and reduce the BP surface for subsequent reaction with alkyl halides. Intercalation compounds have been widely used for the exfoliation and reduction of graphene,[25–27] however, their use with BP remains limited.[28,29] Alkali metals have been used to alter the properties of BP[30,31] but the resulting intercalation complexes suffer from poor ambient stability[32] while intercalation using alkylammonium salts can stabilise BP.[33] Tetrabutylammonium salts have been used for the formation of BP intercalation compounds under electrochemical conditions which enhanced the efficiency of exfoliation,[34,35] while ammonium salts have proven to have a facilitative effect on BP

exfoliation through edge intercalation which overcomes the interlayer van der Waals forces.[29] Here, a scalable protection strategy is presented where simultaneous exfoliation and functionalisation is achieved through sonication of BP in a tetrabutylammonium and aryl iodide solution, as displayed in **Figure 5.1**. The addition of the tetrabutylammonium salt facilitates exfoliation by acting as an intercalation agent, in correlation with theoretical studies.[33] Tetrabutylammonium salts have been used as intercalation agents to form graphene[36–40] and black phosphorus[32,33] intercalation complexes and have also been reported to promote the exfoliation of 2D materials.[34,35,41]

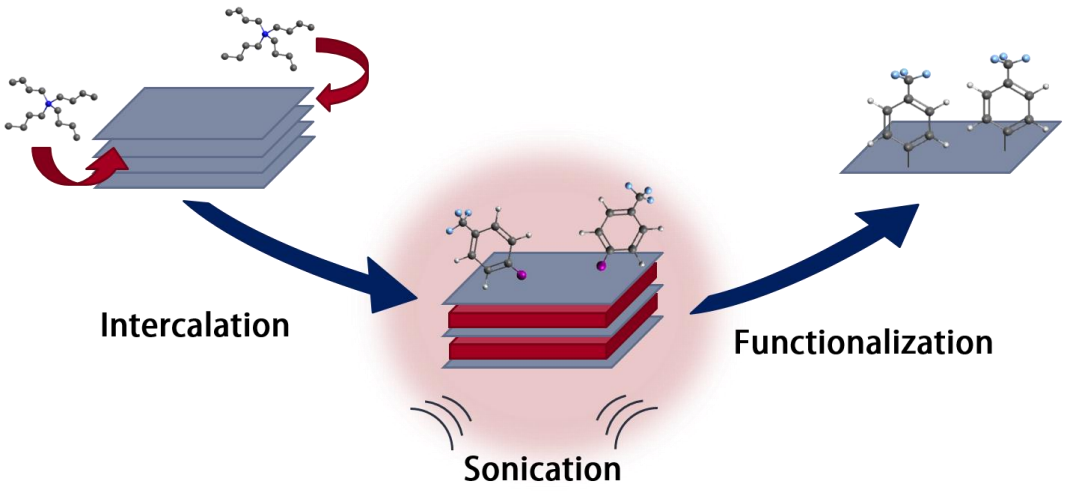

Figure 5.1: Intercalation by TBA followed by functionalisation using an aryl iodide.

Recently, in-situ radical polymerisation with poly(methyl methacrylate) (PMMA) under sonication has been employed to form a BP-polymer hybrid.[19] Ultrasonication has been employed for the simultaneous exfoliation and covalent modification of graphene[42,43] while it has also been shown to improve the efficiency of carbon nanotube functionalisation.[44] The addition of the functionalisation reagent during the exfoliation process ensures functionalisation directly after exfoliation, which significantly enhances the ambient stability due to the minimal exposure to ambient

oxidants, such as oxygen and water. BP oxidation has been proposed to occur at defect sites,[45] with the formation of an initial surface oxide catalysing further oxidation, and therefore a functionalisation strategy that protects oxygen defects during the exfoliation procedure when few-layer flakes are produced is highly desirable. Furthermore, the one-step process using aryl iodides enables the scalable production of functionalised few-layer BP flakes. Aryl iodides have been employed for the functionalisation of carbon surfaces,[46] carbon nanotubes[47] and graphene[48] while offering a number of advantages over diazonium and iodonium salts, including commercial availability and lower reactivity which allows greater control over the functionalisation layer thickness.[46]

The simultaneous exfoliation and functionalisation of BP using a sonochemical approach is described in this chapter. The production of high-quality exfoliated phosphorene nanosheets is demonstrated using STEM, TEM, AFM and Raman analysis, while the functionalised flakes are also analysed using XPS and ATR-FTIR to confirm successful covalent modification and to characterise the surface chemistry. The addition of TBA facilitates exfoliation and results in the formation of flakes with large lateral dimensions. STEM, AFM and XPS analysis confirm the ambient stability was successfully prolonged to a period of 1 week.

5.3 Experimental

5.3.1 Synthesis of Black Phosphorus

BP was synthesised using vapour-phase growth using a previously published procedure.[49] Red phosphorus (99.999%, Sigma-Aldrich, Czech Republic) was placed in a quartz glass ampoule (25mm inner diameter × 120mm length) together with 120

mg of Sn and 60 mg of SnI_4 and melt sealed under high vacuum (1x10-3 Pa). The ampoule was placed horizontally in a muffle furnace and heated to 650 °C over a period of 8 hours and after 5 hours the temperature was cooled to 400 °C for 50 hours and finally to room temperature over a period of 25 hours. The ampoule was opened in an Ar filled glovebox and repeatedly washed in DMF/carbon disulfide mixture and with pure carbon disulfide and finally dried under vacuum for 24 hours. SnI_4 was made by direct reaction of Sn (99.999%, Sigma-Aldrich, Czech Republic) and Iodine (99.999%, Sigma-Aldrich, Czech Republic) in chloroform. The obtained crystals were recrystallised from chloroform.

5.3.2 Exfoliation and Functionalisation

Anhydrous N-methyl-2-pyrrolidone (NMP), acetonitrile (ACN), dimethylformamide (DMF) were purchased from Sigma-Aldrich. Solvents were subjected to 2 purification cycles to remove traces of oxygen and water. One cycle consists of drying over molecular sieves for at least 24 h, degassing using at least 10 freeze-pump-thaw cycles and purging the solvent with Ar for at least 30 min. Black phosphorus was synthesised using vapour-phase growth. The rinsing of BP crystals following synthesis was carried out under inert conditions using dried and degassed DMF. All solvent transfer and handling of BP prior to exfoliation was carried out in a glovebox. BP was exfoliated in (1) a solution of NMP, (2) a 50 mM solution of 4-iodobenzotrifluoride (IBF) with 20 mM tetrabutylammonium hexafluorophosphate (TBAFP), (3) a 50 mM solution of bis(4-fluorophenyl)iodonium triflate (FPI) with 20 mM TBAFP for 10 h in a Schlenk flask under constant flow of Ar using a bath sonicator (Branson 1800). The intercalated sample was immersed in a TBAFP solution for 24 h followed by sonication for 10 min and the addition of an IBF solution for 12 h. The functionalised

BP solution was centrifuged at 2000 rpm for 30 min to exclude unexfoliated material and the supernatant was centrifuged at 14500 rpm for 30 min to obtain an exfoliated sample. The sample was purified using three acetonitrile washes and drop cast onto a Si or titanium coated Si wafer for further analysis.

5.3.3 Characterisation

X-ray photoelectron spectroscopy (XPS) was completed on an Oxford Applied Research Escabase XPS system (base pressure 5×10^{-10} mbar) and a nonmonochromated Al kα X-Ray source at 200 W. Survey spectra were collected at a pass energy of 100 eV, a step size of 0.7 eV, a dwell time of 0.3 s in the 0-1000 eV range. Core level spectra were recorded at a pass energy of 20 eV, a step size of 0.1 eV and a dwell time of 0.1 s. CasaXPS software was used to process spectra with peaks corrected to a Shirley background and fitted to Voigt profiles. Charge correction was applied using the C 1s peak at 285 eV. Attenuated total reflectance Fourier transform infrared (ATR-FTIR) were collected using a Nicolet 6700 Infrared Spectrometer with a liquid cooled HgCdTe detector and a Smart iTR accessory. Spectra were collected in ambient conditions at a resolution of 2 cm^{-1} and averaged over 100 scans. UV analysis was completed on a Thermo Scientific Evolution 60 S UV-Visible spectrophotometer with a resolution of ±0.8 nm using a Xenon light source. Raman scattering spectra were acquired using a QE65PRO OceanOptics spectrometer with a 50 μm width slit and a microscope with a 40 × objective to focus on the surface of substrates. A Laser Quantum GEM DPSS 532 nm laser was used for excitation. Transmission electron microscopy (TEM) analysis was performed on an FEI Titan electron microscope operating at 300 kV. Scanning transmission electron microscopy (STEM) was carried out on an FEI Helios Nanolab 600i scanning electron microscope operating at 20 kV. AFM analysis was carried out on a Park XE-100 AFM

in non-contact mode with SSS_NCHR enhanced resolution tips with XY and Z resolutions of ~2 and 0.05 nm respectively.

5.4 Results and Discussion

5.4.1 Microscopic Analysis of Black Phosphorus flakes

BP was synthesised using vapour-phase growth[49] and characterised using XPS and Raman analysis, as displayed in **Figure 5.2**. The P 2p core level displays a 15.3 % oxide shoulder at 132.1 eV compared to the main P 2p peak. The Raman modes at 367, 444 and 473 cm^{-1} correspond to the A^1_g, B^2_g and A^2_g vibrational modes.[17] The Raman modes and low amount of oxidation observed in the P 2p core level indicate a high crystal quality with a minimal amount of oxide after synthesis of BP.

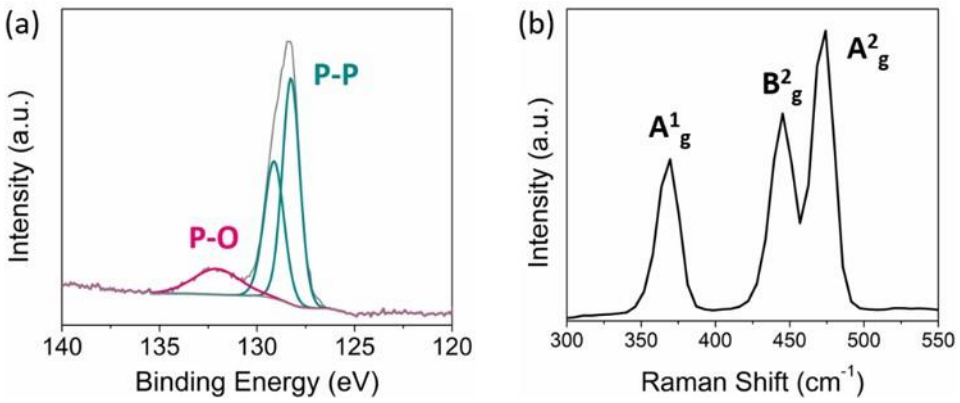

Figure 5.2: (a) P 2p core level of bulk BP displaying P-P peaks at 128.3 and 129.1 eV and P-O shoulder at 132.1 eV. (b) Raman analysis shows peaks at 369, 444 and 474 cm^{-1} which correspond to the A^1_g, A^2_g, and B^2_g modes, indicating the synthesis of crystalline BP.

Exfoliation and functionalisation was carried out by sonication of the BP crystals in a 4-iodobenzenetrifluoride (IBF) and tetrabutylammonium hexafluorophosphate (TBAFP) solution in NMP. The production of few-layer BP flakes was characterised using STEM, TEM and AFM to evaluate the effect of exfoliation and functionalisation

on crystallinity. STEM analysis displays the formation of few-layer BP flakes, as shown in **Figure 5.3**.

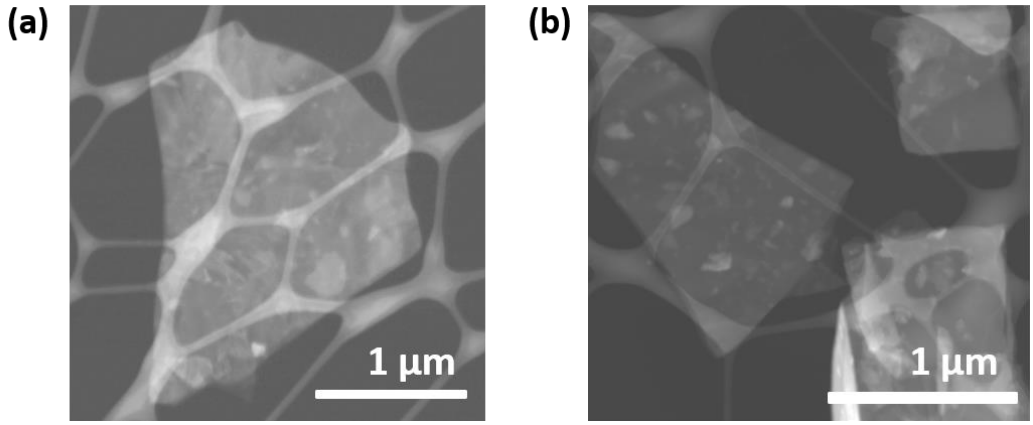

Figure 5.3: STEM analysis of IBF-functionalised BP.

TEM analysis, as shown in **Figure 5.4**, depicts the crystal lattice, with d-spacings of 1.83 and 2.66 Å. The selected area electron diffraction (SAED) pattern in **Figure 5.4**(b) also displays d-spacings of 1.53, 1.86, 2.65 and 3.47 Å, corresponding to the (200), (121), (111) and (010) planes of BP.[21,50,51]

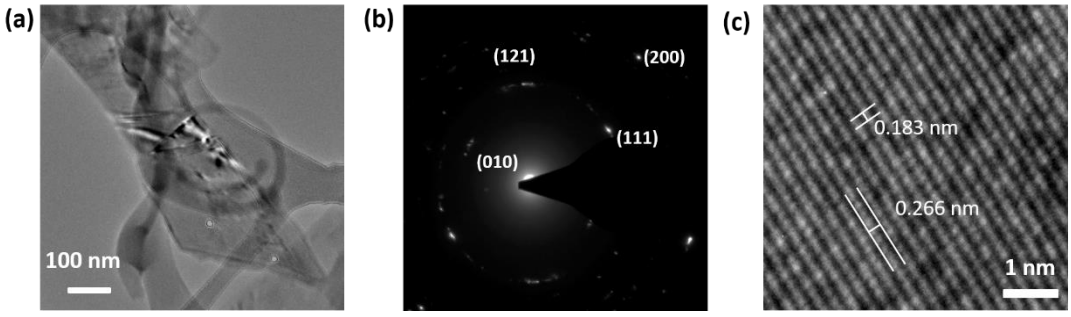

Figure 5.4: TEM analysis with (b) SAED pattern and (c) d-spacings which show the crystallinity of few-layer BP.

Raman characterisation in **Figure 5.5** displays the A^1_g, A^2_g and B^2_g peaks at 366, 444, 473 cm^{-1}, in correlation with literature reports.[17,52] The peak at 520 cm^{-1} can be attributed to the Si substrate used for analysis. TEM and Raman analysis indicate that

the BP flakes maintain their crystallinity during the exfoliation-functionalisation process.

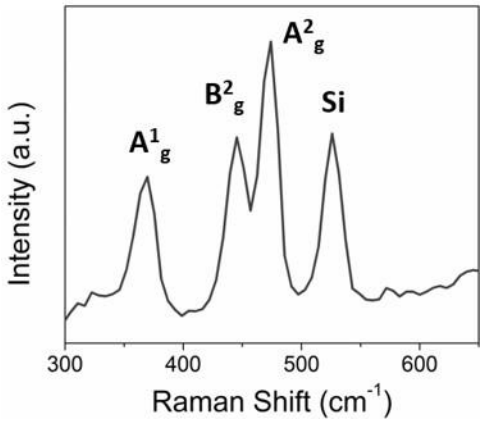

Figure 5.5: Raman analysis displays the presence of A^1_g, A^2_g and B^2_g modes of few-layer BP.

AFM analysis in **Figures 5.6**(a) and (b) shows a height of ~27 nm for IBF functionalised BP and ~16 nm for FPI functionalised BP, confirming the production of few-layer flakes.

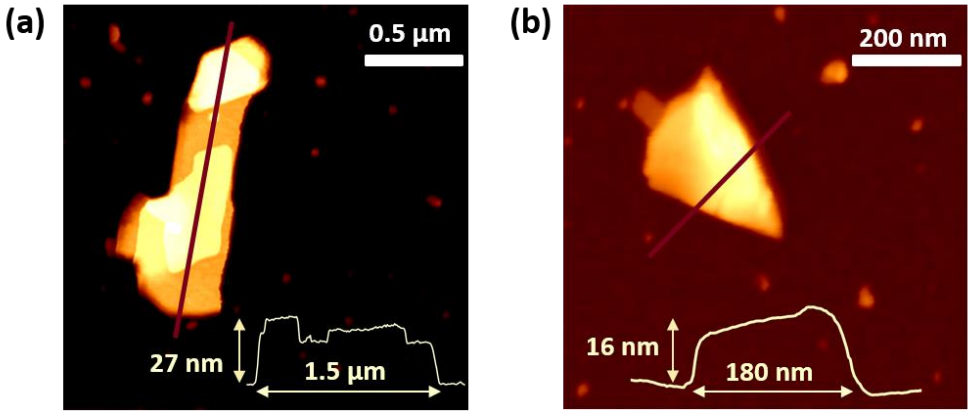

Figure 5.6: AFM analysis of (a) IBF-functionalised and (b) FPI-functionalised BP flakes.

The role of TBAFP was investigated by comparing the heights and lateral dimensions of exfoliated flakes. **Figure 5.7** displays the heights of BP exfoliated using (1)

standard exfoliation in NMP under sonication, (2) exfoliation under sonication in an IBF solution without the presence of an intercalating agent (TBAFP), (3) exfoliation under sonication in the presence of IBF and an intercalating agent (TBAFP) and (4) step-wise exfoliation by exposure to a solution of the intercalating agent, followed by minimal sonication (10 min) and then the addition of IBF.

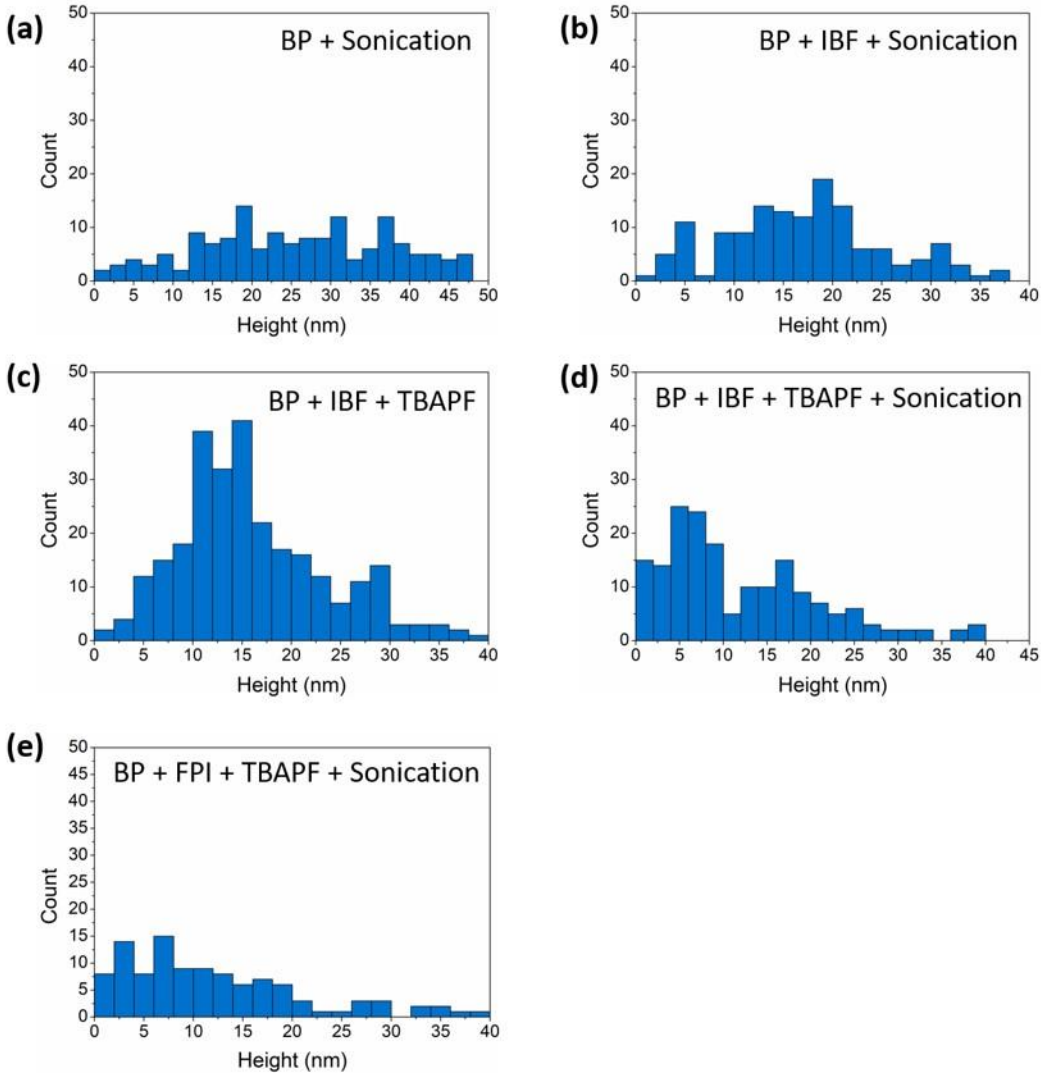

Figure 5.7: AFM analysis displaying the range of heights obtained when exfoliating BP (a) under sonication, (b) in IBF under sonication (without TBAFP), (c) in IBF and TBAFP with minimal sonication (10 min) (d) in IBF and TBAFP under continuous sonication and (e) in FPI and TBAFP under sonication.

Table 5.1 shows an increase in few-layer flakes for BP exfoliated in a solution of IBF and TBAFP under continuous sonication. The percentage of flakes with a height <10 nm was 54 % for BP exfoliated in IBF with the presence of the intercalating agent (TBAFP) and a similar percentage (50 %) was obtained for those exfoliated in FPI and

Table 5.1: Heights of exfoliated BP flakes.

Sample	<10 nm (%)	<20 nm (%)
BP + Sonication	11	37
BP + IBF + Sonication	19	67
BP + IBF + TBAFP	19	74
BP + IBF + TBAFP + Sonication	54	82
BP + FPI + TBAFP + Sonication	50	84

TBAFP. The standard BP exfoliated under sonication (without IBF and TBAFP) only showed 11 % of flakes < 10 nm which was comparable to BP exfoliated without the presence of the intercalating agent and in the stepwise exfoliation with minimal sonication, which both resulted in 19 % of flakes < 10 nm. The increase in few-layer flakes for BP exfoliated in the presence of TBAFP suggests it has a facilitative effect on exfoliation. **Figure 5.8** and **Table 5.2** show the lateral dimensions of the corresponding samples, indicating that the addition of TBAFP facilitates the formation of BP flakes with large lateral dimensions. BP exfoliated in the presence of IBF and TBAFP produced 59 % flakes with a length >0.5 µm and 30 % >1 µm, compared to BP which only provides 9 % flakes >0.5 µm and did not result in the production of flakes with dimensions greater than 1 µm. The exfoliation of BP in the presence of IBF and TBAFP but without constant sonication also showed a slight increase in the

production of few-layer flakes with large lateral dimensions compared to BP, but continuous sonication greatly increased the formation of few-layer flakes with larger lengths. The intercalation of 2D materials is aided by sonication which allows faster diffusion of intercalating species.[29] The increased amount of few-layer flakes with large lateral dimensions for BP exfoliated in the presence of TBAFP under minimal

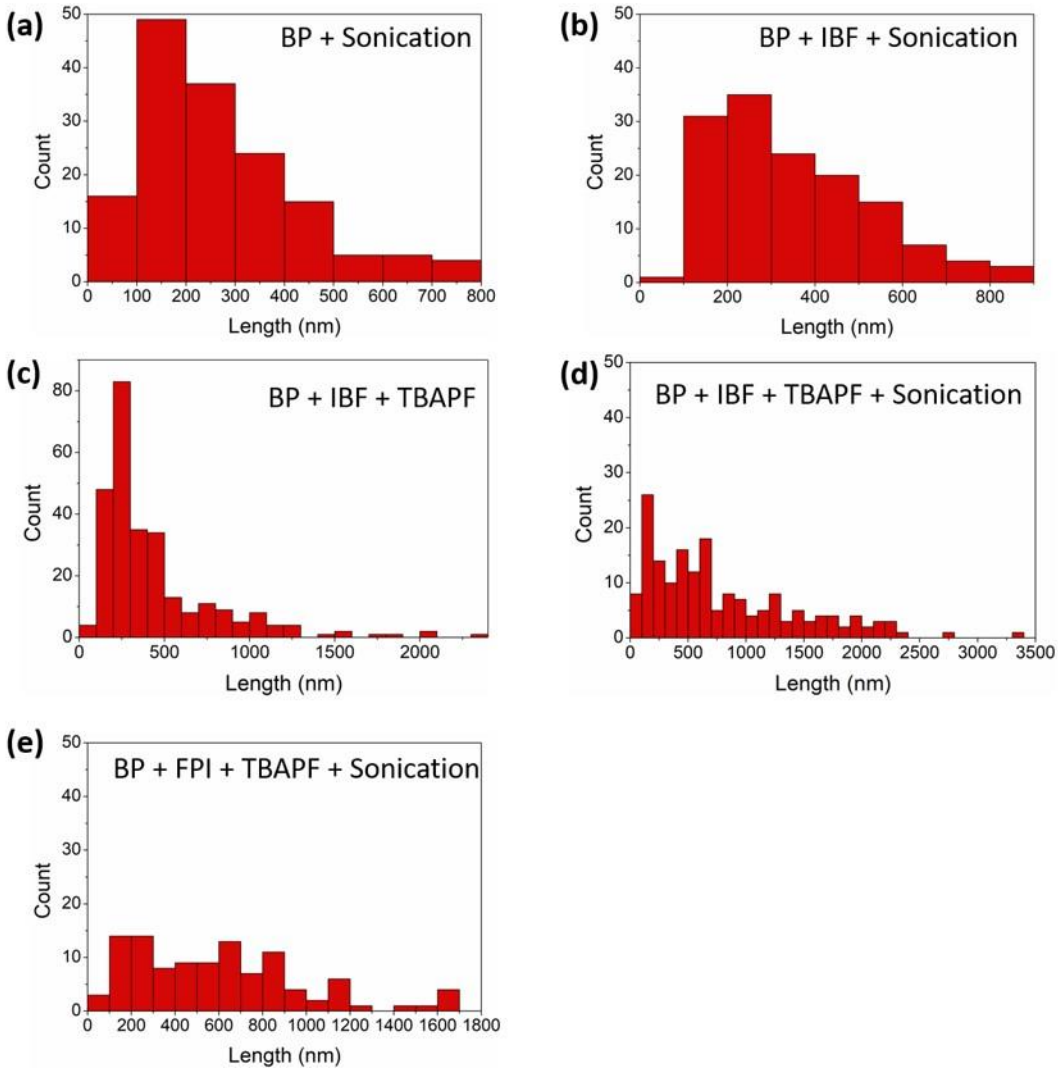

Figure 5.8: AFM analysis displaying the flake lengths obtained when exfoliating BP (a) under sonication, (b) in IBF under sonication (without TBAFP), (c) in IBF and TBAFP with minimal sonication (10 min) (d) in IBF and TBAFP under continuous sonication and (e) in FPI and TBAFP under sonication.

sonication indicates it acts as an intercalating agent that facilitates exfoliation, in correlation with theoretical studies,[33] although prolonged sonication promotes the separation of the layers and aids intercalation.[29] TBA salts have been used for graphene intercalation due to the flexibility of the n-butyl chains[36,39] while the butyl chain length is optimal for BP intercalation compared to tetramethyl and tetraoctylammonium cations.[35] The flattened configuration of TBA displays a diameter of 0.47 nm which closely matches the 0.53 nm interlayer spacing of BP also allowing efficient intercalation.[35,53] The intercalation enhances the formation of few-layer flakes with large lateral dimensions which is beneficial for device applications.

Table 5.2: Lengths of exfoliated BP flakes.

Sample	>0.5 μm (%)	>1 μm (%)
BP + Sonication	9	0
BP + IBF + Sonication	21	0
BP + IBF + TBAFP	26	9
BP + IBF + TBAFP + Sonication	59	30
BP + FPI + TBAFP + Sonication	56	14

5.4.2 Characterisation of the Surface Chemistry of Functionalised Black Phosphorus

The characterisation of functionalised BP flakes using ATR-FTIR analysis indicates reaction of aryl groups with BP. **Figure 5.9**(a) displays the ATR-FTIR analysis of IBF-functionalised BP which shows the presence of a para-substituted out-of-plane C-H bend at 845 cm^{-1}, an in-plane C-H bend at 1014 cm^{-1}, asymmetric CF_3 stretches at

1149 and 1120 cm^{-1} and a symmetric CF_3 stretch at 1318 cm^{-1}, confirming covalent functionalisation of the aryl group.[54–56] The PF_6^- anion cannot be observed at 825 and 737 cm^{-1}, indicating the absence of the counterion on BP.[57,58] The ATR-FTIR analysis of FPI-functionalised BP is displayed in **Figure 5.9**(b). Similarly, covalent attachment can be observed through the presence of an out-of-plane C-H stretches at 800 and 845 cm^{-1}, an in-plane C-H stretch at 1028 cm^{-1} and a C-F stretch at 1260 cm^{-1}.[59] Additionally, the minor presence of a symmetric S=O stretch at 1152 cm^{-1} suggests passivation of the triflate counterion.[57]

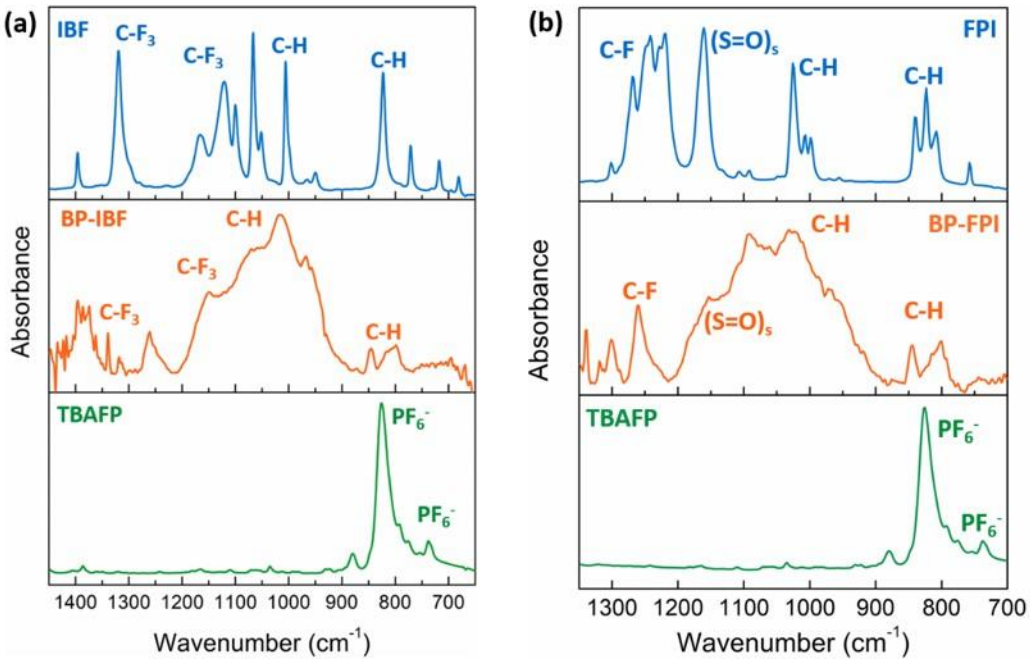

Figure 5.9: ATR-FTIR analysis of (a) IBF-functionalised BP and (b) FPI-functionalised BP.

XPS analysis was used to further characterise the surface chemistry of aryl-functionalised BP.

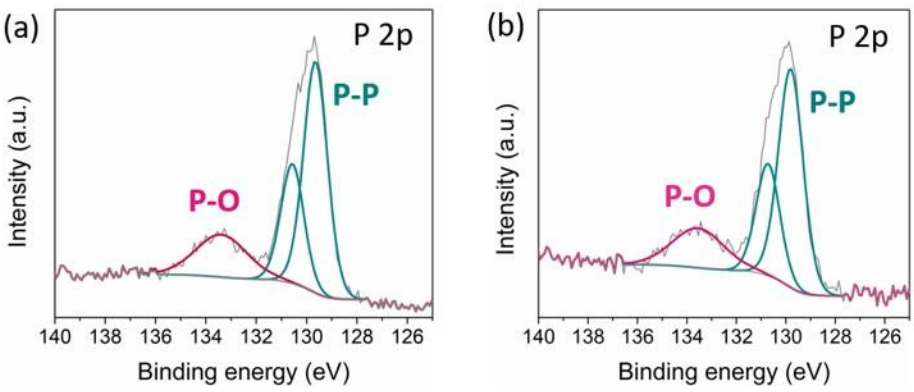

Figure 5.10: P 2p core levels of (a) IBF-functionalised BP and (b) FPI-functionalised BP.

Functionalisation of BP using FPI (20.1 %) and IBF (20.8 %) resulted in minimal oxidation after exfoliation and functionalisation, based on analysis of the P 2p core level, as displayed in **Figure 5.10**.

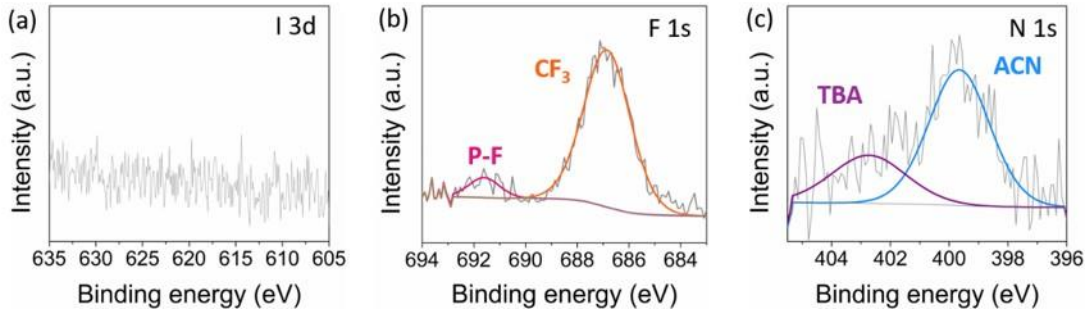

Figure 5.11: XPS analysis of the (a) I 3d, (b) F 1s and (c) N 1s core levels of IBF-functionalised BP.

Figure 5.11(a) shows the absence of the I 3d peak at ~619 eV indicating dissociation of the aryl iodide and subsequent arylation of BP. The F 1s peak shows a contribution at 687 eV which can be attributed to the CF_3 group, suggesting the presence of the CF_3 substituted aryl group on the surface. The F 1s peak also displays a contribution at 691.6 eV, which can be attributed to the fluorination of BP.[22,23] As the electrolyte also contains a source of fluorine, functionalisation using only TBAFP was carried out to confirm the F 1s signal can be attributed to the CF_3 group rather than the PF_6^-

counterion. **Figure 5.12** displays XPS analysis of BP exfoliated in a solution of TBAFP. The absence of a F 1s signal at 687 eV indicates the F 1s peak observed for IBF functionalised sample can be attributed to the CF_3 aryl group rather than the PF_6^- counterion. Furthermore, the absence of a contribution in the P 2p core level at 136.5 eV confirms the absence of PF_6^- in IBF-functionalised BP.

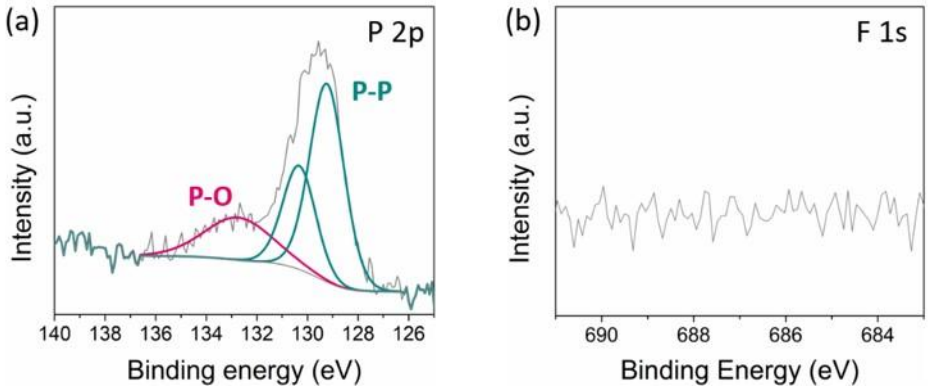

Figure 5.12: The (a) P 2p and (b) F 1s core levels of BP exfoliated in a solution of TBAFP without the presence of IBF did not result in a F 1s signal.

Functionalisation using FPI was also characterised using XPS analysis as shown in **Figure 5.13** which shows the absence of an I 3d peak and the presence of a F 1s peak at 688.5 eV, indicative of the attachment of the fluorinated aryl group.

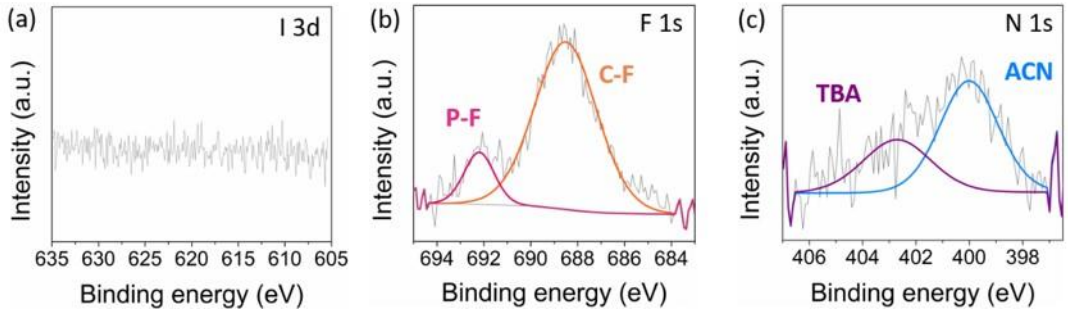

Figure 5.13: (a) I 3d, (b) F 1s and (c) N 1s core levels of FPI-functionalised BP.

In combination, FTIR and XPS of the F 1s core level confirm the covalent attachment of aryl groups on BP using an aryl iodide (IBF) and a diaryliodonium salt (FPI).

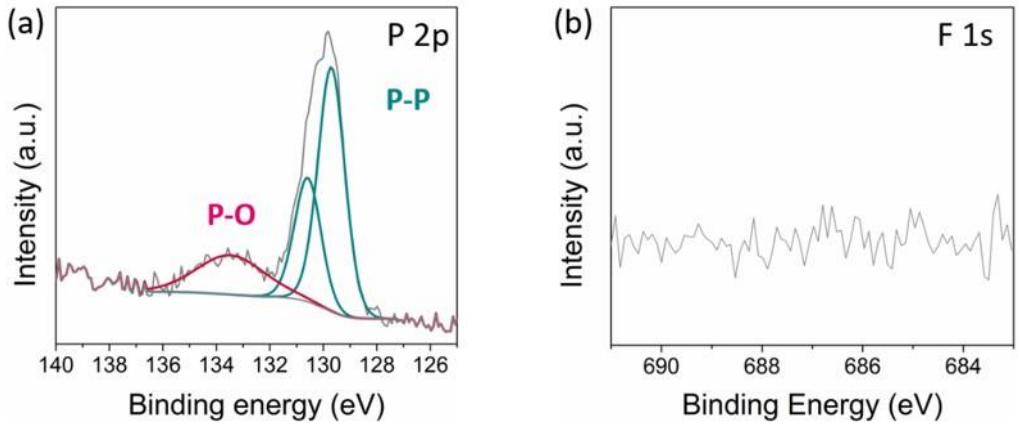

Figure 5.14: The (a) P 2p and (b) F 1s core levels of BP exfoliated in an IBF solution without the presence of TBAFP did not result in covalent attachment, as indicated by the absence of a discernible F 1s signal.

The N 1s core level gives further insight into the surface passivation and more specifically the role of the electrolyte, tetrabutylammonium hexafluorophosphate (TBAFP). When the functionalisation process was carried out without the presence of TBAFP a F 1s signal was not observed, suggesting functionalisation did not occur (**Figure 5.14**). The need for TBAFP during functionalisation is in agreement with literature reports; the covalent functionalisation of BP using iodonium and diazonium salts only gives a high extent of functionalisation in the presence of TBAFP.[11–13,40] The extent of TBAFP passivation was quantified using the XPS analysis. The N 1s peak for IBF-functionalised BP shows a peak at 400.0 eV attributed to solvent passivation and at 402.7 eV corresponding to the binding energy (BE) of tetrabutylammonium (TBA), as displayed in **Figure 5.11**. When BP is exfoliated in a solution of TBAFP alone (**Figure 5.12**) the absence of a F 1s peak indicates the PF_6^-

counterion of TBAFP does not bind to the surface. Additionally, the P 2p peak does not display a contribution for PF_6^- which is observed at 136.5 eV. The absence of a discernible contribution in the P 2p peak associated with PF_6^- indicates TBAFP does not passivate the surface, but rather the TBA interacts with the surface. TBA salts have been reported to facilitate exfoliation[41] and have also been employed as intercalation agents.[36–39] Therefore TBA may play a similar role in the exfoliation of BP which was evaluated by carrying out a stepwise exfoliation-functionalisation procedure, by immersion in a TBAFP solution, followed by minimal sonication (10 min) to separate BP layers and subsequent functionalisation using IBF. The role of TBA as an intercalating agent is confirmed by the AFM analysis where few-layer flakes (2.5-15 nm) are produced when exfoliation is carried out in the presence of TBA with minimal sonication, as displayed in **Figure 5.15**. Exfoliation in the presence of TBAFP resulted in 19 % of flakes with heights greater than 10 nm, an increase compared to the exfoliation of BP without the presence of TBAFP (11 %), considering the solution was subjected to minimal sonication. TBAFP has been employed as an intercalating agent for the exfoliation of graphene and black phosphorus[32–35] while it has been reported to facilitate exfoliation of layered oxides, hydroxides[60] and perovskites,[61] in correlation with our results. The addition of an IBF solution after intercalation and sonication also resulted in the covalent attachment of aryl groups. The presence of a F 1s peak (**Figure 5.16**) indicates the covalent attachment of the aryl group. TBAFP is often added as an electrolyte during the functionalisation of 2D materials using aryldiazonium salts[11,62] but its role is rarely defined, although the addition has been reported to increase the degree of functionalisation.[63] Enhanced functionalisation has been attributed to the intercalation of flakes and stabilisation after exfoliation which allows increased accessibility of the functionalisation reagent

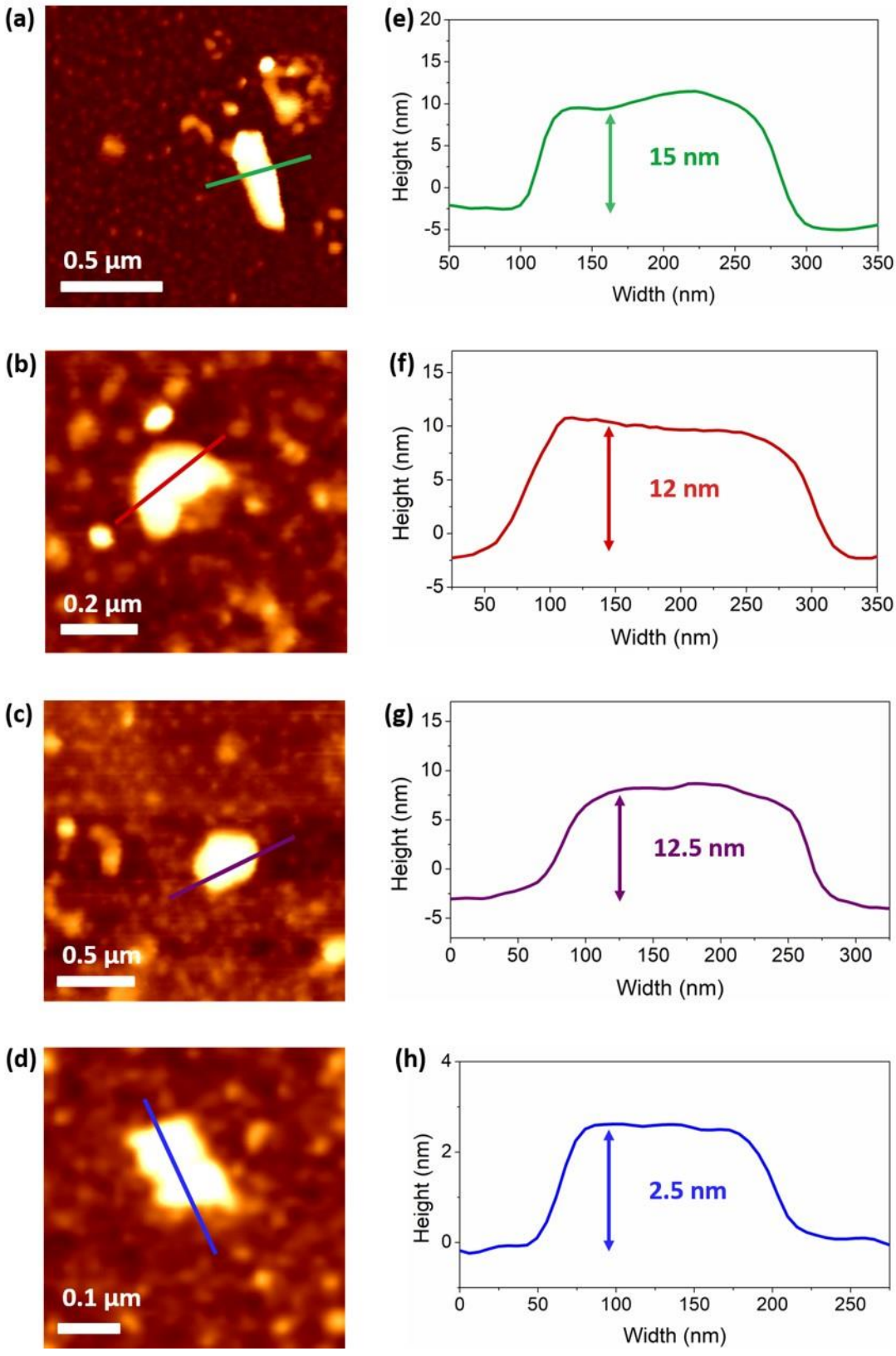

Figure 5.15: (a)-(d) AFM analysis and (e)-(h) corresponding line profiles display the formation of few-layer BP flakes through intercalation of TBA with minimal sonication.

to the basal plane.[40,64–66] The exact role of TBAFP remains unclear but the low extent of functionalisation in the absence of TBAFP suggests it plays a critical role during functionalisation.

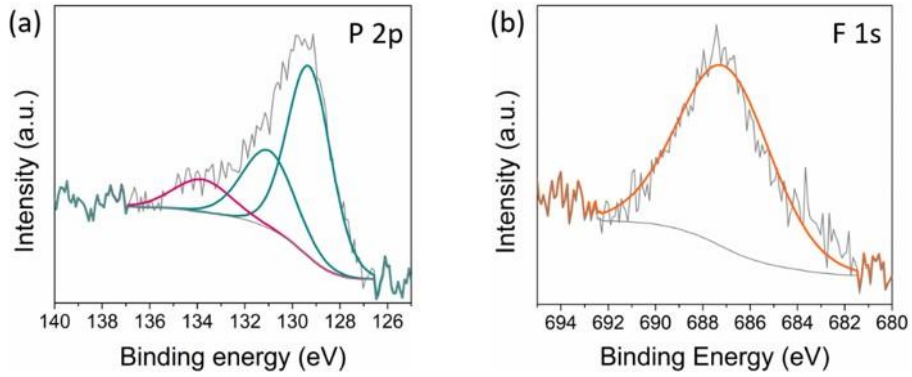

Figure 5.16: (a) P 2p and (b) F 1s core levels for a sample prepared using stepwise intercalation using TBA, followed by minimal sonication (10 min) and exposure to an IBF solution also displayed signs of functionalisation.

The binding of aryl groups to BP has been reported to occur through P-sites, either through cleavage of a P-P bond or insertion of a P-C bond resulting in the formation of a four-coordinate P which can create lattice distortion.[11] DFT studies have suggested the cleavage of a P-P bond occurs during covalent attachment which results in the formation of a 3-coordinate phosphorus with 2 P-P bonds and 1 P-C bond.[12,14] The characterisation of P-C bonds is difficult due to their low concentration and proximity in BE to P-O bonds in the P 2p core level. The attachment of aryl groups could also occur through attachment to existing surface oxide sites which has been observed previously.[12,13,67] The inhibition of the oxide formation over a period of 1 week also confirms this reaction mechanism, as binding to surface oxide sites prevents further oxidation of the BP (**Figure 5.20**).[13]

5.4.3 Solvent Passivation and Ambient Stability of Functionalised Black Phosphorus

Liquid exfoliation often results in solvent passivation which is undesirable for the processing of flakes, as the remaining solvent can have an adverse effect on the electrical characteristics of BP.[68] While a contribution is seen at ~400 eV, the combined exfoliation-functionalisation process significantly reduces solvent passivation. **Figure 5.17** displays the N 1s:P 2p ratios which can be used as an indication of the extent of solvent passivation. Unfunctionalised BP displays a N 1s:P 2p ratio of 0.49 while IBF-functionalised BP results in a reduction to 0.2, indicating the covalent attachment results in disruption of the solvent passivation layer. The N 1s:P 2p ratio reduces over a period of 1 week for both bare and IBF-functionalised BP. The decrease of 60 % in the N 1s:P 2p ratios for FPI and IBF-functionalisation compared to unfunctionalised BP indicates functionalisation successfully removes a large amount of solvent passivation making BP more suitable for device fabrication.

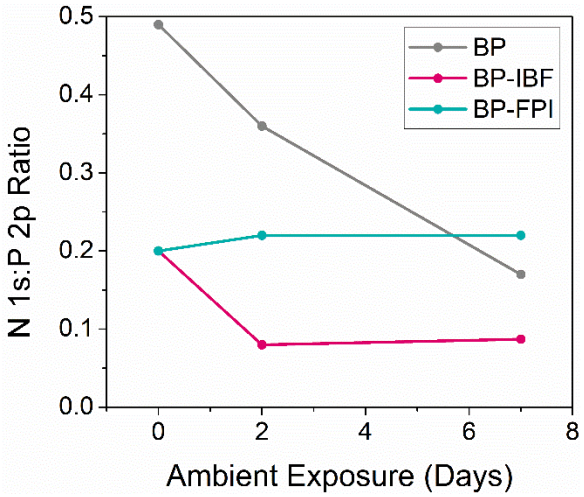

Figure 5.17: The N 1s:P 2p ratio as a function of ambient exposure displays the variation of solvent passivation for unfunctionalised, FPI- and IBF-functionalised BP.

The passivation of BP with aryl groups results in a significant increase in the ambient stability of BP. AFM analysis was used to monitor the oxidation of a functionalised and an unfunctionalised flake over a 1 week period. **Figure 5.18**(a) shows an unfunctionalised flake with a height of ~27 nm, which displays defined edges and a flat surface. Ambient exposure of the flake for 1 week resulted in the formation of a large bump on the flake surface and degradation of the flake edges, which can be attributed to oxidation, as shown in **Figures 5.18**(b)-(c). In comparison, the functionalised BP flake has a height of ~16 nm, which did not show signs of deterioration during 1 week of ambient exposure and maintains its flat surface, as displayed in **Figures 5.18**(d)-(f).

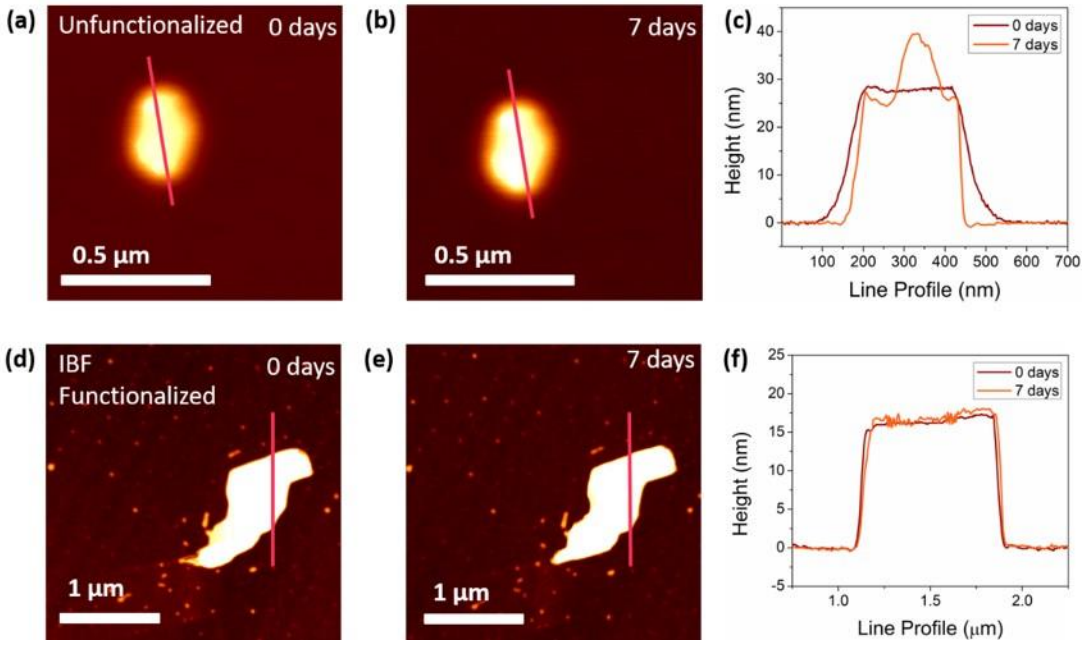

Figure 5.18: AFM analysis of IBF-functionalised BP during (a) 0 to (b) 7 days of ambient exposure and unfunctionalised BP during (d) 0 to (d) 7 days of ambient exposure. Corresponding line profiles for (c) IBF-functionalised and (f) unfunctionalised BP show the surface topography during ambient exposure.

The increased ambient lifetime of functionalised BP was also confirmed using STEM analysis, as shown in **Figure 5.19**. While 1 week of ambient exposure results in the

disintegration of the BP flake, IBF-functionalisation allows preservation of the flake morphology. The loss of edges for unfunctionalised BP can be seen in **Figures 5.19**(a)-(b) and the surface becomes covered in protrusions due to the formation of liquid phosphorus oxidation products.[8] The IBF-functionalised BP flake surpasses the ambient stability of unfunctionalised BP, as shown in **Figures 5.19**(c)-(d). The flake edges remained defined during a 1 week period, while **Figure 5.19**(b) displays the absence of surface protrusions demonstrating the high stability of IBF-functionalised BP.

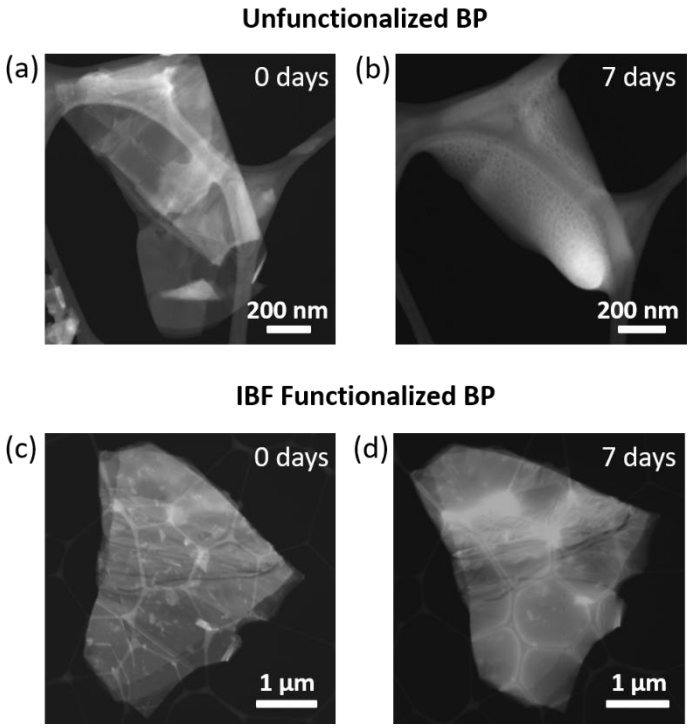

Figure 5.19: STEM analysis of unfunctionalised BP at (a) 0 days and (b) 7 days. IBF-functionalised BP at (c) 0 days and (d) 7 days.

XPS analysis gives a spectroscopic representation of the superior ambient stability of functionalised BP by evaluation of the P 2p and O 1s core levels. The P 2p core level can be used to monitor BP oxidation, as the oxide shoulder at 132-136 eV can be

attributed to the formation of P-O species. **Figures 5.20**(a)-(b) displays the evolution of the P 2p and O 1s core levels of unfunctionalised BP, FPI and IBF functionalised BP. The P 2p core level of freshly exfoliated BP displays an oxide shoulder of 32.7 % compared to the main P 2p peak, which increases to 36.7 % after 2 days and 63.6 % after 1 week. In comparison, the IBF-functionalised BP shows an oxide component of 20.8 % with 2 days of ambient exposure resulting in an increase to 24.2 % and a further increase to 38.0 % after a 1 week period. Similarly, FPI displays a 20.1 % oxide component which rises to 26.9 % and 32.6 % after a 2 day and 1 week period, respectively. The minor increase in the oxide component of the P 2p core level of IBF and FPI-functionalised BP compared to unfunctionalised BP confirms its low reactivity in ambient conditions.

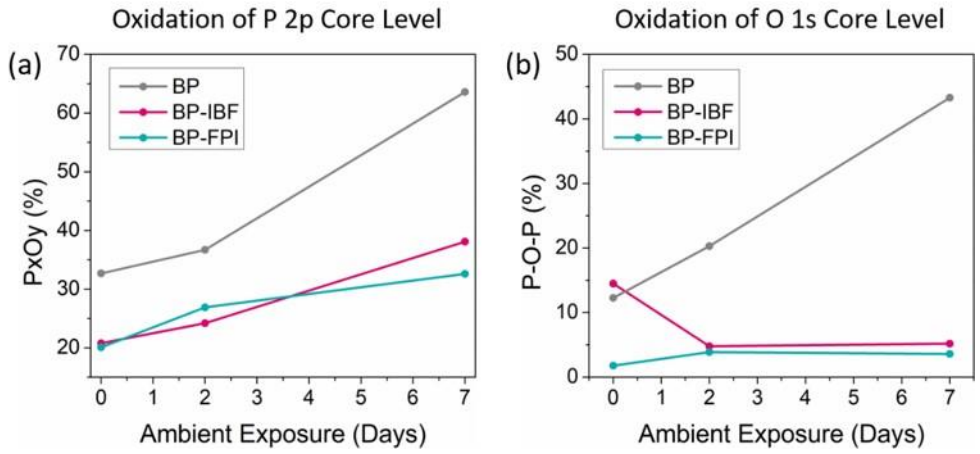

Figure 5.20: Evolution of the (a) P 2p and (b) O 1s core levels over a 1 week period show the superior ambient stability of functionalised BP.

BP oxidation occurs through the formation of bridged and non-bridged oxide species.[8,9,69] While the P 2p component gives an indication of the total oxidation, the O 1s peak allows deconvolution of the bridging and non-bridging species giving further insight into BP oxidation. The evolution of the P-O-P component can be used as an indication of the extent of oxidation, as P-O-P species react further to form

volatile phosphoric acids which are not detected using XPS analysis due to their volatility under vacuum.[8,45,70] Exfoliation of bare BP displays a 12.3 % P-O-P component compared to the total O 1s component. The P-O-P component further increases to 20.3 % after 2 days and 43.3 % after a period of 1 week in ambient conditions, as shown in **Figure 5.20**(b). IBF-functionalisation results in the formation of a similar amount of bridged oxide species (14.5 %) which decreases to 4.8 % after 2 days and 5.2 % after 1 week. FPI did not form a significant amount of P-O-P species (1.8 %). Similarly only a minor amount of P-O-P species were detected over a period of 1 week (3.6 %). Exfoliation of functionalised and unfunctionalised BP results in a similar amount of P-O-P formation, however, after initial oxide formation unfunctionalised BP appears to oxidise further at a considerable rate. The decrease in the P-O-P component for IBF-functionalised BP can be attributed to the evaporation of the volatile phosphorus oxides in the high vacuum XPS chamber.[13] Additional oxidation of functionalised BP is inhibited and followed by removal of phosphorus oxides. FPI functionalisation resulted in minimal P-O-P generation and subsequently only displays minor oxidation over a 1 week period. The P 2p and O 1s core levels indicate IBF and FPI-functionalised BP display superior ambient stability compared to unfunctionalised BP. Oxidation of BP occurs through reaction of oxygen with the BP surface forming non-bridging oxide species which convert to non-bridging species and then phosphoric oxyacids.[8] Therefore a functionalisation strategy that inhibits the formation of P-O-P species preserves the BP and significantly protects it from further oxidation.

5.5 Conclusions

The simultaneous exfoliation and functionalisation of BP was used to produce few-layer flakes with enhanced ambient stability. AFM analysis was used to demonstrate the role of TBA as an intercalating agent that resulted in the formation of a higher proportion of few-layer flakes with large lateral dimensions. The surface chemistry of IBF-functionalised BP was characterised using XPS and ATR-FTIR, which revealed aryl functionalisation. Aryl functionalisation likely occurred through attachment to P- and O-sites, giving enhanced stability of up to 1 week, as demonstrated using STEM, AFM and XPS analysis. The simultaneous exfoliation and functionalisation ensures immediate functionalisation which greatly minimises the oxidation of BP, while solvent passivation is minimised by functionalisation. The reduction in solvent passivation and formation of few-layer flakes with large lateral dimensions demonstrates the simultaneous exfoliation-functionalisation produces flakes more suitable for device fabrication.

5.6 References

(1) Chen, P.; Li, N.; Chen, X.; Ong, W.; Zhao, X. The Rising Star of 2D Black Phosphorus beyond Graphene : Synthesis , Properties and Electronic Applications The Rising Star of 2D Black Phosphorus beyond Graphene : Synthesis , Properties and Electronic Applications. *2D Mater.* **2017**, *5* (1), 014002.

(2) Gusmao, R.; Sofer, Z.; Pumera, M. Black Phosphorus Rediscovered: From Bulk to Monolayer. *Angew. Chemie Int. Ed.* **2017**, *56* (28), 8052–8072.

(3) Li, L.; Yu, Y.; Ye, G. J.; Ge, Q.; Ou, X.; Wu, H.; Feng, D.; Chen, X. H.; Zhang, Y. Black Phosphorus Field-Effect Transistors. *Nat. Nanotechnol.* **2014**, *9* (5), 372–377.

(4) Liu, H.; Du, Y.; Deng, Y.; Ye, P. D. Semiconducting Black Phosphorus: Synthesis, Transport Properties and Electronic Applications. *Chem. Soc. Rev.* **2015**, 2732–2743.

(5) Zhang, Y.; Zheng, Y.; Rui, K.; Hng, H. H.; Hippalgaonkar, K.; Xu, J.; Sun, W.; Zhu, J.; Yan, Q.; Huang, W. 2D Black Phosphorus for Energy Storage and Thermoelectric Applications. *Small* **2017**, *13* (28), 1700661.

(6) Sun, J. A Phosphorene-Graphene Hybrid Material as a High-Capacity Anode for Sodium-Ion Batteries. *Nat. Nanotechnol.* **2015**, *10* (11), 980–985.

(7) Jia, Y.; Xia, F.; Wang, H. Rediscovering Black Phosphorus as an Anisotropic Layered Material for Optoelectronics and Electronics. *Nat. Commun.* **2014**, *5*, 4458.

(8) Van Druenen, M.; Davitt, F.; Collins, T.; Glynn, C.; O'Dwyer, C.; Holmes, J.

D.; Collins, G. Evaluating the Surface Chemistry of Black Phosphorus during Ambient Degradation′. *Langmuir* **2019**, *35* (6), 2172–2178.

(9) Plutnar, J.; Sofer, Z.; Pumera, M. Products of Degradation of Black Phosphorus. *ACS Nano* **2018**, *12* (8), 8390–8396.

(10) Island, J. O.; Steele, G. A.; Zant, H. S. J. van der; Castellanos-Gomez, A. Environmental Instability of Few-Layer Black Phosphorus. *2D Mater.* **2015**, *2* (1), 011002.

(11) Ryder, C. R.; Wood, J. D.; Wells, S. A.; Yang, Y.; Jariwala, D.; Marks, T. J.; Schatz, G. C.; Hersam, M. C. Covalent Functionalization and Passivation of Exfoliated Black Phosphorus via Aryl Diazonium Chemistry. *Nat. Chem.* **2016**, *8* (6), 597–602.

(12) Sofer, Z.; Luxa, J.; Bouša, D.; Sedmidubský, D.; Lazar, P.; Hartman, T.; Hardtdegen, H.; Pumera, M. The Covalent Functionalization of Layered Black Phosphorus by Nucleophilic Reagents. *Angew. Chemie Int. Ed.* **2017**, *56* (33), 9891–9896.

(13) Van Druenen, M.; Davitt, F.; Collins, T.; Glynn, C.; O'Dwyer, C.; Holmes, J. D.; Collins, G. Covalent Functionalization of Few-Layer Black Phosphorus Using Iodonium Salts and Comparison to Diazonium Modified Black Phosphorus. *Chem. Mater.* **2018**, *30* (14), 4667–4674.

(14) Wild, S.; Fickert, M.; Mitrovic, A.; Lloret, V.; Neiss, C.; Vidal-moya, J. Ø. A.; Rivero-crespo, M.; Ø, A. L.; Werbach, K.; Peterlik, H.; Grabau, M.; Wittk, H.; Papp, C.; Steinruck, H.; Pichler, T.; Gçrling, A.; Hauke, F.; Abellan, G.; Hirsch, A. Lattice Opening upon Bulk Reductive Covalent Functionalization of Black Phosphorus. *Angew. Chemie - Int. Ed.* **2019**, *58* (17), 5763–5768.

(15) Abellán, G.; Lloret, V.; Mundloch, U.; Marcia, M.; Neiss, C.; Görling, A.; Varela, M.; Hauke, F.; Hirsch, A. Noncovalent Functionalization of Black Phosphorus. *Angew. Chemie Int. Ed.* **2016**, *55* (47), 14557–14562.

(16) Gusmão, R.; Sofer, Z.; Pumera, M. Functional Protection of Exfoliated Black Phosphorus by Noncovalent Modification with Anthraquinone. *ACS Nano* **2018**, *12* (6), 5666–5673.

(17) Hanlon, D.; Backes, C.; Doherty, E.; Cucinotta, C. S.; Berner, N. C.; Boland, C.; Lee, K.; Harvey, A.; Lynch, P.; Gholamvand, Z.; Zhang, S.; Wang, K.; Moynihan, G.; Pokle, A.; Ramasse, Q. M.; McEvoy, N.; Blau, W. J.; Wang, J.; Abellan, G.; Hauke, F.; Hirsch, A.; Sanvito, S.; O'Regan, D. D.; Duesberg, G. S.; Nicolosi, V.; Coleman, J. N. Liquid Exfoliation of Solvent-Stabilized Few-Layer Black Phosphorus for Applications beyond Electronics. *Nat. Commun.* **2015**, *6*, 8563.

(18) Abellán, G.; Wild, S.; Lloret, V.; Scheuschner, N.; Gillen, R.; Mundloch, U.; Maultzsch, J.; Varela, M.; Hauke, F.; Hirsch, A. Fundamental Insights into the Degradation and Stabilization of Thin Layer Black Phosphorus. *J. Am. Chem. Soc.* **2017**, *139* (30), 10432–10440.

(19) Passaglia, E.; Cicogna, F.; Costantino, F.; Coiai, S.; Legnaioli, S.; Lorenzetti, G.; Borsacchi, S.; Geppi, M.; Telesio, F.; Heun, S.; Ienco, A.; Serrano-ruiz, M.; Peruzzini, M. Polymer-Based Black Phosphorus (BP) Hybrid Materials by in Situ Radical Polymerization: An Effective Tool To Exfoliate BP and Stabilize BP Nanoflakes. *Chem. Mater.* **2018**, *30* (6), 2036–2048.

(20) Cao, Y.; Tian, X.; Gu, J.; Liu, B.; Zhang, B.; Song, S.; Fan, F.; Chen, Y.; Yaming Cao, Xiangyu Tian, Junwei Gu, Bo Liu, Bin Zhang, Sannian Song, Fei

Fan, A.; Chen, Y. Covalent Functionalization of Black Phosphorus with Conjugated Polymer for Information Storage. *Angew. Chemie Int. Ed.* **2018**, *57* (17), 4543–4548.

(21) Zhang, Y.; Dong, N.; Tao, H.; Yan, C.; Huang, J.; Liu, T.; Robertson, A. W.; Texter, J.; Wang, J.; Sun, Z. Exfoliation of Stable 2D Black Phosphorus for Device Fabrication. *Chem. Mater.* **2017**, *29* (15), 6445–6456.

(22) Tang, X.; Liang, W.; Zhao, J.; Li, Z.; Qiu, M.; Fan, T. Fluorinated Phosphorene: Electrochemical Synthesis, Atomistic Fluorination, and Enhanced Stability. *Small* **2017**, *13* (47), 1702739.

(23) Jan Plutnar, Jirí Šturala, Vlastimil Mazánek, Zdenek Sofer, and M. P. Fluorination of Black Phosphorus — Will Black Phosphorus Burn Down in the Elemental Fluorine ? *Adv. Funct. Mater.* **2018**, *28* (35), 1801438.

(24) Yajuan Liu, Pengfei Gao, Taiming Zhang, Xianjun Zhu, Mengmeng Zhang, Muqing Chen, P.; Du, Guan-Wu Wang, Hengxing Ji, Jinlong Yang, and S. Y. Azide Passivation of Black Phosphorus Nanosheets: Covalent Functionalization Affords Ambient Stability Enhancement. *Angew. Chemie Int. Ed.* **2019**, *58* (5), 1479–1483.

(25) Viculis, L. M.; Mack, J. J.; Mayer, O. M.; Thomas, H.; Kaner, R. B. Intercalation and Exfoliation Routes to Graphite Nanoplatelets. *J. Mater. Chem.* **2005**, *15*, 974–978.

(26) Yoo, E.; Kim, J.; Hosono, E.; Zhou, H.; Kudo, T.; Honma, I. Large Reversible Li Storage of Graphene Nanosheet Families for Use in Rechargeable Lithium Ion Batteries 2008. *Nano Lett.* **2008**, *8* (8), 2277–2282.

(27) Englert, J. M.; Dotzer, C.; Yang, G.; Schmid, M.; Papp, C.; Spiecker, E.; Hauke, F.; Hirsch, A.; Gottfried, J. M.; Steinru, H. Covalent Bulk Functionalization of Graphene. *Nat. Chem.* **2011**, *3* (4), 279–286.

(28) Abellán, G.; Neiss, C.; Lloret, V.; Wild, S.; Chac, J. C.; Werbach, K.; Fedi, F.; Shiozawa, H.; Gçrling, A.; Peterlik, H.; Pichler, T.; Hauke, F.; Hirsch, A. Exploring the Formation of Black Phosphorus Intercalation Compounds with Alkali Metals. *Angew. Chemie* **2017**, *56* (48), 15267–15273.

(29) Ng, A.; Sutto, T. E.; Matis, B. R.; Deng, Y.; Ye, P. D.; Stroud, R. M.; Brintlinger, T. H.; Bassim, N. D. Chemically Exfoliating Large Sheets of Phosphorene via Choline Chloride Urea Viscosity-Tuning. *Nanotechnology* **2017**, *28* (15), 155601.

(30) Ren, X.; Lian, P.; Xie, D.; Yang, Y.; Mei, Y. Properties , Preparation and Application of Black Phosphorus/Phosphorene for Energy Storage: A Review. *J. Mater. Sci.* **2017**, *52* (17), 10364–10386.

(31) Zhang, R.; Waters, J.; Geim, A. K.; Grigorieva, I. V. Intercalant-Independent Transition Temperature in Superconducting Black Phosphorus. *Nat. Commun.* **2017**, *8*, 15036.

(32) Wang, C.; He, Q.; Halim, U.; Liu, Y.; Zhu, E.; Lin, Z.; Xiao, H.; Duan, X.; Feng, Z.; Cheng, R.; Weiss, N. O.; Ye, G.; Huang, Y.; Wu, H.; Cheng, H.; Shakir, I.; Liao, L.; Chen, X.; Iii, W. A. G.; Huang, Y.; Duan, X. Monolayer Atomic Crystal Molecular Superlattices. *Nat. Publ. Gr.* **2018**, *555* (7695), 231–236.

(33) Jain, R.; Singh, Y.; Cho, S.; Sasikala, S. P.; Koo, H.; Narayan, R.; Jung, H.; Jung, Y.; Kim, S. O. Ambient Stabilization of Few Layer Phosphorene via

Noncovalent Functionalization with Surfactants – Systematic 2D NMR Characterization in Aqueous Dispersion Ambient Stabilization of Few Layer Phosphorene via Noncovalent Functionalization with Surfactants. *Chem. Mater.* **2019**, *31* (8), 2786–2794.

(34) Huang, Z.; Hou, H.; Zhang, Y.; Wang, C.; Qiu, X.; Ji, X. Layer-Tunable Phosphorene Modulated by the Cation Insertion Rate as a Sodium-Storage Anode. *Adv. Mater.* **2017**, *29* (34), 1702372.

(35) Li, J., Chen, C., Liu, S., Lu, J., Goh, W. P., Fang, H., … Lu, J. Ultrafast Electrochemical Expansion of Black Phosphorus toward High-Yield Synthesis of Few-Layer Phosphorene. *Chem. Mater.* **2018**, *30* (8), 2742–2749.

(36) Cooper, A. J.; Velicky, M.; Kinloch, I. A.; Robert A.W. Dryfe. On the Controlled Electrochemical Preparation of R 4 N + Graphite Intercalation Compounds and Their Host Structural Deformation Effects. *J. Electroanal. Chem.* **2014**, *730*, 34–40.

(37) Chen, Z.; Guo, D.; Si, L.; Xie, G. Nanotribological Properties of Graphite Intercalation Compounds : AFM Studies. *Scanning* **2017**, *2017*.

(38) Wei, L.; Wu, F.; Shi, D.; Hu, C.; Li, X.; Yuan, W.; Wang, J.; Zhao, J.; Geng, H.; Wei, H.; Wang, Y.; Hu, N.; Zhang, Y. Spontaneous Intercalation of Long-Chain Alkyl Ammonium into Edge-Selectively Oxidized Graphite to Efficiently Produce High-Quality Graphene. *Sci. Rep.* **2013**, *3*, 2636.

(39) Sirisaksoontorn, W.; Adenuga, A. A.; Remcho, V. T.; Lerner, M. M. Preparation and Characterization of a Tetrabutylammonium Graphite Intercalation Compound. *J. Am. Chem. Soc.* **2011**, *133* (32), 12436–12438.

(40) Zhong, Y. L.; Swager, T. M. Enhanced Electrochemical Expansion of Graphite for in Situ Electrochemical Functionalization. *J. Am. Chem. Soc.* **2012**, *134* (43), 17896–17899.

(41) Kintao Zhang. *Chemically Derived Graphene: Functionalization, Properties and Applications*; 2018.

(42) Xu, H.; Suslick, K. S. Sonochemical Preparation of Functionalized Graphenes. *J. Am. Chem. Soc.* **2011**, *133* (24), 9148–9151.

(43) Gravagnuolo, A. M.; Morales-narváez, E.; Longobardi, S.; Silva, E. T.; Giardina, P.; Merkoçi, A. In Situ Production of Biofunctionalized Few-Layer Defect-Free Microsheets of Graphene. *Adv. Funct. Mater.* **2015**, *25*, 2771–2779.

(44) Huang, W.; Lin, Y.; Taylor, S.; Gaillard, J.; Rao, A. M.; Sun, Y. Sonication-Assisted Functionalization and Solubilization of Carbon Nanotubes. *Nano Lett.* **2002**, *2* (3), 231–234.

(45) Kuntz, K. L.; Wells, R. A.; Hu, J.; Yang, T.; Dong, B.; Guo, H.; Woomer, A. H.; Druffel, D. L.; Alabanza, A.; Tománek, D.; Warren, S. C. Control of Surface and Edge Oxidation on Phosphorene. *ACS Appl. Mater. Interfaces* **2017**, *9* (10), 9126–9135.

(46) Koefoed, L.; Pedersen, S. U.; Daasbjerg, K. Covalent Modification of Glassy Carbon Surfaces by Electrochemical Grafting of Aryl Iodides. *Langmuir* **2017**, *33* (13), 3217–3222.

(47) Chattopadhyay, J.; Sadana, A. K.; Liang, F.; Beach, J. M.; Xiao, Y.; Hauge, R. H.; Billups, W. E. Carbon Nanotube Salts . Arylation of Single-Wall Carbon

Nanotubes. *Org. Lett.* **2005**, *7* (19), 4067–4069.

(48) Abellán, G.; Schirowski, M.; Edelthalhammer, K. F.; Fickert, M.; Werbach, K.; Peterlik, H.; Hauke, F.; Hirsch, A. Unifying Principles of the Reductive Covalent Graphene Functionalization. *J. Am. Chem. Soc.* **2017**, *139* (14), 5175–5182.

(49) Wang, L.; Sofer, Z.; Pumera, M. Voltammetry of Layered Black Phosphorus : Electrochemistry of Multilayer Phosphorene. *ChemElectroChem* **2014**, *2* (3), 324–327.

(50) Liu, H.; Du, Y.; Deng, Y.; Ye, P. D. Semiconducting Black Phosphorus: Synthesis, Transport Properties and Electronic Applications. *Chem. Soc. Rev.* **2732**, *44* (44), 2732–2743.

(51) Brent, J. R.; Savjani, N.; Lewis, E. A.; Haigh, S. J.; Lewis, D. J.; O'Brien, P. Production of Few-Layer Phosphorene by Liquid Exfoliation of Black Phosphorus. *Chem. Commun.* **2014**, *50* (87), 13338–13341.

(52) Favron, A.; Gaufrès, E.; Fossard, F.; Phaneuf-L'Heureux, A.-L.; Tang, N. Y.-W.; Lévesque, P. L.; Loiseau, A.; Leonelli, R.; Francoeur, S.; Martel, R. Photooxidation and Quantum Confinement Effects in Exfoliated Black Phosphorus. *Nat. Mater.* **2015**, *14* (8), 826–832.

(53) Cooper, A. J.; Wilson, N. R.; Kinloch, I. A.; Dryfe, R. A. W. Single Stage Electrochemical Exfoliation Method for the Production of Few-Layer Graphene via Intercalation of Tetraalkylammonium Cations. *Carbon N. Y.* **2013**, *66*, 340–350.

(54) Naeem, M.; Ansar, K.; Hameed, S.; Ayub, K.; Haq, I.; Tahir, M. N.; Mahmood,

T. Synthesis , Structural Studies and Biological Activities of Three New 2-. *J. Mol. Struct.* **2017**, *1129*, 50–59.

(55) Kumar, R.; Sharma, S.; Pathak, D.; Dhiman, N.; Arora, N. Ionic Conductivity, FTIR and Thermal Studies of Nano-Composite Plasticized Proton Conducting Polymer Electrolytes. *Solid State Ionics* **2017**, *305*, 57–62.

(56) Randle, R.; Whiffen, D. H. The Characteristic Infrared Absorption Frequencies of Aromatic Trifluoromethyl Compounds. *J. Chem. Soc.* **1955**, 1311–1313.

(57) Kathryn E O'Harra, Irshad Kammakakam, Jason E Bara and Jackson, E. M. Understanding the Effects of Backbone Chemistry and Anion Type on the Structure and Thermal Behaviors of Imidazolium Polyimide-Ionenes. *Polym. Int.* **2019**.

(58) Logacheva, N. M.; Baulin, V. E.; Tsivadze, Y.; Pyatova, E. N.; Ivanova, I. S.; Velikodny, Y. A.; Chernyshev, V. V. Ni(II), Co(II), Cu(II), Zn(II) and Na(I) Complexes of a Hybrid Ligand 4'-(4'''-Benzo-15-Crown-5)-Methyloxy-2,2':6',2''-Terpyridine. *Dalt. Trans.* **2009**, *14*, 2482–2489.

(59) Colthup, N. *Introduction to Infrared and Raman Spectroscopy*; Elsevier, 2012.

(60) Ma, R.; Sasaki, T. Two-Dimensional Oxide and Hydroxide Nanosheets : Controllable High-Quality Exfoliation , Molecular Assembly , and Exploration of Functionality Published as Part of the Accounts of Chemical Research Special Issue " 2D Nanomaterials beyond Graphene " . *Acc. Chem. Res.* **2015**, *48* (1), 136–143.

(61) Ebina, Y.; Sasaki, T.; Watanabe, M. Study on Exfoliation of Layered Perovskite-Type Niobates. *Solid State Ionics* **2002**, *151* (1–4), 177–182.

(62) Zhu, H.; Huang, P.; Jing, L.; Zuo, T.; Zhao, Y.; Gao, X. Microstructure Evolution of Diazonium Functionalized Graphene : A Potential Approach to Change Graphene Electronic Structure †. *J. Mater. Chem.* **2012**, *22*, 2063–2068.

(63) Fabian Koehler; Jacobsen, A.; Ihn, T.; Ensslin, K.; Stark, W. J. Chemical Modification of Graphene Characterized by Raman and Transport Experiments. *Nanoscale* **2012**, *4*, 3781–3785.

(64) Bjerglund, E.; Kongsfelt, M.; Shimizu, K.; Bror, B.; Jensen, E.; Koefoed, L.; Ceccato, M.; Skrydstrup, T.; Pedersen, S. U.; Daasbjerg, K. Controlled Electrochemical Carboxylation of Graphene To Create a Versatile Chemical Platform for Further Functionalization. *Langmuir* **2014**, *30* (22), 6622–6628.

(65) Sharma, R.; Baik, J. H.; Perera, C. J.; Strano, M. S. Anomalously Large Reactivity of Single Graphene Layers and Edges toward Electron Transfer Chemistries. *Nano Lett.* **2010**, *10* (2), 398–405.

(66) Lomeda, J. R.; Doyle, C. D.; Kosynkin, D. V.; Hwang, W. F.; Tour, J. M. Diazonium Functionalization of Surfactant-Wrapped Chemically Converted Graphene Sheets. *J. Am. Chem. Soc.* **2008**, *130* (48), 16201–16206.

(67) Artel, V.; Guo, Q.; Cohen, H.; Gasper, R.; Ramasubramaniam, A.; Xia, F. Protective Molecular Passivation of Black Phosphorus. *npj 2D Mater. Appl.* **2017**, *1* (1), 6.

(68) Del Rio Castillo, A. E.; Pellegrini, V.; Sun, H.; Buha, J.; Dinh, D. A.; Lago, E.; Ansaldo, A.; Capasso, A.; Manna, L.; Bonaccorso, F. Exfoliation of Few-Layer Black Phosphorus in Low Boiling Point Solvents and Its Application in Li-Ion Batteries. *Chem. Mater.* **2018**, *30* (2), 506–516.

(69) Wu, S.; He, F.; Xie, G.; Bian, Z.; Luo, J.; Wen, S. Black Phosphorus: Degradation Favors Lubrication. *Nano Lett.* **2018**, *18* (9), 5618–5627.

(70) Edmonds, M. T.; Tadich, A.; Carvalho, A.; Ziletti, A.; O'Donnell, K. M.; Koenig, S. P.; Coker, D. F.; Ozyilmaz, B.; Neto, A. H. C.; Fuhrer, M. S. Creating a Stable Oxide at the Surface of Black Phosphorus. *ACS Appl. Mater. Interfaces* **2015**, *7* (27), 14557–14562.

Chapter 6

Liquid Exfoliation of Antimonene

6. Liquid Exfoliation of Antimonene

6.1 Abstract

Antimonene (AM), the 2D form of Sb, displays a high carrier mobility and a tunable bandgap, which makes it suitable for electrical, energy storage and catalytic applications. While the production of AM has been investigated using numerous bottom-up fabrication methods, studies of the liquid phase exfoliation of AM remain limited. The strong interlayer interactions of Sb makes the production of nanosheets with large lateral dimensions difficult. Here, the exfoliation of AM in various solvents is investigated while the effect of mixed solvent systems on the yield and size of AM flakes is evaluated using uv-visible (UV) spectroscopy and atomic force microscopy (AFM) analysis. The use of common exfoliation solvents, such as N-methyl-2-pyrrolidone and isopropyl alcohol, results in the formation of few-layer flakes with small lateral dimensions. The production of flakes with small areas rather than large few-layer flakes can be attributed to the strong interlayer interactions of Sb. The use of an intercalating agent was employed to facilitate the formation of few-layer flakes with larger lateral dimensions. The intercalation enhances the exfoliation and dramatically minimises the sonication time. X-ray photoelectron spectroscopy (XPS) also revealed minimal oxide formation as a result of exfoliation. The formation of large sheets with minimal oxide formation is advantageous for the use of AM for device fabrication.

6.2 Introduction

AM shows promise in electrical,[1–4] energy storage,[5,6] catalysis[7,8] and medical[9–11] applications due to its electrical properties and tunable bandgap.[12,13] The increased ambient stability of AM[14] compared to black phosphorus (BP) makes it an attractive alternative material with similar properties. AM has been synthesised using various bottom-up approaches, including van der Waals epitaxy growth[1] and chemical vapour deposition,[15] whereas the investigation of the liquid exfoliation of AM has remained limited.[7,16,17] Bottom-up synthesis strategies usually result in a low yield of AM which can be overcome by employing liquid exfoliation.[12] Antimonene quantum dots (AMQDs) were produced by combined ultrasound probe sonication and ice-bath sonication which resulted in the formation of QDs with average dimensions of 3.9 nm in length and 2.6 nm in thickness.[10] Electrochemical exfoliation of AM also resulted in the formation of AMQDs with height of 31.6 nm.[18] The exfoliation of AM in common solvents typically results in the formation of AMQDs rather than nanosheets. While most 2D materials are bound together by weak van der Waals forces which facilitates their exfoliation, AM is characterised by its strong interlayer bonds making the smooth exfoliation of the material problematic.[19] The formation of nanosheets has been facilitated by shear exfoliation,[7] by using a mixed solvent system[16] and by applying a pre-grinding step that separates layers prior to exfoliation.[17] Liquid exfoliation was carried out in a mixed solvent system consisting of isopropyl alcohol (IPA) and water with a matched surface tension to AM.[16] Selecting the correct solvent with a surface tension that matches the material to be exfoliated can promote smooth exfoliation.[20,21] Shear exfoliation has also been explored for the exfoliation of AM, where the shear force exerted by a blender facilitates the formation of nanosheets.[7] Similarly, a pre-grinding step prior to exfoliation results in the formation of Sb plates

due to the shear force applied, which can subsequently be exfoliated to form AM nanosheets with large lateral dimensions.[17]

The selection of common solvents for the exfoliation of AM resulted in the formation of few-layer AM with small widths, indicating their surface tension was not ideal for the exfoliation of AM. The exfoliation of AM in mixed solvent systems facilitated the formation of a higher proportion of few-layer flakes but did not result in a significant improvement in the lateral dimensions of AM flakes. The formation of AM nanosheets with larger lateral dimensions was facilitated by the addition of an intercalating agent, as displayed in **Figure 6.1**.

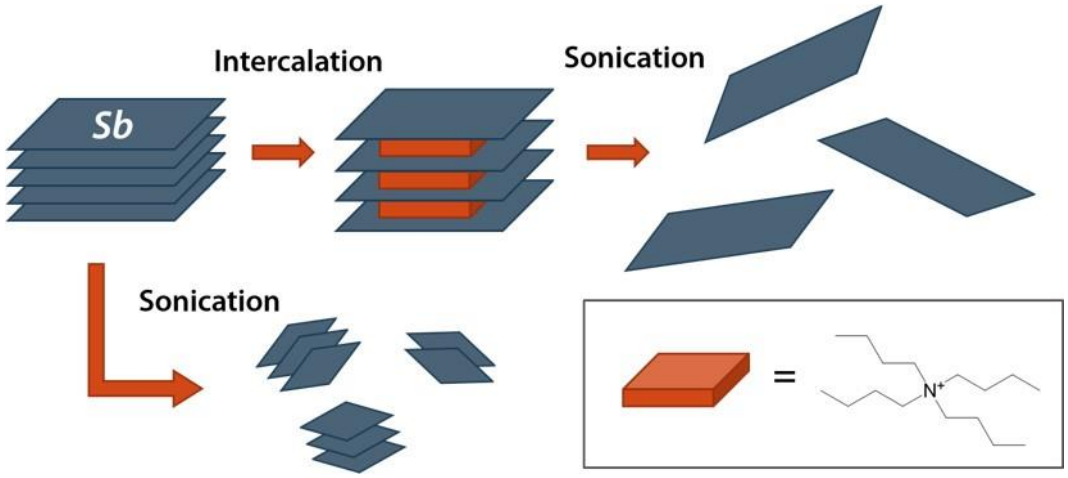

Figure 6.1: The formation of AM nanosheets in the presence of an intercalating agent facilitates the formation of flakes with larger lateral dimensions while sonication in NMP resulted in the formation of QDs.

Intercalating agents have been studied for the formation of graphite[22,23] and black phosphorus[24,25] intercalation compounds. Similarly, the use of intercalating agents has facilitated the formation of BP with large lateral dimensions[26] and they have been used for the reduction of BP to increase its reactivity for subsequent functionalisation.[27]

This chapter describes the use of an intercalating agent to facilitate the exfoliation of AM into nanosheets with larger lateral dimensions. The flake morphologies were characterised using atomic force microscopy (AFM) and scanning transmission electron microscopy (STEM) analysis, while the minimal oxidation of AM flakes was confirmed using X-ray photoelectron spectroscopy (XPS) analysis. The formation of flakes with large lateral dimensions and minimal surface oxidation is useful for the application of AM in devices.

6.3 Experimental

6.3.1 Exfoliation of Antimonene

Sb pellets with a purity of 99.9999 % were purchased from Alfa Aesar. Anhydrous acetonitrile (ACN), ethanol, ethylene glycol, N-methyl-2-pyrrolidone (NMP) was purchased from Sigma Aldrich. Solvents were used as received (without degassing) when investigating the yield and morphology but exfoliation for XPS analysis was carried out in degassed solvents to obtain an accurate reflection of the extent of oxidation. Degassing was carried out using 10 freeze-pump-thaw cycles, followed by 1 h of purging with Ar gas. The Sb pellets were ground up using a mortar and pestle to form a fine powder which was added to a sample vial, followed by bath sonication for 4-16 h in different solvent systems. The intercalated sample was prepared by addition of 20 mM of tetrabutylammonium hexafluorophosphate (TBAFP) to a 50 ml Schlenk flask containing ground Sb powder. Intercalation was carried out for 24 h followed by 1 h of bath sonication. The exfoliated sample was centrifuged at 3000 rpm for 30 min to exclude non-exfoliated material. The exfoliated sample was centrifuged at 14 500 rpm for 1 h, followed by transfer to NMP or rinsing in ACN before drop-casting for further analysis. To evaluate the effect of different solvents

on the sizes of flakes obtained after exfoliation, centrifugation was carried out in NMP to account for the effect of different solvent viscosities on size selection during centrifugation. The exfoliated sample in ACN, ethanol, ethylene glycol or a mixed solvent system was centrifuged at 14 500 rpm for 1 h, followed by transfer to NMP. The sample was then centrifuged at 3000 rpm for 30 min and the supernatant was centrifuged at 14500 rpm to obtain a sample for further analysis. Extinction measurements were carried out in NMP in order to minimise solvent effects on the absorbance value.

6.3.2 Characterisation

XPS analysis was carried out on a VG Scientific ESCAlab Mk II system using an Al Kα X-Ray source (1486.6 eV) at a base pressure of $< 5\times10^{-10}$ mbar. Survey spectra and core level spectra were recorded at 0-1000 eV and a pass energy of 200 eV. Core levels scans were acquired at a pass energy of 20 eV. CasaXPS software was used for spectra processing with peaks corrected to a Shirley background and fitted to Voigt profiles. Charge correction was applied to the C 1s peak at 285 eV. UV analysis was carried out on a Thermo Scientific Evolution 60 S uv-visible spectrophotometer with a resolution of ±0.8 nm using a xenon light source in the 200-1100 nm range. AFM analysis was performed on a Park XE-100 AFM system in non-contact mode with SSS-NCHR enhanced resolution tips, the XY and Z resolution are ~ 2 nm and 0.05 nm. A minimum of 150 flakes were measured for size analysis. STEM analysis was acquired on an FEI Helios NanoLab 600i scanning electron microscope operating at 20 kV.

6.4 Results and Discussion

6.4.1 The Effect of using Common Solvents for Antimonene Exfoliation

The effect of different solvents on the yield and in-solution stability was investigated using uv-visible analysis. Theoretical studies have suggested NMP is suitable for the liquid exfoliation of BP due to its planarity, which acts as a solvent wedge that can intercalate and pry layers apart.[28] The intercalation is only successful if flakes are stabilised after exfoliation[20], which can occur due to hydrogen bonding or the surface tension of certain solvents.[28] **Table 6.1** shows the absorbance values of AM exfoliated in different solvents. Absorbance values at 260 nm were used to estimate the yield of AM flakes following exfoliation in ethylene glycol (EG), IPA, water, NMP and ACN. Exfoliation in NMP resulted in a high yield of AM flakes, followed by H_2O, ACN and IPA while EG did not result in a large amount of flakes, indicating the high viscosity of EG does not facilitate the smooth exfoliation of AM.

Table 6.1: Absorbance values obtained for AM exfoliated in a range of common solvents can give an estimation of the yield.

Solvent	Absorbance	Surface Tension (mN/m)
Ethylene Glycol	0.07	47.7
N-methyl Pyrrolidone	0.35	40.8
Acetonitrile	0.18	30
Isopropyl Alcohol	0.17	23
Water	0.24	72.8

Successful exfoliation has been reported to be dependent on 2 factors: (1) a match between the surface tension of the solvent and the exfoliated material and (2) the

stabilisation of the flakes after exfoliation.[29] A significant amount of research has been carried out on the high-yield exfoliation of graphene which is dependant of the energy cost of exfoliation.[30] A low energy cost of exfoliation occurs when solvent-graphene interactions are minimised which occurs at an optimal surface tension of 40-50 mJ m^{-2} for graphene.[30] In order to optimise the yield of AM, exfoliation was carried out in solvents with various surface tensions, however no link was found between the surface tension and yield, as shown in **Figure 6.2**. In addition to the surface tension,

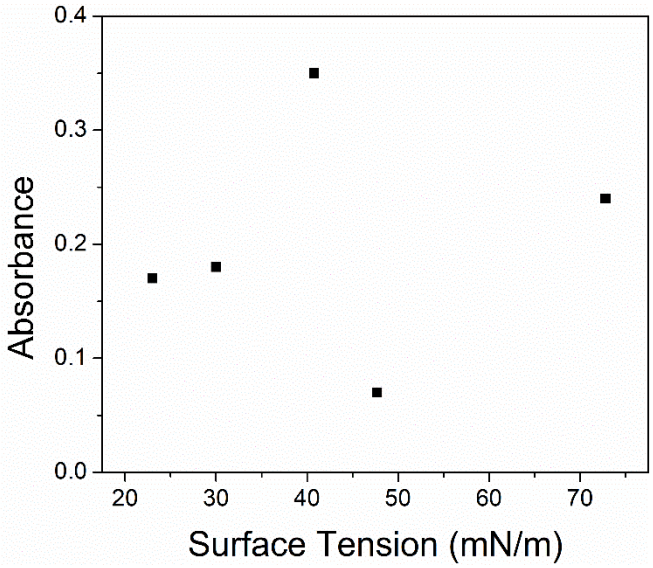

Figure 6.2: Absorbance as a function of the surface tension of the exfoliating solvent.

the solvent molecular size also has an impact on the exfoliation yield due to steric repulsion. Large molecular sizes create a steric repulsion force to overcome the interlayer van der Waals forces, which promotes exfoliation.[31] The high yield obtained from exfoliation in NMP could therefore be attributed to its large molecular size. The high yield obtained in water and IPA also suggest hydrogen bonds have a facilitative effect on exfoliation, most likely by stabilising flakes once exfoliated.

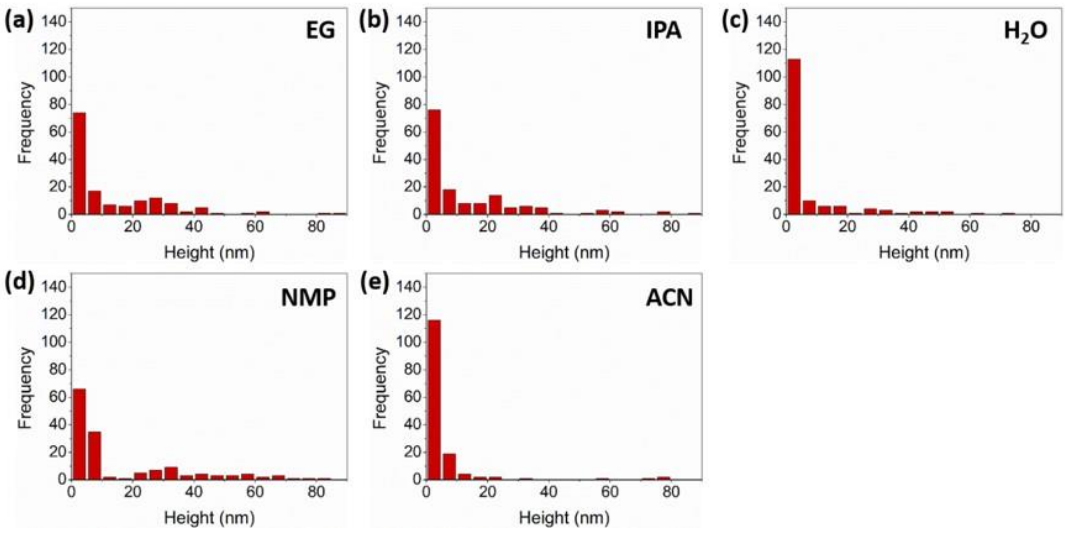

Figure 6.3: Distributions obtained from AFM analysis show the heights of AM flakes exfoliated in (a) EG, (b) IPA, (c) H_2O (d) NMP and (e) ACN.

While the absorbance values give an indication of the yield, the sizes of the flakes must also be considered. AFM analysis was carried out to evaluate the formation of few-layer flakes. **Figure 6.3** and **Table 6.2** show the effect of different solvents on the flake height.

Table 6.2: Effect of different common solvents on the production of few-layer AM flakes.

Solvent	**% <10 nm**
EG	60
IPA	65
NMP	68
H_2O	81
ACN	90

While exfoliation in NMP resulted in a high yield, as assessed using the absorbance values, the flakes contain a range of different sizes and only 68 % of flakes have dimensions below 10 nm in height. The highest proportion of flakes below 10 nm in height were obtained when exfoliation was carried out in H_2O (81 %) or ACN (90 %). A wider distribution of flake heights were obtained when exfoliation was carried out in EG and IPA, with 60 % and 65 % of flakes <10 nm.

When comparing the areas of AM flakes, the solvents that created the highest percentage of few-layer flakes also resulted in the smallest areas, as displayed in **Figure 6.4** and **Table 6.3**. Exfoliation in NMP created 63 % of flakes with areas > 5000 nm^2, while ACN and H_2O only resulted in 26 % and 19 %, respectively. ACN and H_2O resulted in the largest proportion of flakes <10 nm and also had the lowest amount of flakes > 5000 nm^2. Therefore, the formation of few-layer flakes in ACN and H_2O also results in flakes with small lateral dimensions.

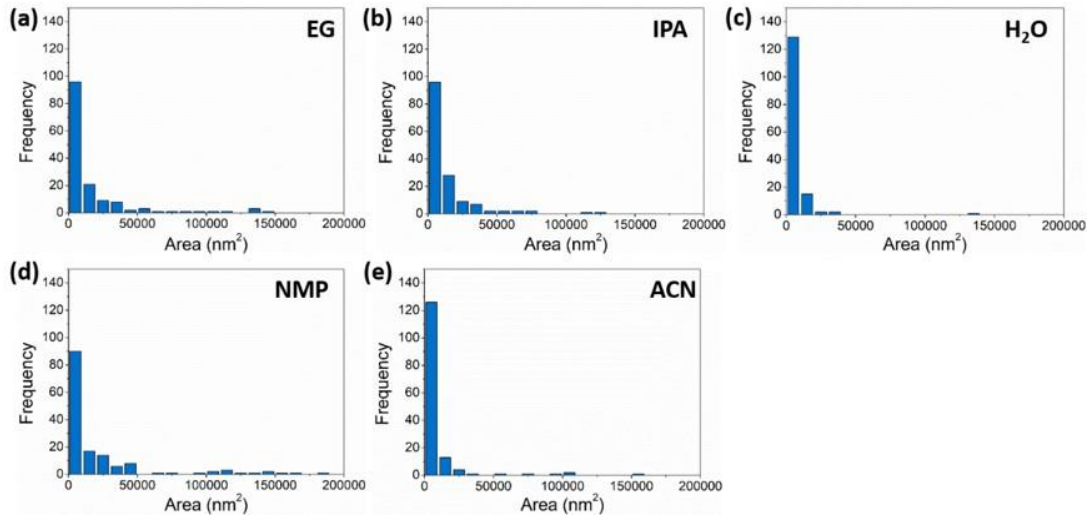

Figure 6.4: Area distributions obtained from AFM analysis for AM exfoliated in (a) EG, (b) IPA, (c) H_2O, (d) NMP and (e) ACN.

Table 6.3: Comparison of the flake areas of AM flakes exfoliated in various common solvents.

Solvent	% >5000 nm^2
EG	43
IPA	43
NMP	63
H_2O	19
ACN	26

STEM analysis in **Figure 6.5** shows the formation of thick flakes with dimensions greater than 100 nm or thin flakes that have very small lateral dimensions.

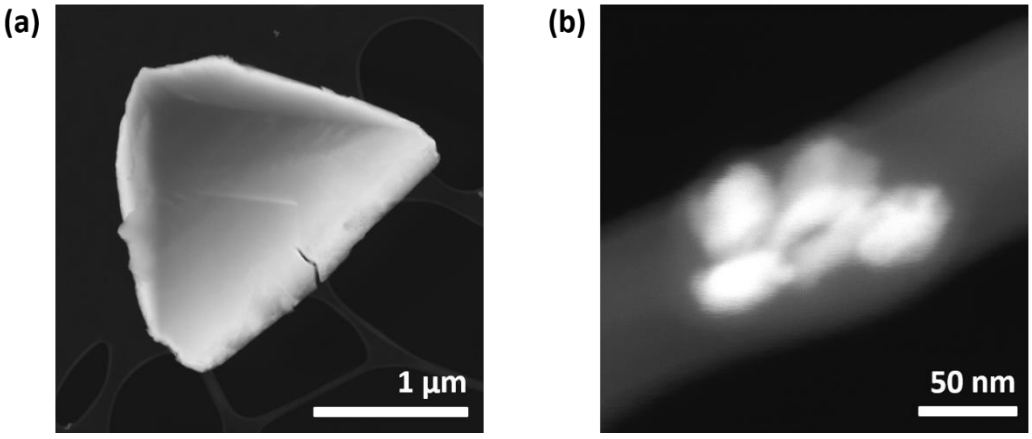

Figure 6.5: STEM analysis of AM flakes exfoliated in IPA.

The effect of different solvents on the in-solution stability was investigated by measuring the absorbance values after letting the solution settle for 24 h after exfoliation, as displayed in **Table 6.4**. NMP and IPA showed a higher absorbance

value than EG, H_2O and ACN, indicating their interactions have a stabilising effect on AM after exfoliation.

Table 6.4: Absorbance values after AM flakes were left in solution for 24 h, giving an indication of their stability in solution.

Solvent	Absorbance
EG	0.09
NMP	0.84
ACN	0.14
IPA	0.81
H_2O	0.17

6.4.2 The Effect of using a Mixed Solvent System for Antimonene Exfoliation

The use of a mixed solvent system has shown promising results for the exfoliation of AM.[16] The combination of two solvents can facilitate efficient exfoliation as one solvent may facilitate the exfoliation, such as the planarity of NMP, while another may stabilise exfoliated flakes, *e.g.* hydrogen bonds of IPA. NMP and IPA both displayed a stabilising effect on AM flakes after exfoliation, as assessed using UV analysis. Therefore, several solvent systems were investigated to determine the optimal system of exfoliation. The yields of various mixed solvent systems is displayed in **Figure 6.6**.

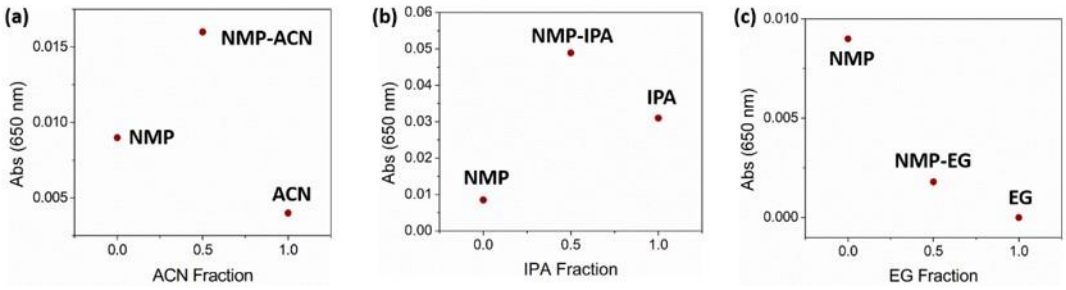

Figure 6.6: Comparison of the yields obtained in (a) NMP-ACN, (b) NMP-IPA and (c) NMP-EG mixed solvent systems.

The yield of AM flakes exfoliated in different solvent systems was evaluated by comparison of the absorbance value. The yield increased for the NMP-ACN and NMP-IPA solvents, while NMP-EG decreases the yield of flakes compared to using NMP alone. The low yield for NMP-EG could be a result of the high viscosity of EG which inhibits the smooth exfoliation of AM.

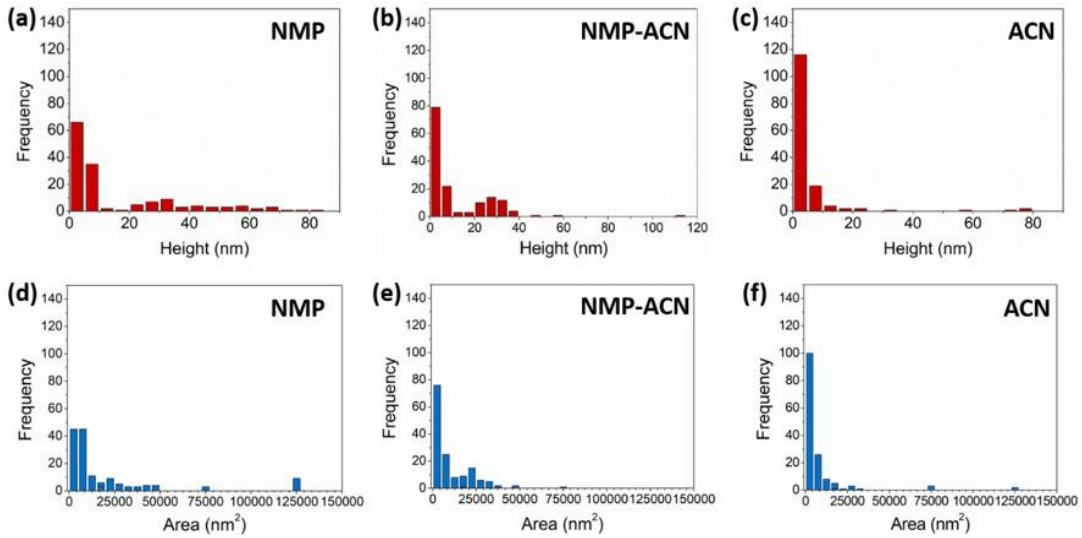

Figure 6.7: Height and area distributions obtained from AFM analysis of AM flakes exfoliated in NMP, ACN and NMP-ACN.

Table 6.5: Comparison of heights and areas of AM flakes exfoliated in ACN, NMP-ACN and NMP.

Solvent System	**NMP**	**NMP-ACN**	**ACN**
<10 nm	68 %	32 %	90 %
>5000 nm^2	63 %	49 %	26 %

The effect of using a mixed NMP-ACN solvent system is displayed in **Figure 6.7** and **Table 6.5**. The percentage of flakes with heights < 10 nm is reduced compared to ACN and NMP alone. The amount of flakes with areas > 5000 nm^2 is improved compared to using ACN alone, but the NMP-ACN solvent system does not improve the dimensions of the flakes significantly.

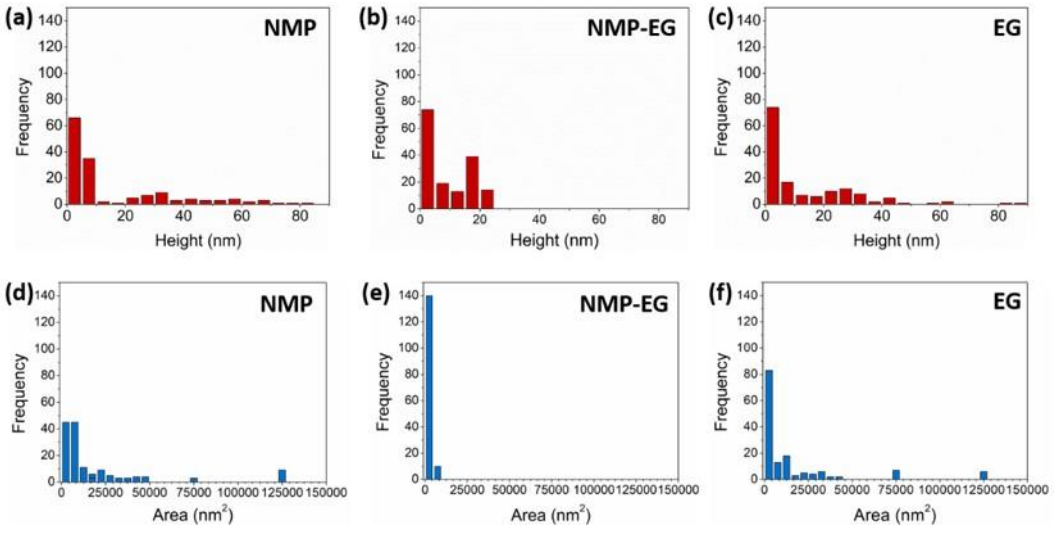

Figure 6.8: Height and area distributions obtained from AFM analysis of AM flakes exfoliated in NMP, NMP-EG and EG.

Table 6.6: Dimensions of AM exfoliated in NMP-EG compared to NMP and EG.

Solvent System	**NMP**	**NMP-EG**	**EG**
<10 nm	68 %	61 %	60 %
>5000 nm^2	63 %	7 %	43 %

The use of NMP-EG did not change the flake height as shown in **Figure 6.8** and **Table 6.6**. A large decrease in the flake area was seen, as only 7 % of flakes had an area > 5000 nm^2, indicating the addition of EG to NMP does not facilitate the formation of larger flakes but reduces the area of exfoliated flakes.

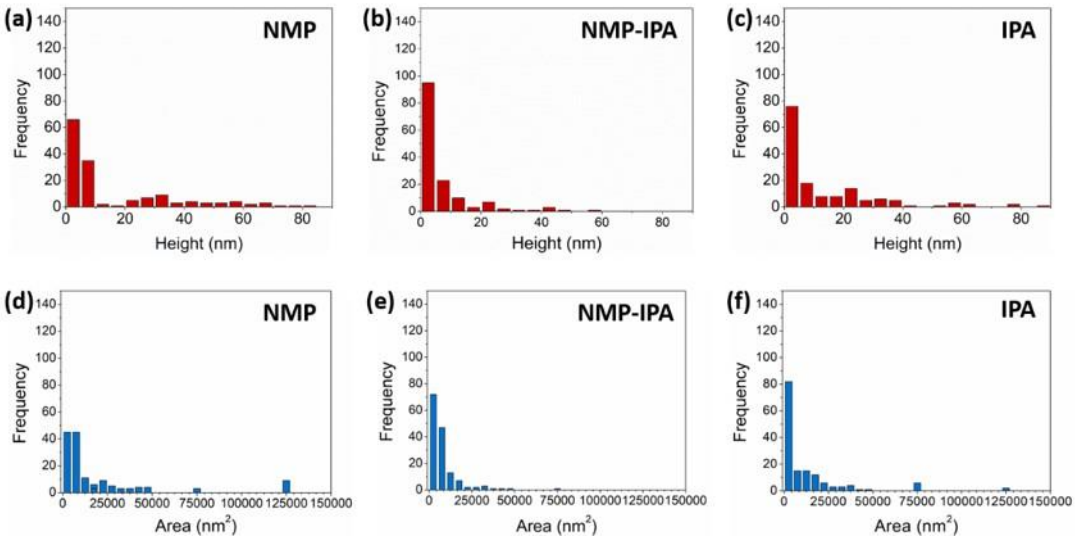

Figure 6.9: Height and area distributions obtained from AFM analysis of AM flakes exfoliated in NMP, NMP-IPA and IPA.

Table 6.7: Comparison of heights and areas of flakes exfoliated in NMP, NMP-IPA and IPA.

Solvent System	**NMP**	**NMP-IPA**	**IPA**
<10 nm	68 %	81 %	65 %
>5000 nm^2	63 %	52 %	43 %

The effect of the NMP-IPA solvent system is displayed in **Figure 6.9** and **Table 6.7**. The use of NMP-IPA as a solvent increases the amount of few-layer flakes to 81 % compared to using IPA (65 %) and NMP (68 %) alone. Although the amount of few-layer flakes can be increased, the use of a mixed solvent system did not result in the smooth exfoliation of large AM flakes, as only 52 % of flakes had areas >5000 nm^2. Therefore, the use of IPA-NMP only improved the proportion of few-layer flakes produced but did not improve the area of AM flakes.

6.4.3 The Effect of using an Intercalating Agent for Antimonene Exfoliation

The use of an intercalating agent has facilitated the formation of large BP flakes.[26] Tetrabutylammonium salts have been used for the intercalation of graphite[32–35] and BP.[36,37] The intercalating agent overcomes the interlayer van der Waals forces by insertion between the layers, promoting exfoliation.[38] The use of an intercalating agent also reduces the sonication time which can minimise defects. Long sonication times have been reported to induce basal plane defects during the production of graphene.[20] **Figure 6.10** and **Table 6.8** show the flake heights and areas obtained when AM is produced in NMP alone and in the presence of tetrabutylammonium hexafluorophosphate (TBAFP).

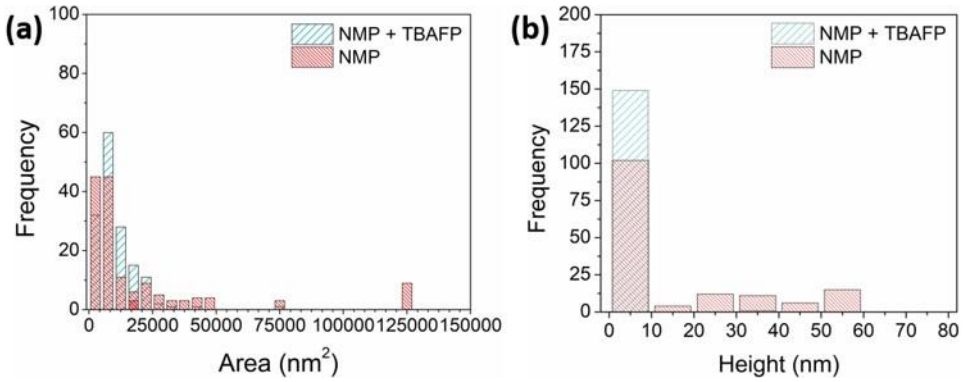

Figure 6.10: Comparison of (a) flake areas and (b) flakes heights of AM flakes exfoliated in NMP alone and in the presence of an intercalating agent (TBAFP).

Table 6.8: Flake heights and areas obtained when using an intercalating agent.

	NMP	**NMP + TBAFP**
< 10 nm	68 %	99 %
> 5000 nm^2	70 %	79 %

An increase in few-layer flakes was observed, with 99 % of flakes < 10 nm when exfoliation occurred in the presence of TBAFP. Additionally, a 9 % increase in flakes with an area > 5000 nm^2 is seen. While only a small increase is seen in larger flakes, TBAFP facilitates the formation of few-layer flakes with larger dimensions. The larger flakes observed during exfoliation in NMP also displayed a higher thickness, while all flakes exfoliated with TBAFP displayed a low height, as displayed in **Figure 6.11**. The sample exfoliated in NMP was sonicated for 6 h compared to 1 h of sonication for the intercalated sample which still resulted in an increase in the production of few-layer flakes using an intercalating agent.

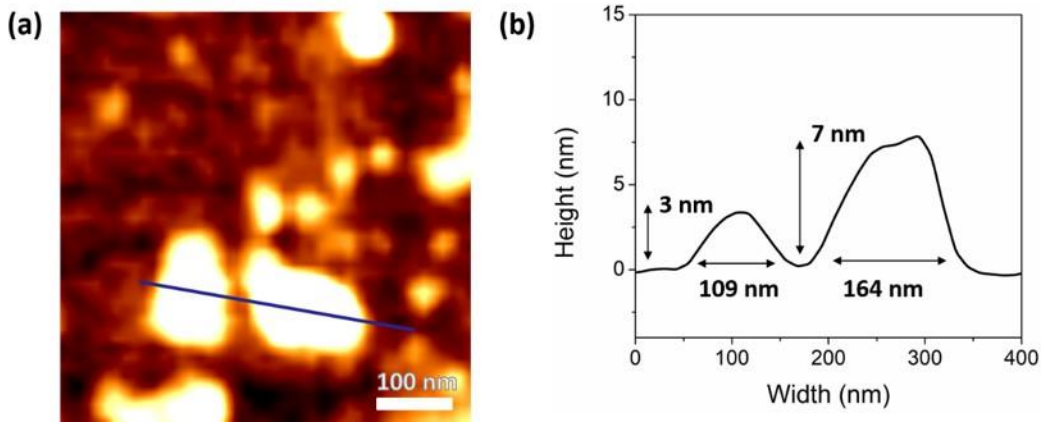

Figure 6.11: AFM analysis of AM flakes exfoliated using an intercalating agent with (b) the corresponding line profile.

The oxidation of flakes was evaluated using XPS analysis which showed the presence of the Sb $3d_{5/2}$, Sb $3d_{3/2}$ and O 1s core level, as shown in **Figure 6.12**. The Sb $3d_{3/2}$ and Sb $3d_{5/2}$ core levels occurred at a BE of 527.6 eV and 539.1 eV, in correlation with values reported for AM.[39] The presence of an oxide layer could be observed at 530.2 eV and 541.1 eV, corresponding to the oxide present in the Sb $3d_{3/2}$ and Sb $3d_{5/2}$ core levels. The BE of the Sb 3d core level can be used to discern between Sb_2O_3 and Sb_2O_5. A BE of 530.2 corresponds to the formation of Sb_2O_3,[39,40] while the ratio of 39:61 of Sb:O is also in correlation with Sb_2O_3.[40] The formation of Sb oxide in the form of Sb_2O_3 is consistent with other reports on AM oxidation.[15] While the Sb 3d core level indicates the oxidation of AM flakes, the oxide content is in correlation with the literature.[7,17,39] Additionally, the formation of AM oxides have been reported to display a direct bandgap rather than the indirect bandgap observed for AM. The formation of a self-passivating oxide layer could therefore be beneficial and further investigation is necessary to assess the ambient stability of oxide formation on AM flakes.

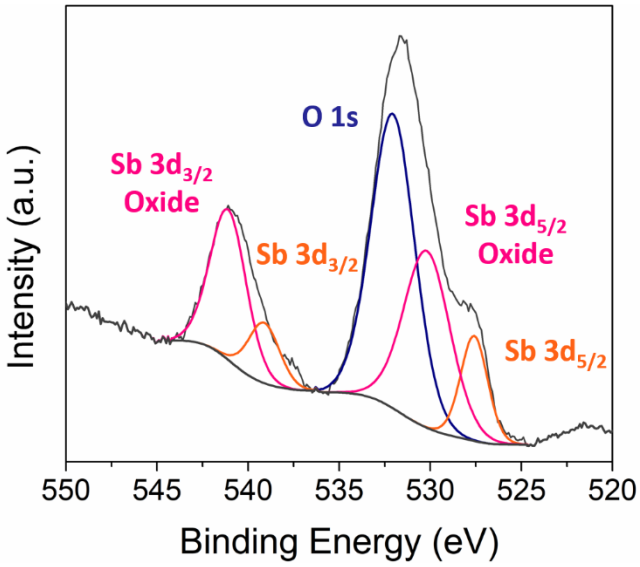

Figure 6.12: XPS analysis of exfoliated AM flakes displaying the O 1s, Sb $3d_{3/2}$ and Sb $3d_{5/2}$ core levels with the corresponding oxide components.

6.5 Conclusions

The exfoliation of AM in various common solvents and mixed solvent systems was investigated. The formation of AM in common solvents resulted in the formation of flakes with small areas and while an IPA-NMP mixed solvent system increased the amount of few-layer flakes, the flake areas remained small. The use of an intercalating agent facilitated the formation of a higher proportion of few-layer flakes which also displayed larger areas. The intercalating agent also minimises sonication time ensuring minimal defect formation while XPS analysis indicated the minimal formation of oxide on AM. The formation of flakes with large lateral dimensions could be useful for device applications.

6.6 References

(1) Ji, J.; Song, X.; Liu, J.; Yan, Z.; Huo, C.; Zhang, S.; Su, M.; Liao, L.; Wang, W.; Ni, Z.; Hao, Y.; Zeng, H. Two-Dimensional Antimonene Single Crystals Grown by van Der Waals Epitaxy. *Nat. Commun.* **2016**, *7*, 13352.

(2) Zhang, S.; Yan, Z.; Li, Y.; Chen, Z.; Zeng, H. Atomically Thin Arsenene and Antimonene: Semimetal-Semiconductor and Indirect-Direct Band-Gap Transitions. *Angew. Chemie - Int. Ed.* **2015**, *54* (10), 3112–3115.

(3) Pizzi, G.; Gibertini, M.; Dib, E.; Marzari, N.; Iannaccone, G.; Fiori, G. Performance of Arsenene and Antimonene Double-Gate MOSFETs from First Principles. *Nat. Commun.* **2016**, *7*, 12585.

(4) Sun, X.; Song, Z.; Liu, S.; Wang, Y.; Li, Y.; Wang, W.; Lu, J. Sub-5 Nm Monolayer Arsenene and Antimonene Transistors. *ACS Appl. Mater. Interfaces* **2018**, *10* (26), 22363–22371.

(5) Tian, W.; Zhang, S.; Huo, C.; Zhu, D.; Li, Q.; Wang, L.; Ren, X.; Xie, L.; Guo, S.; Chu, P. K.; Zeng, H.; Huo, K. Few-Layer Antimonene: Anisotropic Expansion and Reversible Crystalline-Phase Evolution Enable Large-Capacity and Long-Life Na-Ion Batteries. *ACS Nano* **2018**, *12* (2), 1887–1893.

(6) Jing Zhou, Bingyi Yan, Jie Yang, Yun Yang, Wei Zhou, Hao Lan, H. W. and L. G. A Densely Packed Sb2O3 Nanosheets-Graphene Aerogel toward Advanced Sodium-Ion Batteries. *Nanoscale* **2018**, *10* (19), 9108–9114.

(7) Gusmão, R.; Sofer, Z.; Bouša, D.; Pumera, M. Pnictogen (As, Sb, Bi) Nanosheets for Electrochemical Applications Are Produced by Shear Exfoliation Using Kitchen Blenders. *Angew. Chemie* **2017**, *129* (46), 14609–14614.

(8) Jie Zhang, Fengwang Li, Mianqi Xue, Jiezhen Li, Xinlei Ma, LuChen, Xueji Zhang, and D. M. Unlock the Electrocatalytic Activity of Antimony for CO2 Reduction by 2D Engineering Authors: *Angew. Chemie* **2017**, *56* (46), 14718–14722.

(9) Tao, W.; Ji, X.; Zhu, X.; Li, L.; Wang, J.; Zhang, Y.; Saw, P. E.; Li, W.; Kong, N.; Islam, M. A.; Gan, T.; Zeng, X.; Zhang, H.; Mahmoudi, M.; Tearney, G. J.; Farokhzad, O. C. Two-Dimensional Antimonene-Based Photonic Nanomedicine for Cancer Theranostics. *Adv. Mater.* **2018**, *30* (38), 1802061.

(10) Tao, W.; Ji, X.; Xu, X.; Islam, M. A.; Li, Z.; Chen, S.; Saw, P. E.; Zhang, H.; Bharwani, Z.; Guo, Z.; Shi, J.; Farokhzad, O. C. Cancer Therapy Antimonene Quantum Dots : Synthesis and Application as Near- Infrared Photothermal Agents for Effective Cancer Therapy Angewandte. *Angew. Chemie Int. Ed.* **2017**, *56* (39), 11896–11900.

(11) Lu, G.; Lv, C.; Bao, W.; Li, F.; Zhang, F.; Zhang, L.; Wang, S.; Gao, X.; Zhao, D.; Wei, W.; Xie, H. Antimonene with Two-Orders-of-Magnitude Improved Stability for High-Performance Cancer Theranostics. *Chem. Sci.* **2019**, *10* (18), 4847–4853.

(12) Wang, Xin, Jun Song, and J. Q. Antimonene: From Experimental Preparation to Practical Application. *Angew. Chemie Int. Ed.* **2019**, *58* (6), 1574–1584.

(13) Wang, G.; Pandey, R.; Karna, S. P. Atomically Thin Group V Elemental Films: Theoretical Investigations of Antimonene Allotropes. *ACS Appl. Mater. Interfaces* **2015**, *7* (21), 11490-11496.

(14) Ares, P.; Aguilar-galindo, F.; Rodríguez-san-miguel, D.; Aldave, D. A.; Díaz-

tendero, S.; Alcamí, M.; Martín, F.; Gómez-herrero, J. Mechanical Isolation of Highly Stable Antimonene under Ambient Conditions. *Adv. Mater.* **2016**, *28* (30), 6332–6336.

(15) Wu, Q.; Song, Y. J. The Environmental Stability of Large-Size and Single-Crystalline Antimony Flakes Grown by Chemical Vapor Deposition on SiO2 Substrates. *Chem. Commun.* **2018**, *54* (69), 9671-9674.

(16) Gibaja, C.; Rodriguez-San-Miguel, D.; Ares, P.; Gómez-Herrero, J.; Varela, M.; Gillen, R.; Maultzsch, J.; Hauke, F.; Hirsch, A.; Abellán, G.; Zamora, F. Few-Layer Antimonene by Liquid-Phase Exfoliation. *Angew. Chemie - Int. Ed.* **2016**, *55* (46), 14345–14349.

(17) Wang, X.; He, J.; Zhou, B.; Zhang, Y.; Wu, J.; Hu, R.; Liu, L. Bandgap-Tunable Preparation of Smooth and Large Two-Dimensional Antimonene. *Angew. Chemie* **2018**, *130* (28), 8804–8809.

(18) Lu, L.; Tang, X.; Cao, R.; Wu, L.; Li, Z.; Jing, G.; Dong, B.; Lu, S.; Li, Y.; Xiang, Y.; Li, J.; Fan, D.; Zhang, H. Broadband Nonlinear Optical Response in Few-Layer Antimonene and Antimonene Quantum Dots : A Promising Optical Kerr Media with Enhanced Stability. *Adv. Opt. Mater.* **2017**, *5* (17), 1700301.

(19) Sturala, J.; Sofer, Z.; Pumera, M. Chemistry of Layered Pnictogens : Phosphorus , Arsenic , Antimony , and Bismuth Angewandte. *Angew. Chemie* **2019**, *58*, 7551–7557.

(20) Coleman, J. N. Liquid Exfoliation of Defect-Free Graphene. *Acc. Chem. Res.* **2012**, *46* (1), 14–22.

(21) Shen, J.; He, Y.; Wu, J.; Gao, C.; Keyshar, K.; Zhang, X. Liquid Phase Exfoliation of Two-Dimensional Materials by Directly Probing and Matching Surface Tension Components. *Nano Lett.* **2015**, *15* (8), 5449–5454.

(22) Hirsch, A.; Englert, J. M.; Hauke, F. Wet Chemical Functionalization of Graphene. *Acc. Chem. Res.* **2013**, *46* (1), 87–96.

(23) Dresselhaus, M. S.; Dresselhaus, G. Intercalation Compounds of Graphite. *Adv. Phys.* **1981**, *30* (2), 139–326.

(24) Abellán, G.; Neiss, C.; Lloret, V.; Wild, S.; Chac, J. C.; Werbach, K.; Fedi, F.; Shiozawa, H.; Gçrling, A.; Peterlik, H.; Pichler, T.; Hauke, F.; Hirsch, A. Exploring the Formation of Black Phosphorus Intercalation Compounds with Alkali Metals. *Angew. Chemie* **2017**, *56* (48), 15267–15273.

(25) Huang, Z.; Hou, H.; Zhang, Y.; Wang, C.; Qiu, X.; Ji, X. Layer-Tunable Phosphorene Modulated by the Cation Insertion Rate as a Sodium-Storage Anode. *Adv. Mater.* **2017**, *29* (34), 1702372.

(26) Ng, A.; Sutto, T. E.; Matis, B. R.; Deng, Y.; Ye, P. D.; Stroud, R. M.; Brintlinger, T. H.; Bassim, N. D. Chemically Exfoliating Large Sheets of Phosphorene via Choline Chloride Urea Viscosity-Tuning. *Nanotechnology* **2017**, *28* (15), 155601.

(27) Wild, S.; Fickert, M.; Mitrovic, A.; Lloret, V.; Neiss, C.; Vidal-moya, J. Ø. A.; Rivero-crespo, M.; Ø, A. L.; Werbach, K.; Peterlik, H.; Grabau, M.; Wittk, H.; Papp, C.; Steinruck, H.; Pichler, T.; Gçrling, A.; Hauke, F.; Abellan, G.; Hirsch, A. Lattice Opening upon Bulk Reductive Covalent Functionalization of Black Phosphorus. *Angew. Chemie - Int. Ed.* **2019**, *58* (17), 5763–5768.

(28) Sresht, V.; Pádua, A. A. H.; Blankschtein, D. Liquid-Phase Exfoliation of Phosphorene: Design Rules from Molecular Dynamics Simulations. *ACS Nano* **2015**, *9* (8), 8255–8268.

(29) Hanlon, D.; Backes, C.; Doherty, E.; Cucinotta, C. S.; Berner, N. C.; Boland, C.; Lee, K.; Harvey, A.; Lynch, P.; Gholamvand, Z.; Zhang, S.; Wang, K.; Moynihan, G.; Pokle, A.; Ramasse, Q. M.; McEvoy, N.; Blau, W. J.; Wang, J.; Abellan, G.; Hauke, F.; Hirsch, A.; Sanvito, S.; O'Regan, D. D.; Duesberg, G. S.; Nicolosi, V.; Coleman, J. N. Liquid Exfoliation of Solvent-Stabilized Few-Layer Black Phosphorus for Applications beyond Electronics. *Nat. Commun.* **2015**, *6*, 8563.

(30) Hernandez, Y.; Nicolosi, V.; Lotya, M.; Blighe, F. M.; Sun, Z.; De, S.; McGovern, I. T.; Holland, B.; Byrne, M.; Gun'Ko, Y. K.; Boland, J. J.; Niraj, P.; Duesberg, G.; Krishnamurthy, S.; Goodhue, R.; Hutchison, J.; Scardaci, V.; Ferrari, A. C.; Coleman, J. N. High-Yield Production of Graphene by Liquid-Phase Exfoliation of Graphite. *Nat. Nanotechnol.* **2008**, *3* (9), 563–568.

(31) Sajedi-moghaddam, A.; Mayorga-martinez, C. C.; Sofer, Z.; Bousa, D.; Saievar-iranizad, E.; Pumera, M. Black Phosphorus Nanoflakes/Polyaniline Hybrid Material for High- Performance Pseudocapacitors. *J. Phys. Chem. C* **2017**, *121* (37), 20532–20538.

(32) Cooper, A. J.; Velicky, M.; Kinloch, I. A.; Robert A.W. Dryfe. On the Controlled Electrochemical Preparation of R 4 N + Graphite Intercalation Compounds and Their Host Structural Deformation Effects. *J. Electroanal. Chem.* **2014**, *730*, 34–40.

(33) Chen, Z.; Guo, D.; Si, L.; Xie, G. Nanotribological Properties of Graphite Intercalation Compounds : AFM Studies. *Scanning* **2017**, *2017*.

(34) Wei, L.; Wu, F.; Shi, D.; Hu, C.; Li, X.; Yuan, W.; Wang, J.; Zhao, J.; Geng, H.; Wei, H.; Wang, Y.; Hu, N.; Zhang, Y. Spontaneous Intercalation of Long-Chain Alkyl Ammonium into Edge-Selectively Oxidized Graphite to Efficiently Produce High-Quality Graphene. *Sci. Rep.* **2013**, *3*, 2636.

(35) Sirisaksoontorn, W.; Adenuga, A. A.; Remcho, V. T.; Lerner, M. M. Preparation and Characterization of a Tetrabutylammonium Graphite Intercalation Compound. *J. Am. Chem. Soc.* **2011**, *133* (32), 12436–12438.

(36) Wang, C.; He, Q.; Halim, U.; Liu, Y.; Zhu, E.; Lin, Z.; Xiao, H.; Duan, X.; Feng, Z.; Cheng, R.; Weiss, N. O.; Ye, G.; Huang, Y.; Wu, H.; Cheng, H.; Shakir, I.; Liao, L.; Chen, X.; Iii, W. A. G.; Huang, Y.; Duan, X. Monolayer Atomic Crystal Molecular Superlattices. *Nat. Publ. Gr.* **2018**, *555* (7695), 231–236.

(37) Jain, R.; Singh, Y.; Cho, S.; Sasikala, S. P.; Koo, H.; Narayan, R.; Jung, H.; Jung, Y.; Kim, S. O. Ambient Stabilization of Few Layer Phosphorene via Noncovalent Functionalization with Surfactants – Systematic 2D NMR Characterization in Aqueous Dispersion Ambient Stabilization of Few Layer Phosphorene via Noncovalent Functionalization with Surfactants. *Chem. Mater.* **2019**, *31* (8), 2786–2794.

(38) Kintao Zhang. *Chemically Derived Graphene: Functionalization, Properties and Applications*; 2018.

(39) Abellan, G.; Ares, P.; Wild, S.; Nuin, E.; Neiss, C.; Rodriguez-, D.; Miguel, S.; Segovia, P.; Gibaja, C.; Michel, E. G.; Gçrling, A.; Hauke, F.; Julio, G.;

Hirsch, A.; Zamora, F. Ø. Noncovalent Functionalization and Charge Transfer in Antimonene Angewandte. *Angew. Chemie* **2017**, *56* (46), 14389–14394.

(40) Garbassi, F. XPS and AES Study of Antimony Oxides. *Surf. Interface Anal.* **1980**, *2* (5), 165–169.

Chapter 7

Conclusions and Future Work

7. Conclusions and Future Work

7.1 Conclusions and Future Work

The continuation of Moore's Law is dependent on the development of new techniques and materials that allow the advancement of the semiconductor industry. The consistent scaling of transistors results in problems, such as short channel effects,[1,2] which arise from the scaling of bulk 3D materials to smaller dimensions. The use of 2D materials that display atomic thicknesses and high carrier mobilities could extend Moore's Law.[3] The investigation of new 2D materials shows promise, although the research area is still in its infancy. This thesis has focused on addressing some of the challenges faced in the preparation of three materials, Si, black phosphorus (BP) and antimonene (AM), for potential device applications.

Chapter 1 introduced the use of MLD and 2D materials, focusing on BP and AM, to satisfy Moore's law. The use of MLD shows promise in achieving shallow junctions with increased control compared to ion implantation due to the incorporation of surface functionalisation. The MLD strategy is highly compatible with 3D nanostructures which will become increasingly important during the scaling of transistor architectures. The properties of new 2D materials are discussed, which show promise in replacing Si but still suffer from a number of problems. The ambient instability of BP is a key hurdle for the application of material, which can be circumvented using physical or chemical protective layers that prevent exposure to ambient oxygen and water. The production of AM has focused on bottom-up strategies which can be limiting in their yield while the liquid exfoliation remains difficult due to the strong interlayer interactions of AM, preventing its smooth exfoliation.

Chapter 2 describes the doping of Si substrates through oxide-monolayer doping (MLD). The use of an oxide layer facilitates the attachment of non-toxic, inexpensive dopant precursors that can be carried out without the requirement of inert conditions, which are necessary for traditional hydrosilylation reactions. The detailed characterisation of the surface chemistry of phosphonic acid functionalised SiO_2 surfaces using X-ray photoelectron spectroscopy (XPS) and attenuated total reflection-Fourier transform infra-red (ATR-FTIR) spectroscopy highlights the need for controlled functionalisation in obtaining a reproducible peak carrier concentration. The SiO_2 layer also facilitates the attachment of carbon-free precursors while the oxide layer traps carbon before entering the Si substrate, ensuring minimal carbon contamination, as analysed using secondary ion mass spectrometry (SIMS) analysis. The SiO_2 layer provides protection of the Si interface during the rapid thermal anneal (RTA) step which will also become increasingly important as device dimensions are reduced. Further investigation is necessary to reproducibly vary the thickness of the oxide layer in order to tune the dopant depth, even though promising initial results were achieved. The gentle nature of oxide-MLD is highly applicable to 3D architectures, such as nanowires, which requires further research. Mathey *et. al.*[4] and Alphazan *et. al.*[5] used the Si native oxide for MLD applications, while oxide-MLD employed a chemically grown oxide. The use of a HF etch often damages 3D architectures,[6] while oxide-MLD carried out using the native oxide layer present on 3D architectures eliminates the need for HF treatment and allows minimal damage of these nanostructures.

Chapter 3 investigated the ambient degradation of BP while evaluating the effect of oxygen and water. BP degradation occurred through reaction with oxygen which

forms non-bridging oxide species. The non-bridging oxide species convert to bridging oxide species which react further with ambient water to form liquid oxidation products. The evaporation of these volatile oxidation products results in continuous oxidation of the BP surface. The evaluation of the ambient degradation can facilitate the discovery of targeted protection strategies.

Chapter 4 focused on the protection of BP under ambient conditions which has been accomplished using functionalisation with aryl iodonium salts. The stability of BP was prolonged to a period of 2 days using aryl functionalisation which inhibited bridged oxide formation. In comparison, diazonium functionalisation resulted in multilayer formation, non-covalent solvent passivation and oxidation which gives inferior ambient stability to iodonium functionalisation. An investigation of the electrical properties of iodonium functionalised BP is necessary to evaluate the effect of aryl functionalisation. Diazonium functionalisation allowed modification of the electrical properties of BP due to the electron withdrawing nature of the aryl substituents,[7] which is also likely to occur for iodonium functionalised BP if attachment occurs through P-sites, although attachment of aryl groups to O-sites has been reported to preserve the inherent electrical characteristics of BP.[8] The electrical characterisation of functionalised BP is necessary to confirm the effect of functionalisation on the electrical properties.

Chapter 5 explored the simultaneous exfoliation and functionalisation of BP using an intercalating agent. The addition of an intercalating agent facilitated the smooth exfoliation of flakes with large lateral dimensions. Functionalisation using an aryl iodide directly after exfoliation of flakes minimised oxidation and therefore prolonged

the ambient stability of BP to a period of 1 week, as displayed using XPS, scanning transmission electron microscopy (STEM) and atomic force microscopy (AFM) analysis. The use of intercalating agents for BP exfoliation remains limited[9] even though these materials show promise in dramatically modifying the properties of 2D materials, making them more suitable for a variety of applications.[10] The intercalation of graphite has allowed modification of its electrical properties,[11] while the chemical, optical and magnetic properties of materials can also be modified.[10] Similarly, the formation of van der Waals heterostructures,[12,13] where different 2D materials can be selected based on their properties and stacked forming a layered structure, could allow the successful stabilisation and full exploitation of the properties of BP.

Chapter 6 introduced the exfoliation of AM which was carried out in a range of common solvents and mixed solvent systems. The use of these solvents resulted in the formation of few-layer AM flakes with small areas, as demonstrated using AFM and STEM analysis. The use of an intercalating agent promoted the formation of flakes with larger lateral dimensions and minimised sonication time. The smooth exfoliation of AM created large flakes which are more suitable for device applications.

The use of intercalating agents could be developed for the exfoliation of AM, as the exfoliation of BP in ionic liquids has been reported to increase the lateral dimensions of BP flakes,[14] which could also promote the smooth exfoliation of AM. While progress has been made in evaluating the ambient instability of AM,[15–17] further investigation of the surface chemistry of AM is required. In particular the effect of oxygen and water alone, along with the combined effect of oxygen and water on the

AM surface chemistry. The increased ambient stability of AM compared to BP[18] will facilitate its use in applications once it can be produced on a large scale.

The implementation of 2D materials into electronic devices still faces a number of challenges including the controlled, large scale production of 2D materials, the ambient instability and the reliable device fabrication using 2D materials. A promising strategy for the large scale production of 2D materials is liquid phase exfoliation (LPE),[19,20] although the resulting solvent passivation can be detrimental to processing[21] and device performance.[22] The ambient instability can be overcome using covalent functionalisation which also minimises solvent passivation. While advancements in the surface chemistry and functionalisation of BP have been made, the characterisation of the surface chemistry of many 2D materials remains unexplored. 2D materials research has focused mainly on their applications, although understanding the surface chemistry is vital to the development and application of these materials. The chemical functionalisation has allowed the properties of graphene[23,24] and other 2D materials[25–28] to be tailored. Furthermore, the adsorption of ambient molecules on the surface of 2D materials that act as electron acceptor or donors[15] can adversely influence their electrical properties. Isolated 2D materials often display a reduction in carrier mobility which can be attributed to the sensitivity to the environment arising from an increase in the surface-to-volume ratio, highlighting the need for an encapsulating layer that protects and preserves the characteristics of few-layer materials.[29] Once the surface chemistry has been fully elucidated, 2D materials show promise in a variety of applications.

7.2 References

(1) Chhowalla, M.; Jena, D.; Zhang, H. Two-Dimensional Semiconductors for Transistors. *Nat. Rev. Mater.* **2016**, *1* (11), 16052.

(2) Ieong, MIeong, M.; Doris, B.; Kedzierski, J.; Rim, K.; Yang, M. Silicon Device Scaling to the Sub-10-Nm Regime. *Science (80-.).* **2004**, *306* (5704), 2057–2060.

(3) Li, Ming-Yang, Sheng-Kai Su, H-S. Philip Wong, and L.-J. L. How 2D Semiconductors Could Extend Moore ' s Law. *Nature* **2019**, *567*, 169.

(4) Mathey, L.; Alphazan, T.; Valla, M.; Veyre, L.; Fontaine, H.; Enyedi, V.; Yckache, K.; Danielou, M.; Kerdiles, S.; Guerrero, J.; Barnes, J.-P.; Veillerot, M.; Chevalier, N.; Mariolle, D.; Bertin, F.; Durand, C.; Berthe, M.; Dendooven, J.; Martin, F.; Thieuleux, C.; Grandidier, B.; Copéret, C. Functionalization of Silica Nanoparticles and Native Silicon Oxide with Tailored Boron-Molecular Precursors for Efficient and Predictive p -Doping of Silicon. *J. Phys. Chem. C* **2015**, *119* (24), 13750–13757.

(5) Alphazan, T.; Mathey, L.; Schwarzwälder, M.; Lin, T.-H.; Rossini, A. J.; Wischert, R.; Enyedi, V.; Fontaine, H.; Veillerot, M.; Lesage, A.; Emsley, L.; Veyre, L.; Martin, F.; Thieuleux, C.; Copéret, C. Monolayer Doping of Silicon through Grafting a Tailored Molecular Phosphorus Precursor onto Oxide-Passivated Silicon Surfaces. *Chem. Mater.* **2016**, *28* (11), 3634–3640.

(6) Veerbeek, J.; Ye, L.; Vijselaar, W.; Kudernac, T.; van der Wiel, W. G.; Huskens, J. Highly Doped Silicon Nanowires by Monolayer Doping. *Nanoscale* **2017**, *9* (8), 2836–2844.

(7) Ryder, C. R.; Wood, J. D.; Wells, S. A.; Yang, Y.; Jariwala, D.; Marks, T. J.;

Schatz, G. C.; Hersam, M. C. Covalent Functionalization and Passivation of Exfoliated Black Phosphorus via Aryl Diazonium Chemistry. *Nat. Chem.* **2016**, *8* (6), 597–602.

(8) Artel, V.; Guo, Q.; Cohen, H.; Gasper, R.; Ramasubramaniam, A.; Xia, F. Protective Molecular Passivation of Black Phosphorus. *npj 2D Mater. Appl.* **2017**, *1* (1), 6.

(9) Abellán, G.; Neiss, C.; Lloret, V.; Wild, S.; Chac, J. C.; Werbach, K.; Fedi, F.; Shiozawa, H.; Gçrling, A.; Peterlik, H.; Pichler, T.; Hauke, F.; Hirsch, A. Exploring the Formation of Black Phosphorus Intercalation Compounds with Alkali Metals. *Angew. Chemie* **2017**, *56* (48), 15267–15273.

(10) Stark, M. S.; Kuntz, K. L.; Martens, S. J.; Warren, S. C. Intercalation of Layered Materials from Bulk to 2D. *Adv. Mater.* **2019**, 1808213.

(11) Weller, T. E.; Ellerby, M.; Saxena, S. S.; Smith, R. P.; Skipper, N. T. Superconductivity in the Intercalated Graphite Compounds C 6 Yb and C 6 Ca. *Nat. Phys.* **2005**, *1*, 39–41.

(12) Geim, A. K.; Grigorieva, I. V. Van Der Waals Heterostructures. *Nature* **2013**, *499* (7459), 419–425.

(13) Novoselov, K.S., Mishchenko, A., Carvalho, A. and Neto, A. C. 2D Materials and van Der Waals Heterostructures. *Science (80-.).* **2016**, *353* (6298), aac9439.

(14) Ng, A.; Sutto, T. E.; Matis, B. R.; Deng, Y.; Ye, P. D.; Stroud, R. M.; Brintlinger, T. H.; Bassim, N. D. Chemically Exfoliating Large Sheets of Phosphorene via Choline Chloride Urea Viscosity-Tuning. *Nanotechnology*

2017, *28* (15), 155601.

(15) Kistanov, A. A.; Cai, Y.; Kripalani, D. R.; Zhou, K.; Dmitriev, S. V; Zhang, Y. A First-Principles Study on the Adsorption of Small Molecules on Antimonene : Oxidation Tendency and Stability. *J. Mater. Chem. C* **2018**, *6* (15), 4308–4317.

(16) Ji, J.; Song, X.; Liu, J.; Yan, Z.; Huo, C.; Zhang, S.; Su, M.; Liao, L.; Wang, W.; Ni, Z.; Hao, Y.; Zeng, H. Two-Dimensional Antimonene Single Crystals Grown by van Der Waals Epitaxy. *Nat. Commun.* **2016**, *7*, 13352.

(17) Wu, Q.; Song, Y. J. The Environmental Stability of Large-Size and Single-Crystalline Antimony Flakes Grown by Chemical Vapor Deposition on SiO2 Substrates. *Chem. Commun.* **2018**, *54* (69), 9671-9674.

(18) Ares, P.; Aguilar-galindo, F.; Rodríguez-san-miguel, D.; Aldave, D. A.; Díaz-tendero, S.; Alcamí, M.; Martín, F.; Gómez-herrero, J. Mechanical Isolation of Highly Stable Antimonene under Ambient Conditions. *Adv. Mater.* **2016**, *28* (30), 6332–6336.

(19) Ciesielski, A.; Samorı, P. Graphene via Sonication Assisted Liquid-Phase Exfoliation. *Chem. Soc. Rev.* **2014**, *43* (1), 381–398.

(20) Niu, L.; Coleman, J. N.; Zhang, H.; Shin, H.; Chhowalla, M.; Zheng, Z. Production of Two-Dimensional Nanomaterials via Liquid-Based Direct Exfoliation. *Small* **2016**, *12* (3), 272–293.

(21) Neill, A. O.; Khan, U.; Nirmalraj, P. N.; Boland, J.; Coleman, J. N. Graphene Dispersion and Exfoliation in Low Boiling Point Solvents. *J. Phys. Chem. C* **2011**, *115* (13), 5422–5428.

(22) Del Rio Castillo, A. E.; Pellegrini, V.; Sun, H.; Buha, J.; Dinh, D. A.; Lago, E.; Ansaldo, A.; Capasso, A.; Manna, L.; Bonaccorso, F. Exfoliation of Few-Layer Black Phosphorus in Low Boiling Point Solvents and Its Application in Li-Ion Batteries. *Chem. Mater.* **2018**, *30* (2), 506–516.

(23) Kuila, T.; Bose, S.; Mishra, A. K.; Khanra, P.; Kim, N. H.; Lee, J. H. Chemical Functionalization of Graphene and Its Applications. *Prog. Mater. Sci.* **2012**, *57* (7), 1061–1105.

(24) Loh, K. P.; Bao, Q.; Ang, P. K.; Yang, J. The Chemistry of Graphene. *J. Mater. Chem.* **2010**, *20* (12), 2277–2289.

(25) Jiang, S.; Krymowski, K.; Asel, T.; Arguilla, M. Q.; Cultrara, N. D.; Yanchenko, E.; Yang, X.; Brillson, L. J.; Windl, W.; Goldberger, J. E. Tailoring the Electronic Structure of Covalently Functionalized Germanane via the Interplay of Ligand Strain and Electronegativity. *Chem. Mater.* **2016**, *28* (21), 8071–8077.

(26) Jiang, S.; Butler, S.; Bianco, E.; Restrepo, O. D.; Windl, W.; Goldberger, J. E. Improving the Stability and Optical Properties of Germanane via One-Step Covalent Methyl-Termination. *Nat. Commun.* **2014**, *5*, 3389.

(27) Huey, W. L. B.; Goldberger, J. E.; Goldberger, J. E. Covalent Functionalization of Two-Dimensional Group 14 Graphane Analogues. *Chem. Soc. Rev.* **2018**, *47* (16), 6201–6223.

(28) Voiry, D.; Goswami, A.; Kappera, R.; Carvalho, C. De; Kaplan, D.; Fujita, T.; Chen, M.; Asefa, T.; Chhowalla, M. Covalent Functionalization of Monolayered Transition Metal Dichalcogenides by Phase Engineering. *Nat. Chem.* **2014**, *7* (1), 45–49.

(29) Manzeli, S.; Ovchinnikov, D.; Pasquier, D.; Yazyev, O. V; Kis, A. 2D Transition Metal Dichalcogenides. *Nat. Rev.* **2017**, *2* (8), 17033.

Chapter 8

Appendix - Dissemination

8. Appendix – Dissemination

8.1 Publications arising directly from this thesis

1. **Van Druenen, M**.; Collins, G.; Glynn, C.; O'Dwyer, C.; Holmes, J. D. Functionalization of SiO2 Surfaces for Si Monolayer Doping with Minimal Carbon Contamination. *ACS Appl. Mater. Interfaces* **2018**, *10* (2), 2191–2201.
2. **Van Druenen, M**.; Davitt, F.; Collins, T.; Glynn, C.; O'Dwyer, C.; Holmes, J. D.; Collins, G. Evaluating the Surface Chemistry of Black Phosphorus during Ambient Degradation´. *Langmuir* **2019**, *35* (6), 2172–2178.
3. **Van Druenen, M**.; Davitt, F.; Collins, T.; Glynn, C.; O'Dwyer, C.; Holmes, J. D.; Collins, G. Covalent Functionalization of Few-Layer Black Phosphorus Using Iodonium Salts and Comparison to Diazonium Modified Black Phosphorus. *Chem. Mater.* **2018**, *30* (14), 4667–4674.
4. **Van Druenen, M**. Degradation of Black Phosphorus and Protection Strategies (In preparation)
5. **Van Druenen, M**.; Collins, T.; Davitt, F.; Doherty, J.; Collins, G.; Sofer, Z.; Holmes, J.D. Stabilisation of Black Phosphorus using Sonication-Assisted Simultaneous Exfoliation-Functionalisation (In preparation)
6. **Van Druenen, M**.; Collins, T.; Davitt, F.; Collins, G.; Holmes, J. D. Smooth Exfoliation of Antimonene using an Intercalating Agent (In preparation)

8.2 Co-Authored Publications

1. Davitt, F.; Robinson, F.; Hawken, S.; Manning, H.; Biswas, S.; Petkov, N.; **van Druenen, M**.; Boland, J.; Reid, G.; Holmes, J.D. 'Crystallographically Controlled Synthesis of SnSe Nanowires: Potential in Resistive Memory Devices' (In Review)

8.3 Conference Presentations

1. **Van Druenen, M**.; O'Connell, J.; Collins, G.; Holmes, J.D. 'Functionalisation of Silicon Surfaces for Monolayer Doping Applications'. IOP Summer school on nanoScience@Surfaces, 1-4 August 2016, Cavendish Laboratory, Cambridge, UK (Poster)
2. **Van Druenen, M**.; Collins, G.; Davitt, F.; Collins, T.; Glynn, C.; O'Dwyer, C.; Holmes, J. D. 'Covalent Functionalisation of Black Phosphorus' Graphene2018, Dresden, Germany, 26-29 June 2018 (Talk)
3. **Van Druenen, M**.; Collins, G.; Davitt, F.; Collins, T.; Glynn, C.; O'Dwyer, C.; Holmes, J. D. 'Covalent functionalisation of Few-layer Black Phosphorus using Iodonium Salts and Comparison to Diazonium Modified Black Phosphorus' Bristol Centre for Functional Nanomaterials/UCC/Tyndall Symposium on Nanomaterials, Tyndall, Cork, Ireland, 27th July 2018 (Talk)